Lucas F. M. da Silva   *Editor*

Materials Design and Applications III

Advanced Structured Materials

Volume 149

Series Editors

Andreas Öchsner, Faculty of Mechanical Engineering, Esslingen University of Applied Sciences, Esslingen, Germany

Lucas F. M. da Silva, Department of Mechanical Engineering, Faculty of Engineering, University of Porto, Porto, Portugal

Holm Altenbach , Faculty of Mechanical Engineering, Otto von Guericke University Magdeburg, Magdeburg, Sachsen-Anhalt, Germany

Common engineering materials reach in many applications their limits and new developments are required to fulfil increasing demands on engineering materials. The performance of materials can be increased by combining different materials to achieve better properties than a single constituent or by shaping the material or constituents in a specific structure. The interaction between material and structure may arise on different length scales, such as micro-, meso- or macroscale, and offers possible applications in quite diverse fields.

This book series addresses the fundamental relationship between materials and their structure on the overall properties (e.g. mechanical, thermal, chemical or magnetic etc.) and applications.

The topics of *Advanced Structured Materials* include but are not limited to

- classical fibre-reinforced composites (e.g. glass, carbon or Aramid reinforced plastics)
- metal matrix composites (MMCs)
- micro porous composites
- micro channel materials
- multilayered materials
- cellular materials (e.g., metallic or polymer foams, sponges, hollow sphere structures)
- porous materials
- truss structures
- nanocomposite materials
- biomaterials
- nanoporous metals
- concrete
- coated materials
- smart materials

Advanced Structured Materials is indexed in Google Scholar and Scopus.

More information about this series at http://www.springer.com/series/8611

Lucas F. M. da Silva

Editor

Materials Design and Applications III

Editor
Lucas F. M. da Silva
Department of Mechanical Engineering
University of Porto
Porto, Portugal

Preface

This volume of *Advanced Structured Materials* contains selected papers presented at the 3rd International Conference on Materials Design and Applications 2020 (MDA 2020), held in online during 5–6 November 2020. The goal of the conference was to provide a unique opportunity to exchange information, present the latest results as well as discuss issues relevant to materials design and applications. The focus is on fundamental research and application areas in the field of the design and application of engineering materials, predominantly within the context of mechanical engineering applications. This includes a wide range of materials engineering and technology, including metals, e.g. lightweight metallic materials, polymers, composites, and ceramics. Advanced applications include manufacturing of new materials, testing methods, multi-scale experimental and computational aspects. Approximately 155 papers were presented by researchers from nearly 30 countries.

In order to disseminate the work presented in MDA 2020, selected papers were prepared which resulted in the present volume dedicated to 'Materials Design and Applications III'. A wide range of topics are covered resulting in 17 papers dealing with: metals, composites, additive manufacturing, tribology, forming and joining. The book is a state of the art of materials design and applications and also serves as a reference volume for researchers and graduate students working with advanced materials.

The organizer and editor wish to thank all the authors for their participation and cooperation, which made this volume possible. Finally, I would like to thank the team of Springer-Verlag, especially Dr. Christoph Baumann, for the excellent cooperation during the preparation of this volume.

Porto, Portugal
December 2020

Lucas F. M. da Silva

Contents

Part I
Metals

Chapter 1
Mechanical Testing of Extruded Magnesium for the Development of Automobile Seat Frame Structures

S. P. Sikora, L. Bergmann, E. Beeh, and H. Sulaiman

Abstract To validate a novel structural concept in magnesium lightweighting in early development stages, a magnesium alloy of type MgMnCe is characterized at coupon level and validated at profile level. The feasibility of friction stir welding is confirmed to integrate the alloy into the structure. Specimens are extracted from or set up on basis of generic profiles. For characterization among others, miniature tensile specimens in extrusion and transverse direction are utilized. Tensile results show the orthotropic material character of the ME21 alloy used. In transverse direction, stiffness as well as strength increases, while elongation at break decreases. The material shows a strongly nonlinear, irreversible material behavior starting at small loads and a moderate strain rate dependency. On profile level, closed rectangular profiles in four-point bending are used for validation at high impact velocities. These tests reveal large deformation without local failure. This deformation makes the use of closed rectangular profiles promising for the application in seat backrest structures.

Keywords Magnesium alloy · ME21 · Extrusion · Material characterization · Closed profile · Friction stir welding

1.1 Introduction

In large-scale production of vehicle seats, high and ultra-high strength steel alloys prevail because of challenging requirements. The potentials of metal lightweight structures using steel and aluminum are exhausted to a large extent. The German

S. P. Sikora (✉) · E. Beeh
Institute of Vehicle Concepts, Material and Process Applications for Road and Rail Vehicles, German Aerospace Center (DLR e.V.), Stuttgart, Germany
e-mail: sebastian.sikora@dlr.de

L. Bergmann
Institute of Materials Research, Materials Mechanics, Solid-State Joining Processes, Helmholtz-Zentrum Geesthacht GmbH, Geesthacht, Germany

H. Sulaiman
Seat Structure Systems Division, Advanced Manufacturing Engineering, Metal Forming, Faurecia Autositze GmbH, Stadthagen, Germany

national project FUMAS (Functionally Integrated Magnesium Lightweighting for Automobile Seat Structures) aims at weight reduction of a seat structure by using extruded magnesium and a novel process route in manufacturing. A concept for a lighter seat backrest structure is developed, dimensioned and evaluated. This predevelopment process is based on digital as well as experimental methods and is validated with generic substructures. The development process is finalized with an impact test on a prototypical seat structure. The partners of FUMAS are shown in Fig. 1.1.

FUMAS uses a magnesium alloy of type MgMnCe in an extrusion process. The main alloy constituents are about 1.5% manganese, 1% rare earth elements (cerium and lanthanum), mainly being cerium. For simplicity, the material will be called ME21. Other similar ME21 alloys were examined earlier (Gall et al. 2013; Huppmann et al. 2010). Here, the manganese proportion was higher at above 2%, and magnesium sheets were investigated, not applying the material in a structure.

In FUMAS, two concepts have been developed — a primary concept variant utilizing friction stir welding (FSW) and an alternative concept variant basing on injection adhesive bonding (IAB). This work will focus on the FSW concept, which is displayed in Fig. 1.2. The primary concept variant consists of an upper magnesium assembly and a bottom steel assembly. The three-part magnesium frame structure contains a frame profile realized as formed extrusion profile with a thickness of 4 mm and a pair of 2 mm thick surrounding support structures. The steel structure is a state-of-the-art welded assembly of two so-called mobile gussets and the cross member. The shown Mg-Mg lap joint as well as the Mg-St lap joint are joined by means of FSW.

The paper at hand presents fundamental experiments used in the development process of the structure. Experiments concerning the material, the structure and the joining technologies have been used. The ones that are mechanically essential for the solution design will be shown in the following sections — starting with the characterization of the magnesium alloy at coupon level (Sect. 1.2) and continuing to a validation on profile level (Sect. 1.3). The main experimental studies concerning FSW feasibility for the integration of magnesium into the concept complete the main body of this work (Sect. 1.4). Section 1.5 summarizes and concludes.

Fig. 1.1 FUMAS project logo and consortium

Fig. 1.2 Primary FUMAS concept for the seat backrest structure based on friction stir welding of a magnesium and a steel assembly
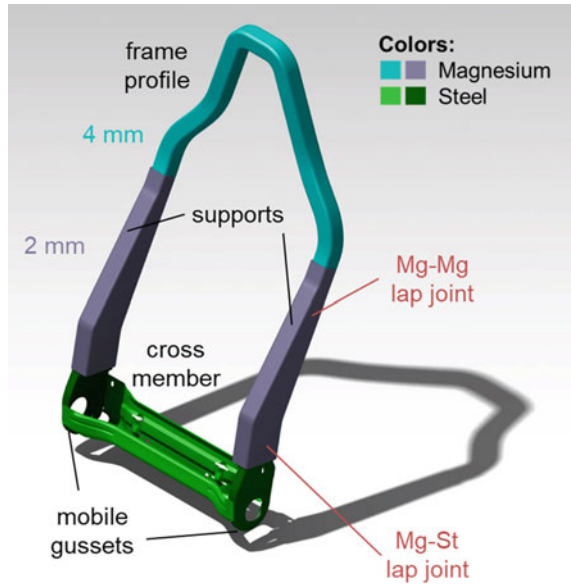
1.2   Characterization at Coupon Level

Based on an early version of the structure concept, generic extruded profiles (Fig. 1.3) were used to extract various coupon specimens — in extrusion direction (ED) and transverse direction (TD). This double chamber profile consists of closed rectangular chambers with wall thicknesses of 2 and 4 mm with a connection, which is 3 mm thick.

Fig. 1.3 Generic profiles used for diverse coupon extraction
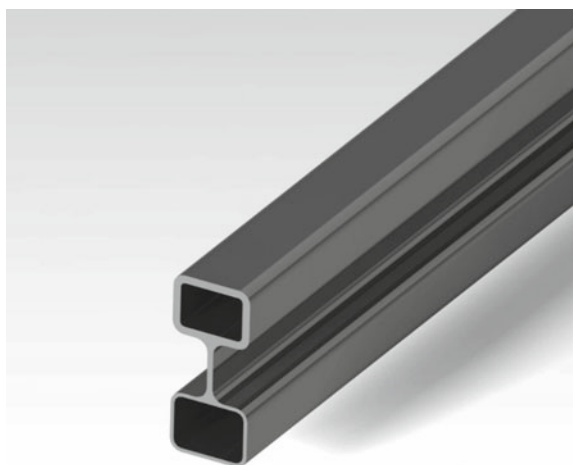
To start the characterization of the ME21 alloy, quasi-static tension and compression tests were conducted to evaluate orthotropy and tension–compression asymmetry of the material. The resulting representative engineering stress–strain curves are shown in Fig. 1.4, where relative displacements were optically determined with greyscale correlation in plane (2D). Standardized tensile tests close to DIN 50,125 were used in extrusion direction, which revealed an ultimate strength of 205 MPa and a break elongation of 16%. In transverse direction, a miniature specimen geometry was chosen to enable extraction from the lid of the rectangular profiles. Consequently, these miniature specimens have a total length of 28 mm, an optical gauge length of 4 mm measuring a rectangular cross section with a width of 3 mm. To prove validity of these specimens, first of all, tests in extrusion direction have been repeated with the miniature geometry. As shown in Fig. 1.4 and as desired, the results are the same as for standardized tests. Therefore, proceeding with the miniature specimens in transverse direction, a significant orthotropy is determined for ME21. The transverse ultimate tensile strength is 229 MPa, and the elongation at break is 12.5%. Also, the stiffness at small strains rises significantly, compare Fig. 1.4. For compression tests, the test of Zhou et al. (2016a) is used. This testing method uses a single-sided groove in a supporting testing apparatus. Lateral support of the thin-walled coupon is required only at the backside of the specimen. This compression test yields the results in Fig. 1.4 in extrusion direction. Differences between tension and compression are significant. But at first glance, the difference of yield strength between tension and compression is smaller than known from other magnesium alloys like AZ31, referring to the studies of Zhou et al. (2016a, b). This depends on the determination and definition of the yield strength.

To investigate the material concerning elastic and plastic (or irreversible) deformation, cyclic quasi-static tensile tests with increasing load were conducted using strain gauges centrally applied on standardized specimens. At constant and equal loading
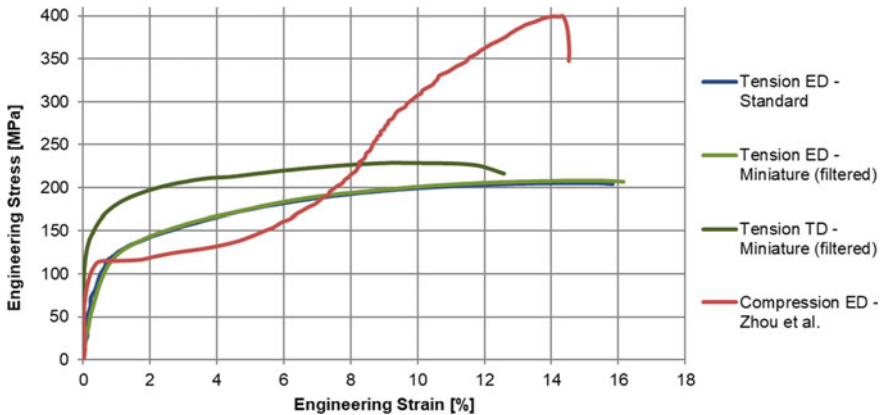
Fig. 1.4 Stress–strain curves in tension and compression for extrusion and transverse direction — orthotropy and tension–compression asymmetry of ME21. Coupon thickness 2 mm
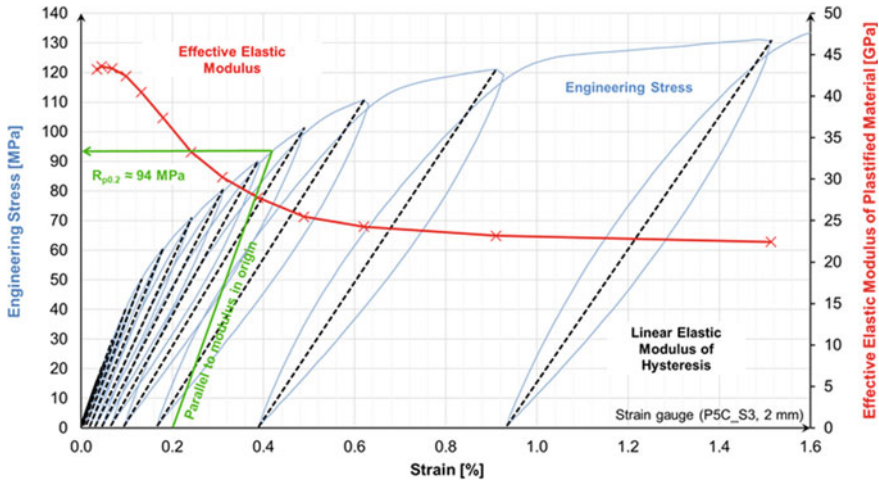
Fig. 1.5 Cyclic quasi-static tensile tests with increasing load — effective elastic stiffness

and unloading traverse velocity, the specimen is loaded up to 20 MPa, unloaded, then loaded to 30 MPa and so on every cycle increasing the load by 10 MPa. The results for a representative specimen are compiled in Fig. 1.5, where hysteresis loops become apparent for unloading and reloading processes. Starting at small loads already, a nonlinear stress–strain behavior is observed, considering the envelope of the curve, and remaining strains in the unloaded states are captured. The upper reversal points (reaching the defined load levels) and the lower reversal points in the unloaded states are used to determine effective elastic moduli of the plastified material for all levels. These linear elasticity magnitudes are also illustrated in Fig. 1.5. For deformation close to zero, i.e., small hysteresis loads, an effective modulus of about 44 GPa is determined, as expected for magnesium alloys. Then, with increasing strain, the effective modulus drops to half of its original value (22 GPa), which denotes a significantly lower stiffness of the plastified material. In the application, this means changing elastic properties when preloads, e.g., from misuse load cases, have affected the material. Revisiting the evaluation of the yield strength, the frequently used yield strength $R_{p0.2}$ is also visualized in Fig. 1.5. It can be found close to 90 MPa, showing that a considerable nonlinearity is neglected using this characteristic. The material shows a strongly nonlinear, irreversible material behavior, which suggests the use of a low plastic limit to model it numerically.

In seat structure development, the most demanding load cases are crash load cases, in this case, especially the rear impact. Therefore, coupon testing to determine the strain rate sensitivity is crucial. Tensile tests according to DIN EN ISO 26203-2 were conducted. A specimen is shown in Fig. 1.6a and the results for representative specimens in Fig. 1.6b for a range of the piston velocity from 0.01 mm/s up to 1000 mm/s — thus covering five orders of magnitude. The results suggest that there is primarily a strain rate dependency in the two lowest orders of magnitude (belonging

(a)

(b)
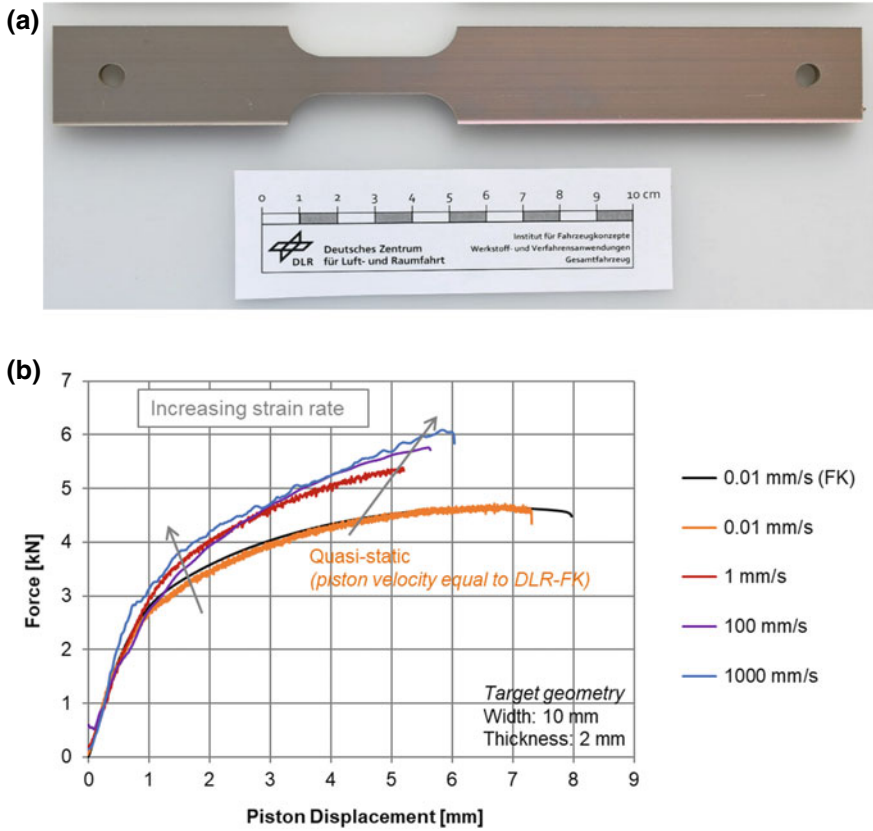
Fig. 1.6 Dynamic tensile tests: **a** specimen, **b** force–displacement curves for different piston veloc-ities. The two different curves at 0.01 mm/s were measured using different machines: a quasi-static (at DLR-institute FK) and a high-velocity testing machine

to range from 0.01 to 1 mm/s piston velocity). Here, strength rises and elongation at break drops. From there to higher strain rates, only a slight increase of strength and elongation at break is observed.

Beyond the presented tests, a big range of further aspects was experimentally covered. It may be emphasized that for all these studies, coupons have been cut from the profiles introduced in Fig. 1.3. Further dependencies that were screened and studied are:

- Material thickness (2 mm / 4 mm): Nearly, no change observed in tensile strength, but increased stiffness and elongation at break for 4 mm thickness.
- Profile instance: No systematic dependencies from profile detected.

- Position in profile (lid or sides, front/center/back): No dependency from extraction side, no changes along profile length found.
- Other stress states tested: Shear, shear tension, notched tension.

As a next step, the material application is validated using profiles.

1.3 Validation at Profile Level

One of the critical requirements in seat development is that the structure may not rupture locally in set crash situations. Many materials tend to embrittle at high strain rates, which is also the concern for magnesium structures. To experimentally study whether the design potentially can bear required loads, bending at high impact velocities was considered. In rear crash situations inertia pushes the passenger into the backrest rapidly resulting in bending of the seat structure with a load at the neck contact, compare Fig. 1.2. From there, the load has to be transferred into the body of the vehicle via the mobile and later the fixed gussets. The first abstraction level of one half of the backrest structure is a rectangular closed profile (single-chamber profile), which also can be extracted from the generic profile in Fig. 1.3. To comply with the length of a backrest structure, a length of 720 mm was chosen. The choice of four-point-bending, an outer rigid anvil distance of 600 mm and an inner one of 200 mm lead to the test setup as shown in Fig. 1.7a. The chamber profiles have an outer rectangular shape of 40 mm in width and 30 mm in height. Here, the upper traverse is the fixed and the piston is the moving component. The inner rigid anvils as well as the inner four-point bending adapter are attached to the piston that is driven by a hydraulic testing machine. Two force transducers are installed between the traverse and the frame of the machine. Figure 1.7a shows an example of a situation after a test of a profile with 4 mm thickness. As desired, in this case, no local rupture or other failure was observed. The tested profile exhibited large plastic deformation, which is considered as extremely good-natured behavior.

Figure 1.7b shows force–displacement results for the two different wall thicknesses 2 and 4 mm for increasing piston velocities. The piston velocities range from 0.1 mm/s up to 10 m/s. At the maximum (36 km/h), this is the magnitude of impacts considered in seat development like required in UN/ECE-R17 or other regulations. Comparing the magnitude of the load at the same piston velocity, it is recognizable that the load transfer increases disproportionately with the profile thickness. Doubling the thickness almost leads to a tripling of the load transferred. This is due to the fact that with the chosen constraints (anvils) in the test, local failure can be observed for 2 mm thickness at anvil contact resulting in local buckling. Thus, for the chosen rectangular profile with 2 mm thickness, the contact and load transfer is not designed appropriately. For 4 mm thickness, this is the case, and therefore smooth, good-natured deformation is induced. This makes lightweighting using extruded magnesium promising for seat development, requiring a suitable design. Also, it has been shown that increasing strain rate does not lead to embrittlement.

(a)

(b)
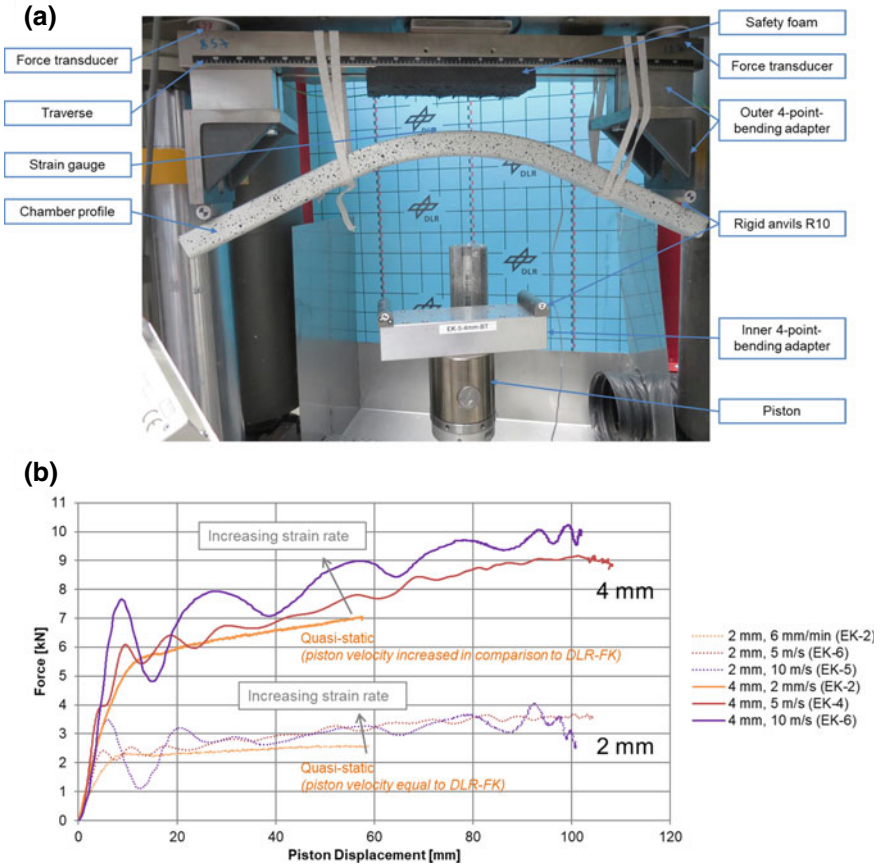
Fig. 1.7 Dynamic profile four-point bending tests: **a** test setup with deformed profile after test, **b** force–displacement curves for different piston velocities for both wall thicknesses 2 and 4 mm. All results determined at the same high-velocity testing machine and filtered. Quasi-static tests stopped earlier than impact tests at high speeds, thus end of curve not comparable

1.4 Integration into Concept with Friction Stir Welding

In FUMAS, as primary joining technology, friction stir welding (FSW) was pursued to integrate magnesium parts into the structure. The process was patented in 1991 by TWI in the UK and by now is mature to be used in large-series production. The main motivation for this welding process is to use an environmentally-friendly process (no additional material or shielding gas). FSW is a solid-state joining process, i.e., the needed energy to perform the process is reached below the melting point of the base material, eliminating re-solidification problems and resulting in less distortion of the welded components. A further advantage of FSW is that due to the intensive mechanical work, during stirring of the material, there is a strong grain refinement

Fig. 1.8 FSW tool geometry
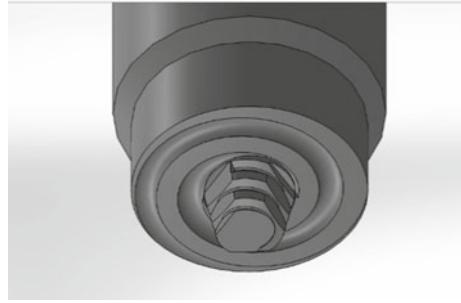
in the stir zone (weld nugget), increasing the mechanical properties in the stir zone (SZ).

ME21-ME21 in butt-joint configuration considering process and quality

In order to develop proper FSW process parameters (rotational speed, welding speed, force) to weld ME21, a FSW tool with a scrolled shoulder and conical threaded probe with 2.75 mm length was used, shown in Fig. 1.8.

In Fig. 1.9a, an example ME21-ME21 butt-joint configuration joining the generic profile is shown. At the joint, the material thickness is 3 mm. A welding speed of 1.5 m/min was used. The resulting welding surface shows an excellent surface finishing — with no flash or underfill, compare Fig. 1.9b. In Fig. 1.9c, the cross section of the weld with the stir zone in the center is shown, which represents the volume of the material subjected to severe mechanical work. This reduces the grain size in the SZ, as can be seen in the microstructure in Fig. 1.9d.

In order to determine the mechanical properties, samples with 20 mm weld length (in depth direction of Fig. 1.9a) have been tested in quasi-static conditions achieving an ultimate tensile strength (UTS) of 110 MPa for the profile specimen. The failure occurred outside the weld at the curvature of the extruded profile, demonstrating that the weld is not the critical location for this butt-joint specimen.

ME21-ME21 in butt- and lap-joint configuration considering process forces

In case the stiffness of the profile is not sufficient to bear and transfer the FSW process forces, the profile collapses, deforms or reveals internal volumetric defects within the joint. Figure 1.10a presents an example of a butt-joint configuration, in which the profile is locally being deformed by the tool producing a volumetric defect inside the joint. Figure 1.10b shows a second example, where the supporting lower joining partner in a lap-joint configuration does not withstand the process forces completely. Therefore, some volumetric defects are observable. In this joint configuration, the tool probe plunges through the upper material until inserted into the lower material between 0.5 mm up to 1 mm, joining both profile lids.
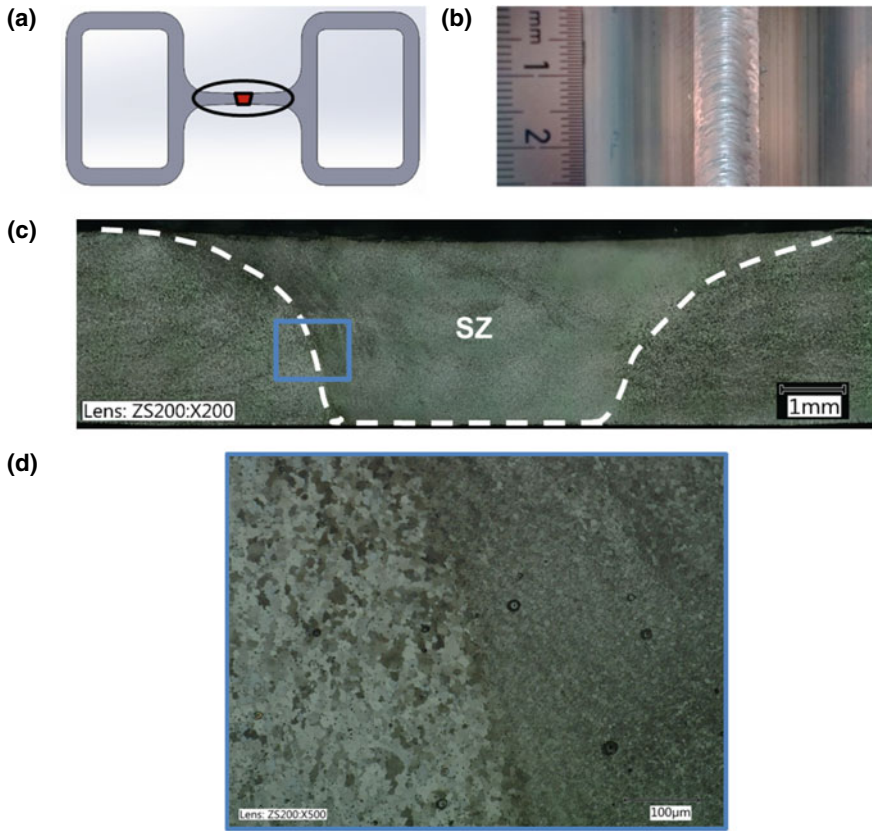
Fig. 1.9 FSW ME21-ME21 butt joint: **a** configuration in generic profile, **b** surface finishing, **c** cross section, **d** microstructural change in the transition zone

ME21-DP1000 in lap-joint configuration considering weldability

In order to produce sound welds in an overlap-joint configuration, the softer material is typically positioned on the side where the tool is contacting first. There is no restriction for metallic material combinations (Suhuddin et al. 2017). Recently, developments in refill FSW at HZG show that it is also possible to weld polymers with metallic materials (André et al. 2018, 2019). In the FUMAS magnesium–steel joint, there is no feasibility to position the steel material on the tool side. Considering the temperature to plasticize steel of around 900 °C, far above the melting temperature of the magnesium, the materials cannot be stirred. With the FSW tool positioned on the magnesium side, the tool plunges through the magnesium scratching the steel surface in order to activate the surface and get improved diffusion bonding. The mechanical anchoring is also increased due to the roughness created at the interface.

Welds were performed using 2 mm thick ME21 and 0.8 mm thick DP1000 with a welding speed of 500 mm/min and tool probe length of the magnesium base material
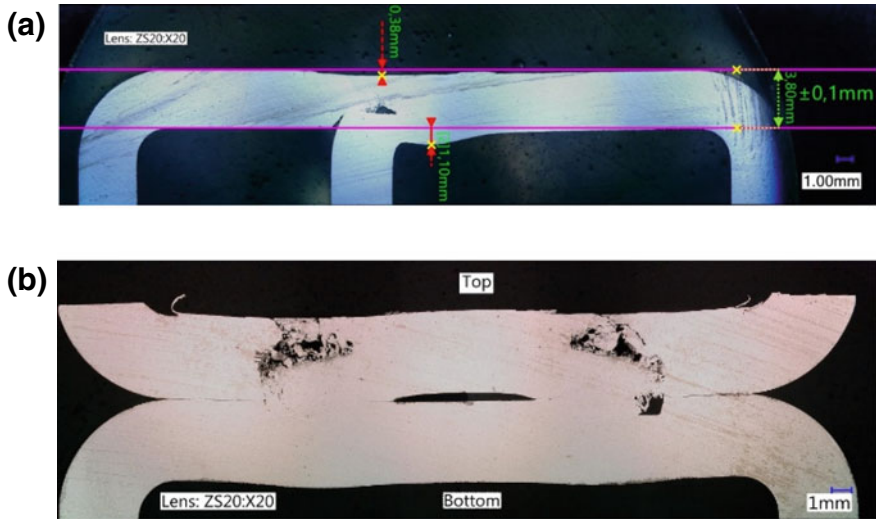
Fig. 1.10 Defects and deformation in FSW ME21-ME21 joints: **a** butt joint in modified generic profile joining lid and corner, **b** lap joint of generic profile lids
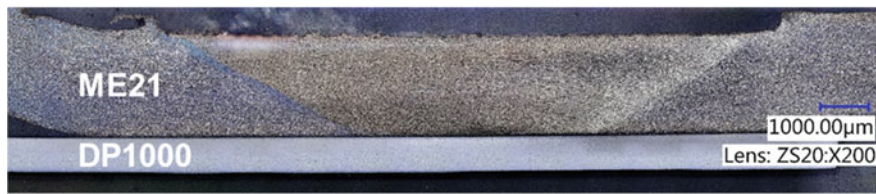
Fig. 1.11 FSW ME21-DP1000 lap joint: cross section

thickness. The cross section shows the stir zone located in the magnesium and no deformation in the steel, compare Fig. 1.11.

In order to determine the mechanical properties of this joint type, single-lap tensile shear specimens 50 mm wide (corresponding to weld length) were cut and were quasi-statically tested. As a result, a UTS of 186 N per mm weld length was obtained.

Referring to Fig. 1.2, in the final seat backrest design, Mg-Mg and Mg-St lap-joints are implemented, for which feasibility according to the shown studies is validated.

1.5 Conclusion

A large variety of experiments enabled the development of a seat backrest structure made of a magnesium alloy of type MgMnCe (ME21) using formed profiles. The key contents and conclusions of this paper are:

- The FUMAS seat frame concept uses an extruded magnesium alloy in a novel way that has yet to be fully exploited.
- Experimental validation ranges from microstructure studies via chamber profiles to a prototypical linear impactor test of the seat structure.
- The magnesium alloy of type MgMnCe has been characterized extensively: It reveals an orthotropic, strongly nonlinear, moderately strain rate dependent stress–strain behavior.
- Structural generic validation has been based on four-point bending of chamber profiles demonstrating large ductile deformations, which are promising for seat development.
- Friction stir welding is applied to integrate magnesium into the concept considering process forces and weldability, focusing on lap-joint configuration. Welding speeds with industrial relevance have been determined.

References

André, N.M., Goushegir, S.M., Scharnagl, N., dos Santos, J.F., Canto, L.B., Amancio-Filho, S.T.: Composite surface pre-treatments: Improvement on adhesion mechanisms and mechanical performance of metal-composite friction spot joints with additional film interlayer. J. Adhes. **94**(9), 723–742 (2018)

André, N.M., dos Santos, J.F., Amancio-Filho, S.T.: Evaluation of joint formation and mechanical performance of the AA7075-T6/CFRP spot joints produced by frictional heat. Materials **12**, 891 (2019)

Gall, S., Coelho, R.S., Müller, S., Reimers, W.: Mechanical properties and forming behavior of extruded AZ31 and ME21 magnesium alloy sheets. Mater. Sci. Eng. A **579**, 180–187 (2013)

Huppmann, M., Gall, S., Müller, S., Reimers, W.: Changes of the texture and the mechanical properties of the extruded Mg alloy ME21 as a function of the process parameters. Mater. Sci. Eng. A **528**, 342–354 (2010)

Suhuddin, U.F.H., Fischer, V., Kostka, A., dos Santos, J.F.: Microstructure evolution in refill friction stir spot weld of a dissimilar Al–Mg alloy to Zn-coated steel. Sci. Technol. Weld. Joining **22**(8), 658–665 (2017)

Zhou, P., Beeh, E., Friedrich, H.E.: A novel testing method for uniaxial compression of thin-sheet magnesium alloys. Exp. Mech. **56**, 513–519 (2016a)

Zhou, P., Beeh, E., Friedrich, H.E.: Influence of Tension-compression asymmetry on the mechanical behavior of AZ31B magnesium alloy sheets in bending. J. Mater. Eng. Perform. JMEPEG **25**, 853–865 (2016b)

Chapter 2
Failure Modes of Anodized Automotive Aluminum Alloys: A Review

N. Laszlo and N. Takacs

Abstract The use of aluminum alloys is showing an ever-increasing trend today due to its favorable properties. Their properties can be further improved and enhanced by surface treatment and modification procedures. Of these processes, anodization is the best known and most commonly used process that can improve the wear and corrosion resistance of aluminum alloys. This is especially important in the automotive industry, where materials often have to be resistant to special stresses. This article provides an insight into the most common types of damage to anodized alloys and anodizing defects.

Keywords Anodizing · Surface treatment · Failure · Defects

2.1 Introduction

Due to the dynamic development of the automotive industry, increasing demands—such as safety and reliability, weight reduction, fuel consumption, and thus emission reductions—cannot be met by "traditional" materials (such as steels) in all cases. As a result, there is an increasing need for alloys with low density and mass, but with adequate mechanical properties (high fatigue limit and strength, elongation of about 10–14%) and well plasticizability (Hirsch 1997; Miller et al. 2000).

In the case of modern material development trends, two directions can be observed. A significant proportion of research focuses on the development of high and ultra-high strength steels, while the demand for the development of light metals, including aluminum, magnesium, and titanium alloys, is constantly growing (Kulekci 2008; Blawert et al. 2004; Sachdey et al. 2012; Hartman et al. 1994; https://www.makin-metals.com/about/uses-of-copper-in-cars/).

N. Laszlo (✉) · N. Takacs
Department of Industrial Materials Technology, Bay Zoltán Nonprofit Ltd. for Applied Research, Igloi str. 2., 3519 Miskolc, Hungary
e-mail: noemi.laszlo@bayzoltan.hu

N. Takacs
e-mail: nora.takacs@bayzoltan.hu

Aluminum alloys can be a suitable alternative to the materials of heavier components in motor vehicles due to their strength/stiffness to weight ratio, formability, and potential for recyclability. The use of aluminum in the automotive industry has grown significantly in recent years. While in the past an average of 110 kg of aluminum was used in cars, today it reaches 250–340 kg (Sears 1997).

The automotive applicability of pure aluminum is limited. Although it has excellent properties in terms of corrosion resistance, its mechanical properties are poor. The introduction of alloying elements can improve its mechanical properties, but their resistance to corrosion decreases (Sukiman and et al. 2013; Sheasby and Pinner 1987). One possible way to overcome this problem is to increase the oxide layer on the surface of aluminum alloys, which can be achieved by electrochemical methods such as anodizing (Grubbs 1997; Konieczny and et al. 2004).

The currently available literature mostly deals only with the mechanical properties (hardness, roughness, wear property) of anodized alloys (Zhao and et al. 2015; Chen and et al. 2009; Shanmughasundaram and Subramanian 2013; Ovundu and et al. 2015; Wei et al. 2005), however, there is relatively little available knowledge about the typical damage modes of anodized aluminum alloys. The investigation of this is important because during the automotive applications the anodized layer can be damaged (wear, scratches, chipping, detachment, etc.), thus, deteriorating the properties and resistance of the aluminum alloy. This paper focuses on the typical failure modes of anodized aluminum alloys.

2.2   Failure Modes

2.2.1   Surface Failure Modes

In the case of anodized aluminum alloys, the damage modes of the layer are mostly in their appearance, source, and category according to the stage of production. These are the earliest types of damage to pits, streaks, or an uneven appearance. There are cases where the cause of the damage was carried by the raw material (e.g., thermomechanical treatment of the raw material or the presence of contaminants) with responsibility. Based on these, the damage modes of anodized alloys can be summarized according to Fig. 2.1

2.2.1.1   Corrosion

Pitting is a typical form of corrosion damage that can occur before, during, and after anodizing (https://www.defects.qualanod.net/3.html; Ajeel et al. 2010). The appearance of pitting a based on the product life cycle—is illustrated in Fig. 2.1. (Short 2003).
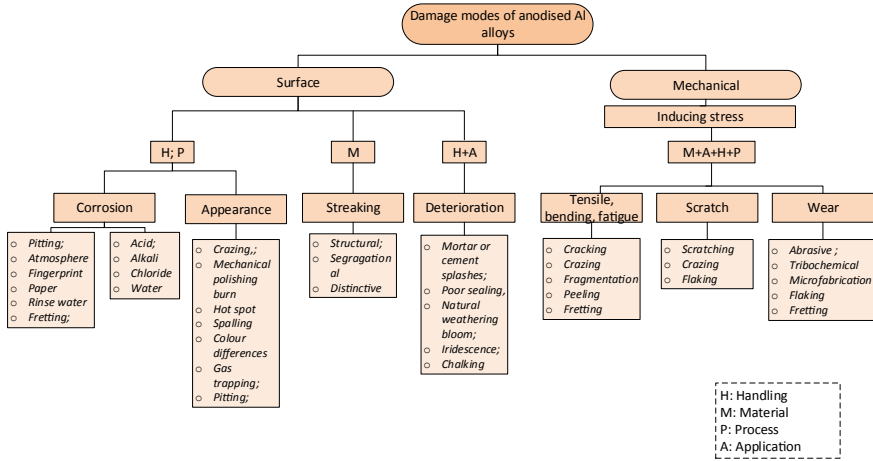
Fig. 2.1 Typical damage modes of anodized aluminum alloys

In case of *atmospheric corrosion* (González 2002; Santana Rodriguez and Snatana Hernández 2003), under operating conditions, the atmospheric environment may be corrosive due to gases released during etching, pyrometallurgical processes, or heat treatments (e.g., sulfur and nitrogen oxides), these gases may attack the surface of the samples. The so-called the appearance of dimples is mostly observed in places where the oxide layer is weakest, such as die lines on extrusions (Fig. 2.2).

Fingerprint corrosion (Short and Sheasby 1974) is a form of damage that occurs after extrusion as a result of pre-anodizing treatment and is caused by sweating of human fingers, as the sweating is acidic, containing chloride ions, which can attack the thin film layer, causing localized, rapid corrosion of the aluminum substrate.
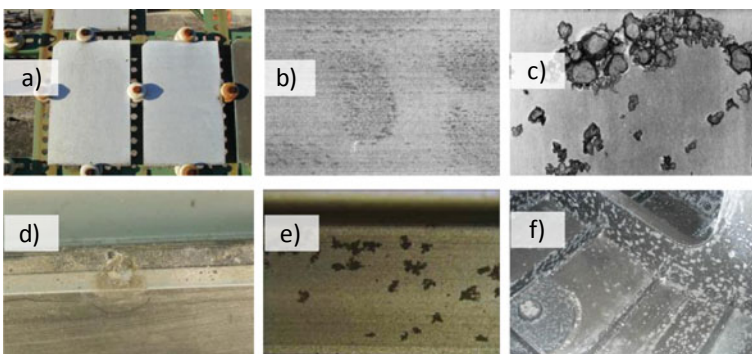
Fig. 2.2 Typical manifestations of corrosion conditions **a** atmosphere corrosion; **b** footprint corrosion; **c** fretting; **d** acid corrosion; **e** rinse water corrosion; **g** pitting; (http://www.defects.qualanod.net/3.html; https://www.amteccorrosion.co.uk/aluminium.html; Short and Sheasby 1974)

In the case of *paper corrosion* (Short and Bryant 1975), acidic radicals (e.g., chlorides) in wet packaging used during the transport or storage of aluminum under unsuitable conditions result in characteristic puncture-like corrosion on the surface of the part, which usually appears after etching or anodizing.

Improper storage in the plant can also cause corrosion, such as accidental splashes caused by acids and alkalis, which can result in the formation of pits before anodizing (Short and Sheasby 1974).

Pitting can occur at several stages of the anodizing pretreatment operation. The so-called rinse water corrosion is a characteristic corrosion form of the rinsing phase following deacidification, which can lead to the formation of white small dimples on the surface.

During the anodizing operation, the cause of pitting is usually the sulfuric acid or oxalic acid used during anodizing. The electrolyte is usually contaminated with chloride ion, and the source of which is the mains water used to produce the electrolyte. Although this may initially be low in concentration, it may be concentrated due to evaporation loss of the electrolyte. Electrolytes can be characterized by so-called with a critical chloride ion concentration of 80 ppm in sulfuric acid-containing electrolyte solutions and 20 ppm in oxalic acid solutions (https://aluminium-guide.com/en/defekty-anodirovaniya-alyuminievyx-profilej-klassifikaciya/). This is because oxalic acid electrolytes are much more sensitive to chloride ions.

Pitting can also occur under the conditions of use of anodized parts, in which case the SO_2 content of the atmosphere can be considered as the main cause.

2.2.1.2 Streaking Defects

Streaking can be defined as the surface roughness of anodized parts, and the origin of which is mostly metallurgical or physical damage to the surface. The reason for the formation of *segregation streaking* (Zhu et al. 2007) is the change in the size distribution of the intermetallic compound particles. The main cause of *structural streaking* (Zhu et al. 2010) is a change in particle size, orientation, and microstructure of the aluminum product. Such strips are mainly observed in extruded products, as extrusion can cause a change in particle size (Dargusch and Keay 2009; Zhu et al. 2012; Short and Bryant 1975). Figure 2.3 shows examples in case of streaking and flecking.

In the case of *flecking*, darker and lighter spots and streaks are observed on the surface due to the uneven distribution of the iron-containing phases. Intermetallic particles such as TiB_2, MgO, or Al_2O_3 spinels can also cause dimples or protrusions on the surface.

2.2.1.3 Non-uniform Appearance

This category includes *crazing, mechanical polishing burn* (https://aluminium-guide.com/en/defekty-anodirovaniya-alyuminievyx-profilej-klassifikaciya/), *hot*
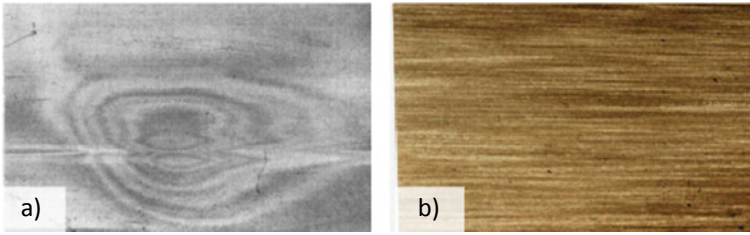
Fig. 2.3 Typical damage modes in case of streaking: **a** segregation streaking; **b** flecking (Short and Bryant 1975)

spot, spalling (ISO 7583:2013)*, color differences, gas trapping, and pitting* (Nakano et al. 2007). The typical manifestations of each defects are illustrated in Fig. 2.4 (Short and Bryant 1975).

These defects are basically created during the process. *Crazing* (https://alumin umsurface.blogspot.com/2009/06/crazing-defects-cracks-in-anodic-layer.html) is damage (https://www.aacron.com/docs/Crazing%20Caused%20By%20Bending%20and%20Forming%20Operations.pdf) in the anodized layer in the form of cracks (Castellero et al. 2008). In case of mechanical polishing burn, the frictional heat generated during the polishing of the alloy due to excessive pressure can cause the surface to overheat, traces of which may form during anodizing, and deteriorating the aesthetic appearance of the product (Short and Bryant 1975).

Spalling (ISO 7583:2013; Fratila-Apachitei et al. 2006) is a form of damage similar to pitting. This defect occurs mainly in the production of duplex films, when too high a current density or the sodium content of the electrolyte solution causes sub-layer corrosion, and the defect is mainly observed for alloys with a high zinc content.
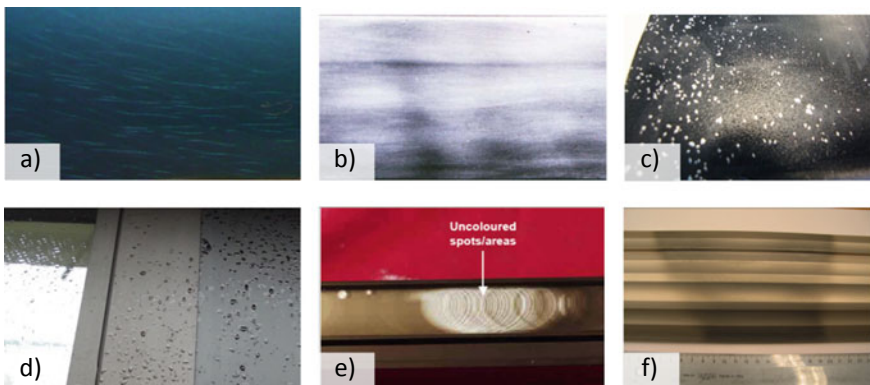
Fig. 2.4 Typical manifestations of defect in case of non-uniform appearance: **a** crazing; **b** mechanical polishing burn; **c** hot spot; **d** spalling; **e** color differences; **f** gas trapping (http://www.defects.qualanod.net/3.html; Short and Bryant 1975)

In the case of a *hot spot*, dark spots appear on the surface of the part with the same orientation as the direction of extrusion. The formation of dark spots is often caused by Mg-Si precipitation (Short and Bryant 1975). For darker spots, the hardness of the part is lower. In some cases, regular-shaped, lighter spots can be observed on the workpiece due to gas bubbles adhering to the surface of the sample during anodizing, which has a masking, insulating effect in the process, therefore, no layer is formed on these surfaces, and this defect is *gas trapping* (Skeldon et al. 1997; Iglesias-Rubianes et al. 2003).

2.2.1.4   Deterioration Defects

These defects occur during normal use. Defects include *pitting, staining due to mortar or cement splashes, staining due to poor sealing, natural weathering bloom, and iridescence* (Furneaux 2011; Ofoegbu et al. 2020). Figure 2.5 illustrates the typical appearance of each defect. In architectural applications, the effect of the wet mortar, due to the logic of the mortar, can damage the anodized layer, which is also indicated by the whitening of the surface in spots. In case of *staining due to poor sealing*, similar to the previous damage, the oxide film is damaged by the chemical reaction that occurs. The surface of anodized parts is often called flowering is observed, which
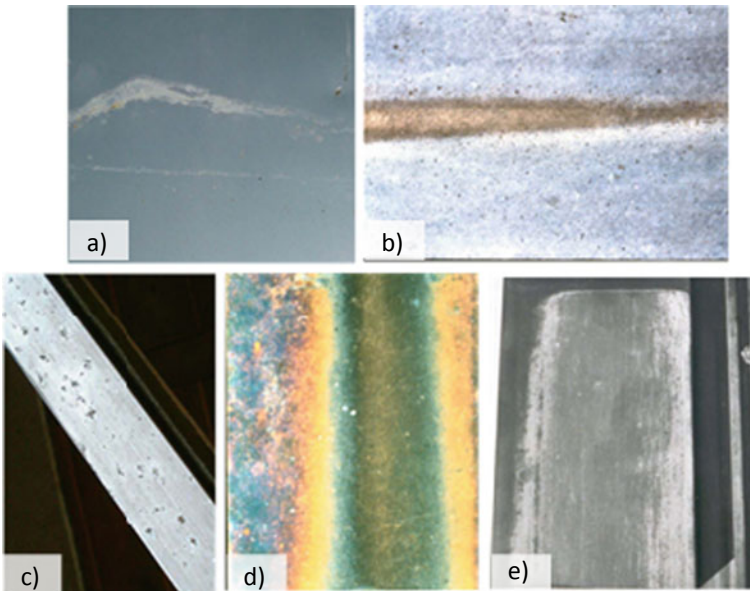
Fig. 2.5 Typical deterioration defects: **a** staining due to mortar or cement splashes; **b** staining due to poor sealing, **c** natural weathering bloom; **d** iridescence; **e** chalking or white bloom on soft anodic films (https://aluminium-guide.com/en/defekty-anodirovaniya-alyuminievyx-profilej-klassi fikaciya/; http://www.defects.qualanod.net/3.html)

occurs in contact with the environment as a result of improper cleaning. In the first 1–2 years of application, the discoloration of the anodized layer is often observed as a result of environmental effects if not properly cleaned.

2.2.2 Mechanical and Tribological Failure Modes

2.2.2.1 Damage Due to Tensile and Bending Stress

Anodized layers are generally brittle, so their tensile strength and elongation are low, but their compressive strength is very significant. The brittleness is higher in the plane perpendicular to the direction of formation (thickening) of the oxide layer; therefore, it tends to crack to a greater or lesser extent when bending the anodized aluminum, depending on the production method, composition, and thickness of the oxide layer. Fine hairline cracks in oxide layers with good pore sealing have little effect on the decorative or protective effect of the coating, but coarser cracks in thicker oxide layers during higher bending can cause local deterioration and cracking of the coating.

During tensile stress (Mearini and Hoffman 1993), the metal core part and the oxide layer stretch together under the effect of the load, until the load-bearing capacity of the brittle hard oxide, respectively, reaches its transformation limit. After crossing the boundary, ever-widening hairline cracks appear in the oxide layer and from then on the load is borne solely by the metal. The groove action of the hairline cracks in the oxide layer naturally affects the load-bearing capacity of the parent metal, so that the specimen ruptures at a lower tensile force than a non-oxidized, smooth-surfaced specimen of similar cross-section.

During the *bending* (Kasi et al. 2017) test, rough cracks appear on the drawn side of the specimens coated with a thick oxide layer in the case of some bending, while on the pressed side, the high compressive strength hard oxide has a definite "supporting" effect. As a consequence, as the bending yield point increases, the residual deformation occurs only under a higher bending load than that of the unoxidized sheet. However, the adhesion of the oxide layer is so strong that the oxide does not bounce off the surface on the drawn side, even if the metal is already torn (Csokán 1975). Figure 2.6 shows the behavior of the anodic oxide coating under bending stress.

2.2.2.2 Wear and Scratch

Anodized layers have a higher hardness than the substrate metal, but due to their porosity, their wear resistance is moderate. In practice, there are many application examples where the frequent use of these layers is scratch (Mishra et al. 2015; Osborn 2014) and wear (Feki et al. 2009; Campbell 1951; Bargui and Wery 2017),

Fig. 2.6 Cracking of the
anodic oxide coating during
bending (A, B, and C oxide
coated aluminum sheet, D
galvanized aluminum sheet)
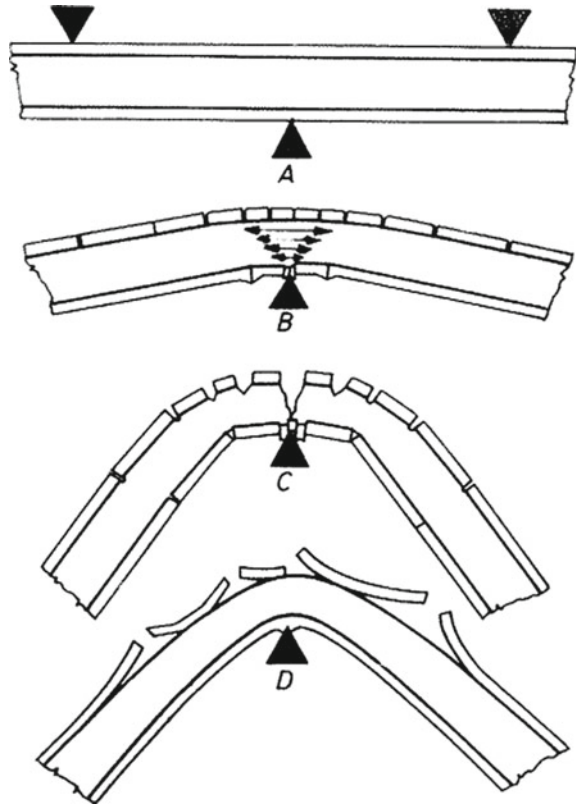
so knowledge of adhesion properties is of paramount importance (Li and Herrmann
2013).

Basically, anodizing can be considered as a long-lasting surface treatment,
however, if the anodized parts are kept at a temperature around 100 °C, the adhesive
properties of the layer deteriorate and can lead to scaly detachment and damage of
the coating. According to research, one of the reasons for this phenomenon is that
due to the hydrogen in aluminum, and the rate of thermal expansion differs between
the oxide layer and the parent metal. Bocking and Reynolds (2013) investigated
the effect of application temperature on adhesion properties for aircraft parts made
of anodized Al7075 alloy. In their research, they pointed out that the intermetallic
compound Al_7Cu_2Fe can be incorporated into the anodized layer. This compound
can be removed from the surface by etching prior to anodization; however, any
intermetallic compound can be incorporated from the base material. This does not
seem to be a problem when used at room temperature. At elevated temperatures,
the anodized layer may dehydrate. This leads to the so-called crazing phenomenon,
which appears in the form of vertical cracks. This alone would not impair adhesion,
however, the particles of the intermetallic compound may act as stress collectors,

Fig. 2.7 Difference between crazing and cracking (https://cdn2.hubspot.net/hubfs/3424216/Brochures/White%20Paper_Crazing%20and%20Forming_20180618.pdf)

contributing to the formation of horizontal cracks between the granules and may cause complete detachment (Bocking and Reynolds 2013). The difference between crazing and cracking is illustrated in Fig. 2.7.

The wear resistance of anodized coatings is significantly affected by the chemical composition of the alloy as well as the anodizing conditions. The layers deposited on pure aluminum have the highest wear resistance, however, the wear resistance of Al–Mg–Si and Al–Zn–Mg alloys can also be considered adequate (Jozefowicz 2005; Fratila-Apachitei et al. 2004). The wear resistance of alloys decreases with increasing alloy concentration. This is especially true for alloys rich in copper and silicon alloys, which can reduce the hardness of coatings as well as their corrosion resistance. Copper with aluminum and other alloying elements can form intermetallic compounds (e.g., $CuAl_2$, Al_2CuMg, and AlCuNi) that can dissolve in the bath during anodization instead of oxidation. Silicon, on the other hand, oxidizes only slightly during anodization. Silicon present in alloys in the form of eutectic crystals can result in inhomogeneity of layer thickness (Fratila-Apachitei et al. 2004; Kwolek et al. 2008).

Mezlini et al. (2007) investigated the effect of sulfuric acid anodizing on the wear resistance of Al 5xxx alloy. Their research has found that sulfuric acid treatment can result in a decrease in wear resistance and an increase in the hardness of the anodized layer (Mezlini et al. 2007). Guezmil et al. studied the tribological properties of Al5754 anodized alloy, revealing that microcracking assisted flaking is the most common of the wear-causing mechanisms (Guezmil et al. 2014).

Santecchia et al. (2020) studied the dry sliding tribological properties of hard anodized AA6082 aluminum alloy. Tribological studies with bearing steel and SI_3N_4 counterparts showed that tribochemical wear was observed when a steel ball was used, and an increase in layer thickness resulted in an improvement in tribololic performance. In contrast, studies with the Si_3N_4 ball show greater degradation of the layer.

In the research of Laszlo and Takacs (2020), the tribological behavior of anodized layers deposited on Al 356 alloy by oxalic acid technology was investigated by ball on disk analysis. The study found that the parameters of anodization significantly affect the tribological performance of a given oxide layer. Depending on their behavior,
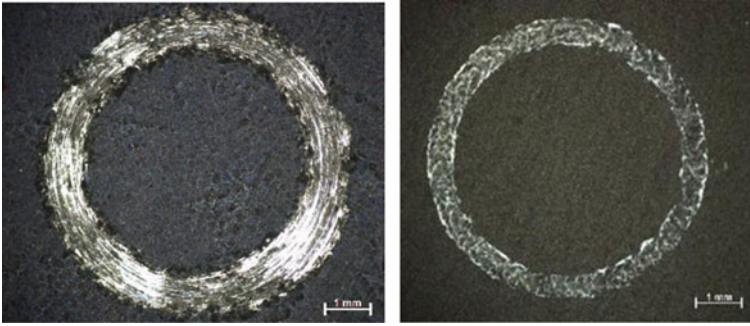
Fig. 2.8 Typical wear patterns of anodized Al356 alloys (Laszlo and Takacs 2020)

premature, subsequent damage, and gradual deteriorientation can be distinguished. However, abrasive wear and microfabrication wear were also observed during the tests. Figure 2.8 is shown 1–1 examples of these wear modes.

Fretting (Sadeler et al. 2009; Mohseni et al. 2014; Sarha et al. 2013) is a form of damage caused by the friction of extruded aluminum sheets. The appearance of fretting is mostly oriented, with a 90° angle to the extrusion axis. The cause of black discoloration is that high-hardness alumina is formed from fine aluminum powder, which oxidizes rapidly upon friction, which can abrade the oxide film.

2.2.2.3 Fatigue

As is known, the fatigue behavior of a given alloy is significantly influenced by the condition of the surface, since fatigue damage has a characteristic appearance on the surface. This is because the material is exposed to significant environmental stress in the event of fatigue (Taylor and Clancy 1991; Wiesner et al. 1994). Research has shown that even surface roughness significantly affects the fatigue resistance of a material, as roughness peaks function as stress collectors, thereby inducing the formation of cracks (Suraratchai et al. 2008).

Although anodizing significantly improves the corrosion resistance of, for example, aluminum alloys, it can reduce the fatigue limit, which is mainly explained by the brittleness and porosity of the oxide layer and the stresses in the layer during anodizing.

Shahzad et al. (2010) conducted research to investigate the effects of fatigue stress on anodized Al7010 aluminum alloys. Their studies have shown that the brittle oxide layer can easily crack under load, and that the microcracks in the layer result in early fatigue crack propagation. Such damage modes are illustrated in Fig. 2.9.

It can be seen in the figures that the Mg_2Si and Al_7Cu_2Fe inclusions present on the surface are a source of fatigue cracks.

Hockauf et al. studied the fatigue behavior of a hard and soft anodic oxide layer deposited on an AA6082 aluminum alloy. It was found that, compared to untreated
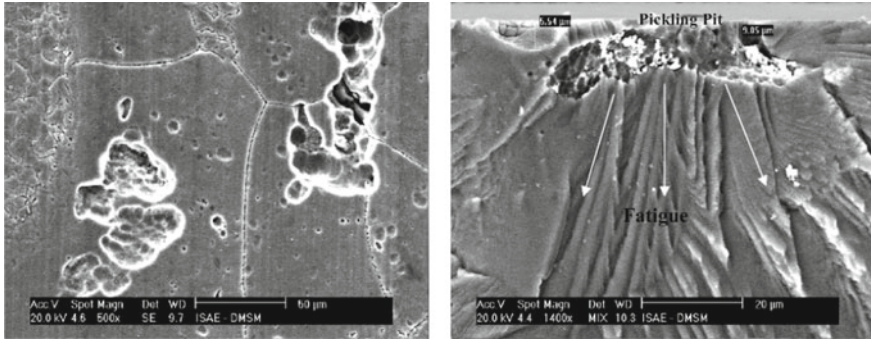
Fig. 2.9 Inclusions induced fatigue crack propagation (Shahzad et al. 2010)

alloys, anodization deteriorated the fatigue strength. At the same time, the soft anodic layer had better fatigue properties than the hard layer (Hockauf et al. 2011).

Overall, it can be stated that the characterization of the behavior of the anodized layer is a complex task from the point of view of fatigue, as fatigue is influenced by several factors (e.g., pickling parameters and characteristics of the deposited layer).

2.3 Conclusion

The present research is intended to summarize and review the typical damage forms of anodized aluminum alloys. The most common errors were systematized during the research work, based on the classification, it can be stated that the formation of an error cannot be linked to a single factor or parameter, and they are mostly based on their complex effect. At the same time, a significant proportion of these defects can occur not only during use, but also at different stages of production. At the same time, the continuation of research also carries many opportunities and directions, such as

- Systematic investigation of the effect of anodizing parameters on various damages and examining ways to eliminate defects;
- Further possibilities for listing faults; and a more detailed theoretical and experimental study of damage mechanisms.

References

Ajeel, S., Kasser, N., Ahmed, B.: Breakdown and pitting formation of anodic film aluminum alloy (3003). Mod. Appl. Sci. **4**(5), 87–101 (2010)

Amtec Guide to Aluminium & Aluminium Alloy Corrosion. https://www.amteccorrosion.co.uk/aluminium.html

Anodizing Defects Catalogue, International quality label for anodising. https://www.defects.qualanod.net/3.html

Bargui, M., Wery, M.: Optimization of mechanical and tribological properties of anodized 5754 aluminium alloy. Surf. Eng. Appl. Electrochem. **53**, 371–382 (2017)

Blawert, C., Hort, N., Kainer K.V.: Automotive applications of magnesium and its alloys. Trans. Ind. Inst. Met. **57** (4), 397–408 (2004)

Bocking, C., Reynolds, A.: Mechanism of adhesion failure of anodised coatings on 7075 aluminium alloy. Trans. IMF (**89**)6, 298–302 (2013)

Campbell, W.: Anodised aluminium surfaces for wear-resistance. Int. J. Surf. Eng. Coat. **28**(1), 273–291 (1951)

Chen, L., et al.: Surface characterization and tribological performance of anodizing micro-textured aluminum-silicon alloys. Mater. **12**, 1–15 (2009)

Castellero, A., Ricchiardi, G., Baricco, M.: Formation of hairline crazing in an anodised aluminium alloy 6061. La Met. Ital. **100**(3), 29–36 (2008)

Copper—A driving force behind the automotive industry. https://www.makin-metals.com/about/uses-of-copper-in-cars/

Crazing defects (cracks) in the anodic layer. https://aluminumsurface.blogspot.com/2009/06/crazing-defects-cracks-in-anodic-layer.html

Crazing of Anodized Finishes Caused By Bending and Forming Operations. https://www.aacron.com/docs/Crazing%20Caused%20By%20Bending%20and%20Forming%20Operations.pdf

Csokán, P., Az alumínium elektrokémiai felületkezelése. Műsz. Könyv. 80–100 (1975)

Dargusch, M.S., Keay, S.M.: Classification of streaking defects on anodized aluminium extrusions. Mater. Sci. For. **618–619**, 349–352 (2009)

Defects anodizing: classification. https://aluminium-guide.com/en/defekty-anodirovaniya-alyuminievyx-profilej-klassifikaciya/

Fratila-Apachitei, L.E., Apachitei, I., Duszczyk, J.: Thermal effects associated with hard anodizing of cast aluminum alloys. J. Appl. Electrochem. **36**, 481–486 (2006)

Feki, M., Wery, M., et al.: Mechanical and abrasive wear properties of anodic oxide layers formed on aluminium. J. Mater. Sci. Tech. **25**(4), 508–512 (2009)

Fratila-Apachitei L.E., Tichelaar F.D., et al.: A transmission electron microscopy study of hard anodic oxide layers on AlSi(Cu) alloys. Electrochem. Act. **49**, 3169–3177 (2004)

Furneaux, R.: Weathering and service life of anodized aluminium. https://www.qualanod.net/weathering-of-anodized-aluminium.html?file=files/qualanod/downloads/weathering%20of%20anodized%20aluminium%20110803.pdf (2011)

González, J.A., Atmospheric corrosion of bare and anodized aluminium in a wide range of environmental conditions. Part I: visual observations and gravimetric results. Surf. Coat. Tech. **153**(2–3), 225–234 (2002)

Grubbs, C.A.: Anodizing of aluminium. Met. Finish. **97**(1), 476–493 (1997)

Guezmil, M., Bensalah, W, et al.: Effect of test parameters on the friction behaviour of anodized aluminium alloy. Int. Schol. Res. Not. 1–9 (2014)

Hartman, A.D., Gerdemann, S.J., Hansen, S.J.: Producing lower-cost titanium for automotive applications. J. Min. Met. Mater. Soc. (TMS), **50**, 16–19 (1994)

Hirsch, J.R.: Aluminium alloys for automotive application. Mater. Sci. Forum **242**, 33–50 (1997)

Hockauf, K., Winter, L., et al.: Einfluss der elektrolytisch anodischen Oxidation auf die Ermüdungsfestigkeit der Aluminiumlegierung AA6082 mit ultrafeinkörnigem Gefüge, Werkstoffw. und Werkstofft. **42**(7), 624–631 (2011)

Iglesias-Rubianes, L., Skeldon, P., et al.: Behaviour of hydrogen impurity in aluminium alloys during anodizing. Thin Sol. Fil. **424**(2), 201–207 (2003)

ISO 7583:2013—Anodizing of aluminium and its alloys—Terms and definitions

Jozefowicz, M.: Hard coat aluminum anodizing. Met. Fin. **103**, 39–41 (2005)

Kasi, J., Kasi, A., Bokhari, M.: Study of cracks in non-planar anodic aluminium oxide membrane. Sci. Int. (Lahore) **29**(2), 71–74 (2017)

Konieczny, J., et al.: The influence of cast method and anodizing parameters on structure and layer thickness of aluminium alloys. J. Mater. Proc. Tech. **157–158**, 718–723 (2004)

Kulekci, M., K.: Magnesium and its alloys applications in automotive industry. Int. J. Adv. Man. Tech. **39**, 851–865 (2008)

Kwolek, P., Krupa, K., et al.: Tribological properties of the oxide coatings produced onto 6061-T6 aluminum alloy in the hard anodizing process. J. Mater. Eng. Perf. **27**, 3268–3275 (2008)

Laszlo, N., Takacs, N.: Tribological examination of anodized Al 356 automotive alloy. In 3rd International Conference on Materials Design and Applications, Uni. Port (2020)

Li, D., Herrmann, A.: Macroscratch testing of anodized coatings. NANOVEA, pp. 1–6 (2013)

Mearini, G.T., Hoffman, R.W.: Tensile properties of aluminum/alumina multi-layered thin films. J. Elect. Mater. **22**, 623–629 (1993)

Mezlini, S., Elleuch, K., Kapsa, Ph.: The effect of sulphuric anodization of aluminium alloys on contact problems. Surf. Coat. Techn. **201**, 7855–7864 (2007)

Miller, W.S., Zhuang, I., et al.: Recent development in aluminium alloys for the automotive industry. Mater. Sci. Eng. A **280**(1), 37–49 (2000)

Mishra, P., Kain, V., et al.: Scratch behavior of aluminum anodized in oxalic acid: Effect of anodizing potential. Surf. Coat. Tech. **283**, 135–147 (2015)

Mohseni, E., Sarhan, A., et al.: A study on surface modification of Al7075-T6 alloy against fretting fatigue phenomenon. Adv. Mater. Sci. Eng. 1–17 (2014)

Nakano, H., Oue, S., et al.: Pitting corrosion resistance of anodized aluminum alloy processed by severe plastic deformation. Mater. Transact. **48**(1), 21–28 (2007)

Ofoegbu, S., Fernandez, F., Pereira, A.: The sealing step in aluminum anodizing: a focus on sustainable strategies for enhancing both energy efficiency and corrosion resistance. Coat. **10**(3), 1–59 (2020)

Osborn, J.H.: Understanding and specifying anodizing. 2014, OMW Corp. 1–10 (2017)

Ovundu, M., et al.: Characterization and tribological properties of hard anodized and micro arc oxidized 5754 quality aluminum alloy. Trib. Ind. **37**(1) 55–59 (2015)

Sachdey, A.K., et al.: Titanium for automotive applications: challenges and opportunities in materials and processing. J. Min. Met. Mater. Soc. (TMS), **64**, 553–565 (2012)

Sadeler, R., Atasoy, S., Totik, Y.: The fretting fatigue of commercial hard anodized aluminum alloy. J. Mater. Eng. Per. **18**(9), 1280–1284 (2009)

Santana Rodriguez, J.J., Snatana Hernández, F.J.: The effect of environmental and meteorological variables on atmospheric corrosion of carbon steel, copper, zinc and aluminium in a limited geographic zone with different types of environment. Corr. Sci., (**45**)4, 799–815 (2003)

Santecchia, E., Cbibbo, M., et al.: Dry sliding tribological properties of a hard anodized AA6082 aluminum alloy. Met. **10**(2), 1–15 (2020)

Sarha, A.D., Zalnezhad, E., Shukor, M.: The influence of higher surface hardness on fretting fatigue life of hard anodized aerospace AL7075-T6 alloy. Mater. Sci. Eng. **560**, 377–387 (2013)

Sears, K.: Automotive engineering: strategic overview **2**(1), 55–68 (1997)

Shahzad, M., Chaussumier, M., et al.: Influence of anodizing process on fatigue life of machined aluminium alloy. Proc. Eng. **2**(1), 1015–1024 (2010)

Shanmughasundaram, P., Subramanian, R.: Wear behavior of eutectic Al-Si alloy-graphite composites fabricated by combined modified two-stage stir casting and squeeze casting methods. Adv. Mater. Sci. Eng. **2**, 1–8 (2013)

Sheasby, P.G., Pinner, R.: The surface treatment and finishing of aluminum and its alloys. ASM Int. **418** (1987)

Short, T.: The identification and prevention of defects on anodized aluminium parts, Metal Finishing Information Services Ltd 2003. https://www.fot.de/uploads/docs/fehlermoeglichkeiten.pdf

Short, E.P., Bryant, A.J.: A review of some defects appearing on anodized aluminium. Trans. IMF, Int. J. Surf. Eng. Coat. **53**(1) 169–177 (1975)

Short, E.P., Sheasby, P.G.: Fingerprint and general atmospheric corrosion on HE9 extrusions. Int. J. Surf. Eng. Coat. **52**, 66–70 (1974)

Skeldon, P., Thompson, G.E., et al.: Evidence of oxygen bubbles formed within anodic films on aluminium-copper alloys. J. Phil. Mag. A **76**(4), 729–741 (1997)

Soderberg, S., Nalewick, J.: Forming and crazing of anodized aluminium, white paper, 1–4. https://cdn2.hubspot.net/hubfs/3424216/Brochures/White%20Paper_Crazing%20and%20Forming_20180618.pdf

Sukiman, N.L., et al.: Durability and corrosion of aluminium and its alloys: overview. Property space, techniques and developments, aluminium alloys. New Trends Fabr. Appl. **2**, 47–99 (2013)

Suratchai, M., Limido, J., Mabru, C., Chieragatti, R.: Modelling the influence of machined surface roughness on the fatigue life of aluminium alloys. Int. J. Fat. **30**, 2119–2126 (2008)

Taylor D., Clancy O.M., The fatigue performance of machined surfaces. Fat. Frac. Eng. Mater. Struc. **14**, 329–336 (1991)

Wei, T., Yan, F., Tian, J.: Characterization and wear and corrosion-resistance of microarc oxidation ceramic coatings on aluminum alloy. J. All. Comp. **389**(1–2), 169–176 (2005)

Wiesner, C., Künzi, H., Ilschner, B.: Characterization of the topography of turned surfaces and its influence on the fatigue life of Al-7075. Mater. Sci. Eng. A **145**, 151–158 (1994)

Zhao, X., et al.: An analysis of mechanical properties of anodized aluminum film at high stress. Surf. Rev. Lett. **22** (1), 1–7 (2015)

Zhu, H., Couper, M.J., Dable, A.K.: Effect of process variables on the formation of streak defects on anodized aluminum extrusions: an overview. High Temp. Mater. Proc. **31**, 105–111 (2012)

Zhu, H., Quan, X., et al.: Investigation of streaking defects on aluminium extrusions. Mater. Sci. For. **561–565**, 341–344 (2007)

Zhu, H., Zhang, X., et al.: The formation of streak defects on anodized aluminum extrusions. J. Min. Met. Mater. Soc. (TMS) **52**, 46–51 (2010)

Chapter 3
Virtual Crack Closure as a Method for Calculating Stress Intensity Factor of Cracks in Metallic Specimens

S. Krscanski and **J. Brnic**

Abstract Stress intensity factor (SIF) is one of the most widely used parameters that characterize the behavior of structures that contain cracks. It can be used in static and fatigue analyses, and it is especially good for describing behavior of cracked structures when only small-scale yielding is present at the vicinity of the crack tip. Various crack growth models are based on this parameter, so it is of great importance to determine SIF accurately. Since more complex structures do not have standard analytical solutions for SIF, finite element analysis (FEA) is commonly used for this purpose. In this work, stress intensity factors calculated by the virtual crack closure technique (VCCT) using FEA results are compared to solutions calculated with the use of available analytical expressions from the literature. SIFs were calculated using a custom-programmed algorithm based on VCCT, which is independent from finite element (FE) code that is used to perform FE analyses. FE analyses were carried out for several standard metal specimen geometries, for a range of different relative crack sizes. Analysis of influence of FE size and type was also performed. Comments on the applicability of VCCT in static and fatigue FE analyses of cracked metallic specimens are given.

Keywords Finite element analysis · Fracture mechanics · Virtual crack closure technique (VCCT) · Stress intensity factor · Metals

Nomenclature

a_0	Initial crack size
a	Crack size
a/w, $\frac{a}{w}$	Relative crack size
Δa	Crack extension, length of the elements at the crack front
Δu	Shear displacement at crack surface node

S. Krscanski (✉) · J. Brnic
Department of Engineering Mechanics, Faculty of Engineering, University of Rijeka, Vukovarska 58, 51000 Rijeka, Croatia
e-mail: sanjink@riteh.hr

Δv	Opening displacement at crack surface node
ΔW	Work required to close the crack along one element side
E	Elasticity modulus
F	Specimen loading force
F_x	Shear force at crack tip
F_y	Opening force at crack tip
G	Strain energy release rate
G_I	Strain energy release rate for crack opening mode I
G_II	Strain energy release rate for crack opening mode II
K	Stress intensity factor
K_I	Stress intensity factor for crack opening mode I
K_II	Stress intensity factor for crack opening mode II
K_III	Stress intensity factor for crack opening mode III
μ	Shear modulus
ν	Poisson ratio
σ	Nominal normal stress
t	Specimen and element thickness
u	x—Coordinate of crack surface node after load
v	y—Coordinate of crack surface node after load
w	Specimen width

3.1 Introduction

Consideration of crack occurrence and the ability of the structure to resist crack growth are of the utmost importance in advanced structural analysis. One of the parameters that enable us to analyze the behavior of a structure with such defects is stress intensity factor K (SIF), and it is commonly used in various available crack growth models (Mohanty et al. 2009a, b). To calculate the value of that parameter for a cracked structure, finite element (FE) analysis can be used (Farahani et al. 2018). Many commercial software packages have implemented various methods of determining SIF, but there are still many FE codes that do not include such an analysis. Usually, for calculating stress intensity factor K in FE analysis, the conventional method established by Paris and Sih (1965) is implemented in FE codes. The biggest drawback of that method is that it requires implementation of a special finite element type and meshing algorithm.

In recent years, most renowned commercial FE software packages have implemented a method called virtual crack closure method or virtual crack closure technique (VCCT). This simple FE post-processing does not require usage of any special finite element types to obtain the value of stress intensity factor at the crack tip from linear elastic finite element analysis (FEA). Most frequent use of this method is for fracture analysis of brittle materials that do not exhibit significant plasticity, i.e., for a delamination of laminated composites.

This method is simple enough that its implementation should not be too difficult for a wide range of elementary two-dimensional (2D) and three-dimensional (3D) FE codes that use basic finite element types and linear elastic analysis. The groundwork for VCCT was first presented in articles from Hellen (1975) and Parks (1978), and the first application of VCCT on finite element analysis was done by Rybicki and Kanninen (1977) and Rybicki et al. (1977). More recent articles that cover VCCT theory and applications to various problems with the use of FE code were published by Krueger (2004), Leski (2007), Tavares et al. (2008) and many more.

In this paper, the basic overview of VCCT theory is given, together with implementation of post-processing procedure that is used to calculate SIF by VCCT in 2D FE models. For three different standard specimen geometries, SIFs are calculated by the use of finite element analysis (FEA) and VCCT and compared with SIFs calculated with the use of analytical expressions available in the literature and standards. Influence of finite element type and size on SIF calculated by the use of VCCT is also analyzed.

3.2 Theoretical Background

3.2.1 Virtual Crack Closure Formulation for 2D FE Model

In the literature, virtual crack closure technique (VCCT) is often called modified or virtual crack closure method (Zehnder 2012). Sometimes, inexact term one-step VCCT is used, neglecting the fact that the basic idea of VCCT is that it is a one-step procedure.

Virtual crack closure technique is derived from the crack closure method or two-step crack closure method that is based on Irwin's crack closure integral (Irwin 1958). VCCT assumes that crack extension from $a + \Delta a$ to $a + 2\Delta a$ does not alter the state at the crack tip significantly, and therefore, the displacements behind the crack tip at node B are approximately equal to the displacements behind the crack tip at node A when crack tips are located at nodes C and B (Fig. 3.1). This enables us to calculate the energy required to close the crack from single FE analysis (Krueger 2004). If a crack is modeled with 4-node 2D elements (Fig. 3.1a), the calculation of the work required to close the crack along one element side can be calculated as

$$\Delta W = \frac{1}{2}[F_{xB} \cdot (u_A - u_{A'}) + F_{xB} \cdot (v_A - v_{A'})] = \frac{1}{2}[F_{xB} \cdot \Delta u_A + F_{yB} \cdot \Delta v_A]$$
$$(3.2.1)$$

where F_{xB} and F_{yB} are shear and opening forces at crack tip node B, and Δu_A and Δv_A are shear and opening displacements at a crack surface node A. When the work required to close the crack is known, strain energy release rate G can be calculated by dividing the work with the created crack surface:
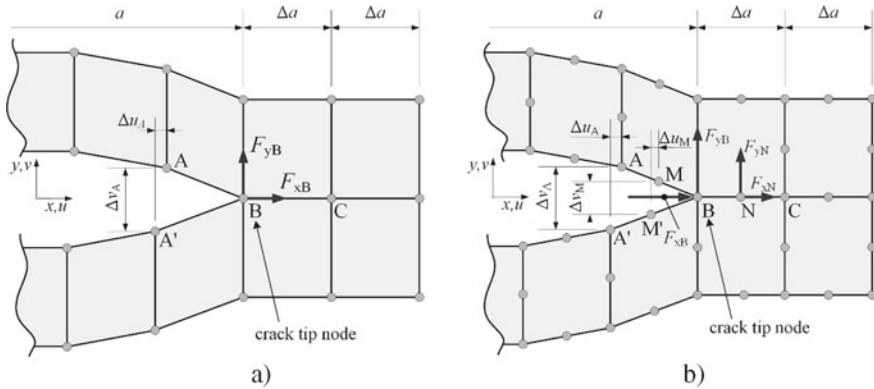
Fig. 3.1 Modified crack closure method for 2D FE model: **a** 4-node element **b** 8-node element

$$G = -\frac{\Delta W}{t \cdot \Delta a} \tag{3.2.2}$$

where t is element thickness and Δa is the length of the elements at the crack front.

If strain energy release rate is calculated for a cracked body modeled with 4-node 2D finite elements, it gives:

$$\begin{aligned} G &= -\frac{1}{2 \cdot t \cdot \Delta a}\big[F_{xB} \cdot (u_A - u_{A'}) + F_{yB} \cdot (v_A - v_{A'})\big] \\ &= -\frac{1}{2 \cdot t \cdot \Delta a}\big[F_{xB} \cdot \Delta u_A + F_{yB} \cdot \Delta v_A\big]. \end{aligned} \tag{3.2.3}$$

From the formula above, we can distinguish two parts of energy release rate, one that is the result of mode I crack opening, and other that is a result of mode II crack opening (in-plane shear opening):

$$G = G_I + G_{II}$$

where G_I and G_{II} are energy release rates for corresponding crack opening modes as follows:

$$G_I = -\frac{1}{2 \cdot t \cdot \Delta a} F_{yB} \cdot \Delta v_A, \tag{3.2.4}$$

$$G_{II} = -\frac{1}{2 \cdot t \cdot \Delta a} F_{xB} \cdot \Delta u_A. \tag{3.2.5}$$

For test cases in this paper, mode I crack opening was the dominant mode, so only calculation of value for G_I was used.

Equivalent to expressions (3.2.3) and (3.2.4), formulation for strain energy release rate for 8-node 2D elements (Fig. 3.1b), for crack opening mode I, is given as

$$G_I = -\frac{1}{2 \cdot t \cdot \Delta a} \big[F_{yB} \cdot (v_A - v_{A'}) + F_{yN} \cdot (v_M - v_{M'}) \big]$$
$$= -\frac{1}{2 \cdot t \cdot \Delta a} \big[F_{yB} \cdot \Delta v_A + F_{yN} \cdot \Delta v_M \big] \qquad (3.2.6)$$

If strain energy release rate is known and there is only small-scale yielding around the crack tip, SIF can be calculated from strain energy release rate (Kuna 2013; Stephens et al. 2001; Gross and Seelig 2011). For plane stress and plane strain states, relation between strain energy release rate and SIF is

$$G = \frac{1}{E^*} \big(K_I^2 + K_{II}^2 \big) + \frac{1}{2\mu} K_{III}^2 \qquad (3.2.7)$$

where K_I, K_{II} and K_{III} are stress intensity factors values for each of the basic crack opening modes and μ represents shear modulus that can be calculated from known values of elasticity modulus E and Poisson ratio v as

$$\mu = \frac{E}{2(1 + v)}. \qquad (3.2.8)$$

Value of E^* in the case of plane stress state is equal to elasticity modulus

$$E^* = E \qquad (3.2.9)$$

and for plane strain state, it can be calculated as

$$E^* = \frac{E}{1 - v^2}. \qquad (3.2.10)$$

If SIF is calculated only for mode I, which is the main crack opening mode in cases studied in this article, the following relations between SIF and strain energy release rate can be derived:

$$\text{Plane stress: } K_I = \sqrt{E \cdot G} \qquad (3.2.11)$$

$$\text{Plane strain : } K_I = \sqrt{\frac{E \cdot G}{1 - v^2}} \qquad (3.2.12)$$

3.3   Specimen Test Cases

The analysis was conducted for three different specimen geometries, as follows:

- finite width plate with through crack on one side (Fig. 3.2a),
- finite width plate with center through crack (M(T) specimen, Fig. 3.2b),
- compact tension specimen (Farahani et al. 2018; ASTM International 2018) (C(T) specimen, Fig. 3.2c) according to ASTM E399/E647.

For the first test case in this paper, finite width edge-cracked tension plate specimen with a width of $w = 50$ mm and thickness $t = 3$ mm was used (Fig. 3.2a). Initial crack size was $a_0 = 4$ mm (a_0 /w = 0.08). Crack is a through crack, i.e., plate is cracked through the whole thickness of the plate. Stress intensity factor values were calculated for loading tension stress of 100 MPa and a range of relative crack sizes from 0.08 to 0.68.

The second test case used was finite width plate with center through crack (middle-tension or M(T) specimen, Fig. 3.2b) with a width of $w = 80$ mm and thickness $t = 4$ mm. Loading tensile stress of 80 MPa and an initial crack size of $2a_0 = 20$ mm were used. Stress intensity factor values were calculated for relative crack sizes ranging from 0.25 to 0.9.
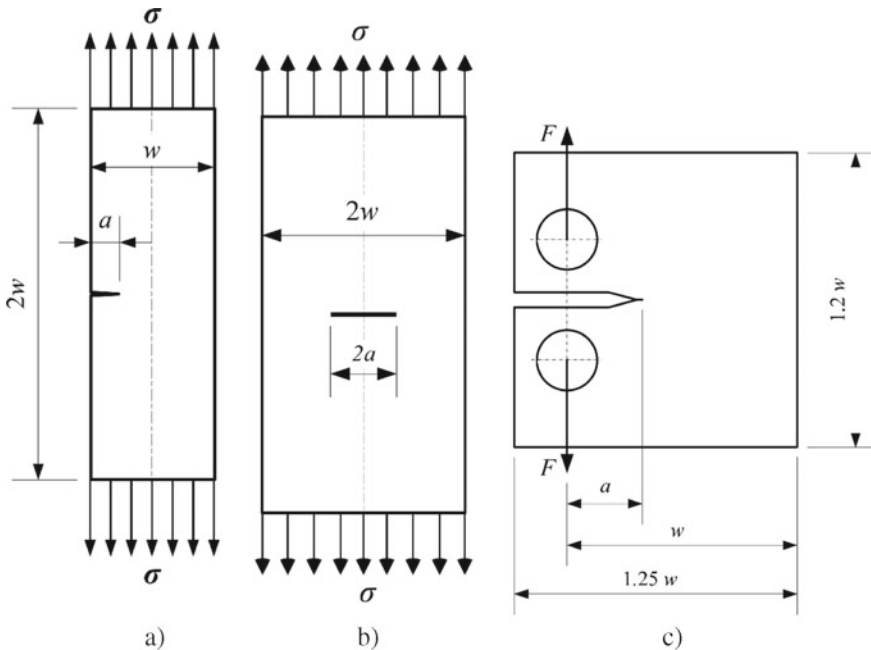
Fig. 3.2 Test case specimen geometry dimensions **a** Case I: Geometry of finite width edge-cracked tension plate **b** Case II: Geometry of finite width plate with center crack (M(T) specimen) **c** Case III: C(T) specimen geometry in accordance with ASTM E 399 and ASTM E 647

Table 3.1 Dimensions used for test case specimens

Test case specimen	I	II	III
w, mm	50	80	50
t, mm	3	4	12.5
a_0, mm	4	10	12.5

The third test case used in this paper was standard ASTM compact tension specimen (C(T) specimen, Fig. 3.2c), in accordance with ASTM E 399 and E 647 (ASTM International 2018), with eccentric force loading of 10 kN. The width of the specimen was set at $w = 50$ mm and thickness at $t = 12.5$ mm. Stress intensity factor values were calculated for a range of relative crack sizes from 0.25 to 0.9.

All relevant data concerning reference geometries in Fig. 3.2 is presented in Table 3.1.

3.3.1 Analytical Expressions for Calculation of Stress Intensity Factors

For all mentioned cases, there are available analytical and/or empirical expressions that give a correlation between SIF and relative crack size. Values obtained from mentioned expressions are used for comparison of SIF calculated by VCCT.

For case I, SIF for crack opening mode I can be calculated by analytical expression first proposed by Irwin (Stephens et al. 2001):

$$K_{\mathrm{I}} = \sigma\sqrt{a} \cdot \left[1.99 - 0.41\left(\frac{a}{w}\right) + 18.7\left(\frac{a}{w}\right)^2 - 38.48\left(\frac{a}{w}\right)^3 + 53.85\left(\frac{a}{w}\right)^4 \right]. \tag{3.3.1}$$

Comparison of VCCT results for case II is evaluated in relation to two expressions available in the literature (Stephens et al. 2001). According to Irwin, SIF can be calculated from the expression

$$K_{\mathrm{I}} = \sigma\sqrt{\pi a} \cdot \left[\frac{w}{\pi a}\tan\left(\frac{\pi a}{w}\right) \right]^{\frac{1}{2}} \tag{3.3.2}$$

and according to Fedderson, SIF can be calculated as

$$K_{\mathrm{I}} = \sigma\sqrt{\pi a} \cdot \left[\sec\left(\frac{\pi a}{w}\right) \right]^{\frac{1}{2}}. \tag{3.3.3}$$

For case III, reference analytical value of SIF is calculated from an expression available in ASTM standard (ASTM International 2018):

$$K_{\mathrm{I}} = \frac{F}{t \cdot w^{\frac{1}{2}}} \cdot \frac{\left(2 + \frac{a}{w}\right)}{\left(1 - \frac{a}{w}\right)^{\frac{3}{2}}}$$
$$\cdot \left[0.866 + 4.64\left(\frac{a}{w}\right) - 13.32\left(\frac{a}{w}\right)^{2} + 14.72\left(\frac{a}{w}\right)^{3} + 5.6\left(\frac{a}{w}\right)^{4}\right] \quad (3.3.4)$$

In Eqs. (3.3.1), (3.3.2) and (3.3.3), nominal normal stress σ is calculated as:

$$\sigma = \frac{F}{t \cdot w}. \quad (3.3.5)$$

3.3.2 Finite Element Models

FE analysis was conducted for various loads, finite element types and finite element sizes (Table 3.2). For all three test case geometries, 2D finite elements were used. According to all dimensions given, all specimens were considered to be in plane stress state and were accordingly modeled with the appropriate type of finite elements (Fig. 3.3).

For analyzing mesh size influence on SIF results, different mesh refinements on the crack path were used, and several meshes with different sizes of 8-node elements were created for all three geometries. Furthermore, to gain insight on the influence of element type around crack tip on calculated SIF results, finite element meshes were created in two varieties for each test case geometry—mesh modeled with 4-node elements and mesh modeled with 8-node elements around the crack tip. Also, model symmetry was used if possible, so that edge-cracked plate and C(T) specimen were modeled as vertically symmetric, and middle-tension specimen was modeled as vertically and horizontally symmetric. Pinholes for test machine grips on C(T) specimen were not modeled since the model with modeled grip in the hole does not provide any significant changes to the stress field around the crack tip. C(T) specimen force load was attached to the node in the appropriate position.

Table 3.2 Loads and finite element types and sizes for test case specimens

Test case specimen	Load	FE type used	FE size around the crack tip, mm
I	100 MPa	4-node	2
		8-node	0.5; 1; 2; 5
II	80 MPa	4-node	1
		8-node	0.5; 1; 2; 4
III	10 kN	4-node	0.5; 1; 2; 4
		8-node	2
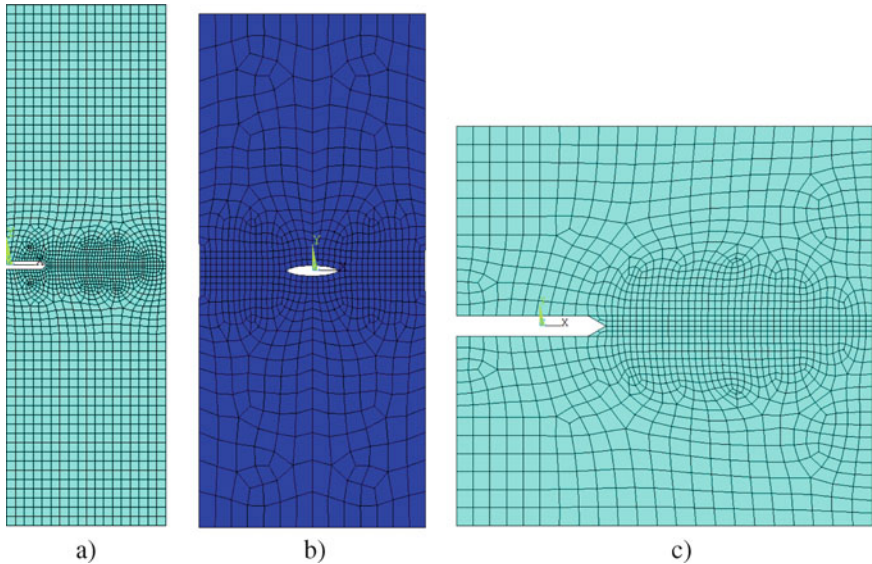
Fig. 3.3 Test case specimen finite element meshes **a** Case I; **b** Case II (deformed FE mesh); **c** Case III

3.4   Computer Algorithm for SIF Calculation

To generate FE models and obtain needed data for SIF calculation, a custom-programmed computer algorithm was made in Ansys APDL. VCCT procedure is used for SIF calculation, and it can be programmed in any programming language as a post-processing procedure on top of any FE software that can be the source for needed data. The basic flow diagram for the computer algorithm used is shown in Fig. 3.4.

3.5   Results and Discussion

3.5.1   Edge-Cracked Tension Plate

For case I, VCCT has proven to give results of calculated SIF comparable with those obtained by the use of Eq. (3.3.1). The VCCT method has shown good correlation with the Irwin analytical solution, regardless of the size of the element used (Fig. 3.5 and Fig. 3.6). Especially, small deviation from analytical solution was achieved for a relative crack size smaller than 0.72. Even relatively coarse FE mesh with an element size of 5 × 5 mm gives good SIF values. However, selection of reasonably

START

Input material and geometry data

Material model creation

Finite element type selection

Geometry creation

Finite element mesh creation

Creation of loads and boundary conditions

Linear FE analysis

Extraction of nodal forces and displacements F_{ij}, v_{ij}

SIF calculation

$a = a_{max}$ NO

YES

Write calculated data to database file K_{1ij}, a_{ij}

END

SIF calculation in detail:

Strain energy release rate calculaton

$$G_{ij} = -\frac{1}{2 \cdot t \cdot \Delta a}\left[F_{y_{ij}} \cdot \Delta u_{ij} + F_{y_{ij}} \cdot \Delta v_{ij} \right]$$

YES Plane-strain? NO

$E^* = E$

$$E^* = \frac{E}{(1 - v^2)}$$

SIF calculation

$$K_{ij} = \sqrt{G_{ij} \cdot E^*}$$

K_{ij} solutions for crack length a_i and load F_j / σ_j

Fig. 3.4 APDL script flow diagram

sensible element size of 2×2 mm is used in other analyses for this case, as to reduce unnecessary waste of CPU resources.

In addition, SIF results are very accurate regardless of using 4- or 8-node 2D finite elements (Fig. 3.7). However, 8-node elements have shown somewhat better results with a deviation from Irwin solution of less than 3% for relative crack sizes equal to or less than 0.72. If we compare that with results obtained from 4-node elements, it can be seen that a model with 4-node elements deviates up to 7% for the same range of relative crack sizes (Fig. 3.8).

Larger deviation from values obtained with the use of Irwin Eq. (3.1) can be observed for SIF results for a relative crack size of bigger than 0.72. This deviation
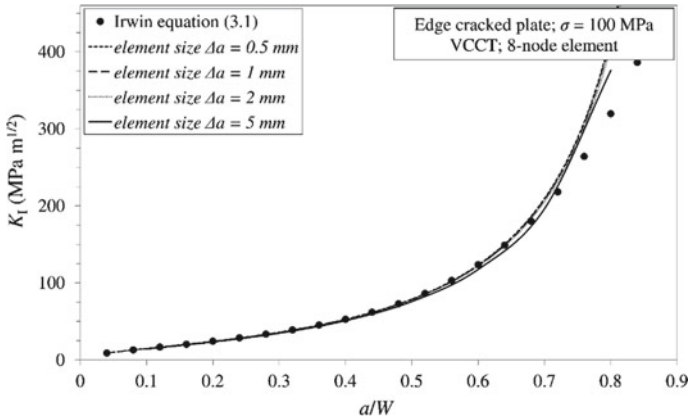
Fig. 3.5 Influence of finite element size at the crack tip on calculated SIF for case I
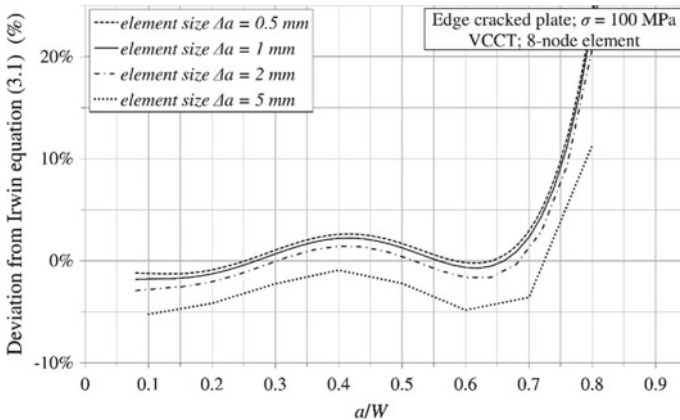
Fig. 3.6 Deviation of calculated SIF for different finite element sizes from the analytical solution for case I according to Irwin

from analytical results is the consequence of bad FE model because; in this case, the remaining crack ligament was modeled with only a few elements.

3.5.2 Plate with Center Crack

For a plate with center crack (M(T) specimen, case II), VCCT results had also shown good correlation with an analytical solution available from the literature, especially with Federsson Eq. (3.3.3) (Fig. 3.9). If we compare results obtained from VCCT to the solutions of Irwin Eq. (3.3.2), it can be seen that correlation is worse with

Fig. 3.7 Influence of finite element type on calculated SIF for case I
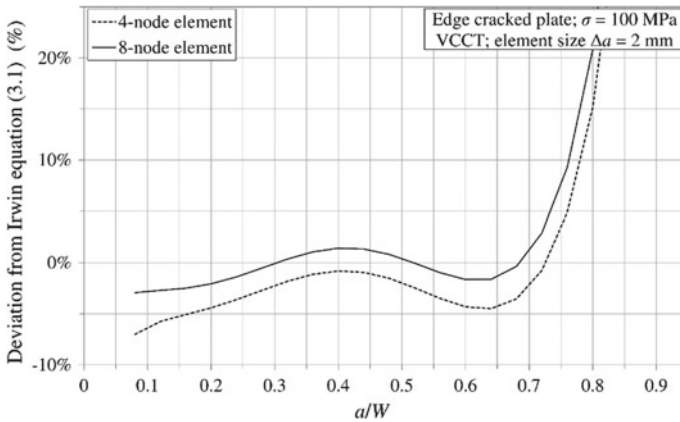
Fig. 3.8 Deviation of calculated SIF from the analytical solution for case I according to Irwin

the increase of relative crack size (Fig. 3.10a). In that case, VCCT provides results comparable with Eq. (3.3.2) (deviation ~ 10% or less) only for a relative crack size $a/w \leq 0.7$. In comparison with Eq. (3.3.3), especially, accurate results from VCCT are obtained for a finite element size of less or equal to 1×1 mm ($\Delta a \leq 1$ mm). However, it is not recommended to use coarser mesh at the crack front as it can be seen that deviation of SIF results from Eq. (3.3.3) jumps considerably if 4×4 mm ($\Delta a = 4$ mm) elements are used to mesh crack front (Fig. 3.10b). In case finer mesh is used ($\Delta a \leq 2$ mm) in conjunction with the crack front meshed with 8-node elements, deviation from Fedderson Eq. (3.3.3) solution is less than 1.3% for a complete range of relative crack size analyzed in case II ($0.25 \leq 2a/w \leq 0.9$). Even if a crack front of a M(T) specimen is meshed with 2×2 mm 4-node 2D finite elements, deviation
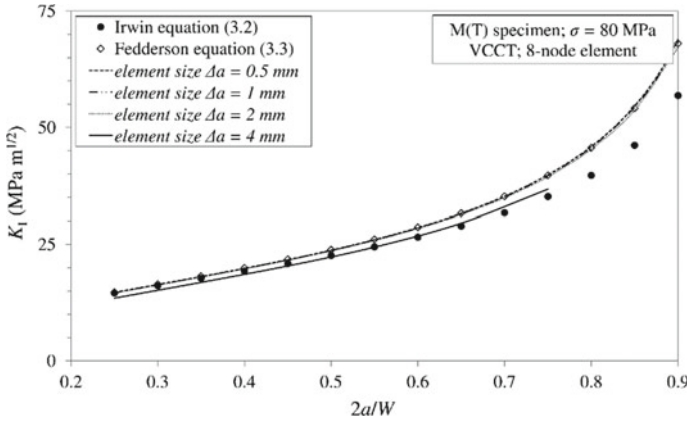
Fig. 3.9   Influence of finite element size at the crack tip on calculated SIF for case II
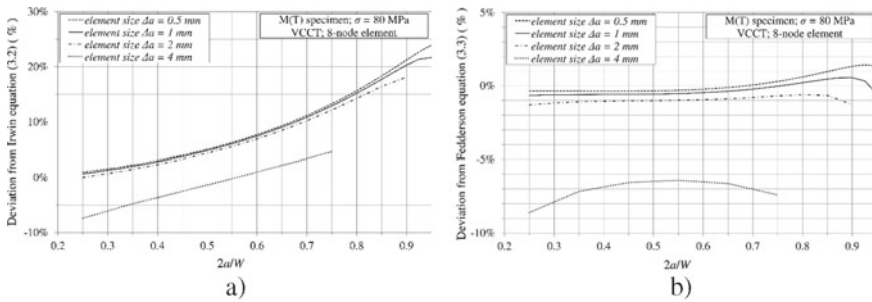
Fig. 3.10   Deviation of calculated SIF for different finite element sizes for case II: **a** from the analytical solution according to Irwin; **b** from the analytical solution according to Fedderson

from Fedderson equation solution is approx. 3% for $0.25 \leq 2a/w \leq 0.8$ and between 3 and 5% for $2a/w > 0.8$ (Figs. 3.11 and 3.12).

3.5.3   C(T) Specimen

In case III (C(T) specimen), SIF solutions obtained with VCCT showed reasonably good agreement with SIF values obtained from expression given in the ASTM standard E399 (3.4). SIF solutions obtained from VCCT proved to be more accurate for smaller sizes ($\Delta a \leq 2$ mm) of finite elements in front of the crack tip. It can be seen that element size of 4×4 mm produced the worst results in relation to ASTM equation (Figs. 3.13 and 3.14). In relation to that results, the recommendation is to use element size of $\Delta a \leq 2$ mm around the crack tip for the calculation of SIF using VCCT.
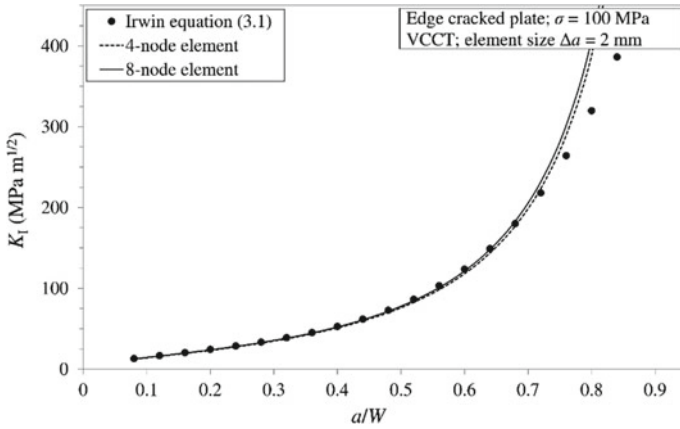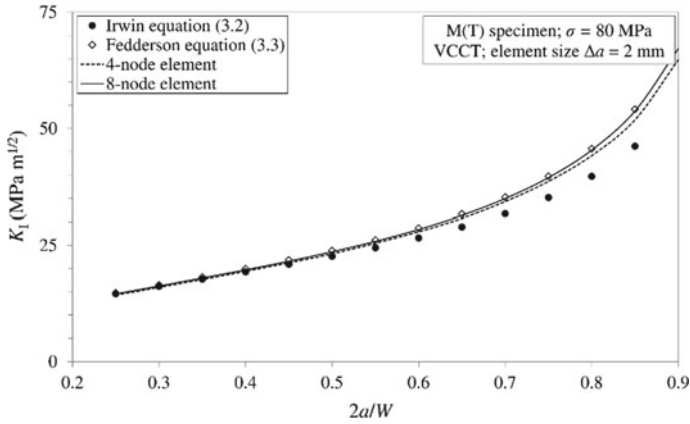
Fig. 3.11 Influence of finite element type on calculated SIF for case II
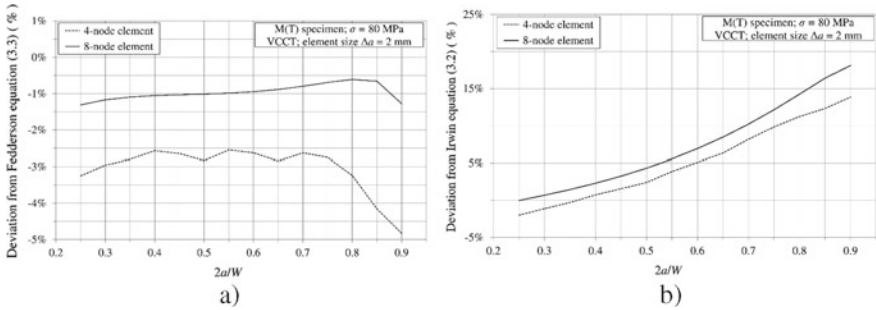
Fig. 3.12 Deviation of calculated SIF from the analytical solution for case II according to: **a** Fedderson equation; **b** Irwin equation
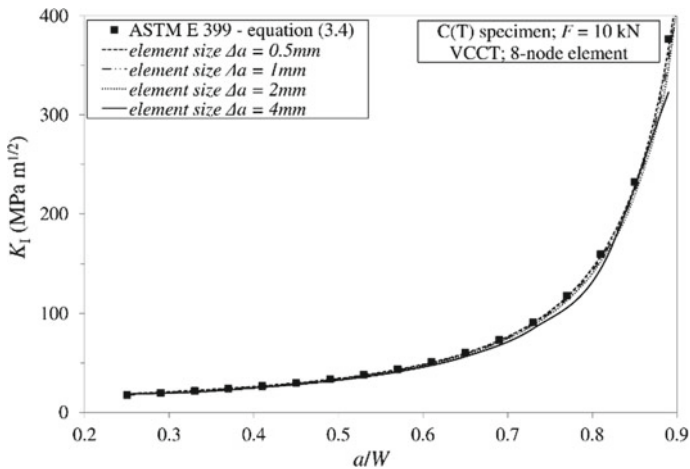
Fig. 3.13 Influence of finite element size at the crack tip on calculated SIF for case III
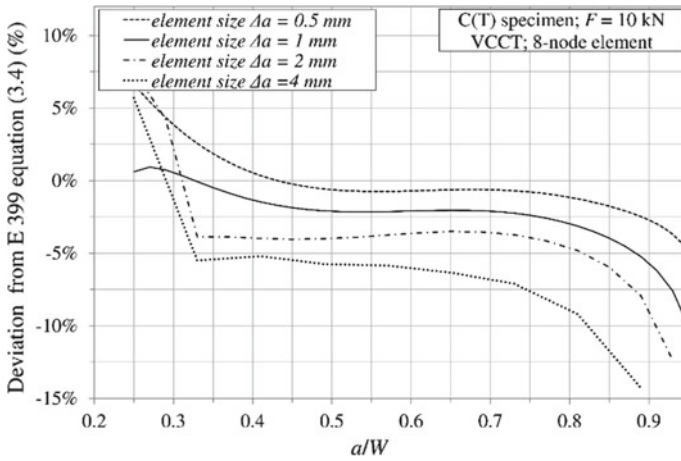
Fig. 3.14 Deviation of calculated SIF for different finite element sizes from the analytical solution available in ASTM

When using 1×1 mm finite elements ($\Delta a = 1$ mm), use of both 4-node and 8-node finite elements proved to be appropriate for SIF calculation, although 8-node elements again yielded better results (Figs. 3.15 and 3.16). For a relative crack range $0.25 \leq 2a/w \leq 0.7$, SIF results for an FE model with 8-node 2D elements deviated from analytical solution approx. 1–2%, while for an FE model using 4-node 2D elements results deviated approx. 1–4%. Significant loss of accuracy in SIF calculation can again be seen for a relative crack size bigger than 0.8, albeit to a
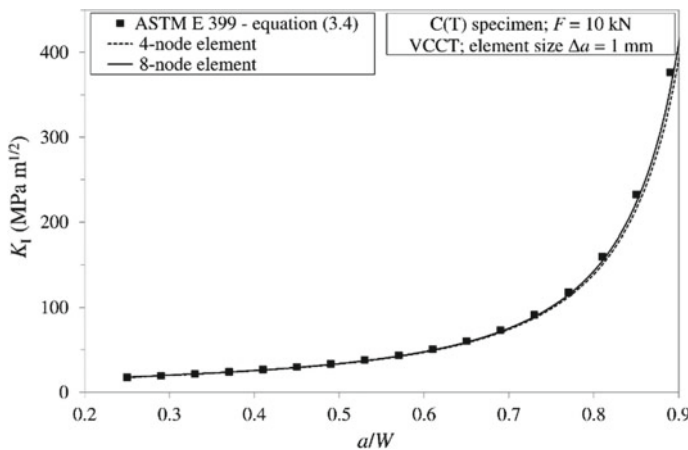
**Fig. 3.15** Influence of finite element type on calculated SIF for case III
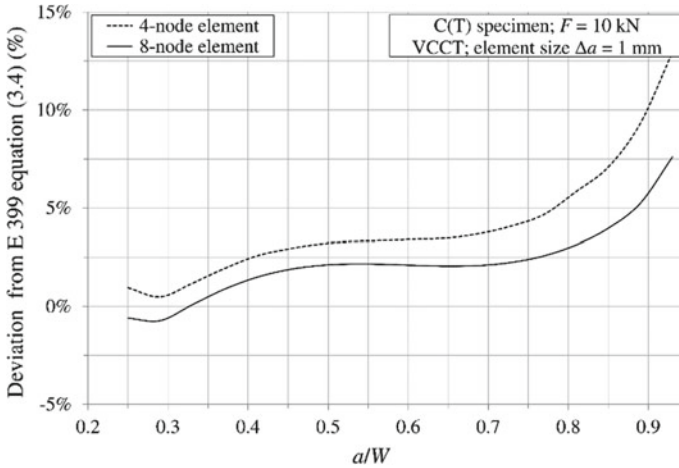
Fig. 3.16 Deviation of calculated SIF from the analytical solution for case III

lesser extent than in case I (Figs. 3.14 and 3.16). Once again, this can be attributed to a poor quality of FE model with crack ligament only consisting of several finite elements.

3.6 Conclusion

In this paper, stress intensity factor solutions obtained with the help of 2D virtual crack closure method were studied. Results were obtained for three different model geometries of metal specimens and compared to solutions from conventional analytical expressions available in the literature and ASTM standard. Influence of finite element size and type on calculated SIF solution was studied.

In conclusion, it can be said that 2D VCCT has proven as a reliable method for calculating stress intensity factor in cracked metal bodies. Use of VCCT yielded results similar to solutions obtained from conventional analytical expressions available in the literature. It is recommended to use 8-node 2D finite elements of a relatively small size ($\Delta a = 1 - 2$ mm) for best results, although, if needed, 4-node 2D finite elements yield sufficiently accurate results.

References

Annual Book of ASTM Standards, Volume 03.01.: E399–12e3–Standard Test Method for Linear-Elastic Plane-Strain Fracture Toughness KIc of Metallic Materials. ASTM International, West Conshohocken, USA (2018)

Farahani, B.V., Tavares, P.J., Belinha, J., Moreira, P.M.G.P.: Compact tension fracture specimen: Experimental and computational implementations on stress intensity factor. J. Strain Anal. Eng. Des. **53**(8), 630–647 (2018)

Gross, D., Seelig, T.: Fracture Mechanics with an Introduction to Micromechanics, 2nd edn. Springer, Heidelberg (2011)

Hellen, T.K.: On the method of virtual crack extension. Int. J. Numer. Methods Eng. **9**, 187–207 (1975)

Irwin, G.R.: Fracture. Handbuch der Physik. Springer-Verlag, Heidelberg (1958)

Krueger, R.: Virtual crack closure technique: History, approach and applications. Appl. Mech. Rev. **57**(2), 109–143 (2004)

Kuna, M.: Finite Elements in Fracture Mechanics: Theory-Numerics-Applications. Springer Science+Bussiness Media, Dordrech (2013)

Leski, A.: Implementation of the virtual crack closure technique in engineering FE calculations. Finite Elem. Anal. Des. **43**(3), 261 (2007)

Mohanty, J.R., Verma, B.B., Ray, P.K.: Prediction of fatigue crack growth and residual life using an exponential model: Part I (constant amplitude loading). Int. J. Fatigue **31**, 418–424 (2009a)

Mohanty, J.R., Verma, B.B., Ray, P.K.: Prediction of fatigue crack growth and residual life using an exponential model: Part II (mode-I overload induced retardation). Int. J. Fatigue **31**, 425–432 (2009b)

Paris, P., Sih, G.: Stress analysis of cracks. STP381–Fracture toughness testing and its applications, ASTM international, West Conshohocken (1965)

Parks, D.M.: Virtual Crack Extension: A General Finite Element Technique for j-integral Evaluation. Proceedings of the First International Conference on Numerical Methods in Fracture Mechanics. pp. 464–472, Pineridge Press, Swansea, England (1978)

Rybicki, E.F., Kanninen, M.F.: A finite element calculation of stress inensity factors by a modified crack closure integral. Eng. Fract. Mech. **9**, 931–938 (1977)

Rybicki, E.F., Schmueser, D.W., Fox, J.: An energy release rate approach for stable crack growth in the free-edge delamination problem. J. Compo. Mater. **11**, 470–487 (1977)

Stephens, R.I., Fatemi, A., Stephens, R.R., Fuchs, H.O.: Metal Fatigue in Engineering. 2nd edn, Wiley, New York (2001)

Tavares, S.M.O., Moreira, P.M.G.P., Pastrama, S.D., de Castro, P.M.S.T.: Stress intensity factors by numerical evaluation in cracked structures. Proceeding of 11th Portuguese Conference on Fracture, pp. 315–324, Lisbon, Portugal (2008)

Zehnder, A.T.: Fracture Mechanics. Springer, Dordrecht (2012)

Chapter 4
Multiscale Modeling for Residual Stresses Analysis of a Cast Super Duplex Stainless Steel

A. P. O. Costa, R. O. Sousa, L. M. M. Ribeiro, A. D. Santos, and J. M. A. César de Sá

Abstract Chemical, physical, thermal, and mechanical behavior of complex alloys, such as super-duplex stainless steels (SDSS), is largely dependent on the characteristics of its multiphase microstructure which is controlled by chemical composition and cooling rate in the temperature range of 1000 to 300 °C. During solidification, a microstructure composed of ferrite, austenite, and non-ideal phases can be formed, introducing residual stresses due to the different coefficient of thermal expansion and elastoplastic properties of the phases. Since residual stresses may have a significant impact on components, causing distortion and early failure, it is critical to understand their origin (at the microscale) and effect (at the macroscale). Multiscale material modeling provides an opportunity to analyze the material in different scales, leading to the optimization of material design and behavior. This work addresses the effect of distribution and volume fraction of phases on the magnitude and gradient of residual stresses on a cast SDSS specimen. The numerical method for the homogenization of the material properties is also addressed. The procedure followed consisted of modeling the microstructure by assigning phases properties to the features in optical micrographs and generating a finite element mesh to compute the macroscopic material properties. The software OOF was used to model the microstructures and ABAQUSTM/CAE was applied to simulate the cooling of the specimen and to analyze the residual stresses.

Keywords Finite element analysis · Duplex stainless steel · Multiscale models · Homogenization · Elasticity properties · Heterogeneous materials · Micromechanics · Residual stress · Microstructure · OOF2 · ABAQUS · Casting process

A. P. O. Costa (✉) · R. O. Sousa · L. M. M. Ribeiro · A. D. Santos · J. M. A. C. de Sá
INEGI, Institute of Science and Innovation in Mechanical and Industrial Engineering, Porto, Portugal
e-mail: acosta@inegi.up.pt

A. P. O. Costa · A. D. Santos · J. M. A. C. de Sá
Department of Mechanical Engineering, University of Porto, Porto, Portugal

R. O. Sousa · L. M. M. Ribeiro
Department of Metallurgical and Materials Engineering, University of Porto, Porto, Portugal

4.1 Introduction

Multiscale science and engineering is a relatively new field (Zohdi and Wriggers 2008; Horstemeyer 2009; Belytschko and Borst 2010; Aboudi et al. 2013). The multiscale materials modeling lies on predicting relations between microstructural morphology, processing, and the final properties. Its use encompasses a variety of computational techniques as molecular dynamics, multiscale finite element methods, computational homogenization, to name a few.

Most of the engineering materials are considered continuum homogeneous at the macroscale. However, at the micro or nanoscale, all real materials are heterogeneous (Fish 2014). This heterogeneous nature has a significant impact on material properties at the macroscale as they depend strongly on the spatial distribution of the phases of different crystal structures, grains of different orientations, size and shape, and structural defects. Besides, thermal–mechanical loading may also affect these microstructural features.

Super duplex stainless steels are advanced materials with both high mechanical properties and corrosion resistance. The microstructure is composed of ferrite and austenite which is achieved by controlling the chemical composition and cooling rate in the temperature range of 1000 °C to 300 °C. The alloying elements such as Cr, Mo, Ni, and N play an important role in the stabilization of the duplex microstructure (Nilsson et al. 2000), but a slow cooling rate from high temperature may lead to the precipitation of detrimental secondary phases, such as sigma (σ) and chi (χ) (Sousa et al. 2019). Furthermore, during cooling thermal stresses are developed owing to differences in the coefficient of thermal expansion (CTE) and elastoplastic properties of the aforementioned phases. An interesting point is that the distribution of phases may affect the local stresses and, therefore, the response of the material under a given loading condition. In cast components, the distribution of phases depends on the cooling rate that varies along their geometry. For example, a slower cooling rate enhances the formation of secondary phases.

To understand how the heterogeneous microstructure influences the residual stresses, a new framework has been developed through multiscale modeling using the finite element method (Zienkiewicz 1971; Fish and Belytschko 2007; Sousa Neto et al. 2011). The proposed methodology uses real microstructures to capture the essential features that impact the residual stresses at the microscale. Then, a homogenization procedure is implemented to translate the microscopic behavior into the macroscopic response of the material.

4.2 Experimental Procedure

C-ring specimen

The SDSS 25Cr-7Ni-Mo–N was prepared by induction melting and poured into a sand mold to produce the C-ring specimen, as shown in Fig. 4.1. Because of its unique

Fig. 4.1 C-ring specimen along with the regions for microstructural analysis. The dimensions are given in millimeters
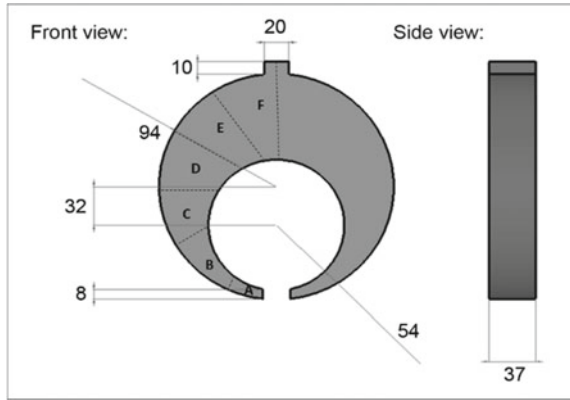
shape, the cooling rate varies throughout the geometry, causing the non-uniform distribution of phases.

The C-ring was divided into six regions (from A to F), as shown in Fig. 4.1. These regions present a variable cross-section, causing a decrease in the cooling rate from A to F. From each region, a sample was taken for optical microscopy (OM) analysis and quantification of phases by image segmentation.

Numerical model

A 2-D finite element model was created and used for different boundary conditions to predict the elasticity matrix $C_{(3x3)}$ and thermal expansion coefficients at the macroscale, based on the microstructure of different regions of the specimen.

In order to extract that information, finite element representative volume elements (RVEs) were created from optical microscopy images. These RVEs were subjected to appropriated boundary conditions (Zohdi and Wriggers 2008), as represented in Figs. 4.2 and 4.3 so that homogenized elasticity matrices and thermal expansion coefficients could be used at the macroscale in the different regions analyzed.

Results of stress and strain components were obtained using ABAQUS software (ABAQUS Unified FEA 2013) and collected, together with the respective space location (coordinates), using a developed Python script. That script generates an excel file with all necessary information for the homogenization procedure to be performed by means of a created MATLAB (MATLAB 2017) script.
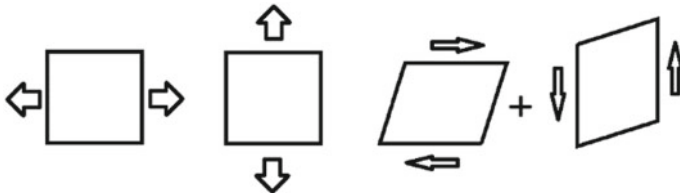
Fig. 4.2 RVE and representative boundary conditions considered for the mechanical problem

Fig. 4.3 RVE and
representative boundary
conditions for the thermal
problem
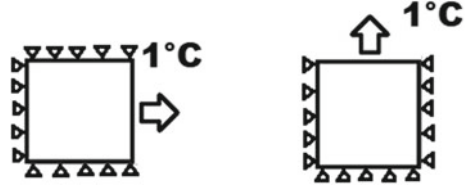
To obtain the elasticity matrix the first simulation is traction on the RVE, in the
X-direction, keeping $\varepsilon_{22} = \gamma_{12} = 0$, by imposing $\varepsilon_{11} = 1$. The coefficients of the
first column of the elasticity matrix are then obtained by integrating and averaging
the stress components using a Gaussian quadrature technique through all the finite
elements of the mesh as:

$$C_{11} = \frac{1}{V} \sum_{i=1}^{ne} \sum_{k=1}^{np} ((\sigma_{11})_k N_k * w_k * |J_k|) \tag{4.1a}$$

$$C_{21} = \frac{1}{V} \sum_{i=1}^{ne} \sum_{k=1}^{np} ((\sigma_{22})_k N_k * w_k * |J_k|) \tag{4.1b}$$

$$C_{31} = \frac{1}{V} \sum_{i=1}^{ne} \sum_{k=1}^{np} ((\sigma_{12})_k N_k * w_k * |J_k|) \tag{4.1c}$$

where ne represents the numbers of elements, np is the number of integration points
per element, C_{j1}, $j = 1,3$ are the coefficients of the elasticity matrix corresponding
to the first column. At each integration point, $(\sigma_{ij})_k$ is the stress components, N_k
is the element shape functions values, w is the quadrature weights, and J_k is the
determinant of the Jacobin matrix. V is the volume of the RVE.

Similarly, in a second simulation, traction on the RVE, in the Y-direction is estab-
lished, imposing $\varepsilon_{11} = \gamma_{12} = 0$ and $\varepsilon_{22} = 1$. The coefficients of the second column
of the elasticity matrix are then obtained as:

$$C_{12} = \frac{1}{V} \sum_{i=1}^{ne} \sum_{k=1}^{np} ((\sigma_{11})_k N_k * w_k * |J_k|) \tag{4.2a}$$

$$C_{22} = \frac{1}{V} \sum_{i=1}^{ne} \sum_{k=1}^{np} ((\sigma_{22})_k N_k * w_k * |J_k|) \tag{4.2b}$$

$$C_{32} = \frac{1}{V} \sum_{i=1}^{ne} \sum_{k=1}^{np} ((\sigma_{12})_k N_k * w_k * |J_k|) \tag{4.2c}$$

Finally, a pure shear state is imposed, $\varepsilon_{11} = \varepsilon_{22} = 0$, and $\gamma_{12} = 1$ and the
coefficients of the third column of the elasticity matrix are then obtained as:

$$C_{13} = \frac{1}{V} \sum_{i=1}^{ne} \sum_{k}^{np} ((\sigma_{11})_k N_k * w_k * |J_k|) \tag{4.3a}$$

$$C_{23} = \frac{1}{V} \sum_{i=1}^{ne} \sum_{k}^{np} ((\sigma_{22})_k N_k * w_k * |J_k|) \tag{4.3b}$$

$$C_{33} = \frac{1}{V} \sum_{i=1}^{ne} \sum_{k}^{np} ((\sigma_{12})_k N_k * w_k * |J_k|) \tag{4.3c}$$

To calculate the homogenized thermal expansion coefficients, two thermal states were imposed on the RVE in X and Y-directions, as shown in Fig. 4.3.

The thermal expansion may be obtained, in each case, as $\varepsilon^T = \alpha(\Delta T)$ and, therefore, as in this case $\Delta T = 1°C$ the homogenized thermal expansion coefficients can be obtained as:

$$\alpha_{11} = \frac{1}{V} \sum_{i=1}^{ne} \sum_{k=1}^{np} ((\varepsilon_{11})_k * N_k * w * |J_k|) \tag{4.4}$$

$$\alpha_{22} = \frac{1}{V} \sum_{i=1}^{ne} \sum_{k=1}^{np} ((\varepsilon_{22})_k * N_k * w * |J_k|) \tag{4.5}$$

A multiscale analysis was performed in this research by using representative OM micrographs from the six regions of the C-ring.

4.3 Results and Discussion

Microstructural characterization

The microstructure of the C-ring is shown in Fig. 4.4. A bright γ-phase, a light-gray δ-phase, and dark-gray particles of σ-phase can be observed.

The volume percentage of phases formed in the six regions is displayed in Fig. 4.5.

The results show that the destabilization of the δ-phase with the formation of σ-phase is greatly affected by the cooling rate. Figure 4.5 suggests that the higher cross-section area leads to an increasing amount of sigma phase due to the decrease in the cooling rate. This heterogeneous distribution of phases in the C-ring may affect the local stresses, due to differences in the properties summarized in Table 4.1.

Numerical results

Initially, in order to validate the MATLAB script, an example of a square with 20 × 20 nm with a triangle finite element mesh was used. The Young's modulus of 200 GPa and Poisson's ratio of 0.3 were assigned to all the elements, using a sparse and a refined mesh, as shown in Fig. 4.6. The comparison of the elasticity matrices
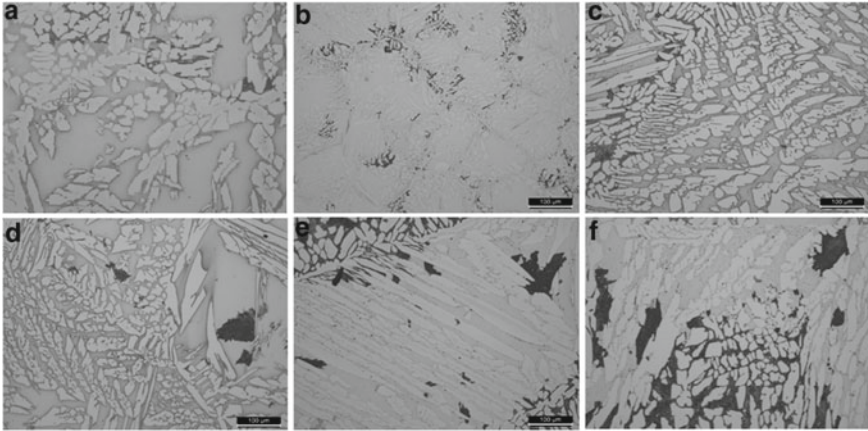
Fig. 4.4 Optical micrographs taken from six regions of the C-ring, showing the as-cast microstructure containing γ-phase (brightest phase), δ-phase (light-gray phase), and σ-phase (dark-gray phase)
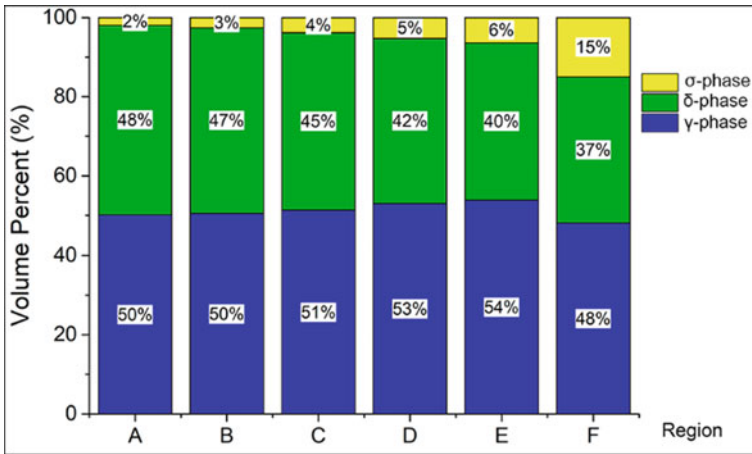
Fig. 4.5 Distribution of the volume percent of phases in the six regions of C-ring

Table 4.1 Microstructural phase properties

Phase	Young's modulus (GPa)	Poisson's ratio	CTE (10^{-6}°C^{-1})
γ-phase	189	0.3	17.2
δ-phase	220	0.3	10.4
σ-phase	201	0.3	17.6

Fig. 4.6 Sparse and refined triangle meshes
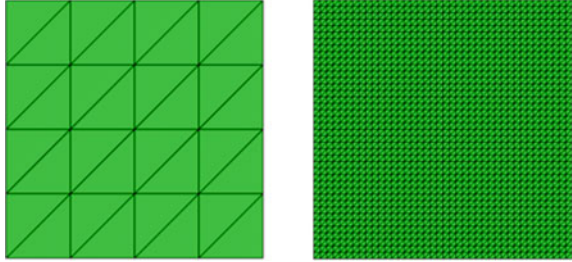
obtained for both meshes, with the theoretical matrix is shown in Table 4.2. The script was considered valid as a minimal error was obtained. When different phases are involved the accuracy of results may depend on the mesh. Therefore, structured and unstructured meshes were also tested.

The last test was made in an RVE, with dimensions of 648×864 nm supposing that it was a homogeneous material with E = 200 GPa and Poisson rate of 0.32. In this case, structured unstructured meshes, as shown in Fig. 4.7, were tested. The results depicted in Table 4.3 are acceptable in both cases, with a much smaller error and time of evaluation for the solution with the structured mesh.

Finally, a MATLAB script to predict the expansion coefficients in the X and Y-directions in a 2-D problem was also tested. Again, for that purpose, a homogenous material was considered, and the exact results were obtained, as shown in Table 4.4.

Table 4.2 Comparison of the elasticity matrices obtained with sparse and refined meshes with the theoretical matrix

Example	Elasticity matrix found	Elasticity matrix theory	Error (%)
32 elements	$\begin{bmatrix} 219780.21 & 65934.6 & 0 \\ 65934.06 & 219780.21 & 0 \\ 0 & 0 & 76923.07 \end{bmatrix}$	$\begin{bmatrix} 219780 & 65930 & 0 \\ 65930 & 219780 & 0 \\ 0 & 0 & 76920 \end{bmatrix}$	0.0033
3200 elements	$\begin{bmatrix} 219780.21 & 65934.6 & 0 \\ 65934.06 & 219780.21 & 0 \\ 0 & 0 & 76923.07 \end{bmatrix}$		0.0033

Fig. 4.7 Unstructured and structured meshes
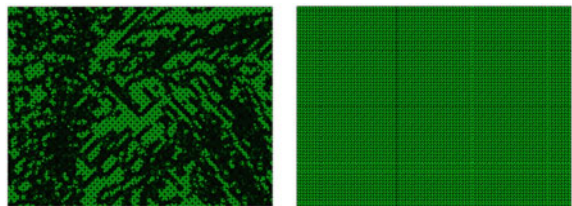
Table 4.3 Comparison of the elasticity matrices obtained with structured and unstructured meshes with the theoretical matrix

Example	Elasticity matrix found	Elasticity matrix theory	Error (%)	Time (min)	Element number
Unstructure mesh	$\begin{bmatrix} 222820 & 71300 & 0 \\ 71300 & 222820 & 0 \\ 0 & 0 & 80130 \end{bmatrix}$	$\begin{bmatrix} 222820 & 71300 & 0 \\ 71300 & 222820 & 0 \\ 0 & 0 & 75760 \end{bmatrix}$	8.3×10^{-2}	360	52,414
Structure mesh	$\begin{bmatrix} 222820 & 71300 & 0 \\ 71300 & 222820 & 0 \\ 0 & 0 & 75760 \end{bmatrix}$		3.1×10^{-6}	60	11,008

Table 4.4 Thermal expansion coefficient comparison with theory coefficient in x and y-directions

Direction	Expansion coefficient ($\times 10^{-6\circ}C^{-1}$)	Expansion coefficient ($\times 10^{-6\circ}C^{-1}$)	Error (%)
X	12	12	0.00
Y	12	12	0.00

Microscale analysis

The OOF2 software (OOF software 2019) was used to obtain the finite element mesh for the RVE by a microstructural mapping. This software uses the pixel color to distinguish different phases and to generate a mesh from real images. The file with the mesh information built-in OOF2 was exported to ABAQUS. The meshes from the six OM micrographs are shown in Fig. 4.8.

These meshes represent REVs in which appropriate boundary conditions were applied, as mentioned before, to obtain the elasticity matrices and the thermal expansion coefficients at the macroscale. A Python file was used to extract the required information to the MATLAB code, as previously indicated.

The results for the homogenized parameters to be used at the macroscale, for the six different regions are given in Table 4.5.

Figures 4.9, 4.10, 4.11, 4.12, 4.13 and 4.14 show the deformation in each case to obtain the thermal expansion coefficients. It is evident the different deformation behavior of each phase, in each case, and how, potentially, residual stresses and strains may occur locally due to this fact.

Macroscale analysis

The C-ring specimen, divided into six regions, was submitted to a thermal gradient, and the resulting thermal stresses were analyzed at the macroscale. Figure 4.15 shows the six regions, considering only one half of the specimen due to symmetry conditions.
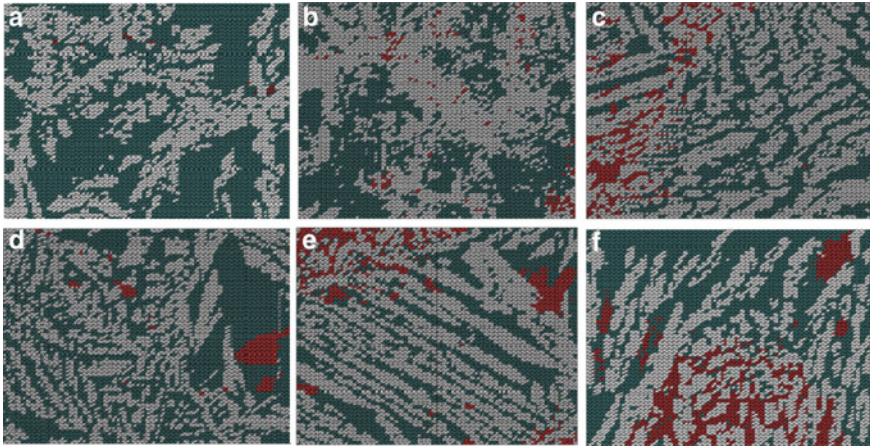
Fig. 4.8 OOF2 meshes based on the OM micrographs from region A to F of the C-ring, gray area (γ-phase), green area (δ-phase), and red area (σ-phase)

The initial temperature was set to 900 °C. In this analysis, the mold was not considered. Figure 4.16 shows the points where mechanical boundary conditions were considered to prevent rigid body motion and to assure symmetry. An unstructured mesh of triangle elements was utilized, and the final temperature was set to 20 °C.

The resulting von Mises stress distribution is shown in Fig. 4.17. It is clear that stress concentrations appear in the transition zones between different regions.

In Fig. 4.18, the deformation of the part, with a magnification factor of 3, is shown. In Fig. 4.19, assuming throughout the part only the properties obtained from the OM micrograph of region F and the same thermal story, the deformation of the part is also shown, for the same magnification factor. It is clear how the attribution of different properties to different locations of the part according to different microstructure patterns may affect the final geometry at the end of the cooling stage.

4.4 Conclusions

Multiscale modeling, together with the recent technological advances in the computational area brings an advantage to design, process, and evaluation of the materials' behavior. This method is a powerful tool that makes it possible to predict the material behavior at the macroscale by analyzing it at smaller scales. In this research, several simulations were carried out at the microscale scale, using a C-ring cast part. Resultant residual stresses due to the inhomogeneity at the microscale were predicted by obtained homogenized properties at the macroscale.

Table 4.5 Results of elasticity matrices and thermal expansion coefficients for the six regions of the C-ring

Micrography	Elasticity matrices	Thermal expansion coefficient ($\times 10^{-6}$ °C^{-1})	
		X-direction	Y-direction
A	$\begin{bmatrix} 226600 & 67950 & 90 \\ 67950 & 226460 & 50 \\ 150 & 30 & 79310 \end{bmatrix}$	13.206	13.195
B	$\begin{bmatrix} 198380 & 90 & 170 \\ 90 & 198240 & 140 \\ 220 & 210 & 99080 \end{bmatrix}$	13.731	13.738
C	$\begin{bmatrix} 215550 & 64600 & -60 \\ 64590 & 215360 & -80 \\ -160 & -70 & 75490 \end{bmatrix}$	14.381	14.387
D	$\begin{bmatrix} 220850 & 66070 & 60 \\ 66220 & 220300 & 60 \\ 110 & 90 & 77120 \end{bmatrix}$	13.283	13.286
E	$\begin{bmatrix} 215730 & 64700 & 220 \\ 64690 & 215560 & 170 \\ 360 & 190 & 75530 \end{bmatrix}$	14.362	14.388
F	$\begin{bmatrix} 222600 & 66790 & -30 \\ 66790 & 222650 & 10 \\ -130 & 30 & 77960 \end{bmatrix}$	14.420	14.420

At the microstructural scale analysis, the OOF2 software was employed to generate a finite element mesh from real images, representing an RVE.

A procedure was developed to obtain homogenized mechanical and thermal properties at the macroscale from the microstructural scale information, using ABAQUS and codes developed in Python and MATLAB for that purpose. Appropriate boundary conditions were considered and unstructured and structured meshes were tested in order to reduce numerical errors.

Finally, the c-ring part produced by casting was analyzed. Different properties were attributed to different regions of the part according to different microstructure patterns, resulting from different local cooling rates. Their influence on the final properties was observed, namely in thermal expansion effects and in the formation and location of residual stress in the part.
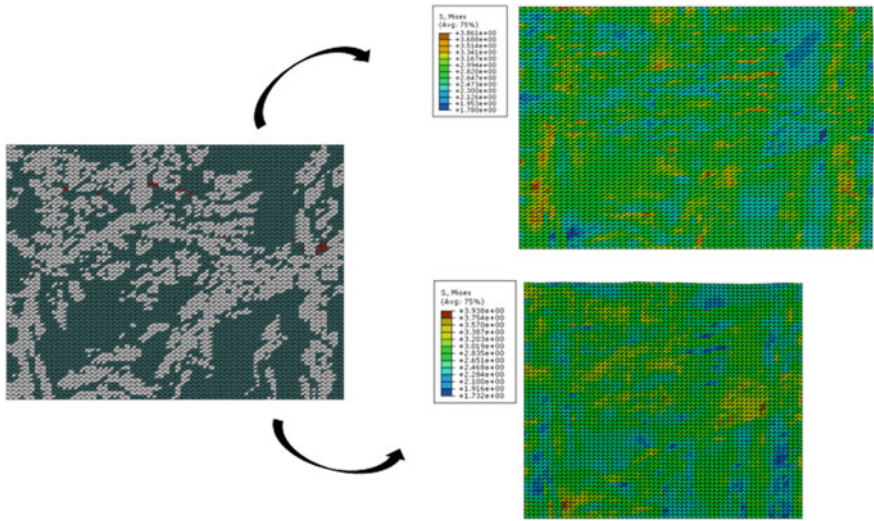
Fig. 4.9   Mesh of region A. Thermal deformation in x and y-directions
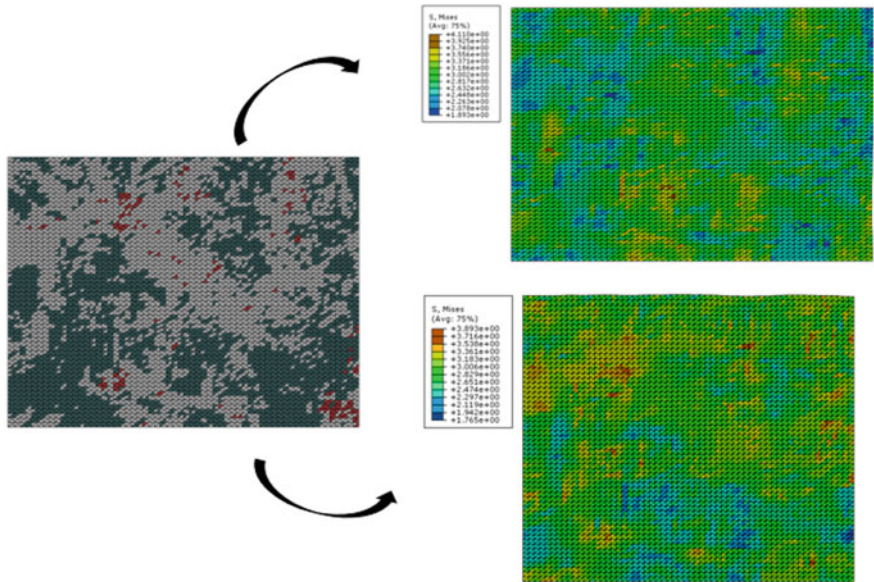
Fig. 4.10   Mesh of region B. Thermal deformation in x and y-directions
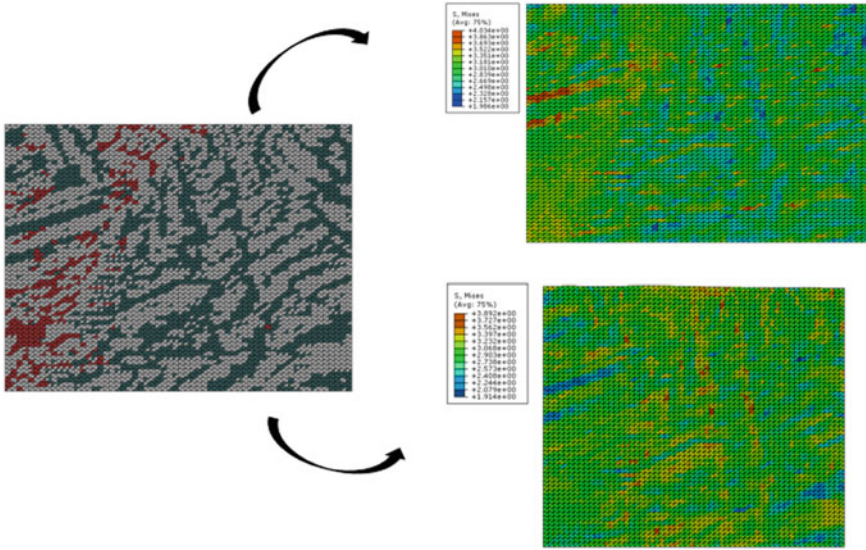
Fig. 4.11 Mesh of region C. Thermal deformation in x and y-directions
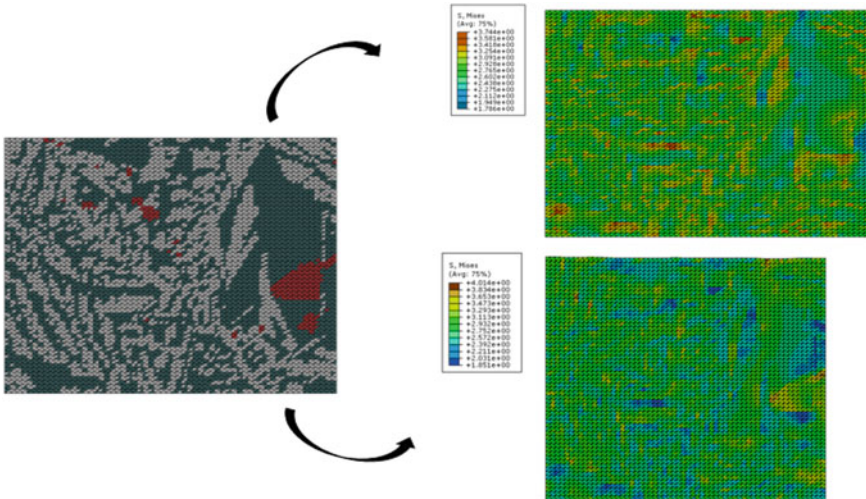
Fig. 4.12 Mesh of region D. Thermal deformation in x and y-directions
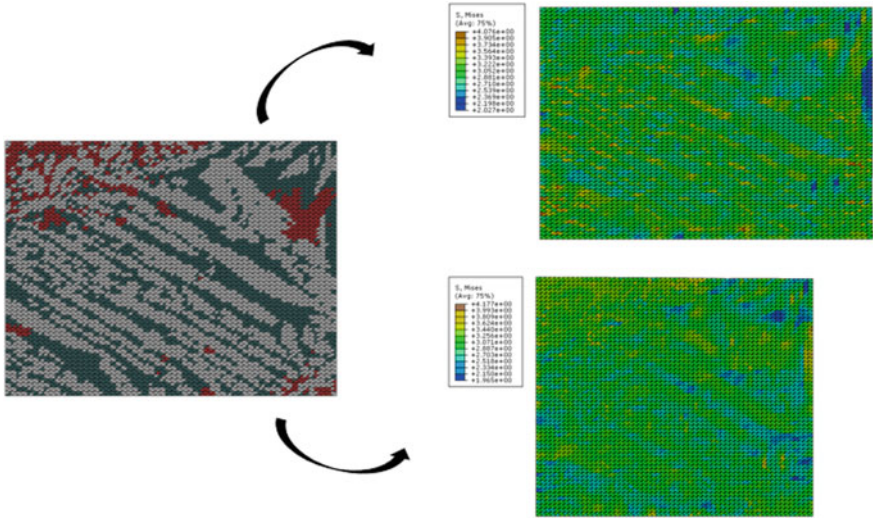
Fig. 4.13 Mesh of region E. Thermal deformation in x and y-directions
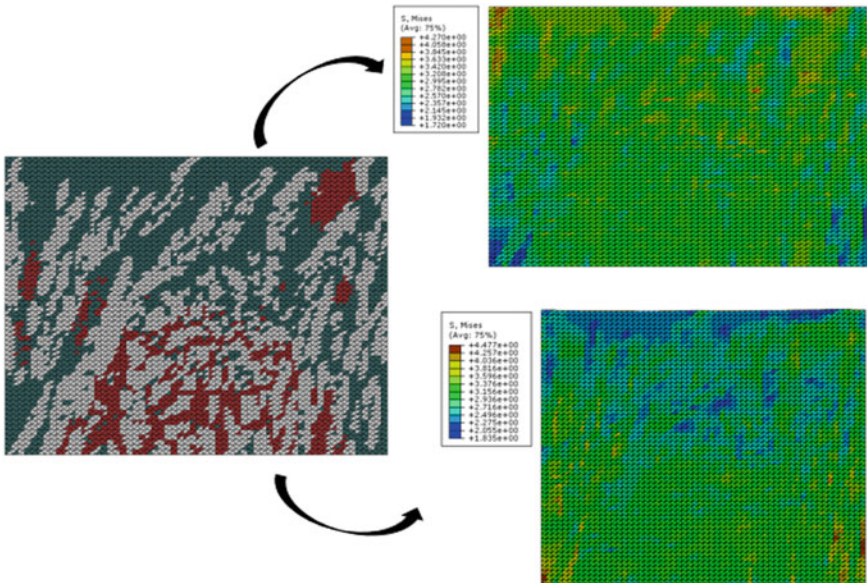
Fig. 4.14 Mesh of region F. Thermal deformation in x and y-directions

Fig. 4.15 C-ring model
divided into six regions
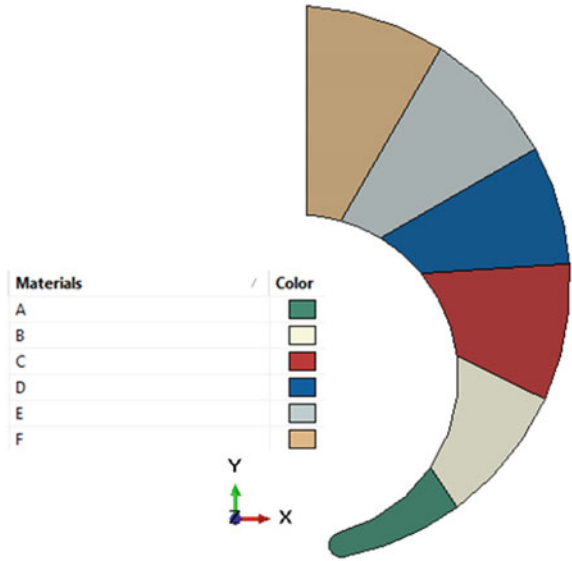
Fig. 4.16 Vertex 3 was fixed
in the X and Y-directions
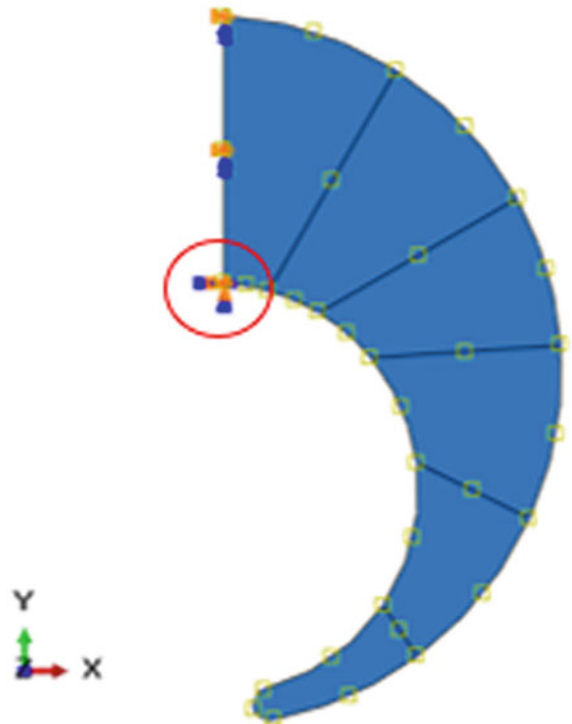
Fig. 4.17 Thermal stress analysis at C-ring
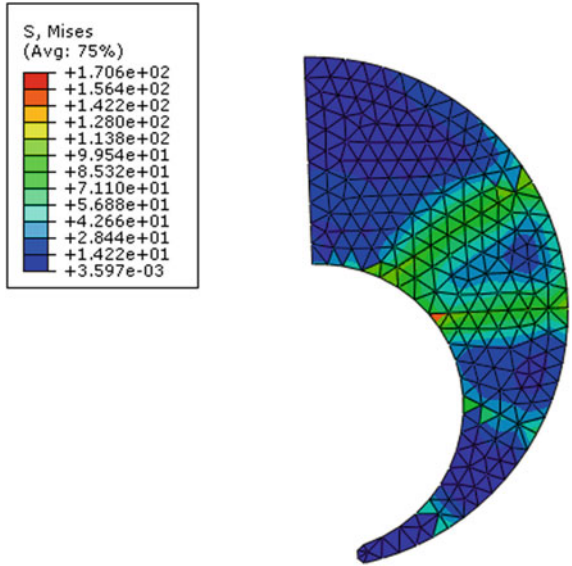
Fig. 4.18 Thermal deformation analysis at C-ring, scale factor 3
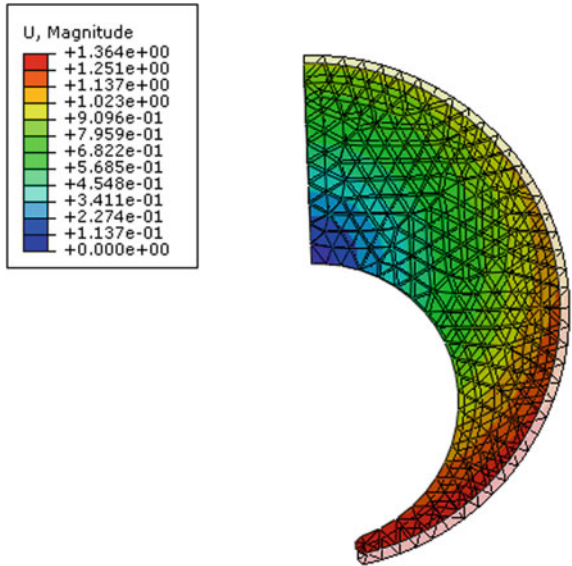
Fig. 4.19 Thermal
deformation analysis at
C-ring, homogeneous
part—scale factor 3
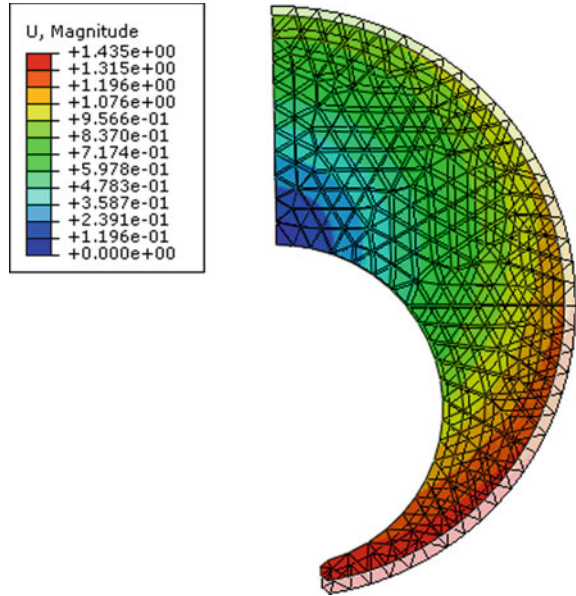
References

ABAQUS Unified FEA, Simulia, Dassault Systems, France (2013)

Aboudi, J., Arnold, S.M., Bednarcyk, B.A.: Chapter 3—Fundamentals of the Mechanics of Multi-
phase Materials, pp. 87–145. Micromechanics of Composite Materials, Butterworth-Heinemann
(2013)

Belytschko, T., de Borst, R.: Multiscale methods in computational mechanics. Int. J. Numer. Meth.
Eng. **89**(8–9), 939–1271 (2010)

de Sousa Neto, E.A., Peric, D., Owen, D.R.J.: Computational Methods for Plasticity: Theory and
Application. Wiley (2011)

Fish, J.: Practical Multiscaling. Wiley (2014)

Fish, J., Belytschko, T.: First course in finite elements. Wiley & Sons, Ltd (2007)

Horstemeyer, M.F.: Multiscale modeling: a review. In: Leszczynski, J., Shukla, M.K. (eds.) Practical
Aspects of Computational Chemistry, pp. 87–135. Springer Science Business Media (2009)

MATLAB- The Matworks, Inc, USA (2017)

Nilsson, J.-O., et al.: Mechanical Properties, Microstructural Stability and Kinetics of sigma-phase
Formation in 29Cr-6Ni-2Mo-0.38N Superduplex Stainless Steel. Metallurgical and Materials
Transactions A. vol. 31(A), pp. 35–45 (2000)

OOF software, National Institute of Standards and Technology, U.S. Commerce Department, USA (2019)

Sousa, R.O., et al.: On the Precipitation of Sigma and Chi Phases in a Cast Super Duplex Stainless Steel. Metallurgical and Materials Transactions A, vol. 50A, pp. 4758–4778. Metallurgical and Materials Transactions A, Issue 10 (2019)

Zienkiewicz, O.C.: The Finite Element Method in Structural and Continuum Mechanics. McGraw-Hill, London (1971)

Zohdi, T.I., Wriggers, P.: An Introduction to Computational Micomechanics, Lectures Notes in Applied and Computational Mechanics. Spinger, Berlin Heidelberg (2008)

Part II
Composites

Chapter 5
Phono-Absorbent Behavior of New Fiberglass Plates from Mixed Plastic Material Wastes

M. A. Platon, O. Nemes, A. E. Tiuc, O. Vasile, and S. Paduretu

Abstract Circular economy and waste recycling are a priority domain in European policies. In the case of glass fiber reinforced polymer (GFRP), waste storage is prohibited; therefore, alternative options are encouraged: thermal, chemical, or mechanical recycling and comprehensive recovery. If thermal and chemical recycling are more suitable for carbon fiber reinforced polymer (CFRP), due to the higher market value obtained after recycling; for GFRP, the most adequate approach is mechanical recovery, due to several reasons: higher added value, reduced costs and loop closing, according to the circular economy. In this work, we propose an energy-saving thermo-mechanical recycling method for the mixed plastic wastes, to obtain composite material plates. The method is economically efficient, and so far, it is the best for this type of waste, considering the cost–benefit ratio. The sound absorption behavior of the obtained plates was analyzed to define the possibility of using them for the reduction of the environmental noise. The data obtained was analyzed, and the results were compared with the characteristics of other materials which could be replaced by this new material.

Keywords Polymers · Waste · Recycling · Phono-absorbent

M. A. Platon · O. Nemes (✉) · A. E. Tiuc
Department of Environmental Engineering and Sustainable Development Entrepreneurship,
Technical University of Cluj-Napoca, 103-105 Muncii Boulevard, 400641 Cluj-Napoca, Romania
e-mail: Ovidiu.Nemes@imadd.utcluj.ro

O. Vasile
Department of Mechanics, University POLITEHNICA of Bucharest, 313 Splaiul Independenței,
060042 Bucharest, Romania

S. Paduretu
Department of Modern Languages and Communication, Technical University of Cluj-Napoca,
103-105 Muncii Boulevard, 400641 Cluj-Napoca, Romania

5.1   Introduction

Circular economy and waste recycling represent a priority domain in European policies. It is well known that recycling is a primary issue of European environmental policies. Lately, discussions regarding recycling are increasing in number, in the context of the circular economy (Vermesan et al. 2020). Thus, until recycling is achieved, it is desirable to keep a product in use for as long as possible, but also to obtain an easy and efficient reintegration into the production flow and, as much as possible to the highest percentage. According to the European environmental legislation for GFRP, waste storage is prohibited (Correia et al. 2011) and the other ways to process the waste are thermal, chemical, or mechanical recycling and comprehensive recovery.

Each method has both advantages and disadvantages and must be analyzed also in terms of cost–benefit ratio. If thermal and chemical methods come with a higher price due to the energy consumption, as far as CFRP is concerned, these methods are still suitable due to the higher market value of the fibers on the market, as compared to GFRP (Potluri and Ketha 2015). For GFRP, the most adequate recycling methods are: mechanical recycling, by using it as a filler in concrete structures or rebars, manholes covers, and comprehensive recovery which, due to the time required for the separation of components, has a disadvantage, also the market value of the recycled is much lower than the initial value of the product.

In this paper, we studied a thermomechanical recycling method based on thermoforming principles. The method is adequate for the mixed plastic wastes, as long the main polymeric compounds: poly(methyl methacrylate) (PMMA) and acrylonitrile butadiene styrene (ABS) are thermoplastic polymers. By recycling the studied wastes, we may get more use out of a composite material, so more resistant than the classic wood composites (LDF, plywood, etc.). Our analysis focuses on the important acoustic behavior in case of potential usage of the waste for manufacturing of the interior walls for living spaces. Of course, the mechanical properties and the behavior in a humid environment are important, but in the case of indoor use, sound insulation is essential.

5.2   Experimental Part

5.2.1   Materials

The mixed waste originates from the production process of sanitary ware (bathtubs). The constituents are ABS and PMMA with a ratio of 90% ABS and 10% PMMA, mixed with fiberglass, available as chips with $5 \div 10$ mm dimensions (Fig. 5.1a). For the experimental part, 10 samples were molded using 150 g of waste. The samples are 142 mm in diameter and 10 mm in thickness, as shown in Fig. 5.1c. The main components of the molding system (Fig. 5.1b) are: the cylindric shape, temperature
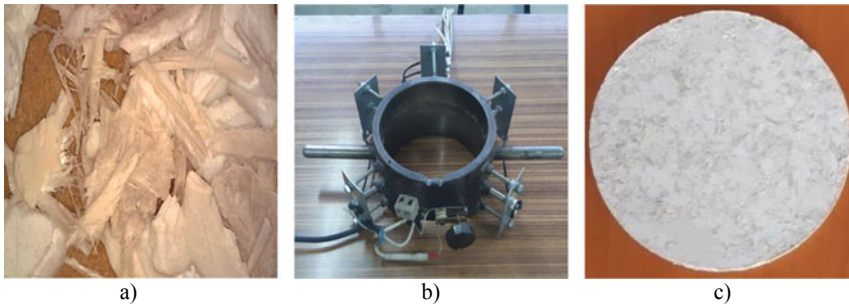
Fig. 5.1 Materials and equipment. **a** Waste chips; **b** molding system; **c** produced sample

Table 5.1 Process parameters

Sample code	Temperature (°C)	Pressure (MPa)
T130_P317	130	3.17
T130_P445	130	4.45
T135_P317	135	3.17
T135_P445	135	4.45
T135_P637	135	6.37
T140_P637	140	6.37
T150_P317	150	3.17
T150_P637	150	6.37
T150_P955	150	9.55

sensors, and two electrical resistance heating (ERH) embedded in the plates that close the cylinder. The used process parameters are presented in Table 5.1. Usually, the pressure and temperature/sample fluctuate between 0.7 ÷ 0.15 MPa and 130 ÷ 150 °C, in order to have range of parameters as wide as possible, that provides a better understanding of the material's phono-absorbent behavior. For comparison, the other materials used were: low-density fiberboard (LDF) and rubber granules with 1 ÷ 3 mm in diameter, made of recycled tires granules and 15% flexible bicomponent polyurethane foam, with a 10 mm thickness.

Also, the working temperature was established considering the melting point of the constituents (204 ÷ 238 °C for ABS, 130 °C for PMMA) so as to avoid material melting and also to exceed the glass transition temperature of 105 °C (for ABS and PMMA), for a more facile thermoforming in the highly elastic zone (Fig. 5.2).

The samples were coded as shown in Table 5.1. The value after letter T is representing the temperature and pressure after letter P.

The sample material is considered a composite material with short and unoriented fibers due to its constituents. The glass fiber, consisting of roving units, behaves
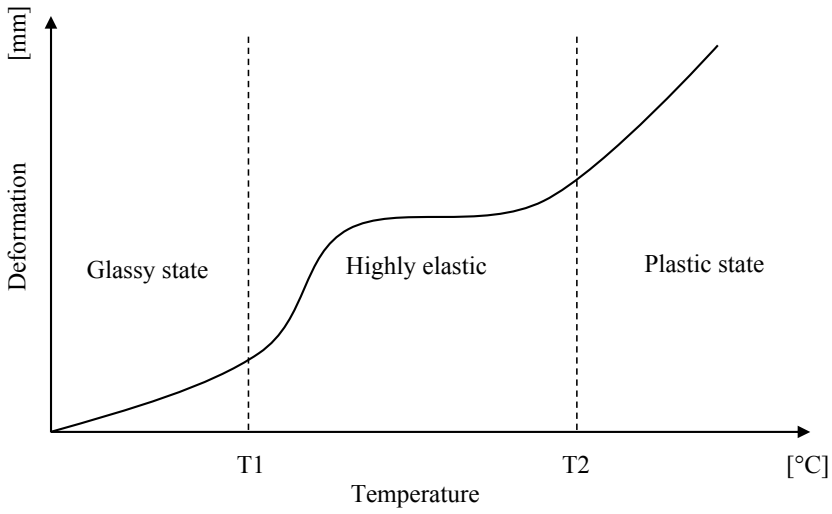
Fig. 5.2 Deformation versus temperature

like a reinforcement and the ABS, PMMA polymers act as the matrix. The phono-absorption tests were carried on circular specimens having 63.5 mm in diameter, as required by the test equipment (Figs. 5.3 and 5.4).
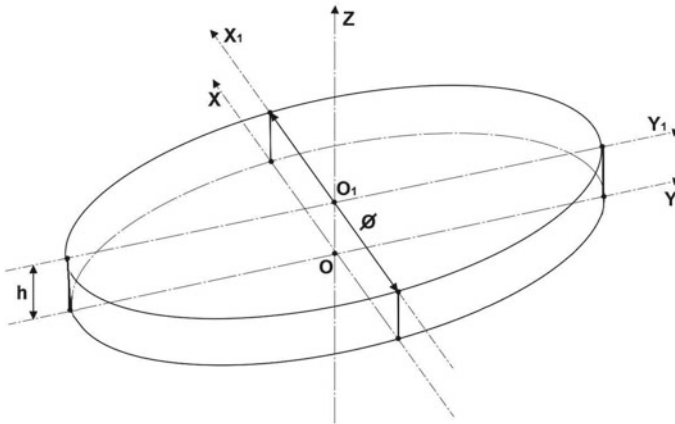
Fig. 5.3 Sample geometry
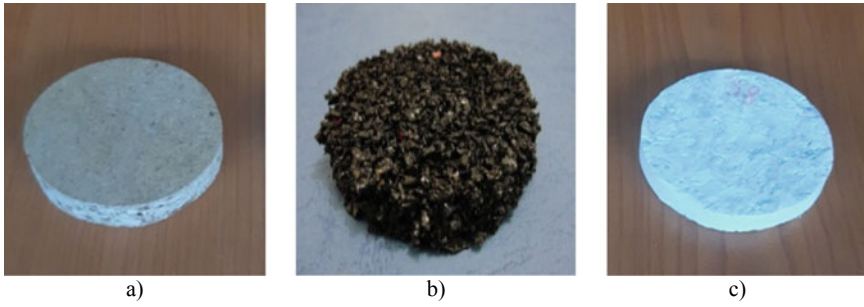
Fig. 5.4 Specimens ready for phono-absorption test. **a** LDF; **b** rubber; **c** mixed waste

5.3 Methods

5.3.1 Sound Absorption Test

Sound absorption is the property of a body or material to absorb the ambiental sound. The method of measuring the sound absorption coefficient using the impedance tube is based on the fact that the reflection coefficient at normal incidence (r) can be calculated from the transfer function H_{12}, measured between two microphone positions at different distances from the sample. The incident transfer function (HI) and the reflecting waves (H_R) between the microphone positions are defined as (Tiuc et al. 2018):

$$H_I = \frac{p_{2I}}{p_{1I}} = e^{-jk \cdot (x_1 - x_2)} = e^{-jk \cdot s} \tag{5.1}$$

$$H_R = \frac{p_{2R}}{p_{1R}} = e^{-jk \cdot (x_1 - x_2)} = e^{-jk \cdot s} \tag{5.2}$$

where s is the distance between the two positions of the microphone; x_1 and x_2 are the distance from the reference point to position 1 and 2 of the microphone; p_I and p_R are the sound pressure that propagates in the incident and reflected direction, jk is a complex wavenumber.

The transfer function $H12$ for the total sound field can be calculated using the formula:

$$H_{12} = \frac{p_2}{p_1} = e^{-jk \cdot (x_1 - x_2)} = e^{-jk \cdot s} \tag{5.3}$$

The reflection coefficient r at the sample surface, $x = 0$, is:

$$r = \frac{H_{12} - H_I}{H_R - H_{12}} e^{2jk \cdot x_1} \tag{5.4}$$
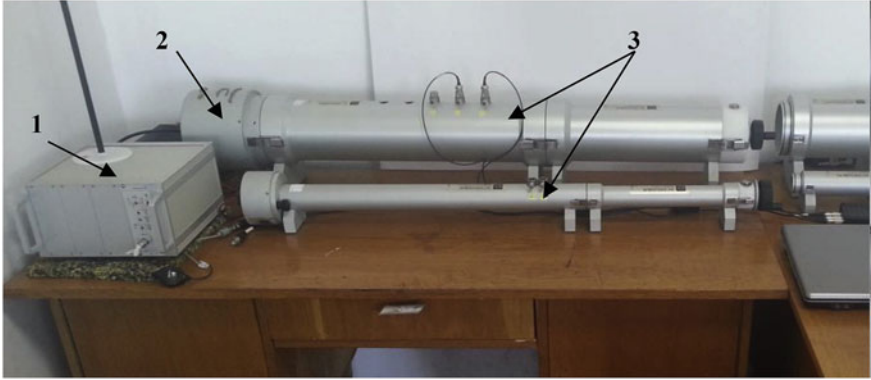
Fig. 5.5 Experimental stand

The sound absorption coefficient at normal incidence is calculated by formula (Tiuc et al. 2018):

$$r = 1 - |r|^2 \tag{5.5}$$

The experimental stand used (Fig. 5.5) for the sound absorption coefficient measurement contains: Signal amplifier (1); White noise generator and acquisition system (2); Impedance tube (3) (Tiuc et al. 2019). The measurements were performed by the two microphones transfer method using the ISO 10534-2 Standard (Standard SR EN ISO 10534-2), used for testing with horizontally mounted specimens. A Brüel & Kjaer model 4206 tube was used to measure different acoustic parameters for a frequency of $100 \div 3200$ Hz. The average diameter of the tube is 63.5 mm, so the specimens were cut circularly having this diameter.

5.3.2   Surface Morphology

For the analysis of the surface morphology, it was used a *Phuture R* portable digital electronic microscope, with a 7 inch. LCD screen and a resolution of 12 megapixels, with image magnification from 1 to $1200\times$.

5.4   Result and Discussions

5.4.1   Results of the Phono-Absorption Test

The results of the phono-absorption test was centralized into several tables and a graph, in order to have a comparative view for a better analysis.

The average value for the superior part ($\alpha = 0.39$) is slightly lower than the average value for the inferior part ($\alpha = 0.4$), which indicates a sentient better acoustic behavior generated by the unidirectionally molding process (Fig. 5.6 and Table 5.2).

The letter "S" in the sample code stands for the superior part of the sample, according to the thermoforming position and the letter "I" is for the inferior part (Fig. 5.7). In the situation when the coefficient is lower for the superior part, this is due to a better thermo-compaction which leads to a better surface quality of the material in this part (thermoforming is vertically unidirectional) which creates a layer with a higher degree of compaction (Figs. 5.8a and 5.9a), less porous than the inferior part. For LDF samples, the obtained values of the sound absorption coefficient are close, but this does not indicate the homogeneity of the constituents, but it demonstrates instead a bidirectional manufacturing process. Also, it can be noticed that the acoustic behavior is significantly better in the frequency range of $1500 \div 2500$ Hz.

The sound absorption coefficient of the mixed waste samples is higher than LDF for all samples, and lower than that of the rubber, due to its porosity and constituents. Mamtaz et al. (2016) observed that factors like particle size, bulk density, and sample layer thickness have an influence on the acoustic absorption.
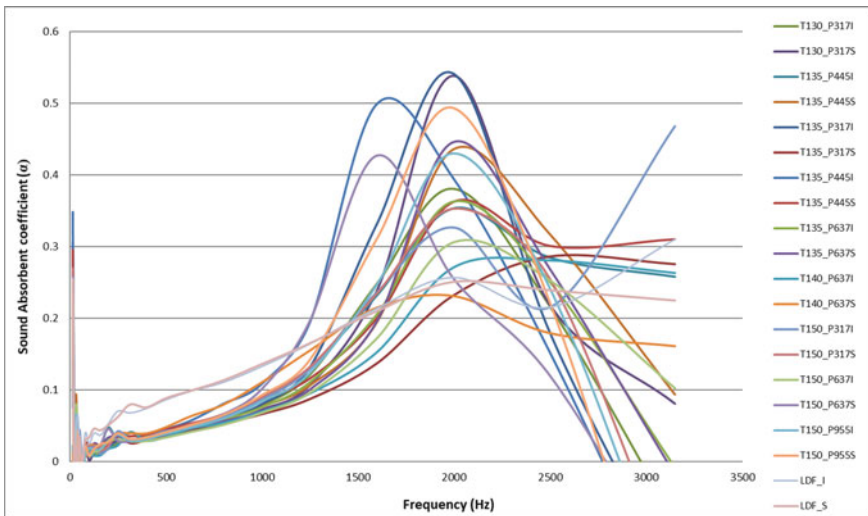
Fig. 5.6   Variation of the sound absorption coefficient with the process parameters and frequency

Table 5.2 Results for phono-absorption testing

Sample code	Sound absorption coefficient	
	Superior part	Inferior part
LDF	0.25	0.31
Rubber	0.72	0.72
T130_P317	0.53	0.38
T130_P445	0.43	0.35
T135_P317	0.28	0.54
T135_P445	0.36	0.49
T135_P637	0.44	0.36
T140_P637	0.23	0.28
T150_P317	0.35	0.46
T150_P637	0.42	0.3
T150_P955	0.49	0.42
Average value for mixed waste samples	0.39	0.40
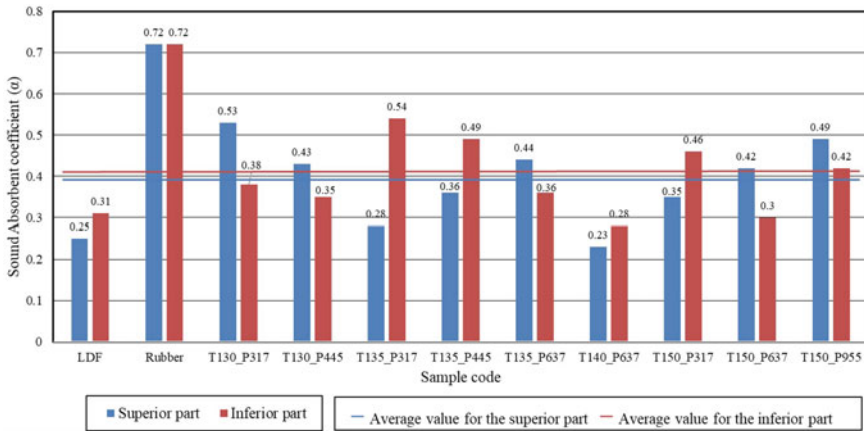
Fig. 5.7 Variation of the sound absorption coefficient with the superior and inferior part

5.4.2 Results for Surface Morphology

Figure 5.8 reveals the surface morphology; regarding the superior part, we can notice a better compaction and adhesion between fiberglass and polymers. For the inferior part, due to the nature of the molding process, there is a higher degree of roughness generated by a lack of adhesion.

Both images demonstrate the particularities of the material, the fact that the composite and fiberglass act as a reinforcement/bonding element and the polymers (ABS, PMMA) behave as the matrix.
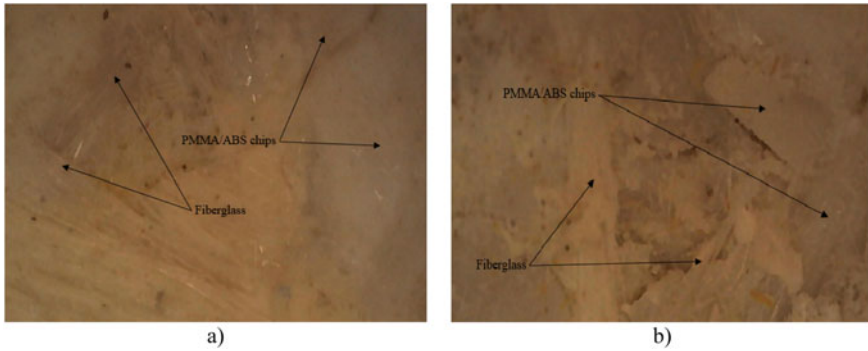
Fig. 5.8 Surface morphology for mixed waste sample: **a** superior part; **b** inferior part

Fig. 5.9 Surface morphology for LDF: **a** superior part; **b** inferior part

For LDF, the image with the superior part shows the same level of roughness as the inferior one, due to the bidirectional manufacturing process that led to an almost similar acoustic behavior. Also, the LDF average value for the sound absorption coefficient ($\alpha = 0.28$) is 30% lower than the average value for the mixed waste plates ($\alpha = 0.4$) which indicates a much higher porosity for mixed waste plates.

5.5 Conclusions

The studied waste, taking in consideration the sound absorbing behavior, can replace the LDF but it does not manifest the acoustical qualities of rubber. This behavior can be explained by the density and the reduced porosity of the material. The advantages of porous materials are the wide absorption frequency range, low cost, and easy molding, as compared to the other materials, such as the well-known perforated panels and membrane resonators (Cao et al. 2018).

In terms of the cost per produced unit, it is not likely to be able to estimate a cost because so far there have been only limited series produced from this kind of mixed waste and it is difficult to estimate the energy consumption, but it is obvious that incineration is not sustainable (Pickering 2005) and the outputs obtained by mechanical recycling are not ready-to-use, the recycled can be used as filler or as reinforcement in new composite materials (Ribeiroa et al. 2013) which increases the cost of operation and production. The studied method saves time and energy as compared to other methods. Also, the newly obtained material can be subject to different use: reinforcing elements for sanitary products, interior panels, components in different mechanical structures, tiles, etc. (García et al. 2014).

References

Cao, L., Fu, Q., Si, Y., Ding, B., Yu, J.: Porous materials for sound absorption. Compos. Commun. **10**, 25–35 (2018)

Correia, J.R., Almeida, N.M., Figueira, J.R.: Recycling of FRP composites: reusing fine GFRP waste in concrete mixtures. J. Clean. Prod. **19**, 1745–1753 (2011)

García, D., Vegas, I., Cacho, I.: Mechanical recycling of GFRP waste as short-fiber reinforcements in microconcrete. Constr. Build. Mater. **64**, 293–300 (2014)

Mamtaz, H., Fouladi, M.H., Al-Atabi, M., Namasivayam, S.N.: Acoustic absorption of natural fiber composites. J. Eng. **5836107** (2016)

Pickering, S.J.: Recycling technologies for thermoset composite materials—current status. Compos. A **37**, 1206–1215 (2005)

Potluri, R., Ketha, K.K.: Comparison between GFRP and CFRP composite power take-off shaft in helicopters for prescribed torque and geometrical constraints. J. Mater. Sci. Mech. Eng. **2**(3), 214–219 (2015)

Ribeiroa, M.C.S., Meira-Castro, A.C., Silva, F.G., Santos, J., Meixedo, J.P., Fiúzaa, A., et al.: Reuse assessment of thermoset composite wastes as aggregate and filler replacement for concrete-polymer composite materials: a case study regarding GFRP pultrusion wastes. Resour. Conserv. Recycl. **104**, 417–426 (2013)

Standard SR EN ISO 10534-2: Determination of Sound Absorption Coefficient and Acoustic Impedance with the Interferometer

Tiuc, A., Vasile, O., Vermesan, H., Nemes, O., Borlea, S.I.: New multilayered composite for sound absorbing applications. Roman. J. Acoust. Vib. **15**(2), 115–121 (2018)

Tiuc, A.E., Nemes, O., Vermersan, H., Toma, A.C.: New sound absorbent composite materials based on sawdust and polyurethane foam. Compos. B **165**, 120–130 (2019)

Vermesan, H., Mangau, A., Tiuc, A.E.: Perspectives of circular economy in Romanian space. MDPI Sustainability **12** (2020)

Chapter 6
Methodology to Simulate Veneer-Based Structural Components for Static and Crash Load Cases

G. Piazza, D. B. Heyner, E. Beeh, and H. E. Friedrich

Abstract The increased public interest in green technology combined with new environmental policies results in the need for lightweight vehicles with a reduced global environmental impact. A method that is gaining importance is the reduction of the cradle-to-grave carbon footprint of utilized materials. For structural components, one promising approach is the utilization of biomaterials such as veneer-based hybrid materials since wood is a natural carbon storage. The specific properties of wood are comparable to aluminum and magnesium, and thus have the potential to replace some structural and semi-structural components of a vehicle. When required, the hybridization of veneer-based materials with traditional materials, such as metal sheets, can further increase its structural performance. While it is technologically possible to implement such a material concept, a key challenge is the application-oriented simulation of non-hybridized and hybridized wooden structures. A suitable simulation method and material model must be found and validated. At the Institute of Vehicle Concepts of the German Aerospace Center, the methodology to simulate beech veneer-based structural components for static and crash load cases has been developed over the last three years. The characteristics of the veneer were determined in order to fit a material model in LS-Dyna which was then implemented in various simulation approaches for wooden structures. The findings were also transferred to simulate hybridized structures. This paper presents the chosen approach to simulate a hybridized generic structure that represents a door impact beam. It compares simulation results of different three-point flexural bending tests with testing results. The findings were generated in the project "For^(s)tschritt". The fully qualified simulation approach and material model will contribute to the structural application of non-hybridized and hybridized veneer-based composites in modern vehicle structures.

Keywords Crash · Simulation · Veneer · Structural

G. Piazza (✉) · D. B. Heyner · E. Beeh · H. E. Friedrich
German Aerospace Center (DLR e.V.), Institute of Vehicle Concepts, Pfaffenwaldring 38-40, Stuttgart, Germany
e-mail: Giovanni.Piazza@dlr.de

6.1 Introduction

Lightweight construction has once again come to the fore of the automotive industry due to strict emission guidelines, rising energy costs, and legal limits for the vehicle weight of electric vehicles. Options include the substitution by materials of lower density and the use of multi-material systems. A pure material substitution with lighter materials is only suitable if individual properties as well as the integration of the component into the assembly or the overall structure are considered and optimized. The economy must not suffer compared to existing construction methods. The same applies to the use of multi-material systems.

Furthermore, in addition to lightweight construction, the ecological consideration of vehicles, both during utilization phase and production phase, is becoming a focus of politics, society, and thus also the automotive industry. While greenhouse gas emissions can be reduced during utilization phase through lightweight construction, the greenhouse gas emissions during production phase highly depend on the materials used. Depending on the process route, steels as well as classic lightweight construction materials, such as aluminum or magnesium alloys, but also new lightweight construction materials such as carbon fiber reinforced plastics (CFRP) or glass fiber reinforced plastics (GFRP) generally tend to have a poorer balance in comparison with wood derivates (Bergman and Alanya Rosenbaum 2016; Kelly and Dai 2019).

Given the political, economic, and ecological boundary conditions mentioned above, there is a need for efficient, holistic, and sustainable lightweight construction solutions. One approach is the use of renewable raw materials, such as wood and wood derivatives, in non-load-bearing but also in load-bearing structures in vehicles. With weight-specific material characteristics in fiber direction that are comparable to or better than classic lightweight construction materials, wood offers a sustainable and economical alternative. The last two columns in Table 6.1 show the weight-specific characteristics for bending, where applicable along fiber direction (*l*), according to Ashby (2004).

6.2 Properties of Veneer and Veneer-Based Components

6.2.1 Properties of Veneer

Wood consists mainly of the three structural substances cellulose, hemicellulose, and lignin. Analogous to CFRP materials, cellulose is the long, longitudinal fibers, while lignin forms the matrix. The hemicellulose consists of significantly shorter fibers and connects individual cellulose fibers crosswise with one another. This creates support in the cross direction. When manufacturing veneer a stem is typically peeled around its longitudinal direction. Therefore, veneer layers are orthotropic materials where the properties are defined in longitudinal (L), tangential (T), and radial (R) directions, see Fig. 6.1. Depending on the used material model, the directions in the simulation

Table 6.1 Technical comparison of materials (Klein 2011; Niemz 2006)

Material	Density (g/cm^3)	Young's modulus E (MPa)	Ultimate strength UTS (MPa)	$(E)^{1/2}$/Density[a] (MPa)$^{1/2}$/(g/cm^3)	$(UTS)^{2/3}$/Density[a] (MPa)$^{2/3}$/(g/cm^3)
Aluminum	2.30–2.80	70.000	45–500	95–115	5–27
Beech	0.54–0.91	~14.350 (*l*)	100–140 (*l*)	132–222	24–50
CFRP	~1.50	~140.000 (*l*)	~1.700 (*l*)	~250	~95
GFRP	~2.00	~44.500 (*l*)	~1.100 (*l*)	~105	~53
Magnesium	~1.74	45.000	100–300	122	12–26
Steel	7.85–7.87	210.000	340–1.800	58	6–19

[a]Higher values are better

Fig. 6.1 Illustration of the orthotropic directions of veneer
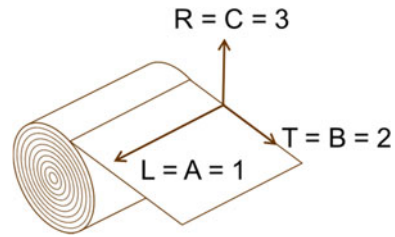
are also described with "A" or "1" for the longitudinal and "B" or "2" for tangential, respectively, "C" or "3" for radial direction.

In the studies carried out in project "For$^{(s)}$tschritt", veneer made of beech wood was used. The properties in-plane were determined through simple tensile tests mainly in L and T directions (see Fig. 6.3 left) as well as compression tests (see Fig. 6.3 right). Testing showed the expected orthotropic material behavior.

6.2.2 Properties of Veneer-Based Layered Composites

As a natural material wood in general has scattering characteristics. For example, scatter in Young's moduli are depending on the amount of fibers in a cross-section which changes depending on the position in a tree. Scatter in failure strength is depending on the amount and size of imperfections in a given specimen. By using veneer-based layered composite, the scatter can be reduced since on the one hand the used veneers are preselected such as the number of imperfections within them are reduced, and on the other hand the usage of multiple veneers leads to a statistically averaging of the characteristics.

The behavior can mostly be described by the classical laminate theory (Reddy 1987) with the following assumptions:

- Each layer is ideally linear elastic
- The thickness of each layer is small compared to its width and length
- The thickness of each layer is constant
- Plane-stress due to small thickness of a layer
- Deformations are small in order to use first-order deformation theory
- Euler–Bernoulli beam theory is valid
- Layers are glued together ideally.

Failure occurs in tension regardless of orientation when failure strain is exceeded. In compression, global buckling or local buckling of individual fibers with subsequent crack formation in loading direction occurs in grain respectively in a uni-directional (UD) laminate. A combination of local buckling with subsequent crack formation and shear failure occurs when individual layers are oriented differently toward each other (see Fig. 6.2). For bending, failure occurs mainly due to exceeding of failure

UD laminate [0]$_n$ with 5x1,5 mm   Plywood [0-90]$_n$ with 5x1,5 mm
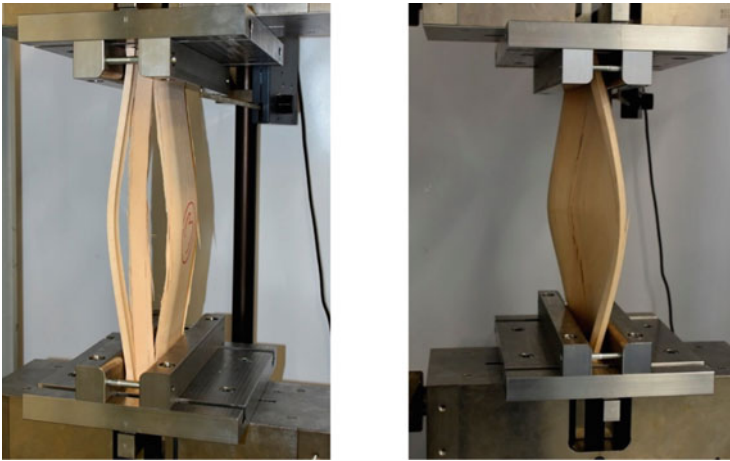
Fig. 6.2 Failure of a hat profile made of UD laminate (left) and plywood (right) in compression

strain on the side under tension. Delamination due to exceeding of normal stress (out-of-plane) in compression and of shear stress in bending can occur.

6.3   Modeling of Veneer-Based Layered Composites

6.3.1   Finite Element Method and Solver LS-Dyna

In the present load case with high plastic deformations and crack formations, the nonlinear material behavior of the veneer-based layered composite cannot be calculated using classical methods, e.g., the calculation of an analytical solution. An approximation method must therefore be used to calculate the complex behavior during impact simulations. Therefore, the finite element method (FEM) is used (Klein 2012). FEM is a numerical approximation method used in the present work to calculate strengths and deformations occurring due to the intrusion of a pole into the component.

With the help of computer-aided engineering (CAE), a network from elements and nodes that map the geometry as well as the definition of the properties of the component is created in a pre-processor. Boundary conditions, loads, and contact definitions are then applied at individual nodes. The data is then transmitted to an equation solver. In this paper, the solver LS-Dyna was used (Lee 2019). Finally, the results of the solver are read in a post-processor and displayed graphically. For example, deformations or stresses occurring during the side impact can be made visible at defined time steps.
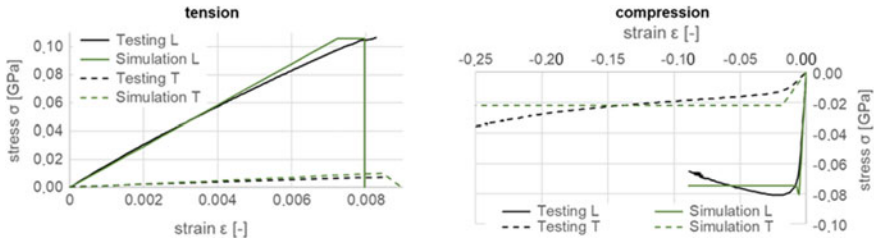
Fig. 6.3 Properties in tensile tests (left) and compression test (right)

In this paper, keywords and input parameters from LS-Dyna will be shown in italics.

6.3.2 Material Model *MAT_054

In order to model the single veneer layers for the FEM solver, LS-Dyna the material model *MAT_ENHANCED_COMPOSITE_DAMAGE (*MAT_054) is used. Figure 6.3 shows the comparison between simulation and testing for beech veneer. While the behavior parallel to fiber in the simulation is in line with testing, for the behavior in compression transversal to fiber a trade-off has to be done between in ultimate strength and failure strain respectively absorbed energy.

6.3.3 In-Plane Properties

The properties of the single layers of a (sub-)laminate are represented through the layered shell approach. A shell layer is modeled at the center of the physical height of the laminate it represents. A numerical integration point is defined within the element for each veneer layer. The thickness and orientation of the single layers as well as their material models are defined locally in the integration points of the shell (see Fig. 6.4). Hence, different ply stacks can be defined in a single shell layer. Multi-material systems, which can for example also consist of different woods, can also be defined through the layered shell modeling approach.

6.3.4 Out-of-Plane Properties

Testing showed that bending a laminated structure often leads to delamination in the middle of the component (see Fig. 6.5) due to exceeding of shear stress
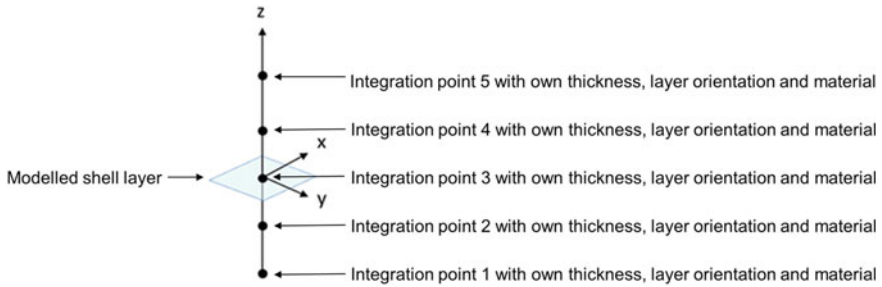
Fig. 6.4 Example of a layered shell representing a component with five layers
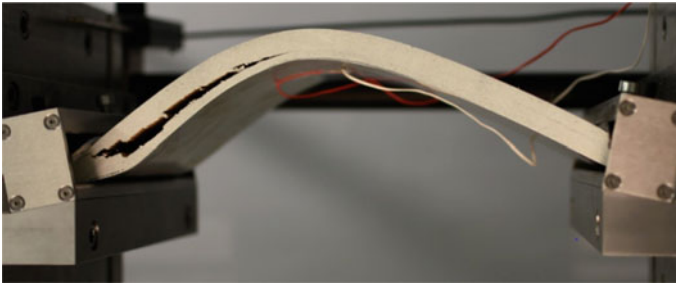
Fig. 6.5 Example of a component with delamination in the middle due to exceeding of sheer stress

(Roubins and Reddy 1993). To enable delamination in the simulation, the components were modeled with at least two layers of shell elements, where each of the layer represented a sub-laminate as described above in Sect. 6.3.3. The contact interface between the shell layers was modeled through the keyword *CONTACT_AUTOMATIC_ONE_WAY_SURFACE_TO_SURFACE* with *Option 11*. This activates a contact algorithm that is equivalent to using cohesive zone elements with a fracture model based on a bilinear traction–separation law, a mixed-mode delamination criterion as well as a damage formulation (LS-DYNA 2013).

Main parameters of the fracture model are the normal failure stress in tension (*NFLS*) and the shear failure stress (*SFLS*) between the two shell layers as well as the mode I and mode II critical strain energy release rates (G_{Ic} respectively G_{IIc}) when delaminating. The parameter *CN* determines the normal stiffness of the material in the interlaminar region. For the tangential stiffness *CT*, a scale factor (*CT2CN*) with a value between 0 and 1 is used on the normal stiffness—hence, $CT = CT2CN \times CN$. The description of the mixed-mode loading treatment will not be described in this paper but can be found in LS-DYNA (2013).

For illustration a mode I, crack opening model is shown in Fig. 6.6. The bilinear behavior shows first the rise of stress with the slope *CN* from zero stress up to a value of *NFLS* and then the drop to zero. The area under the curves corresponds to the mode I critical strain energy release rate G_{Ic}. After reaching the displacement at which
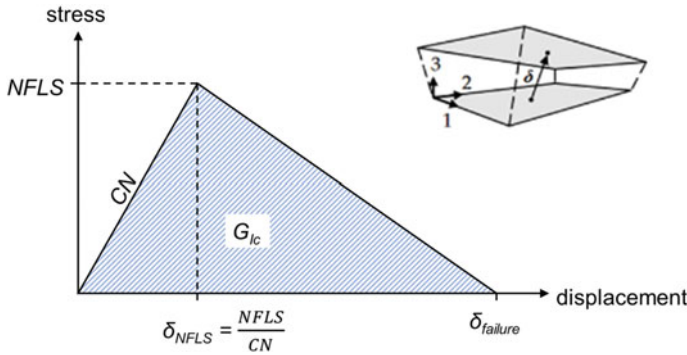
Fig. 6.6 Bilinear law used for mode I crack opening to describe delamination

failure occurs ($\delta_{failure}$), the interface between master segment and slave nodes turns to a surface to surface contact and can only be loaded on compression (LS-DYNA 2013). Mode II crack opening is described analogously with the corresponding parameters.

6.4 Simulation of Generic Veneer-Based Components

To represent a realistic load case, a generic structure comparable to a door impact beam was locked at. Door impact beams are a safety feature in today's vehicles that protect the driver respective the passengers during a side impact. As the name suggests, it is mounted in the door and absorbs energy from a side impact while maintaining structural integrity.

6.4.1 Calibration Through Quasi-Static Three-Point Bending Flexural Test (3PB)

To calibrate the contact interface described in Sect. 6.3.4, three-point bending flexural tests (3PB) on a universal testing machine (UTM) were carried out and simulated. A 10-inch diameter pole (254 mm) impacted the generic beam made of 16 veneer layers with 2.0 mm thickness and a steel strip with a thickness of 1.2 mm. The test setup and the trapezoidal cross-section can be seen in Fig. 6.7.

In simulation, the beam was modeled by two shell layers for the wooden part each representing a sub-laminate with the orientation [90–0–90–0–0–90–0–90] (see Sect. 6.3.3) in order to allow delamination in the wooden part in simulation (see Sect. 6.3.4). The steel strip was modeled through a third shell layer and was on
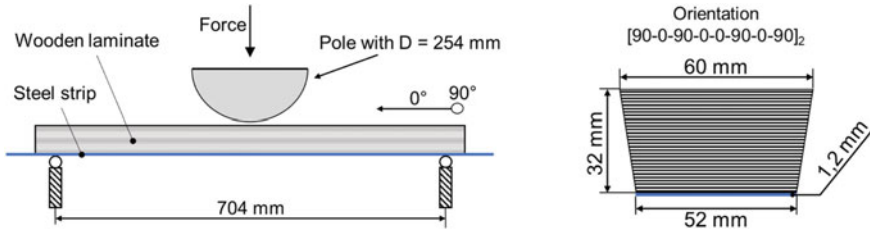
Fig. 6.7 UPM—sketched test setup (left) and cross-section (right)

purpose not included into the lower sub-laminate in order to allow a possible delamination between steel strip and wooden part. The three layers of shell elements can be seen in Fig. 6.8 top right.

The comparison between testing and simulation showed that a similar course of the force–displacement curve (see Fig. 6.8 bottom) could be achieved. Furthermore, the fracture pattern could be mapped to good approximation (see Fig. 6.8 top).
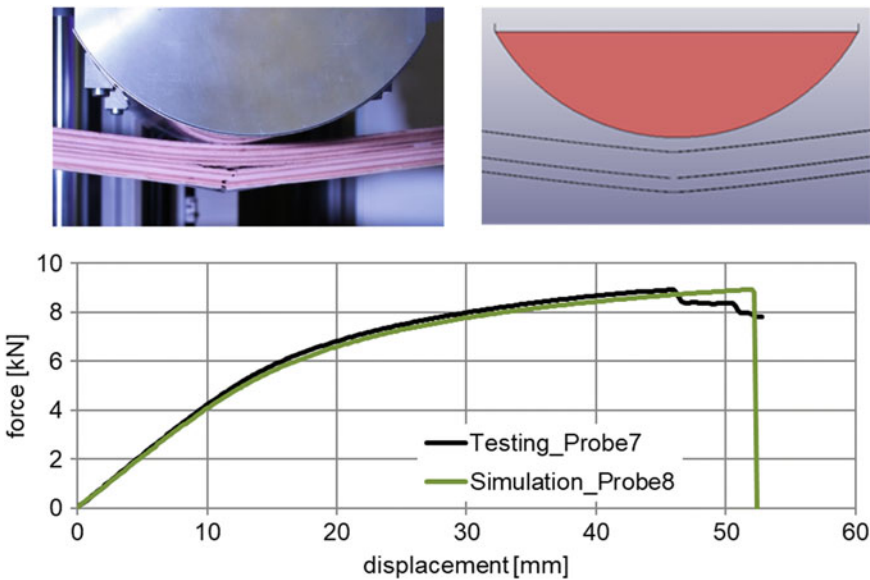
Fig. 6.8 UTM—comparison between testing and simulation model with calibrated material card of bending line (top) and of force–displacement curves (bottom)

6.4.2　Validation Through Quasi-Static 3PB with Boundary Conditions

On the static load test facility (SLTF), a hydraulic cylinder pushed the pole into the hybridized wooden beam, in approximation to the quasi-static door impact test according to FMVSS 214S with a pole of 10-inch diameter (254 mm). In contrast to the tests at the UPM, self-constructed absorber units (AU) were mounted on the steel strip at the beam endings (see Fig. 6.9 top and middle for test setup and Fig. 6.9 bottom for absorber units). The AU provided a defined motion while maintaining a constant retention force of about 10 kN by pulling a blade through an aluminum tube.

The AU were modeled using solids in combination with *MAT_HONEYCOMB* in the simulation. A parameterized force–displacement curve is used such that the force level was adapted to the same retention force planned for the experiment.
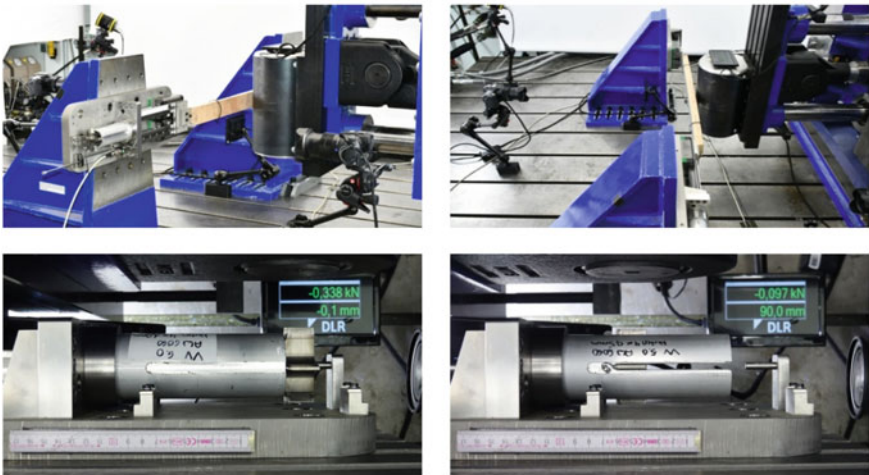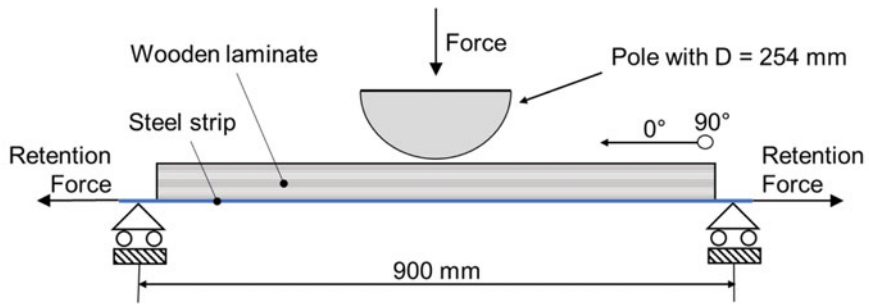
Fig. 6.9 SLTF—sketched test setup (top), pictures from testing (middle), and absorber units (bottom)

In testing, the two blades cut the tubes very asymmetrically (99.8 mm with 59.6 mm) due to friction between pole and beam, manufacturing tolerances of blades and aluminum tubes of the absorber units as well as imperfections in the testing setup. In simulation, the blades cut 80.7 mm into one AU and 86.8 mm into the other. Since the simulation is idealized, this more symmetrical distribution was expected. The simulation showed that the location and type of failure in the laminate led to small asymmetry. The combined penetration depth of both blades added up to 167.5 mm in simulation and 159.4 mm in testing. Hence, the overall kinematics in simulation is in good approximation to testing.

In Fig. 6.10, testing and simulation are compared. The qualitative course of the two force–displacement curves at the pole is similar although absolute values in simulation tend to be smaller. The height of the first peak in simulation is 8.67 kN in comparison with 9.93 kN in testing (−12.7%). Furthermore, a second failure (red
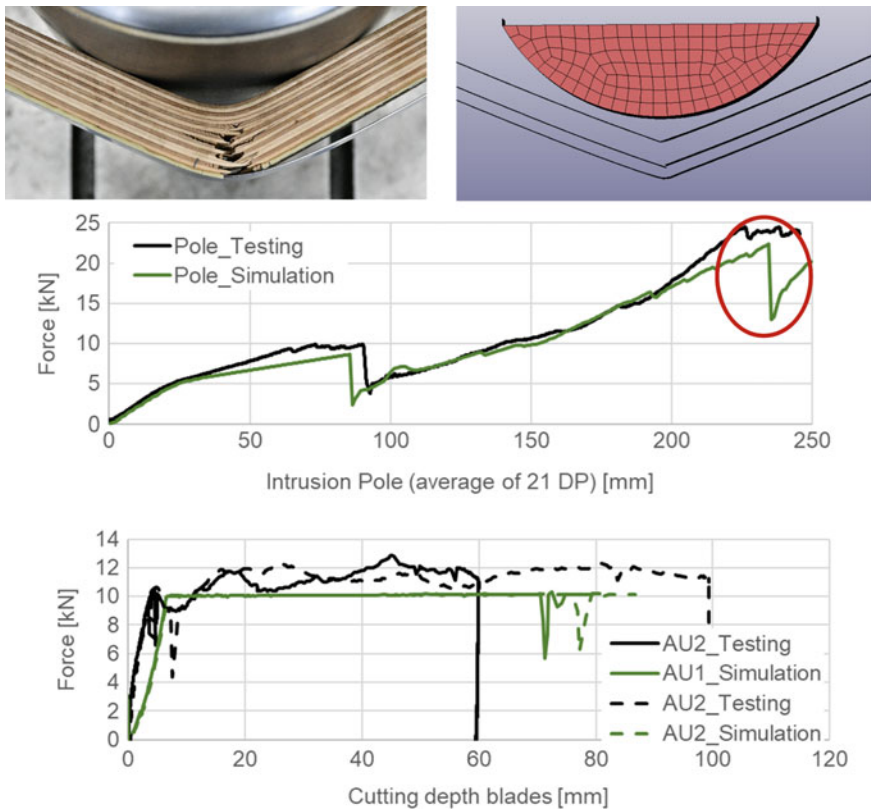
Fig. 6.10 SLTF—comparison between testing and simulation of bending line (top), force–displacement curves of poles (center), and force–displacement curves of the absorber units (bottom)

circle) occurs in simulation. The energy required during testing was 2765 J, while it was 2573 J (-6.9%) in simulation.

The discrepancy in peak force could be partly attributed to higher forces in the AUs in testing (around 11 kN instead of the expected 10 kN). The difference at an intrusion greater 200 mm was attributed to failure of single integration points and numerical deletion of those integration points in the layered shell on the side under compression.

With these findings, the simulation approach and the material model are considered validated.

6.4.3   Expansion of Dynamic Behavior Through High-Speed 3PB with Boundary Conditions

To simulate high-speed events like crash or impact, dynamic material properties have to be transferred into simulation.

For this purpose, a drop tower was used in combination with the absorber units. The pole is used as an impactor with a mass of 84.3 kg and an impact velocity of close to 5 m/s. The test setup can be seen in Fig. 6.11. Boundary conditions are analogous to the tests carried out on the static load test facility (see Fig. 6.9 top).

A reduced test setup was transferred to the simulation. With knowledge generated within the project "For[(s)]tschritt" by high-speed testing of small specimen, the static material model of *MAT_054* was roughly expanded by introducing strain-rate-dependent curves for the individual strengths. The material model was afterward
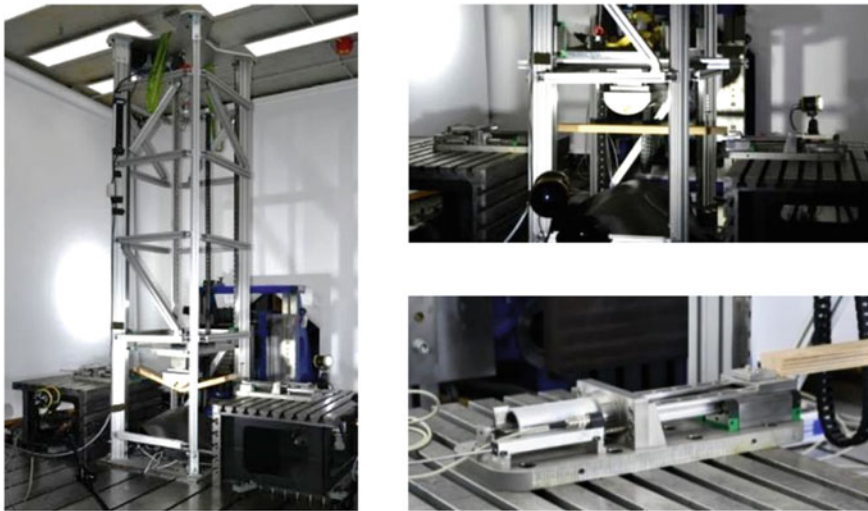
Fig. 6.11 Drop tower—pictures of test setup
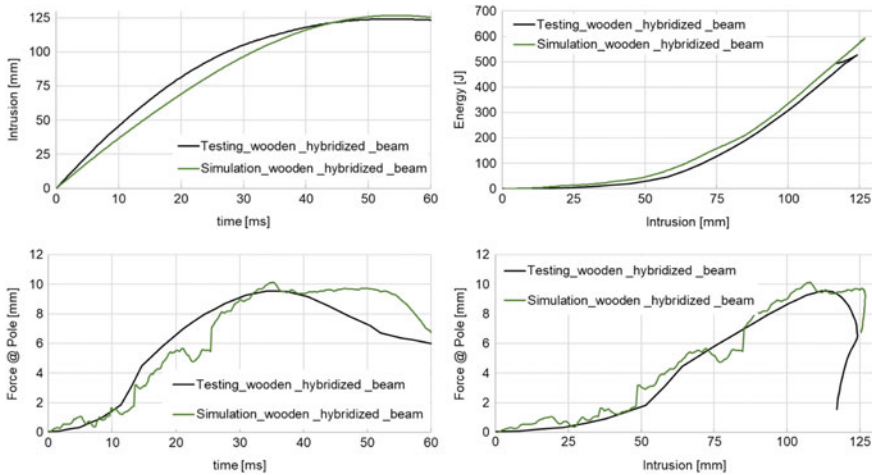
Fig. 6.12 Drop tower—displacement–time curve of poles (top left), energy–displacement curve (top right), force–time curve (bottom left), and force–displacement curve (bottom right)

refined with the knowledge gained from the high-speed three-point bending flexural tests.

Figure 6.12 shows the result of the comparison between testing and simulation for the drop tower test. Test results can be reproduced to a good approximation.

6.5 Summary

The presented paper puts forward a validated simulation approach for veneer-based multi-material components. Comparison between test and simulation with subsequent evaluation has taken place and shows good agreement. The global behavior in bending but also the local behavior in the event of failure could be mapped to a good approximation.

Hence, a transversal isotropic material model is available to simulate quasi-static, e.g., equivalent loads and high-speed events, such as impact or crash, in LS-Dyna.

Work is still needed on refining the dynamic parameters of the material model and hence on reducing the discrepancy between simulation and testing.

Afterward, approval-relevant crash load cases as well as those required by consumer protection agencies can be simulated in order to determine the potential of a specific assembly in comparison with the reference assembly.

References

Ashby, M.F.: Materials Selection in Mechanical Design, 3rd edn. Elsevier (2004)

Bergman, R., Alanya Rosenbaum, S.: Cradle-to-gate life cycle assessment of laminated veneer lumber production in the United States. For. Prod. J. **67** (2016)

Kelly, J.C., Dai, Q.: Life-cycle analysis of vehicle lightweighting: a review. In: Meyers, R. (ed.) Encyclopedia of Sustainability Science and Technology. Springer, New York (2019)

Klein, B.: Lightweight-Construction. Wiesbaden (2011)

Klein, B.: FEM—Grundlagen und Anwendungen der Finite-Element-Methode im Maschinen- und Fahrzeugbau, 9th edn. Vieweg+Teubner Verlag (2012)

Lee, R.: LS-DYNA for Engineers—A Practical Tutorial Book, 1st edn. BW Publications (2019)

LS-DYNA: Keyword User's Manual, Volume II: Material Models. Livermore Software Technology Corporation (LSTC) (2013)

Niemz, P.: Holzphysik. Institut für Baustoffe, Eidgenössische technische Hochschule, Zürich (2006)

Reddy, J.N.: A generalization of two-dimensional theories of laminates composite plates. Commun. Appl. Numer. Methods **3**, 173–180 (1987)

Roubins, D.H., Reddy, J.N.: Modelling of thick composites using a layerwise laminate theory. Int. J. Numer. Methods Eng. **36**, 655–677 (1993)

Chapter 7
Numerical Simulation of Impact Behaviour of Multi-cell Thin-Walled Structures with Configurable Thermal Trigger Design

N. Peixinho and P. Resende

Abstract This study presents numerical results for thin-walled octagonal structures subjected to impact loading and analysed for different section and trigger solutions. Triggers are usually considered in crashworthiness applications as geometrical features introduced to promote crash initiation, reduction of peak loads and promotion of efficient energy absorption deformation modes. In this study, the improvement potential of the introduction of thermal triggers is analysed. These are obtained, in concept, through localized heat treatment in selected aluminium alloys wherein a softened region works as trigger area. The main objective of such approach is to absorb impact energy in a progressive and controlled manner with higher efficiency and moderate peak loads. In the present implementation, two different alternatives for section design complimented with geometric and thermal trigger options are analysed. The application is studied recurring to numerical simulation of representative base octagonal geometry and an alternative complex multi-cell section design that is suitable for extrusion manufacturing process. The alternative geometry is allowed for significant improvements in specific absorbed energy. Both geometric and thermal trigger solutions are allowed for reduction in peak loads while maintaining or improving energy absorption parameters.

Keywords Thin-walled structures · Crashworthiness · Numerical simulation

7.1 Introduction

The various structural requisites for automotive structures include strength, stiffness, fatigue, being crashworthiness a particularly relevant one that has driven multiple design and materials/manufacturing developments. Considering also objectives of fuel usage reduction tied to mandatory reductions in CO_2 emissions, the development of lighter and more efficient crash-related structures is of significant importance.

N. Peixinho (✉) · P. Resende
MEtRiCS—Mechanical Engineering and Resource Sustainability Centre, University of Minho, Guimarães, Portugal
e-mail: peixinho@dem.uminho.pt

Tubular structures are considered primary elements to obtain controlled and reproducible crush response and energy absorption. For that purpose, the overall section and part design is considered, and in particular several trigger or crush initiators designs can be used. Zhang and co-authors (2009) studied a concept wherein a buckling initiator near the impact end was composed of a pre-hit column and pulling strips. The initial peak force of the square tube could be reduced by approximately 30% while the deformation mode and energy absorption were maintained. Marsolek and Reimerdes (2004) considered non-axisymmetric folding patterns as an improved method to control the absorption of kinetic crash energy. The trigger geometry mechanism was optimized for different loads allowing for reduced peak load (Marsolek and Reimerdes 2004). A more common geometrical trigger implementation was further developed by Rai and co-authors (2019) through the design of cut-out holes. The development of different concepts for trigger design has considered using thermal modification of metal alloys in localized areas that can provide a larger global deformation of a part and higher energy absorption before failure. This concept has been tested with aluminium alloys using the controlled manipulation of material properties such as strength, work hardening and ductility by means of non-homogenous heating (Bjørneklett and Myhr 2003). In a crashworthiness design application, the buckling of crash boxes can be controlled by imposing local soft zones, defined as thermally induced triggers (Peixinho et al. 2012; Fjær et al. 2005). For an effective implementation of such strategy, robust design tools are required as well as techniques to achieve the thermal treatment. Numerical simulations are an important enabler that requires, however, adequate description of geometry an loading conditions as well as relevant material properties (Costa et al. 2016; Peixinho et al. 2002, 2005).

This paper presents numerical results for thin-walled octagonal structures subjected to impact loading and analysed for different section and trigger geometries. The improvement potential of the introduction of thermal and conventional triggers is analysed. A numerical simulation procedure is detailed and results are presented and discussed for different approaches on a representative industrial design.

7.2   Numerical Models

The base structure considered for the numerical study is an octagonal section tubular column of aluminium 6061-T4. The section wall thickness is 1.2 mm, and the length of the column is 100 mm. This base geometry, presented in Fig. 7.1, was considered a representative geometry used by a local company that manufactures crashbox structures. An alternative design, being considered for extrusion manufacturing, is presented in Fig. 7.2. This geometry takes advantage of the extrusion process that allows for a multi-cell design, which can provide improvements in the efficiency of energy absorption (Abdullah et al. 2020).

The trigger designs are presented in Fig. 7.3. These are studied in two variations: a geometric trigger consisting of three lines of cut sections in the octagonal column faces and a thermal trigger design ideally obtained through local heating in areas
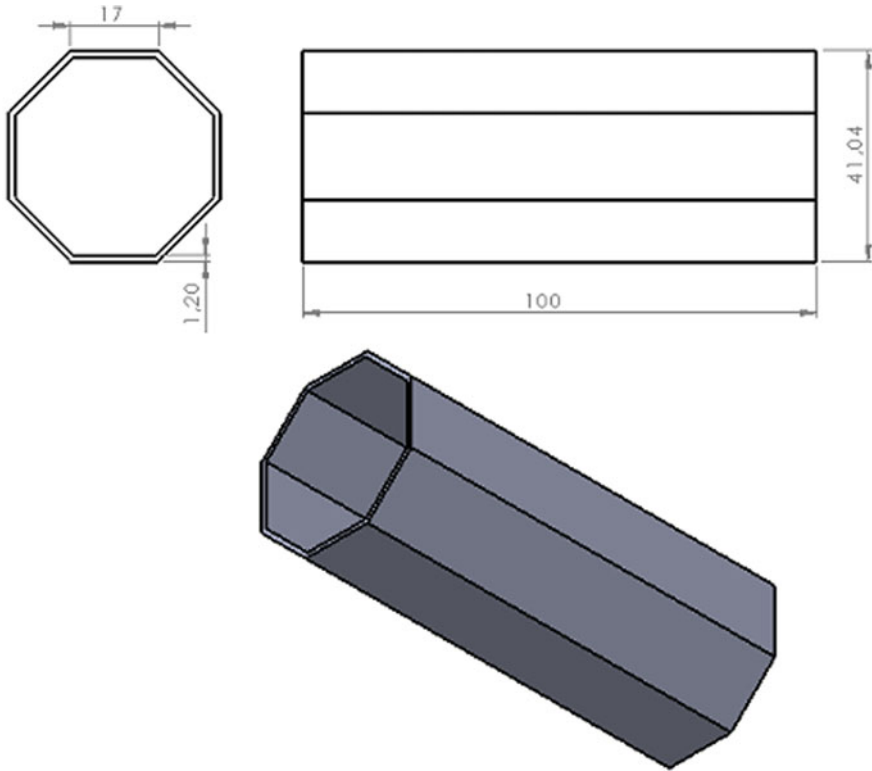
Fig. 7.1 Base reference design (Ref. A), dimensions in mm

chosen for triggers. The thermal trigger areas are presented in Fig. 7.3 as the indicated trigger lines. These were modelled in the numerical simulations through the modification of the mechanical properties. The location of these triggers on aluminium alloy was defined after several iterations in order to precisely induce deformation in the preferred zones. The main expected advantages of the thermal trigger design are improvements in energy absorption and crashworthiness parameters as well as tooling simplification for a design without geometric triggers.

The mechanical properties of the aluminium alloy 6061-T4 were obtained by static tensile tests, and the properties of the heat affected zone (HAZ) are considered as 60% less than the base material according to the Vickers micro-hardness tests (Peixinho et al. 2012). The complete true stress–strain curves used in the simulations is presented in Fig. 7.4. As the aluminium is insensitive to the strain rate effect, this effect is neglected in the finite element modelling.

The numerical simulations were performed using the commercial software ANSYS Workbench, in particular the module "Explicit Dynamics" (Chen and Liu 2018) that is generally used for nonlinear simulation of large deformation impact events. The loading condition consists on the impact of a rigid mass (50 kg) at an
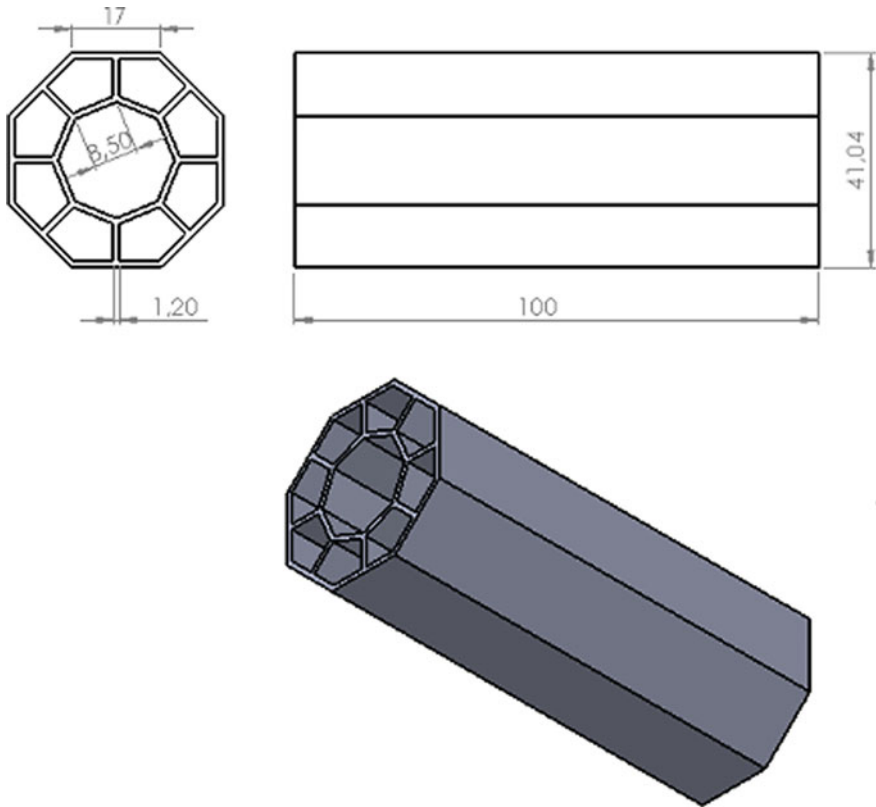
Fig. 7.2 Candidate improvement multi-cell design (Ref. B)

initial speed of 13 m/s on the top section of the tubular models being the lower part
clamped. The finite element formulation selected for numerical of modelling was
Belytschko-Lin-Tsay shell element of four nodes with twelve degrees of freedom in
each node. Five integration points were used in the thickness direction. The contact
between the rigid wall and the model is defined as surface–surface interaction with
a friction coefficient 0.1. Self-contact with a friction coefficient 0.1 is defined on the
model walls.

7.3   Results and Discussion

Results obtained from numerical simulations are presented considering the following
crashworthiness parameters: absorbed energy and specific absorbed energy, peak load
($P_{\max}$), crushing force efficiency (CFE); deformed shapes and load–time curves. The
CFE parameter is a measure of the uniformity of collapse force. It is defined as the
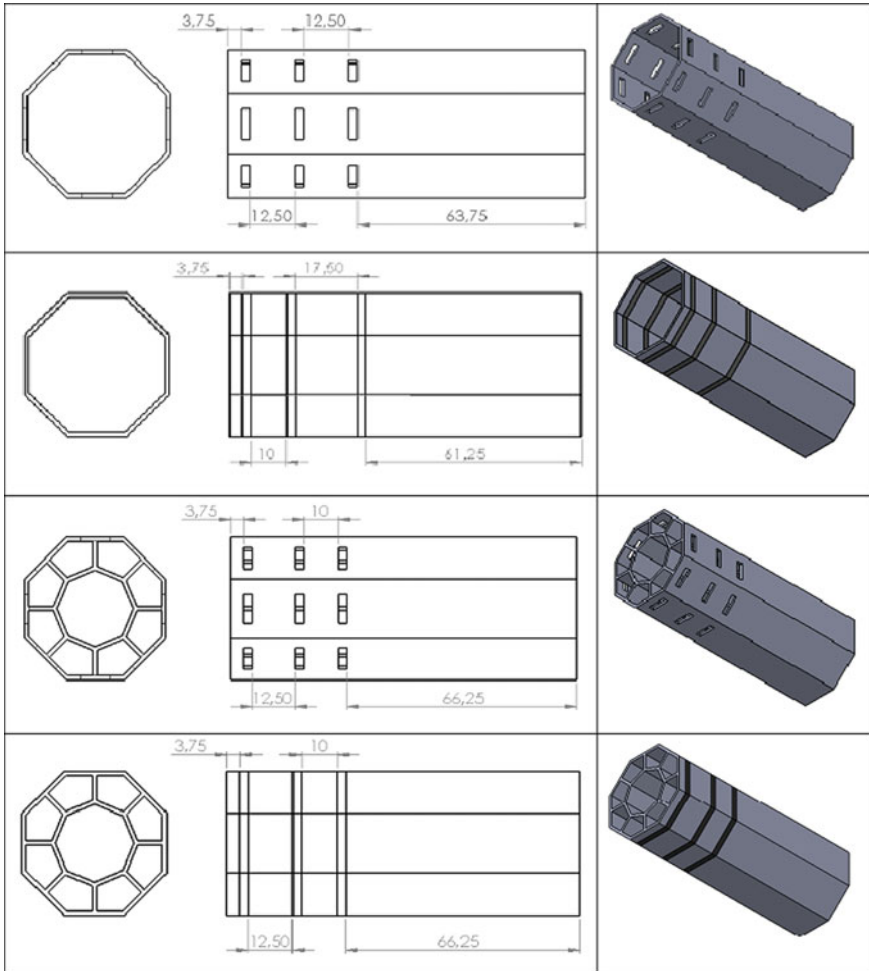
Fig. 7.3 Trigger design and references. From top: Ref. A with geometric triggers (GT) (A_GT); Ref. A with thermal triggers (TT) (A_TT); Ref. B with geometric triggers (B_GT) and geometry B with thermal triggers (B_TT)

ratio of mean crushing load (P_{avg}) to initial peak load (P_{max}). This parameter is relevant to understand the trigger influence: triggers are intended to lower the maximum load (in order to reduce accelerations in occupants) but without significantly affect energy absorption and mean crushing load. A higher parameter of CFE is indicative of good crush force efficiency.

Figure 7.5 presents final deformed shapes of the base reference geometries, without triggers. Load–time curves for these geometries are presented in Figs. 7.6 and 7.7. The overall results for crashworthiness parameters are presented in Tables 7.1, 7.2
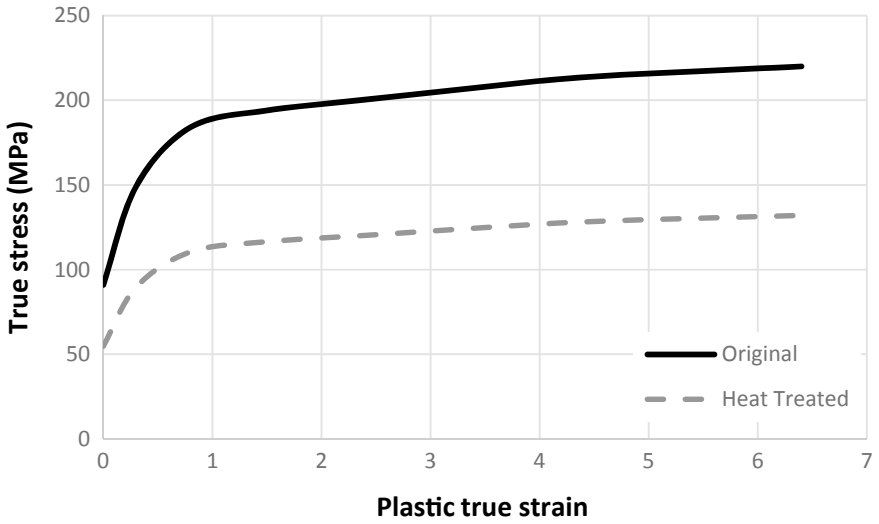
Fig. 7.4 Original and thermal treated 6061-T4 material true stress versus plastic true strain curves
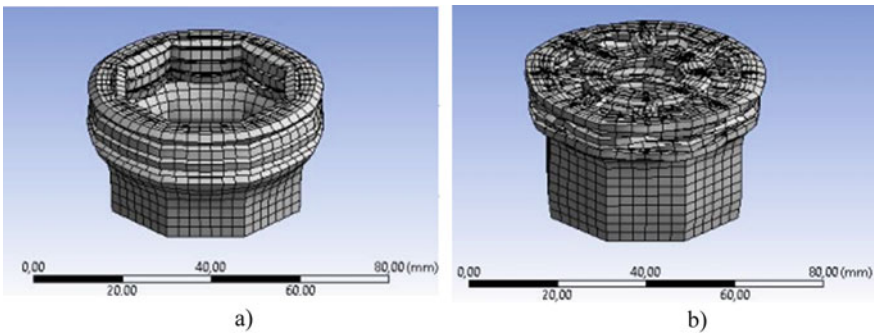
Fig. 7.5 Final deformed shapes: **a** geometry Ref. A; **b** geometry Ref. B
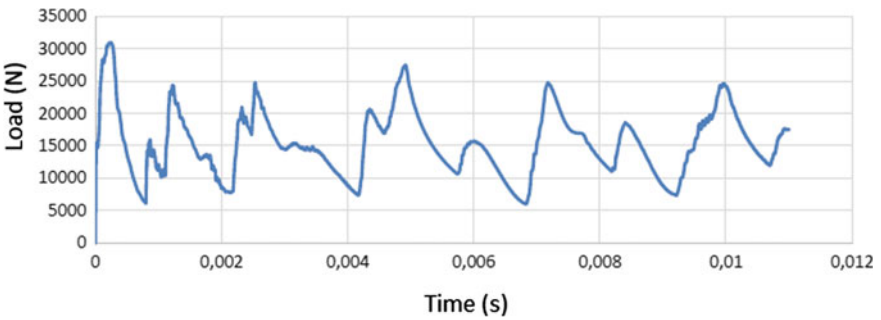
Fig. 7.6 Load–time curve, Ref. A
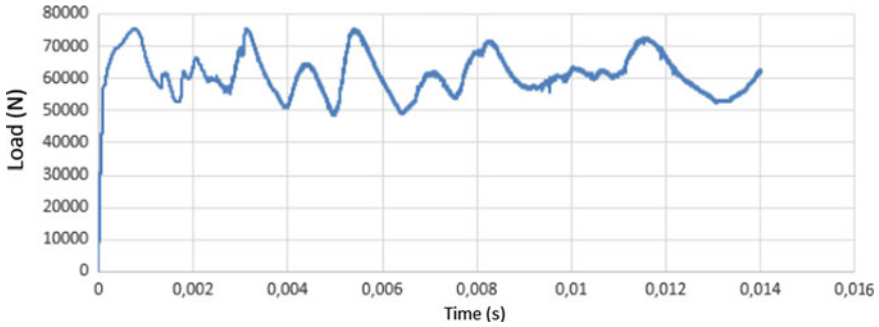
Fig. 7.7 Load–time curve, Ref. B

Table 7.1 Crashworthiness parameters. Comparison of A and B reference geometries

Structure Ref.	Mass (kg)	E_A (J)	$P_{máx}$ (N)	SEA (kJ/kg)	CFE
A	0.0452	1109	30,905	24.56	0.497
B	0.0928	4125	75,527 **(+144.4%)**	44.47 *(+81%)*	0.807 *(+62.4%)*

Table 7.2 Crashworthiness parameters. Comparison of Ref. A and trigger designs

Structure Ref.	Mass (kg)	E_A (J)	$P_{máx}$ (N)	SEA (kJ/kg)	CFE
A	0.0452	1109	30,905	24.56	0.497
A_GT	0.0435	1146 *(+3.3%)*	24,445 *(−20.9%)*	26.36 *(+7.3%)*	0.646 *(+30.0%)*
A_TT	0.0452	1165 *(+5.0%)*	24,671 *(−20.2%)*	25.80 *(+5.0%)*	0.656 *(+32%)*

and 7.3. The improvements in key parameters are indicated as percentage variation to the reference initial case.

The comparison of the base reference geometries (Table 7.1) indicates a significant improvement in energy absorption of the Ref. B multi-cell geometry, and in a more relevant parameter, the specific energy absorption. Therefore, it is a strong candidate for improvement. As expected, considering the higher loads involved, the maximum load is significantly higher; however, the CFE parameter is more favourable. This means that the geometry is intrinsically very efficient since it can be made lighter

Table 7.3 Crashworthiness parameters. Comparison of Ref. B and trigger designs

Structure Ref.	Mass (kg)	E_A (J)	$P_{máx}$ (N)	SEA (kJ/kg)	CFE
B	0.0928	4125	75,527	44.47	0.807
B_GT	0.0911	4244 (+2.9%)	71,744 (−5%)	46.60 (+4.8%)	0.857 (+6.2%)
B_TT	0.0928	4229 (+2.5%)	73,472 (−2.7%)	45.59 (+2.5%)	0.839 (+4.0%)
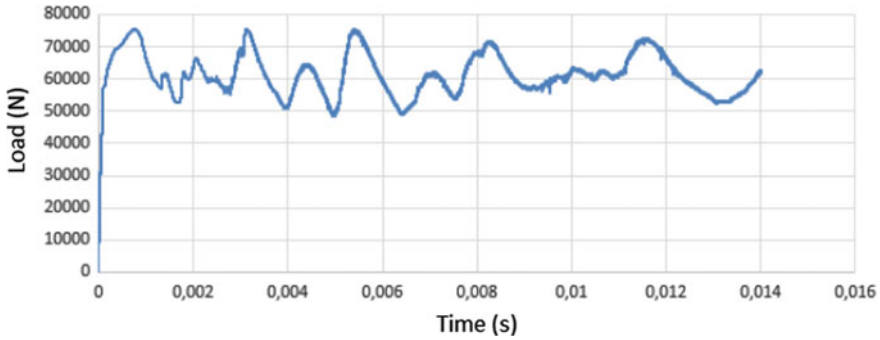
Fig. 7.8 Load–time curve, Ref. B_TT

and thinner, within the manufacturing process limits, in order to lower the peak load to acceptable levels.

Regarding the efficiency of the trigger designs used it is possible to observe that these are very effective for the Ref. A geometry, allowing for a significant reduction in the peak load while improving other crashworthiness parameters. Both geometry and thermal trigger designs allow for similar improvements in the crashworthiness behaviour. However, for the Ref. B design the trigger influence is much lower, although still providing a reduction in peak load and improvement in the other crashworthiness parameters. This results from the crushing mode and inherent stiffness of the multi-cell geometry since the triggers are only placed in the external surface. As a representative comparison reference, Fig. 7.7 presents the load–time curve for the response of the multi-cell geometry with thermal trigger. In comparison with Fig. 7.6, the results highlight an overall similar response wherein the introduction of triggers does not change significantly the deformation mode and crushing loads (Fig. 7.8).

7.4 Conclusions

This study presented numerical results for thin-walled octagonal structures subjected to impact loading and analysed for different section and trigger solutions. Two different alternatives for section design complimented with thermal or geometrical trigger solutions were proposed.

The ability to tailor peak loads through both thermal and geometrical trigger design was validated in the numerical simulations. The obtained results were indicative of a high effectiveness of the thermal and geometrical triggers in the original octagonal thin-walled section with improvements in specific absorbed energy and crush force efficiency while allowing for a significant reduction of peak loads. For the multi-cell

design, the thermal triggers were less effective regarding peak load reduction and crashworthiness parameters. The multi-cell design, as a base reference geometry, demonstrated higher specific energy absorption than the original octagonal section.

References

Abdullah, N.A.Z., Sani, M.S.M., Salwani, M.S., Husain, N.A.: A review on crashworthiness studies of crash box structure. Thin-Walled Struct. **153**, 106795 (2020)

Bjørneklett, B.I., Myhr, O.R.: Materials design and thermally induced triggers in crash management. In: Proceedings IBEC Conference (2003)

Chen, X., Liu, Y.: Finite Element Modeling and Simulation with ANSYS Workbench, 2nd edn. CRC Press (2018)

Costa, S., Mendonça, J., Peixinho, N.: Study on the impact behaviour of a new safety toe cap model made of ultra-high-strength steels. Mater. Des. **91**(5), 143–154 (2016)

Fjær, H.G., Bjørneklett, B., Myhr, O.R.: Microstructure based modelling of Al-Mg-Si alloys in development of local heating processes for automotive structures. In: Proceedings 2005 TMS Annual Meeting (2005)

Marsolek, J., Reimerdes, H.G.: Energy absorption of metallic cylindrical shells with induced non-axisymmetric folding patterns. Int. J. Impact Eng. **30**, 1209–1223 (2004)

Peixinho, N., Jones, N., Pinho, A.: Determination of crash-relevant material properties for high-strength steels and constitutive equations. SAE Trans. J. Mater. Manuf. **111**(Section 5), 1019–1025 (2002)

Peixinho, N., Jones, N., Pinho, A.: Application of dual-phase and TRIP steels on the improvement of crashworthy structures. Mater. Sci. Forum **502**, 181–186 (2005)

Peixinho, N., Soares, D., Vilarinho, C., Pereira, P., Dimas, D.: Experimental study of impact energy absorption in aluminium square tubes with thermal triggers. Mater. Res. **15**(2) (2012)

Rai, V., Ghasemnejad, H., Watson, J.W., Gonzalez-Domingo, J.A., Webb, P.F.: Developed trigger mechanisms to improve crush force efficiency of aluminium tubes. Eng. Struct. **199** (2019)

Zhang, X.W., Su, H., Yu, T.X.: Energy absorption of an axially crushed square tube with a buckling initiator. Int. J. Impact Eng. **36**(3), 402–417 (2009)

Chapter 8
Stiffness and Damping Properties of a Composite Beam Design

M. Ferreira, N. Peixinho, V. Carneiro, P. Ribeiro, J. Meireles, and D. Soares

Abstract This work presents a characterization of dynamic mechanical properties of composite beams that were 3D-printed using fused filament fabrication. Two materials were used in the manufacturing process: a flexible material was used as filler of the hollow section (FilaFlex—Polyether-Polyurethane elastomer) while polylactic acid (PLA) polymer was used for the external wall of the beam. The main objective for such material integration is to enhance damping properties without compromising the overall stiffness. Dynamic mechanical analysis (DMA) was used to determine the inherent beam stiffness (storage modulus) and damping (tanδ), to assess the influence of void-filling volume fraction in the dynamic properties and therefore optimize the beam static and dynamic performance. At room temperature, it was shown that the introduction of low contents of flexible filling actually generated an increased in stiffness due to the changes the filament orientation to accommodate the filling material. Regarding the damping performance, it was proved that the introduction of filling enhanced internal friction. It was possible to optimize both stiffness and damping of the beam design by finding the most beneficial combination of these properties.

Keywords Hybrid beam · Dynamic mechanical analyser · Stiffness · Damping

8.1   Introduction

The use of different materials in structures can provide advantages when conflicting requisites are needed (Ashby 2005). The concept of hybrid structures is widely used in sandwich materials where a light core and stiff outer skin provide efficient use of materials for different applications (Condé 2005).

M. Ferreira · N. Peixinho (✉) · P. Ribeiro · J. Meireles
MEtRiCS—Mechanical Engineering and Resource Sustainability Centre, University of Minho, Guimarães, Portugal
e-mail: peixinho@dem.uminho.pt

V. Carneiro · D. Soares
CMEMS—Centre for Micro-Electro Mechanical Systems, University of Minho, Guimarães, Portugal

This study presents a concept wherein a structural beam is composed of two materials: a polymer (PLA—polylactic acid polymer and an elastomer (Filaflex—Polyether-Polyurethane elastomer). The concept proposal intends to combine a polymer material for stiffness and the elastomer for damping properties. The combination of these materials can provide the opportunity for tailoring damping for a specific application. The use of different materials, such as combinations of metal foams (Kulshreshtha and Dhakad 2020), honeycomb and lattice sandwich structures (Rupani et al. 2017), has been used with advantage in engineering applications (Gibson and Ashby 1997).

Although there are some studies on the mechanical behaviour concerning the combination of materials for structural and damping applications, they are generally not correlated. Sarlin et al. (2012) analysed the damping properties of laminated structures consisting of steel, rubber or epoxy adhesive and glass fibre reinforced epoxy composite. Damping properties of the structures were investigated through the loss factors that were determined by the frequency response function of the samples.

A different approach to a multi-material beam was presented by Eloy et al. (2019). In their study, sandwich panels with carbon/epoxy composite skins and a magnetorheological elastomer honeycomb core in different proportions of magneto/elastomer were manufactured and studied numerically and experimentally. Their results demonstrated that it is possible to use such sandwich structures in situations where it is desired to reduce the vibration levels since they were able to decrease vibration amplitudes and change the natural frequency of the system by only changing the magnetic field intensity. In previous studies by Korobko et al. (2012), the resonance frequencies of a three-layered beam, supporting constructions made from aluminium, and the inner layer (from magnetorheological elastomer) were calculated and the dependence of vibrations on induction of the applied magnetic field was obtained.

The use of different materials in hybrid structures can also have applications in energy absorption. Bodaghi et al. (2020) presented a study on dual-material auxetic meta-sandwiches by four-dimensional printing technology intended for reversible energy absorption applications. The meta-sandwiches were developed based on an understanding of hyper-elastic feature of soft polymers and elastoplastic behaviour of shape memory polymers. Dual-material lattice-based meta-structures with different combinations of soft and hard components were fabricated by 4D printing fused deposition modelling technology. The feasibility and performance of these reversible dual-material meta-structures were assessed experimentally and numerically.

In the present study, structural box beams were manufactured consisting of inner and outer layers of, respectively, Filaflex and PLA. Samples without filling were also manufactured for comparison purposes. The samples were tested on a Dynamic Mechanical Analyser (DMA) to determine the storage modulus, internal friction (tanδ) and vitreous transition temperature (Tg). An optimal combination of core/layer materials was derived considering the combination of sample stiffness and damping.

8.2   Materials and Methods

Samples were manufactures by fused filament fabrication using a dual-extruder BCN Sigma 3D printer. The overall printing parameters used are presented in Table 8.1. The materials used are a thermoplastic polyester polylactic acid (PLA) and a Thermoplastic Polyether-Polyurethane elastomer with commercial designation Filaflex. Table 8.2 presents physical and mechanical properties of the selected materials.

The beam design choices have the purpose to analyse the influence of box-shaped beams with different internal void sections that can be filled with the flexible Filaflex material or left empty. The tubular specimens are also compared to a solid section PLA beam. The representative beam geometry is presented in Fig. 8.1. Table 8.3 details the overall dimensions and design parameters.

The dynamic mechanical behaviour is evaluated by TA Instruments Q800 dynamic mechanical analyser. This technique measures the instantaneous stiffness of materials as a function of time, temperature and frequency. In addition to basic material properties, DMA is commonly used to measure glass transition temperatures and secondary transitions, orientation caused by processing, cold crystallization, cure optimization, filler effects in composites, amongst others (Menard et al. 2008). For mechanical and damping analysis, the DMA can provide an accurate measurement of material stiffness (modulus) but also other important mechanical properties such as damping, creep and stress relaxation.

According to Fig. 8.2, samples were tested in a dual-cantilever configuration in a with a 5 μm constant amplitude, while the temperature was risen from room temperature (25 °C) to 80 °C with a 1 °C/min heating rate in an inert atmosphere. Samples were also subjected to a frequency sweep with 5, 10 and 20 Hz.

Table 8.1 Additive manufacturing parameters

Lh – Layer height (mm)		0.1
Nd – Nozzle diameter (mm)		0.3
NT – Nozzle Temperature (°C)	PLA	210
	Filaflex	230
Speed (mm/s)		10
BT – Bed Temperature (°C)		60

Table 8.2 Characteristic material properties

Property	PLA	Filaflex
Density (g/cm^3)	1.25	1.14
Glass transition temperature (°C)	70	−30
Young's modulus (MPa)	3500	48
Tensile strength (MPa)	35	42
Elongation at break (%)	6	665
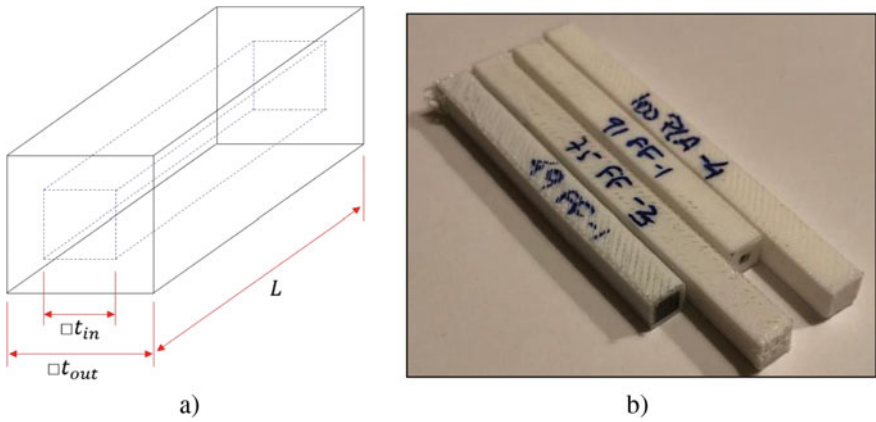
Fig. 8.1 **a** Geometric parameters **b** Representative manufactured samples

Table 8.3 Overview of sample design parameters

Tout (mm)	L (mm)	Fill	tin (mm)	Sample Ref.
5	50	No	0	100% PLA
			1.5	91% PLA + 9% Void
			2.5	75% PLA + 25% Void
			3.5	49% PLA + 51% Void
		Yes	1.5	91% PLA + 9% FilaFlex
			2.5	75% PLA + 25% FilaFlex
			3.5	49% PLA + 51% FilaFlex

Fig. 8.2 DMA equipment and detail of clamping system

8.3 Results and Discussion

(i) Temperature-dependent viscoelastic behaviour

Figure 8.3 shows the temperature-dependent storage modulus of the tested samples. These results show a typical behaviour thermomechanical of a polymeric materials, displaying an initial stage (T < Tg) in which the material displays a perfectly solid configuration. In this first stage, there is a slight storage modulus decrease due to temperature induced softening of the polymeric matrix. When the temperature is risen past the glass transition temperature (T > Tg), the matrix transitions into a rubbery state and there is a significant decrease in sample stiffness.

During the transition between the two regimes (i.e. T ~ Tg), there it is expected that there is a significant increase in internal friction, as the polymer chains change configuration and consequently dispend a significant portion of the imposed hysteretic energy. This behaviour is perfectly observable in Fig. 8.4.

The comparison between the stiffness (Fig. 8.3) and thermomechanical damping (Fig. 8.4) reveals that in samples without filling, has expected, as the void volume fraction increases, there is a reduction in stiffness. However, in samples with filling, this is not always true. It is determined that the introduction of small volume fractions of filling (e.g. 91%PLA + 9% Filaflex), there is even an increase in stiffness. The authors propose that this elevation in storage modulus is promoted by the reconfiguration of PLA layers to accommodate the filling, reduced impact in overall moment of area and internal pressure caused by the filling. This is reflected in the increase in the height of damping peaks in Fig. 8.4.

According to Fig. 8.5, it is apparent that frequency in not a key aspect in the change of this transition regime (i.e. Tg). Although the increase in frequency is able to promote a slight increase in the overall Tg, it may be observed that these changes
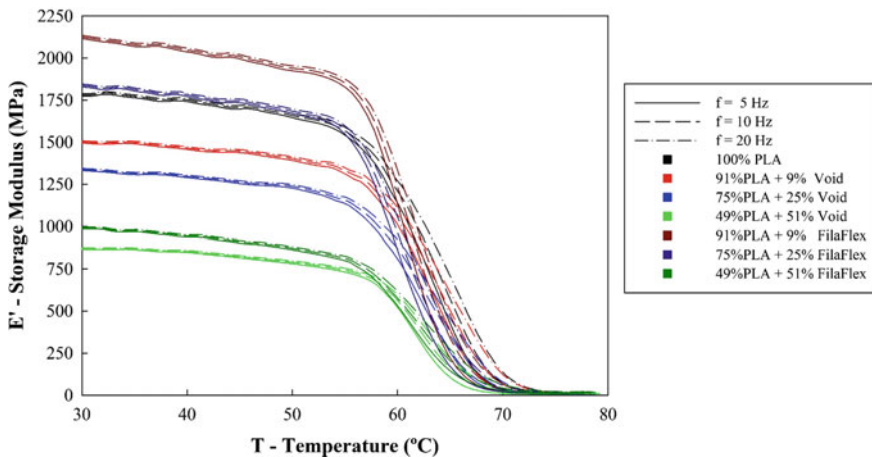
Fig. 8.3 Temperature-dependent storage modulus
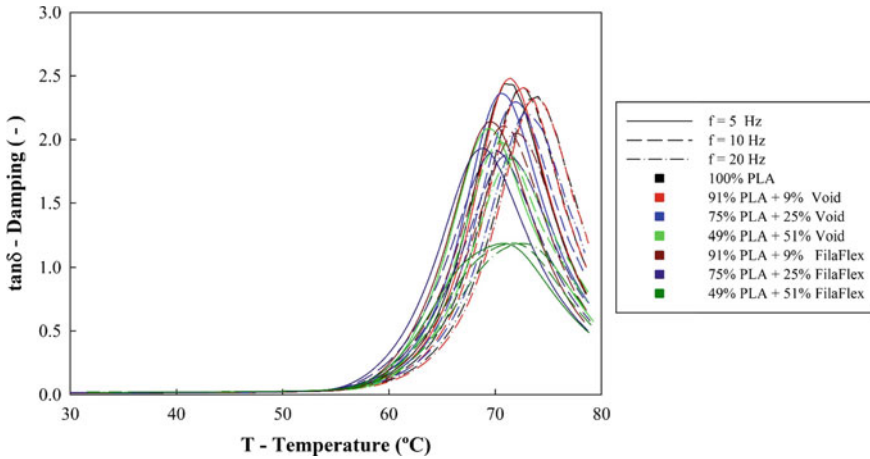
Fig. 8.4 Temperature-dependent internal friction
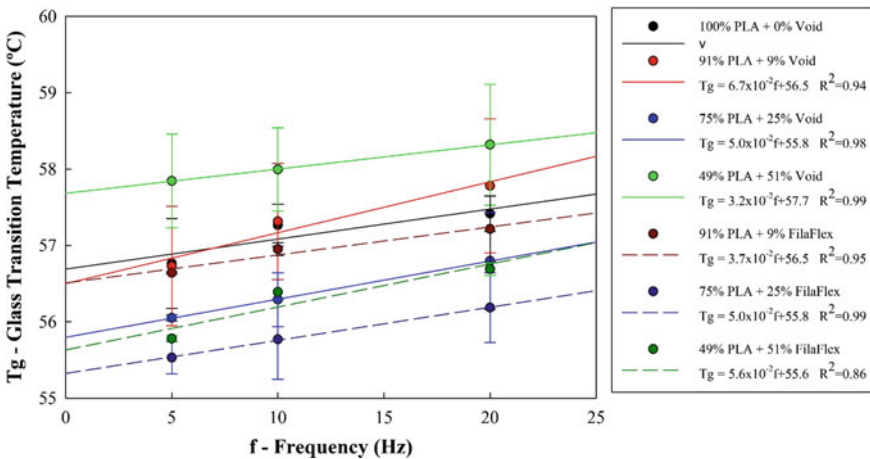
Fig. 8.5 Frequency-dependent glass transition temperature (Tg)

are much more significant when the overall volume fraction of the components is changed.

(ii)   Room temperature viscoelastic behaviour

The variation in frequency is also not a relevant factor in the overall stiffness of the samples at room temperature, as shown in Fig. 8.6. The results reveal the same behaviour portrayed in Fig. 8.3, where small volume fraction of Filaflex fillings (e.g. 9% Filaflex) is eventually able to generate an increase in stiffness.

Figure 8.7, however, allows a better representation of the variation of sample damping at room temperature. It is shown that as the samples are subjected deformed
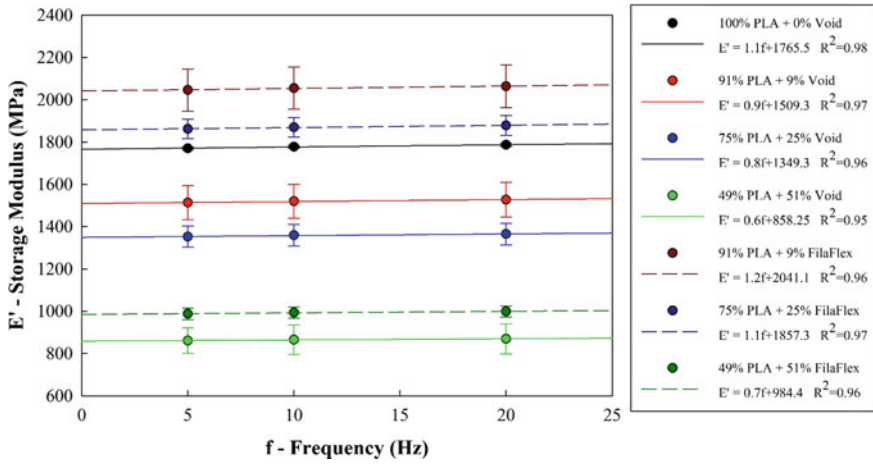
Fig. 8.6 Frequency-dependent storage modulus at room temperature
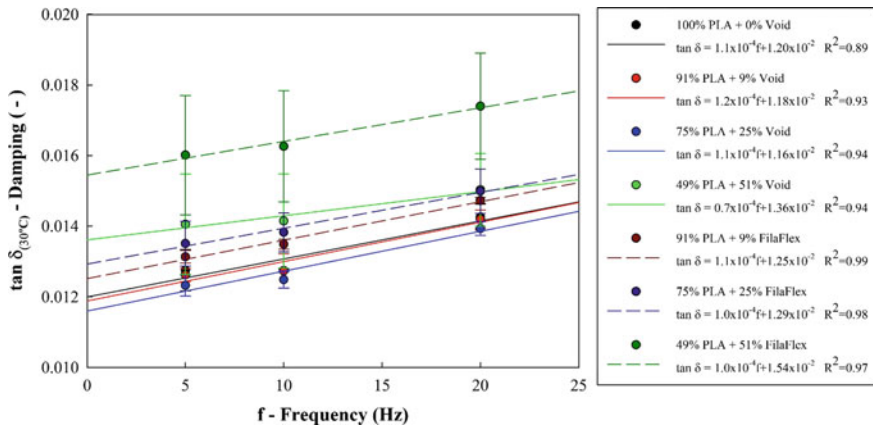
Fig. 8.7 Frequency-dependent damping at room temperature

with higher frequencies, there is also an increase in damping. More importantly, there is a large increase in damping as the volume fraction of Filaflex is increased. This enhancement in damping has to be attributed to the filling itself, since the samples with the correspondent void volume fraction do not display the same behaviour.

The analysis of these results suggests that the filling with Filaflex can improve both damping and stiffness. To evaluate an optimal percentage of filler with the elastomeric material, a performance index (Pi) was developed, as presented in Eq. (8.1). This index joins two terms that aim to maximize stiffness and damping. Their sum represents the Performance index that is graphically plotted in Fig. 8.8 for the present set of experimental results. A third-order polynomial interpolation was applied to the
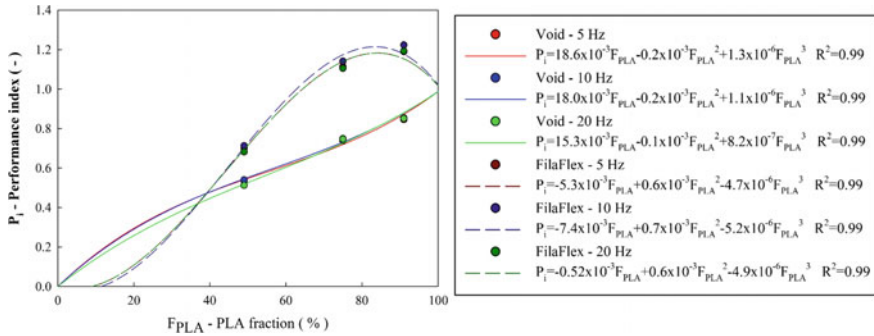
Fig. 8.8 Performance index as a function of PLA fraction

results, and it is shown that indeed samples with Filaflex filament are able to generate an optimized correlation between stiffness and damping. An optimal combination of volume fractions was identified at for a volume fraction of 82% PLA.

$$P_i = \frac{E'(f)}{E'_{\text{MAX}}} + \frac{\tan \delta(f)}{\tan \delta_{\text{MAX}}} \tag{8.1}$$

8.4　Conclusions

This work presents a characterization of the dynamic mechanical properties of composite beams that were 3D-printed using fused filament fabrication. Two materials were used in the manufacturing process: a flexible material was used as filler of the hollow section while PLA was used for the external walled part of the beam. The inherent beam stiffness (storage modulus) and damping (tanδ) were obtained experimentally in order to assess the influence of void and flexible filling in the dynamic properties and therefore optimize the beam performance.

While the increase in Filaflex volume fraction seems to reduce the overall glass transition temperature, it was shown that at room temperature, the introduction of low contents of flexible filling generated an increase in stiffness, which can be attributed to the high residual stresses introduced in the manufacturing process. Regarding damping performance, Filaflex filling also enhances room temperature internal friction. It was possible to optimize both stiffness and damping of the beam design with an 82% PLA fraction providing the most beneficial combination of these properties. Therefore, it was possible to design and manufacture composite beams with favourable combinations of mechanical properties.

References

Allen, H.G.: Analysis and Design of Structural Sandwich panels. Pergamon Press

Ashby, M.: Materials Selection in Mechanical design, 3rd edn. Pergamon Press (2005)

Bodaghi, M., Serjouei, A., Zolfagharian, A., Fotouhi, M., Rahman, H., Durand, D.: Reversible energy absorbing meta-sandwiches by FDM 4D printing. Int. J. Mech. Sci. **173**, 105–451 (2020)

Eloya, F., Gomes, G., Ancelotti Jr., A., da Cunha, Simões., Jr, S., Bombard, A., Junqueira, D.: A numerical-experimental dynamic analysis of composite sandwich beam with magnetorheological elastomer honeycomb core. Compos. Struct. **209**, 242–257 (2019)

Gibson, L.J, Ashby, M.F. (1997). Cellular solids: Structure and properties, 2nd edn. Cambridge University Press

Korobko, E., Mikhasev, G., Novikova, Z., Zhurauski, M.: On damping vibrations of three-layered beam containing magnetorheological elastomer. J. Intell. Mater. Syst. Struct. **23**(9), 1019–1023 (2012)

Kulshreshtha, A., Dhakad, S.K.: Preparation of metal foam by different methods: A review. Mater. Today: Proc. **26**, 1784–1790 (2020)

Menard, K.P.: Dynamic mechanical analysis: a practical introduction, 2nd edn. CRC Press (2008)

Rupani, S.V., Jani, S.S., Acharya, G.D.: Design, Modelling and manufacturing aspects of honeycomb sandwich structures: a review. Int. J. Sci. Dev. Res. **2**, 526–532 (2017)

Sarlin, E., Liu, Y., Vippola, M., Zogg, M., Ermanni, P., Vuorinen, J., Lepistö, T.: Vibration damping properties of steel/Rubber/composite hybrid structures. Compos. Struct. **94**, 3327–3335 (2012)

Part III
Additive Manufacturing

Chapter 9
Combining Structural Optimization Solutions Using FFF Manufacturing

E. F. C. Bastos, B. Athayde Malafaya, A. I. L. Pais, M. C. Marques, J. L. Alves, and J. Belinha

Abstract In the industry, the need to reduce the manufacturing cost and CO_2 emissions makes structural optimization an important computational tool to develop and design products with the required and necessary mechanical properties and as light as possible. Additive manufacturing is nowadays used to produce structural optimized products due to the possibility of producing complex shapes with high accuracy. In this work, a topology software developed by the research team and an already validated commercial software capable to structurally optimize a structural component and deliver its prototype are used. A cross-analysis was performed to validate and compare the results. Advanced numerical discretization techniques combined with algorithms of evolutionary structural optimization were applied in the process. Several optimized structures were produced using FFF technology and experimentally tested. The chosen material was PLA with a Young's modulus of 3145 MPa. It was verified that the optimization tools are suitable to reduce the parts weight and, at the same time, maintain the structural performance. Thus, it is expected to reduce the part costs and the CO_2 emissions resulting from their production with this approach, without risking the required mechanical properties.

Keywords Additive manufacturing · FEM · Meshless methods · Topology optimization

9.1 Introduction

Structural optimization can be defined as the optimal design creation of a mechanical part, automatically, based in structural considerations (Swedish Research Council (VR) (https://www.math.kth.se/optsyst/Struc.html)). The goal is to achieve the best

E. F. C. Bastos · B. Athayde Malafaya · A. I. L. Pais (✉) · M. C. Marques · J. L. Alves
Faculty of Engineering of the University of Porto, INEGI, Porto, PT, Portugal
e-mail: up201505588@fe.up.pt

J. Belinha
School of Engineering, Polytechnic of Porto (ISEP), Porto, PT, Portugal

113

component subject to a given set of structural functional requirements and performance constrains. The huge importance of structural optimization is related to several factors. However, the main one is to produce the lightest part with a desired mechanical behaviour. In several cases, it can lead to a reduction in the carbon dioxide (CO_2) emissions. If less material is used to produce a new part, with the same functionality as the old one, a reduction chain of emissions can be created, from manufacturing processes until effective use. It also reduces the time spent on development process, by reducing the number of design iterations in comparison with traditional approaches and, most importantly, provides a commercial advantage to companies that produce lighter parts, with better mechanical performance. The conditions and requirements that define the operation of the component are the functional requirements, for example the weight of the component, directions and magnitudes of the applied loads, location of the supports and material properties. The performance constrains are the acceptable structural behaviour, for example the maximum allowable stress, deflection, minimum heat dissipation rate, etc. (Bendsoe and Sigmund 2003). The requirements mentioned above are also nominated as design criteria (Colin Donald Chapman 1994).

Structural optimization can be divided into size, shape and topology optimization, depending on the geometric feature (Bendsoe and Sigmund 2003; Christensen and Klarbring 2008). In the case of sizing optimization, only the dimension of a structure is changed, i.e., the cross-sectional width of a beam. With shape optimization, the idea is to vary the shape, in a domain, to produce a contour or form of the boundary of the structure domain, which is the design variable. The integration domain for the differential equations is chosen in an optimal way. New boundaries are not formed because the connectivity of the structure is not changed. Finally, topology optimization, firstly introduced in 1988 by Bendsoe and Kikuchi (Martin Philip Bendsoe 1988), is the most widely applied form of structural optimization. Since then there has been a tremendous development in the number of approaches to solve this problem (Sigmund and Maute 2013). It aims to achieve the best optimal layout of a structure within a specific region.

There are some important variables that must be defined a priori. These are the applied loads, the design restrictions, such as holes or solid areas, the volume of the structure and support conditions. The physical shape, size and connectivity of the structure are unknown for this problem (Bendsoe and Sigmund 2003). In a discrete case, like a truss structure, it is achieved by taking off parts from the truss structure. In a continuum-type structure, the optimization results in areas ideally without thickness and others with a fixed maximum thickness. Normally computational software is applied to solve these problems, associated to numerous different methods (Christensen and Klarbring 2008).

9.1.1   Topology Optimization Approaches

Nowadays, topology optimization is related to different approaches to solve the optimization problem. There are gradient-based topology optimization approaches and non-gradient-based ones. Some of the gradient-based techniques for continuum problems are the homogenization method (Martin Philip Bendsoe 1988), the solid isotropic material with penalization method (SIMP) (Bendsoe and Sigmund 2003; Rozvany 2009), the level set approach (Wang et al. 2003; Allaire and Jouve 2002) and the bidirectional evolutionary structural optimization method (BESO) (Azamirad and Arezoo 2016; Tanskanen 2002; Xia et al. 2018). The non-gradient-based optimization approaches are based in random processes, for example genetic algorithms (Colin Donald Chapman 1994), artificial immune algorithms and simulated annealing (Sigmund 2011).

According to Sigmund (2011), the gradient optimization approaches totally outperform the non-gradient-based approaches in all aspects, due to their huge computational cost of the non-gradient approaches and, although non-gradient approaches use a global search, it is unlikely they find a global optimum solution, being their only advantage the fact that they are easy to implement since do not make the use of gradients.

In this work, only SIMP and BESO are used as approaches to solve the optimization problem.

9.1.1.1   SIMP

SIMP is a very popular method in industrial software due to its simplicity and computational efficiency. This method takes the density ρ of an element as the design variable to control where there should be material and voids.

Equation (9.1) is used to define the element density,

$$\rho_e = x^e \rho_0. \tag{9.1}$$

where x^e is the relative density and ρ_0 is the density of the reference material. The relative density can vary between $x^e_{\min}$ and 1 ($0 < x^e_{\min} < x^e \leq 1$). $x^e_{\min}$ is a very small number to avoid singularities, in that case the element is empty, and in the case that x^e is equal to 1, the element consists in solid material.

To avoid intermediate densities, which are undesirable in the optimal design, a penalty is applied when calculating the element stiffness,

$$\mathbf{K}^e = \left(x^e\right)^p \mathbf{K}^0 \tag{9.2}$$

where $\mathbf{K}^0$. is the stiffness matrix of an element consisting of solid material and $p > 1$. is the penalization factor. Experience shows that in problems where volume constraint is active, to obtain 0–1 designs, $p \geq 3$ is required (Zhang and Zhu 2018). In some

simple optimization problems, both the objective function and all the constrains are written as explicit functions of the design variables. However, the same is impossible, or very difficult, for larger problems. The solution is to create a sequence of explicit subproblems that are aroxations of the original problem and solve these subproblems instead. Most structural optimization problems are non-convex problems and to solve them, convex approximations are chosen (Christensen and Klarbring 2008).

Several mathematical methods were developed to solve the optimization problem, including sequential linear programming (SLP), sequential quadratic programming (SQP), convex linearization (COLIN), optimality criteria (OC) and method of moving asymptotes (MMA). Methods involving OC are efficient for problems with many variables and few constrains. In the case of several constrains, the SLP is used.

9.1.1.2 BESO

To explain BESO, first the evolutionary structural optimization method must be explained. This method removes inefficient material from the structure, in each interaction, to obtain the optimal solution. In a structure, any material under low stress is assumed to be inefficient, being removed (Azamirad and Arezoo 2016; Tanskanen 2002; Xia et al. 2018). To complete the optimization process is important to define the conditions under which an element is removed, being the von Mises stress the most commonly criteria that is used. The von Mises stress of an element σ_v^e is compared with the von Misses stress of the whole structure σ_v^M. After each iteration, the points that satisfy (9.3) are deleted (Zhang and Zhu 2018),

$$\sigma_v^e / \sigma_v^M \leq RR_i. \tag{9.3}$$

In Eq. (9.3), RR_i is the rejection ratio for iteration i. In every numerical analysis, points are removed using the same rejection ratio until occurs convergence. An evolutionary rate ER is added to create a new rejection ratio RR_{i+1},

$$RR_{i+1} = ER + RR_i. \tag{9.4}$$

The numerical analysis starts again and, considering the new rejection ratio, points are removed until convergence is achieved again. The ESO method can raise some questions, about how to ensure the solution is not a local minimum and whether deleted elements can return.

To answer these questions, a so-called bidirectional ESO (BESO) has developed. This method evolution allows elements to be added and removed and, with that, achieves the global optimum solution,

$$\sigma_v^e / \sigma_v^M \geq IR_i. \tag{9.5}$$

To identify the conditions under which material can be added to the structure, the inequality (9.5) need to be satisfied, where the IR_i is the inclusion ratio (Zhang and Zhu 2018).

9.1.2 Natural Neighbour Radial Point Interpolation Method

Normally topology optimization approaches are formulated based on element design variables. The finite elements are used to represent the topology of structures, fields of displacement and strains, assuming that the element densities and relevant material properties are constant within each element (Nguyen et al. 2008). However, there are also other numerical methods that can be implemented in topology approaches, such as meshless methods, which are relatively simple to implement. These methods can provide sufficient solution accuracy for a certain type of problems, without requiring the need for mesh connectivity. There are several different meshless methods available, being each one adequate to solve a specific type of problem (Belytschko et al. 1996; Luo et al. 2013).

Meshless methods are an alternative to the finite element method (FEM) and are used to solve partial differential equations, where the nodes can be arbitrarily distributed and, instead of using elements, the field functions are approximated with an influence domain around the node. A significant number of methods was developed in the last years; however, the most relevant one for this topology optimization study is the natural neighbour radial point interpolation method (NNRPIM) (Dinis et al. 2009).

Study of the geometry and definition of the solid domain and contour, defining the boundary conditions, natural and essential and discretize the problem domain and boundary following a nodal distribution which can be regular or irregularly distributed are the steps needed to fulfil in order to apply this method (Belinha 2014).

9.1.2.1 Nodal Connectivity

In meshless methods, the nodes can be arbitrarily distributed. Moreover, the field functions are approximated within an influence domain rather than an element. The domains should overlap with each other as opposite to the FEM, where the domains, the elements, cannot overlap (Belinha 2014; Gu 2005). The influence domains are the nodes inside a determined area or volume for a said point of interest. Several meshless methods apply this concept (Nguyen et al. 2008; Belytschko et al. 1994; Liu et al. 1995; Atluri and Zhu 1998; Wang and Liu 2002). The performance of the method is affected by the size and shape of the influence domains, as each domain should have approximately the same number of nodes. The most commonly used technique is having fixed influence domains although it is not the most appropriate approach.

In the case of the NNRPIM, the concept of influence domains is replaced with the concept of influence cells obtained from the Voronoi (1908) diagram of the nodal distribution. The influence cell assures approximately the same number of nodes inside each influence domain which is important for the performance of the method. The neighbouring Voronoi cells from another cell constitute the first-order influence cell. A second-order influence cell also includes the neighbouring cells from the first-order cell.

9.1.2.2   Nodal Integration

The definition of the system of equations which describes the ruling physical phenomenon being studied is one of the main drivers in increasing the computation cost of the method. The weak form of the Galerkin is an example of a variational method that can be used to obtain this system. Contrary to the FEM, where the integration mesh is coincident with the element mesh, in meshless methods, the degree of the shape function is generally unknown and therefore the background integration mesh cannot be established a priori. Nodal-based integration has been applied with the NNRPIM to one-, two- and three-dimensional domains (Dinis et al. 2008, 2009; Moreira et al. 2014) and more recently with the natural radial element method (Belinha et al. 2013a, b, c) (NREM).

This is a truly meshless method because only the spatial information regarding the nodal distribution is necessary to build the background integration mesh. After the domain is discretized, either with a regular or with and irregular nodal distribution, the Voronoi cells for each node are determined and divided into smaller subcells. If the nodal distribution is regular, the Voronoi cells are divided in triangular subcells instead of quadrilateral subcells if the domain is two-dimensional. The size A_{V_I} of the Voronoi cell V_I can be obtained through the sum of the size $A_{S_{I_i}}$ of each subcell S_{I_i}. The weight $\widehat{w_I}$ of each integration point is the sum each of the areas of the respective subcells, that is, it is the area of the respective Voronoi cell V_I. For the one-dimensional domain, A represents lengths and for the two-dimensional domain A represents areas and for the three-dimensional domain, A represents a volume. If a single integration point is inserted in the barycentre of the subcells using subcells triangular and quadrilateral, the simplest integration scheme can be established. The spatial location of the integration point is given by (9.6)

$$\boldsymbol{x}_I = \frac{\sum_{i=1}^{n} \boldsymbol{x}_{S_I} A_{S_{Ii}}}{\sum_{i=1}^{n} A_{S_{Ii}}} \tag{9.6}$$

In this work, the three-dimensional case is used, in that case if the nodal distribution is regular the 3D Voronoi cell will be divided in tetrahedral subcells whereas for irregular nodal distributions the subcells will be hexahedral.

9.1.2.3 Shape Functions

In meshless methods, it is necessary to apply an interpolation technique based on a moving local nodal domain to construct the shape function which approximates the study variable, the same does not apply in the FEM, where the domain is divided into elements and therefore the shape functions can be obtained with stationary element-based interpolation. In the construction of the meshless shape function, the concept of support domain is introduced. This consists in sets of nodes which contribute to the construction of the shape function and is usually coincident with the interest domain of the point of interest x_I. The size and shape of the support domain have a relevant influence in the accuracy of the shape function and therefore must be carefully chosen.

The support domain, similarly to the influence domain, is centred in the interest point x_I. which can be a node or an integration point. Most of the times the support domains are rectangular or circular shaped. It is possible to define the size of the support domain through (9.7) where β_s is a dimensionless parameter governing the size of the support domain and d_a is the average nodal spacing inside the support domain.

$$d_s = \beta_s d_a \tag{9.7}$$

The average nodal spacing (Liu and Gu 2005) can be determined from (9.8) where d is the dimension of the problem domain $\Omega \subset \mathbb{R}^d$. The physical size of the support domain is D which can represent a length, area or volume, depending on the dimension.

$$d_a = \frac{D^{\left(\frac{1}{d}\right)}}{n^{\left(\frac{1}{d}\right)} - 1} \tag{9.8}$$

In the NNRPIM, the nodal set that constitutes the influence cell of an interest point x_I is the same nodal set used to construct the RPI shape functions for that interest point so it is not necessary to determine a support domain.

The radial point interpolators (RPI) is a numerical technique belonging to the point interpolator methods (PIM), combining polynomial basis functions and radial basis functions to construct the shape functions.

Considering an interest point x_I with an influence domain defined by $X_I = \{x_1, x_2, ..x_n\} \in \mathbb{R}^d$. The objective is to construct a RPI shape function using a polynomial basis function combined with the multiquadrics radial basis function (MQ-RBF), which requires two parameters γ and p, defined during the pre-processing phase.

The MQ-RBF requires a size parameter d_a defined as (Duan 2008) (9.9)

$$r_i(x_i) = \left(d_{iI}^2 + (\gamma d_a)^2\right)^p \tag{9.9}$$

Since the NNRPIM considers the influence cell as the support domain, the size d_a can be defined as the size of the Voronoi cell of the point of interest x_I, or $d_a = \widehat{w}_i$ if the point of interest is an integration point where $\widehat{w}_i$ is the weight of the integration point.

Then, the polynomial vector for the interest point x_I, $p(x_I)$ is defined. Its dimension is dependent on the monomials $[m \times 1]$. For example, in the two-dimensional space, the polynomial is defined as

$$p(x_I) = \left\{ 1 x_I \; y_I \; x_I^2 \; x_I \; y_I \; y_I^2 \right\}^T \tag{9.10}$$

Following this step, the MQ-RBF vector $r(x_I)$ is constructed through

$$\begin{aligned} r(x_I) &= \left\{ r_1(x_I) r_2(x_I) \ldots r_n(x_I) \right\}^T \\ &= \left\{ r(x_1 - x_I) r(x_2 - x_I) \ldots r(x_n - x_I) \right\}^T \end{aligned} \tag{9.11}$$

The distances d_{Ii}. between the interest point and all the nodes inside the influence domain of the point of interest x_I are determined. Then, the component of the MQ-RBF is determined using (9.4). The dimension of the MQ-RBF vector $r(x_I)$ will be $[n \times 1]$.

Then, the radial moment matrix $\boldsymbol{R}$.is determined with

$$\boldsymbol{R} = \begin{bmatrix} \left(d_{11}^2 + (\gamma d_c)^2 \right)^p & \left(d_{12}^2 + (\gamma d_c)^2 \right)^p & \cdots & \left(d_{1n}^2 + (\gamma d_c)^2 \right)^p \\ \left(d_{21}^2 + (\gamma d_c)^2 \right)^p & \left(d_{22}^2 + (\gamma d_c)^2 \right)^p & \cdots & \left(d_{2n}^2 + (\gamma d_c)^2 \right)^p \\ \vdots & \vdots & \ddots & \vdots \\ \left(d_{n1}^2 + (\gamma d_c)^2 \right)^p & \left(d_{n2}^2 + (\gamma d_c)^2 \right)^p & \cdots & \left(d_{nn}^2 + (\gamma d_c)^2 \right)^p \end{bmatrix} \tag{9.12}$$

Then, the polynomial moment matrix $\boldsymbol{P}$ $[n \times m]$ is determined with

$$\boldsymbol{P} = \begin{bmatrix} p_1(\boldsymbol{x}_1) & p_2(\boldsymbol{x}_1) & \cdots & p_n(\boldsymbol{x}_1) \\ p_1(\boldsymbol{x}_2) & p_2(\boldsymbol{x}_2) & \cdots & p_n(\boldsymbol{x}_2) \\ \vdots & \vdots & \ddots & \vdots \\ p_1(\boldsymbol{x}_n) & p_2(\boldsymbol{x}_n) & \cdots & p_n(\boldsymbol{x}_n) \end{bmatrix} \tag{9.13}$$

The total moment matrix $\boldsymbol{M}$ with size $[(n + m) \times (n + m)]$ is defined using the radial moment matrix R and the polynomial moment matrix P as in

$$\begin{bmatrix} \boldsymbol{R} & \boldsymbol{P} \\ \boldsymbol{P}^T & \boldsymbol{Z} \end{bmatrix} \left\{ \begin{matrix} a(\boldsymbol{x}_I) \\ b(\boldsymbol{x}_I) \end{matrix} \right\} = \boldsymbol{M}_T \left\{ \begin{matrix} a(\boldsymbol{x}_I) \\ b(\boldsymbol{x}_I) \end{matrix} \right\} = \left\{ \begin{matrix} u_s \\ z \end{matrix} \right\} \tag{9.14}$$

Then $\boldsymbol{M}^{-1}$ is determined. The MQ-RBF vector $r(\boldsymbol{x}_I)$ and the polynomial vector $p(\boldsymbol{x}_I)$ are assembled in one single line vector $\left\{ r(\boldsymbol{x}_I)^T p(\boldsymbol{x}_I)^T \right\}$ with size $[1 \times (n + m)]$.

Finally, the interpolation function

$$\varphi(x_I)^T = \{\varphi_1(x_I)\varphi_2(x_I)\ldots\varphi_n(x_I)\} \tag{9.15}$$

is given by

$$u_h(x_I) = \left\{ \boldsymbol{r}(x_I)^T \boldsymbol{p}(x_I)^T \right\} \boldsymbol{M}_T^{-1} \begin{Bmatrix} \boldsymbol{u}_s \\ \boldsymbol{z} \end{Bmatrix} = \left\{ \boldsymbol{\varphi}(x_I)^T \boldsymbol{\psi}(x_I)^T \right\} \begin{Bmatrix} \boldsymbol{u}_s \\ \boldsymbol{z} \end{Bmatrix} \tag{9.16}$$

The RPI shape function first-order partial derivatives can be obtained applying

$$\left\{ \boldsymbol{\varphi}(x_I)^T_{,\xi} \boldsymbol{\psi}(x_I)^T_{,\xi} \right\} = \left\{ \boldsymbol{r}(x_I)^T_{,\xi} \boldsymbol{p}(x_I)^T_{,\xi} \right\} \boldsymbol{M}_T^{-1} \tag{9.17}$$

The RPI shape function second-order partial derivatives can be obtained applying (9.13) and (9.14)

$$\left\{ \boldsymbol{\varphi}(x_I)^T_{,\xi\eta} \boldsymbol{\psi}(x_I)^T_{,\xi\eta} \right\} = \left\{ \boldsymbol{r}(x_I)^T_{,\xi\eta} \boldsymbol{p}(x_I)^T_{,\xi\eta} \right\} \boldsymbol{M}_T^{-1} \tag{9.18}$$

$$\left\{ \boldsymbol{\varphi}(x_I)^T_{,\xi\xi} \boldsymbol{\psi}(x_I)^T_{,\xi\xi} \right\} = \left\{ \boldsymbol{r}(x_I)^T_{,\xi\xi} \boldsymbol{p}(x_I)^T_{,\xi\xi} \right\} \boldsymbol{M}_T^{-1} \tag{9.19}$$

9.1.3   3D Printing

Additive manufacturing, more commonly named 3D printing, together with structural optimization, can be used in the manufacturing process of the final product or, as usual, used to produce prototypes quickly. Often the prototype material behaves similarly to the final manufacturing material, making possible to mechanically test the prototypes and extrapolate results, predicting the final model performance. Therefore, additive manufacturing together with structural optimization enhances the product development cost, velocity and quality. This work puts in practice the application of structural optimization with additive manufacturing prototyping, being fused filament fabrication (FFF) the used process. The term FFF appeared as an alternative to the fused deposition modelling (FDM), a term trademarked by Stratasys but with the same principle (Redwood et al. 2017).

This process starts with the creation of a CAD model, which is converted to STL or IGES format files. STL is an abbreviation of stereolithography and IGES of Initial Graphics Exchange Specification. These files are imported into software who slices the part in the different layers, produces the printing paths and creates support and fixations to the build plate if necessary. The paths are sequences of g-code that the machine will read. There is a considerable amount of printing parameters that can be defined to print the parts, however, according to the material type, there are default settings for the desired quality. Despite all the existent literature (Chacón et al. 2017;

Santana et al. 2017; Pei et al. 2015; Ebel and Sinnemann 2014; Tymrak et al. 2014), either academic or "self-thought", only after some months of experience is the user able to understand well all the consequences of all the parameters and change them to achieve defined requirements.

It is important to understand that this process will not produce parts with the same performance of an injected part in the same material. Even with 100% infill, there are gaps all over the part, and because the layered process resistance is different according printing directions, the process generates anisotropy and other defects due to inherent porosity.

9.1.4 Objective

The objective of this work is to conduct structural optimization on a part subject to complex loading and then validate the structural optimization result through experimental testing. The experimental testing is made inexpensive as it is done with a PLA 3D printed part. The results for the original part, made of steel, are extrapolated from the results on the 3D printed part since both materials present a similar behaviour in the elastic domain.

9.2   Materials and Methods

The metal part presented in Fig. 9.1c is part of an autonomous satellite vehicle, produced by Consoveyo, which is still being fully tested and commissioned. That reason together with the need of space and weight reduction, which are especially important parameters, implies that all the parts should be optimized in their geometry, manufacturing process and characteristics.

(a)   (b)   (c)
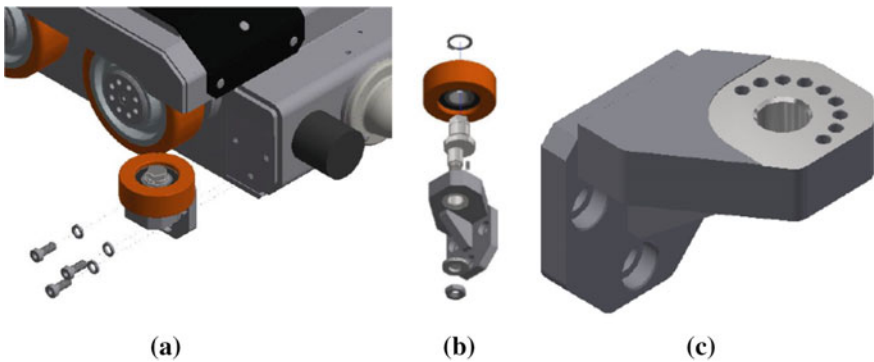
Fig. 9.1 Guiding roller's, **a** placement, **b** assembly, **c** support

It is a guiding roller's assembly, in fact it guides the vehicle on the rock's rails, within a previously set tolerance. It must support previously defined loads that arise on the roller from the vehicle running askew. As shown in Fig. 9.1, the assembly is fixed on a machined surface of the satellite structure, using three fasteners, and has a right and left configuration.

The possible changes in the geometry should preserve the functionality of the part, enabling the correct fixation on the satellite and preserving the desired clearances with the satellite rails.

9.2.1 Simulation Model

The original part, Fig. 9.2a, has a small design domain to apply topology optimization, and to improve results. It was expanded, as shown in Fig. 9.2b, fulfilling at the same time all the geometrical requirements and enable the optimization process to find a
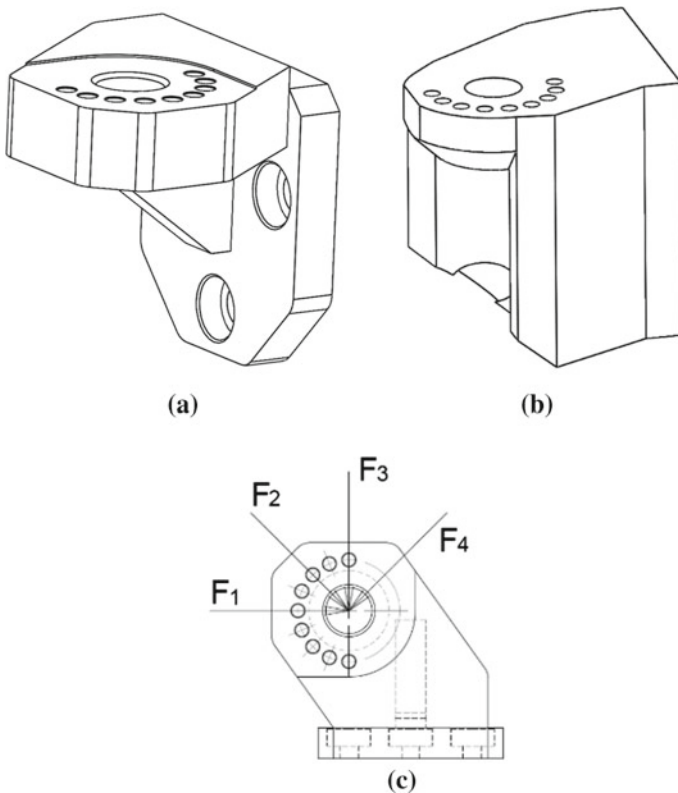
Fig. 9.2 3D design models. **a** Original model, **b** expanded design model **c** load simplification

Table 9.1 EN S235 JR steel properties (Ovako: Steel Navigator and com/steel-grades/s235/ 2020)

Material	Yield strength	Density	Poisson	Elastic modulus
	(MPa)	(g/cm^3)	Ratio	E (GPa)
EN S235 JR	235	7.8	0.3	210

better solution. The bearing load (F1, F2, F3 and F4) applied by the pin was simplified into four sequential load cases shown in Fig. 9.2c.

In this work, it is used a topology software using FEM and meshless methods developed by the research team, FEMAS, and an already validated commercial software, Abaqus. The 3D model created for optimization was the same for both Abaqus and FEMAS and is shown in Fig. 9.2b.

- The Abaqus finer assembly includes 211,033 elements (C3D4), while only 119,762 elements were chosen as design variables.
- In FEMAS–FEM, the model finer discretization has 27,647 3D-T4 elements. All the elements were design variables and had only one integration point.
- In FEMAS–NNRPIM, the discretization was a nodal irregular distribution with 8612 nodes and all the nodes were design variables. A first-order influence cell was used. A full integration scheme was used. The c and p parameters were 0.0001 and 0.9999, respectively, and a constant interpolation function was used $\boldsymbol{p}^T(x) = \{1\}$.

Table 9.1 shows the properties of the material considered in the simulations, steel EN S235 JR.

The same magnitude, 4600 N, was used in the four different applied load cases which were placed, one at a time. During the optimization which considered the influence of all load cases being alternately applied, the design is adjusted to the stiffness requirements and the mass is minimized by removing material.

9.2.2 3D Printing

The resulting models from Abaqus, FEMAS-FEM, FEMAS-NNRPIM topology optimization, were printed using FFF additive manufacturing process. For each topology optimization results, three specimens were printed. *PrusaSlicer* software was used to create the g-code and the printing parameters were defined according to the work of Silva (Silva 2019) who worked with a similar printer and the same brand of PLA. The 3D printer is based in a *Creality ender 3*, a low-cost desktop printer. The properties of the used material, polylactic acid (PLA), are shown in Table 9.2 and dimensions in Table 9.3.

Table 9.2 Formfutura properties of premium PLA (F.: Technical data sheet—Premium PLA. 2015)

Properties	Typical value	Test method
Density (g/cm^3)	1.24	ASTM D1505
Melt flow rate (g/10 min)	6.0	–
Impact strength (KJ/m)	6.0	ASTM D882
Tensile strength (Mpa)	105	ASTM D882
Tensile modulus (Mpa)	3145	ASTM D882
Elongation at break (%)	175	–
Flexural strength (MPa)	54.4	–
Flexural modulus (MPa)	2364.3	–
Print temperature (°C)	190–225	–
Melting temperature (°C)	210 ± 10	–
Viscat. softening temp. (°C)	62	ISO 306

Table 9.3 Formfutura premium PLA dimensions (F.: Technical data sheet—Premium PLA. 2015)

Diameter	Tolerance	Roundness
1.75 mm	0.05 mm	95%

9.2.3 Mechanical Tests

The 3D printed models were tested with the objective of simulate the applied loads in a real situation. Each specimen was submitted to four different displacements, one at time. The direction of the applied displacement cases is shown in Fig. 9.2c and during the mechanical tests, the models were always under elastic behaviour.

Two auxiliary testing parts needed to be made to fix the models and apply the displacements in the desired angles. A pin was also needed do enable the force transmission to from the testing machine to the part and simulate the real load cases application. These parts were produced in aluminium alloy to behave like a rigid structure ensuring that the plastic model support all the forces.

9.3 Results

This work was composed of three main tasks: the topology optimization; the 3D printing; and the experimental tests. This section will show the results of all tasks.

9.3.1 Topology Optimization Results

Regarding the computer simulations, all the shown weight reductions are relatively to the original part, and not to the model created to increase the design domain.

The objective function used in Abaqus was the energy stiff measure, and all the simulations converged to the volume restriction, minimizing the objective function value. In FEMAS, the resultant loads were calculated and applied directly on the model, the material law is linear kill, and the optimal criteria is the effective von Misses stress. The decrease and increase ratio are 10% and 2%, respectively. The maximum number of times that a point remodels is 3.

In both software, the area contacting with the screw was defined without any degree of freedom.

9.3.2 Abaqus

Figure 9.3 has shown the stress and displacement fields of the topology optimized from the last two iterations of the study in Abaqus. In all the simulations, the maximum stress values are bigger than the yield strength of 235 MPa, however
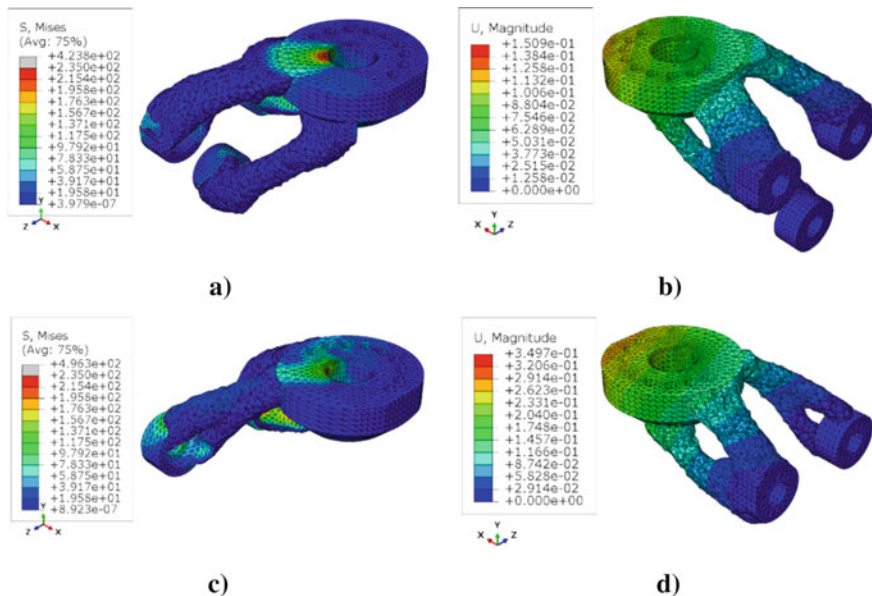
Fig. 9.3 Abaqus topology optimization results. **a** Front view of the stress distribution after fifth iteration, **b** rear view of displacement distribution after fifth iteration, **c** front view of the stress distribution after sixth iteration, and **d** rear view of displacement distribution after sixth iteration

it occurs in few specific nodes due to load application conditions and can be ignored. Overall, all the first five optimized parts have acceptable stresses.

In the optimization corresponding to Fig. 9.3c and d, the topology optimization process removed one support, and because the action lines of the loads, a rotation angle is created. Because of that the topology optimization process stops.

Table 9.4 has shown the main properties of the resultant models from the optimization, being **K** the stiffness and **k** the specific stiffness.

For a better understanding, two graphs are shown in Fig. 9.4 allowing the analysis of the stiffness behaviour along the course of the optimization iterations.

Table 9.4 Abaqus topology optimization results

Iteration	Max. Displacement	Mass Reduction	Mass	Force	K	k
	(mm)	(%)	(Kg)	(N)	(N/mm)	(N/mm Kg)
1	4.82E−02	7967	6.73E−01	4.60E+03	9.55E+04	1.42E+05
2	6.78E−02	19,348	5.90E−01	4.60E+03	6.79E+04	1.15E+05
3	9.21E−02	32,023	4.97E−01	4.60E+03	5.00E+04	1.00E+05
4	1.02E−01	37,598	4.56E−01	4.60E+03	4.49E+04	9.84E+04
5	1.18E−01	43,103	4.16E−01	4.60E+03	3.90E+04	9.37E+04
6	2.88E−01	56,690	3.17E−01	4.60E+03	1.60E+04	5.04E+04
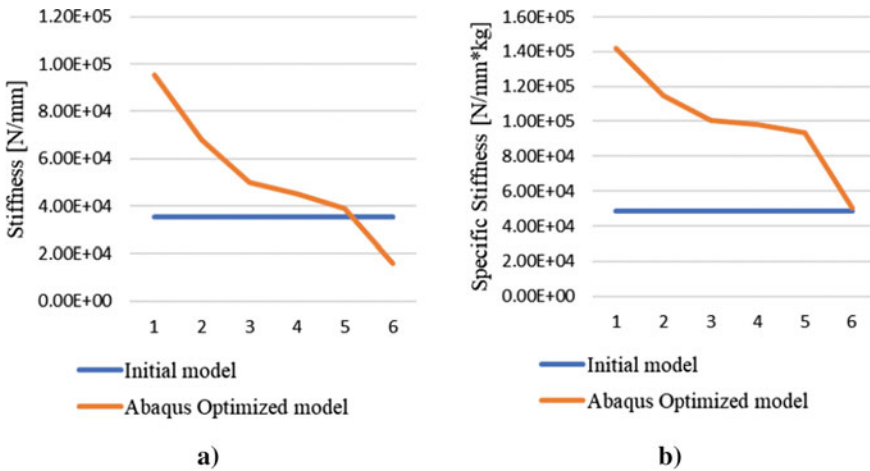
Fig. 9.4 Numerical results. **a** Stiffness evolution in each iteration and **b** specific stiffness evolution during each iteration

9.3.2.1 Femas

In FEMAS, the performing topology optimization using FEM needed several itera-
tions by the program until the model mean density converged to the value predefined.
After a visual inspection it was shown that, the best result is the 9th iteration run by
the program. Figure 9.5a and b is possible to see the resultant discretization model
from iteration 9 without the values with lower density.

As performed with FEM, in the case of NNRPIM, several iterations where also
needed, and a visual inspection has shown that it took 8 iterations to obtain the best
results in terms of continuity and mass reduction. It is possible to see the resultant
discretization model from this iteration without the values with lower density in
Fig. 9.5c and d.
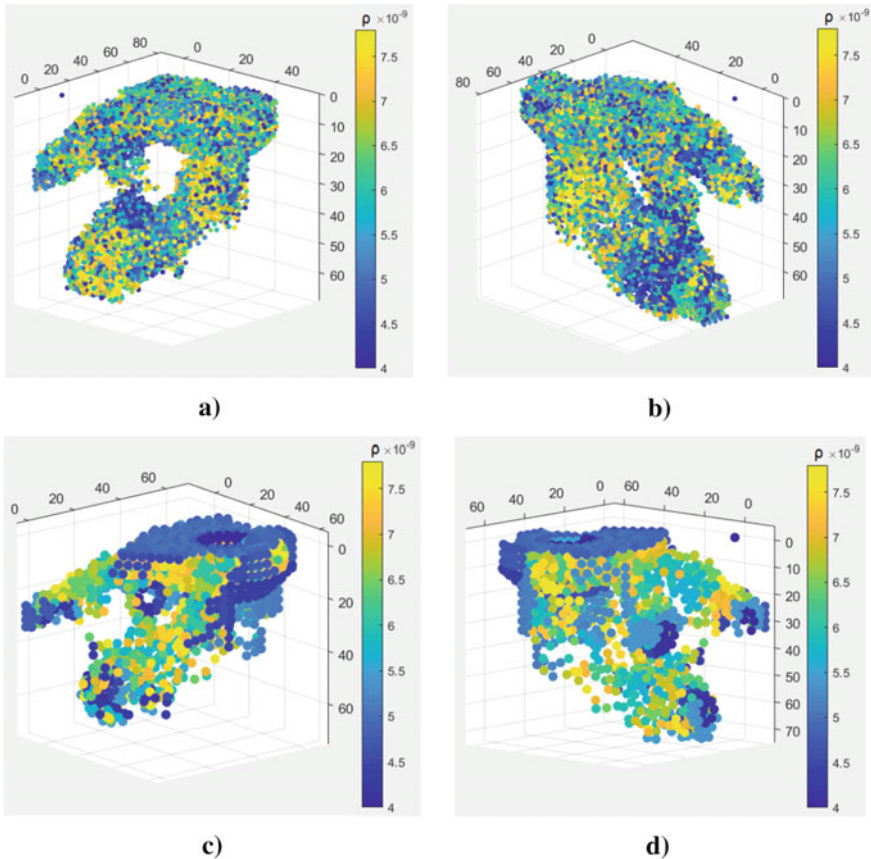
Fig. 9.5 Best scatter plots from FEMAS—FEM. **a** front view **b** rear view NNRPIM **c** front view
d rear view

For both numerical approaches, the creation of a rotation angle, led to the separation of one of the three supports by the action lines of the loads. Because of that the topology optimization process stops, as in Abaqus.

9.3.2.2 Structural Evaluation of the Optimized Results

All models were subject to a linear-elastic analysis of the behaviour of these new structure configurations. This analysis was conducted in Abaqus. To construct the models for this simulation with static analysis, all the models needed post-processing. The optimized structure in Abaqus which had a fine discretization only required some smoothing and slight surface fixing in order to create a volume mesh which could be re-imported to Abaqus. In FEMAS, both models had a courser discretization due to the computing time of the analyses, and a bigger smoothing and surface finishing operation was needed before creating a volume mesh. The post-processing was performed using Autodesk Meshmixer for smoothing and Materialize 3-Matic for surface fixing.

The CAE model resultant from Abaqus topology optimization includes 44,725 linear tetrahedral elements of type C3D4.

The CAE-models obtained from topology optimization using FEMAS, through FEM and NNRPIM analyses, have 63,700 and 65,626 linear tetrahedral elements of type C3D4, respectively.

Table 9.5 shows the stiffness of the structures for each load case (F1, F2, F3 and F4).

Because all the loads have the same level of importance, to decide which optimized model has the best performance, only the worst stiffness values of each model should be compared. In this case, the model created in FEMAS using FEM is the one with the best performance. However, the mass reduction was different in all the optimizations, and that needs to be considered. Table 9.6 has shown the mass values and its reduction in comparison with the mass of the original model.

Using the values present in Table 9.6 it is possible to calculate the specific stiffness (k) and construct Table 9.7.

Table 9.5 Stiffness of the optimized models and initial model resultant from numerical analysis

Model	Stiffness [N/mm]			
	F1	F2	F3	F4
Initial	6.26E+04	**3.55E+04**	3.62E+04	6.17E+04
Abaqus-FEM	4.73E+04	**3.83E+04**	4.39E+04	4.96E+04
FEMAS-FEM	1.32E+05	7.95E+04	**6.27E+04**	7.09E+04
FEMAS-NNRPIM	1.01E+05	6.98E+04	**5.04E+04**	5.53E+04

Table 9.6 Optimized models mass reduction

Model	Mass (kg)	Mass reduction (%)
Initial	7.28E−01	–
Abaqus-FEM	3.64E−01	49.97
FEMA-FEM	6.02E−01	17.27
FEMAS-NNRPIM	5.18E−01	28.91

Table 9.7 Specific Stiffness of the optimized models and initial model from numerical analysis

Model	Specific stiffness [N/mm* kg]			
	F1	F2	F3	F4
Initial	8.60E+04	**4.88E+04**	4.97E+04	8.48E+04
Abaqus-FEM	1.30E+05	**1.05E+05**	1.20E+05	1.36E+05
FEMAS-FEM	2.19E+05	1.32E+05	**1.04E+05**	1.18E+05
FEMAS-NNRPIM	1.95E+05	1.35E+05	**9.73E+04**	1.07E+05

9.3.2.3   3D Printing

Figure 9.6 shows three models produced by 3D printing where it is possible to verify the structure configuration of the three optimization analyses.

All the produced models were weighted in a HLD 300 scale (Dini Argeo 2020), and the values are registered in Table 9.8.

a)   b)   c)
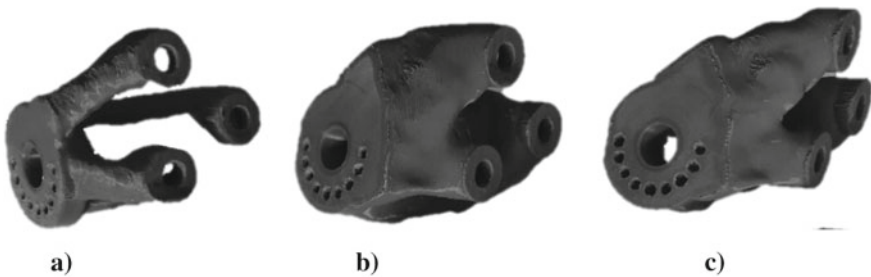
Fig. 9.6 Topology optimized 3D printed models **a** Abaqus **b** FEMAS FEM **c** FEMAS NNRPIM

Table 9.8 Mass of 3D printed models

Model	Mass (g)	Theoretical mass (g)	Difference (%)
Abaqus-FEM	56.002±0.148	57.911	−3.297±0.255
FEMAS-FEM	90.192±0.282	95.763	−5.810±0.294
FEMAS-NNRPIM	77.342±0.286	82.281	−6.003±0.347

Table 9.9 Stiffness of 3D printed models

Model	Stiffness [N/mm]			
	F1	F2	F3	F4
Abaqus-FEM	403.948±14.787	452.807±15.142	411.523±14.953	545.369±39.121
FEMAS-FEM	705.066±20.961	690.852±16.681	525.000±14.648	552.775±28.648
FEMAS-NNRPIM	511.952±6.817	542.332±21.945	529.871±14.944	481.522±7.898

9.3.2.4   Experimental Test

Table 9.9 summarizes the stiffness values obtained from the mechanical tests of the models printed in PLA. Each part had the 4 load cases tested in a sequence and each load case was tested for a vertical displacement of the load cell of 1 mm in order to make sure that no load case brings the structure beyond the elastic limit.

With the results obtained for the PLA models, a stiffness extrapolation to Steel EN S235 JR can be made and compared with the obtained numerical results. Since both materials present a linear behaviour in the elastic domain, the displacements observed in the two materials will be directly proportional to the ratio of the elasticity modulus of both materials. Therefore, the stiffness of a part made of steel can be calculated from the measured stiffness in the PLA part.

$$K_{\text{Steel}} = K_{\text{PLA}} \times \frac{210000(E_{\text{Steel}})}{3145(E_{\text{PLA}})} \qquad (9.20)$$

Applying Eq. (9.20) to the stiffness values of the 3D printed models, presented in Table 9.9, it is possible to extrapolate, from the mechanical tests, the value of the steel stiffness, resulting in Table 9.10.

These results are to be compared with the values obtained from the numerical analysis of the optimized specimens where the approximated error between the experimental and the numerical can be seen in Table 9.11.

9.4   Discussion

Analysing the topology optimization results from Abaqus, shown in Fig. 9.3, and considering that the optimized part should have a better or at least similar stiffness than the initial, according to Table 9.4 and Fig. 9.4, the optimization number 6 can be excluded from the options available. It was expected due to the removal of one support in the optimization process. The optimization that fulfils this requirement and at the same time has the biggest mass reduction is optimization 5. Considering the specific stiffness, it is possible to understand that, although the stiffness of optimization 5 is only slightly superior to the original, the gain in specific stiffness is considerably

Table 9.10 Stiffness extrapolation from PLA to EN S235 JR Steel

Model	Extrapolated stiffness [N/mm]			
	F1	F2	F3	F4
Abaqus–FEM	26,972.680±987.367	30,235.126±1011.072	27,478.483±998.452	36,415.736±2612.213
FEMAS-FEM	47,079.109±1399.622	46,130.022±1113.835	35,055.644±978.086	36,910.254±1912.903
FEMAS-NNRPIM	34,184.394±455.189	36,212.948±1465.326	35,380.893±997.851	32,152.502±527.370

Table 9.11 Extrapolated error between the numerical and experimental values

Model	Extrapolated Stiffness error [%]			
	F1	F2	F3	F4
Abaqus-FEM	43.0±2.1	21.1±2.6	37.4±2.3	26.5±5.3
FEMAS-FEM	64.3±1.1	42.0±1.4	44.1±1.6	47.9±2.7
FEMAS-NNRPIM	66.1±0.5	48.1±2.1	29.7±2.0	41.8±1.0

better than the original, making optimization number 5 a resultant model with a better performance.

After the static analysis of the optimized models from Abaqus, FEMAS-FEM and FEMAS-NNRPIM, analysing the stiffness from Table 9.7 is FEMAS-FEM the Topology optimization with the best lowest stiffness, however in Abaqus the mass reduction is bigger than in FEMAS-FEM, and because of that the term of comparation is going to be the specific stiffness. Analysing Table 9.5 and considering the worst specific stiffness case for each model, it is possible to conclude that the Abaqus model is the one who presents the higher specific stiffness in the worst case, and consequently the best performance.

Still in Table 9.5 it is possible to compare the stiffness value resultant from the optimization 5 with the value resultant from the statical analysis of the smoothed model. The stiffness error is $\frac{|3.90E4-3.83E4|}{3.90E4} \simeq 1.8\%$, which is very acceptable, and therefore validates the statical analysis.

A visual comparation of the 3D printed models shows that, in the model printed from Abaqus optimization, there are single extensions from the supports to the shaft placement area, and a bigger volume reduction when compared with FEMAS, as shown in Fig. 9.7.

Comparing the results obtained with FEMAS, more precisely, FEM and NNRPIM, both have similar results, Fig. 9.8. Their main difference can be found in the existent connection between two supports for the case of NNRPIM. The difference between the results in both software can be explained by the difference in optimization algorithm. Whereas Abaqus uses the optimization algorithm implemented in TOSCA, FEMAS runs the optimization according to the BESO algorithm. Therefore, it can be said that the optimization approach was more relevant to the structure configuration than the numerical method.

In Table 9.8 is calculated the error between the 3D model part and the 3D printed one, and as expected, the FFF process created a porous part, although the infil was set for 100%. This is a very known limitation of this process.

Having the stiffness values resultant from the mechanical tests, the stiffness of the parts made of steel (EN S235 JR) was extrapolated from the experimental tests run on PLA. A similar error value was expected for all the load cases and models; however, the stiffness error has a huge variation for the majority load cases and the printed models, making unfeasible this extrapolation. There are, however, some reasons that can justify the results. The fact that the printing process is anisotropic is the one with the most importance. This anisotropy makes that the behaviour to a solicitation along
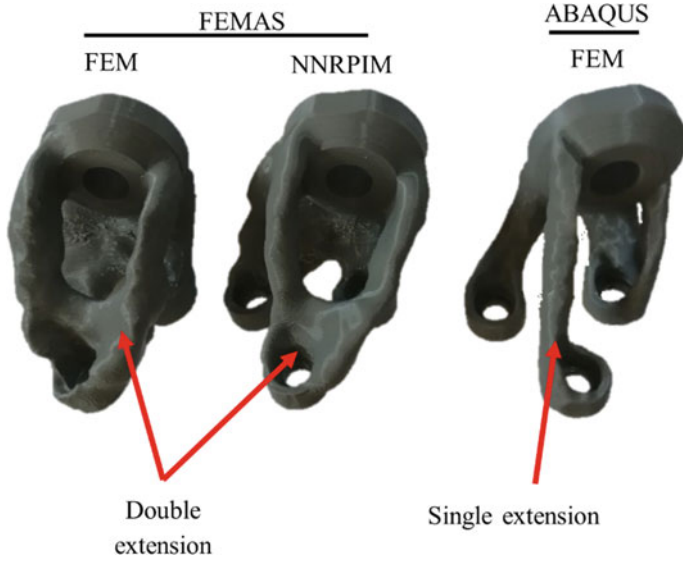
Fig. 9.7 Differences between Abaqus and FEMAS Topology optimization results

Fig. 9.8 Differences from
FEMAS—FEM and
FEMAS—NNRPIM
topology optimized models
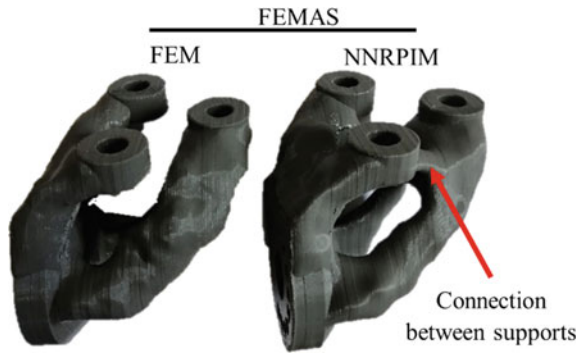
the printing layer deposition is quite different from the behaviour of a solicitation perpendicular to that direction. Although the printing direction was performed in a way so as to obtain the most homogeneous behaviour of the part, the loads applied to the part result in multiple directions solicitations of the layers.

It also possible to verify that the two models from FEMAS, have a similar error for all the loads, excepting load case F3, and distinct values with error from Abaqus model. This is justified with the difference in the level of porosity, detected in Table 9.8. The models with the same level of porosity have similar error magnitudes and higher porosity levels lead to a higher extrapolation error.

9.5   Conclusion

Through the optimized numerical models analysed and comparisons made between them and the original part it was possible to conclude that:

1. Abaqus has achieved a 50% reduction of the mass, and still slightly better stiffness when compared to the initial part. In fact, the result from Abaqus was the overall optimized model with the best specific stiffness. The results from FEMAS did not achieve such a big reduction of mass, only 17% for FEM and 29% for NNRPIM, highly influenced by the smoothing process.
2. Comparing the results from FEMAS obtained using FEM and NNRPIM, it is possible to conclude that the results were very similar, both optimizations converged, although that was not for an absolute optimal solution. This allows to conclude that meshless methods are suitable for topology optimization.
3. Between FEMAS and Abaqus, it is evident that the results are slightly different. This is a result of the different topology approaches used by the programs. It was possible to conclude that Abaqus, using SIMP, is able to achieve an optimal solution, even if it is a local optimum and not absolute, while FEMAS using BESO can converge, however to a non-optimal solution. This conclusion is in accordance with the literature.
4. After the model optimization, smoothing and surface fixing was performed on all the results. In Abaqus the smoothing was small, but in FEMAS, the smoothing was severe for FEM and NNRPIM, leading to the conclusion that most of the time the results from topology optimization need a post-processing.
5. The error between the extrapolated stiffness, from 3D printed models to steel ones, was huge and distinct in the majority according the load case and printed model, making this extrapolation unfeasible.
6. Overall, all the programs produced optimized lighter models and with better mechanical behaviour.

References

Allaire, G., Jouve, F.: Optimal design of micro-mechanisms by the homogenization method. Rev. Eur. des Eléments. **11**, 405–416 (2002)
Atluri, S.N., Zhu, T.: A new meshless local petrov-galerkin (MLPG) approach in computational mechanics. Comput. Mech. **22**, 117–127 (1998). https://doi.org/10.1007/s004660050346

Azamirad, G., Arezoo, B.: Structural design of stamping die components using bi-directional evolutionary structural optimization method. Int. J. Adv. Manuf. Technol. **87**, 969–979 (2016). https://doi.org/10.1007/s00170-016-8344-7

Belinha, J.: Meshless Methods in Biomechanics: Bone Tissue Remodelling Analysis. Springer International Publishing (2014)

Belinha, J., Dinis, L.M.J.S., Natal Jorge, R.M.: The natural radial element method. Int. J. Numer. Methods Eng. **93**, 1286–1313 (2013a). https://doi.org/10.1002/nme

Belinha, J., Dinis, L., Jorge, R.M.N.: Composite laminated plate analysis using the natural radial element method. Compos. Struct. **103**, 50–67 (2013b)

Belinha, J., Dinis, L.M.J.S., Natal Jorge, R.M.: Analysis of thick plates by the natural radial element method. Int. J. Mech. Sci. **76**, 33–48 (2013c). https://doi.org/10.1016/j.ijmecsci.2013.08.011

Belytschko, T., Lu, Y.Y., Gu, L.: Element-Free Galerkin Methods. Int. J. Numer. Methods Eng. **37**, 229–256 (1994)

Belytschko, T., Krongauz, Y., Organ, D., Fleming, M., Krysl, P.: Meshless methods: an overview and recent developments. Comput. Methods Appl. Mech. Eng. **139**, 3–47 (1996)

Bendsoe, M.P., Sigmund, O.: Topology Optimization: Theory, Methods, and Applications. Springer, Berlin Heidelberg (2003)

Chacón, J.M., Caminero, M.A., Garc\$\\$'\$\\$ia-Plaza, E., Núñez, P.J.: Additive manufacturing of PLA structures using fused deposition modelling: Effect of process parameters on mechanical properties and their optimal selection. Mater. Des. **124**, 143–157 (2017)

Christensen, P.W., Klarbring, A.: An Introduction to Structural Optimization. Springer, Netherlands (2008)

Colin Donald Chapman: Structural Topology Optimization Via The Genetic Algorithm (1994)

Dini Argeo: HLD300, http://www.diniargeo.com/prd/scales/laboratory-scales/hld-150g-600g-en.aspx (2020)

Dinis, L.M.J.S., Jorge, R.M. Natal, Belinha, J.: Analysis of 3D solids using the natural neighbour radial point interpolation method. Comput. Methods Appl. Mech. Eng. **196**, 2009–2028 (2007). https://doi.org/10.1016/j.cma.2006.11.002

Dinis, L.M.J.S., Natal Jorge, R.M., Belinha, J.: Analysis of 3D solids using the natural neighbour radial point interpolation method. Comput. Methods Appl. Mech. Eng. **196**, 2009–2028 (2007). https://doi.org/10.1016/j.cma.2006.11.002

Dinis, L.M.J.S., Natal Jorge, R.M., Belinha, J.: Analysis of plates and laminates using the natural neighbour radial point interpolation method. Eng. Anal. Bound. Elem. **32**, 267–279 (2008). https://doi.org/10.1016/j.enganabound.2007.08.006

Duan, Y.: A note on the meshless method using radial basis functions. Comput. Math. with Appl. **55**, 66–75 (2008)

Ebel, E., Sinnemann, T.: Fabrication of FDM 3D objects with ABS and PLA and determination of their mechanical properties. RTe j. 2014, (2014)

Futura, F.: Technical data sheet—Premium PLA. (2015)

Gu, Y.: Meshfree methods and their comparisons. Int. J. Comput. Methods **2**, 477–515 (2005)

Liu, G.-R., Gu, Y.-T.: An introduction to meshfree methods and their programming. Springer Science & Business Media (2005)

Liu, W.K., Jun, S., Zhang, Y.F.: Reproducing kernel particle methods. Int. J. Numer. methods fluids. **20**, 1081–1106 (1995)

Luo, Z., Zhang, N., Wang, Y., Gao, W.: Topology optimization of structures using meshless density variable approximants. Int. J. Numer. Methods Eng. **93**, 443–464 (2013). https://doi.org/10.1002/nme.4394

Martin Philip Bendsoe: Noboru Kikuchi: Generating optimal topologies in structural design using a homogenization method. Comput. Methods Appl. Mech. Eng. **71**, 197–224 (1988)

Moreira, S., Belinha, J., Dinis, L., Jorge, R.M.N.: Análise de vigas laminadas utilizando o natural neighbour radial point interpolation method. Rev. Int. Métodos Numéricos para Cálculo y Diseño en Ing. **30**, 108–120 (2014)

Nguyen, V.P., Rabczuk, T., Bordas, S., Duflot, M.: Meshless methods: a review and computer implementation aspects. Math. Comput. Simul. **79**, 763–813 (2008). https://doi.org/10.1016/j.matcom.2008.01.003

Ovako: Steel Navigator, https://steelnavigator.ovako.com/steel-grades/s235/ (2020)

Pei, E., Lanzotti, A., Grasso, M., Staiano, G., Martorelli, M.: The impact of process parameters on mechanical properties of parts fabricated in PLA with an open-source 3-D printer. Rapid Prototyp. J. (2015)

Redwood, B., Schöffer, F., Garret, B.: The 3D Printing Handbook: Technologies, Design and Applications. 3D Hubs B.V. (2017)

Rozvany, G.I.N.: A critical review of established methods of structural topology optimization. Struct. Multidiscip. Optim. **37**, 217–237 (2009)

Santana, L., Alves, J.L., Netto, A. da C.S.: A study of parametric calibration for low cost 3D printing: Seeking improvement in dimensional quality. Mater. Des. **135**, 159–172 (2017)

Sigmund, O.: On the usefulness of non-gradient approaches in topology optimization. Struct. Multidiscip. Optim. **43**, 589–596 (2011)

Sigmund, O., Maute, K.: Topology optimization approaches. Struct. Multidiscip. Optim. **48**, 1031–1055 (2013). https://doi.org/10.1007/s00158-013-0978-6

Silva, C.M.M. da: 3D printing of gyroid structures for superior structural behaviour (2019)

Swedish Research Council (VR): Structural Optimization, (2013) https://www.math.kth.se/optsyst/Struc.html

Tanskanen, P.: The evolutionary structural optimization method: theoretical aspects. Comput. Methods Appl. Mech. Eng. **191**, 5485–5498 (2002). https://doi.org/10.1016/S0045-7825(02)00464-4

Tymrak, B.M., Kreiger, M., Pearce, J.M.: Mechanical properties of components fabricated with open-source 3-D printers under realistic environmental conditions. Mater. Des. **58**, 242–246 (2014). https://doi.org/10.1016/j.matdes.2014.02.038

Voronoi, G.: Nouvelles applications des paramètres continus à la théorie des formes quadratiques. J. für die reine und Angew. Math. **134**, 198–287 (1908)

Wang, J.G., Liu, G.R.: A point interpolation meshless method based on radial basis functions. Int. J. Numer. Methods Eng. **54**, 1623–1648 (2002). https://doi.org/10.1002/nme.489

Wang, M.Y., Wang, X., Guo, D.: A level set method for structural topology optimization. Comput. Methods Appl. Mech. Eng. **192**, 227–246 (2003). https://doi.org/10.1016/S0045-7825(02)00559-5

Xia, L., Xia, Q., Huang, X., Xie, Y.M.: Bi-directional evolutionary structural optimization on advanced structures and materials: a comprehensive review. Arch. Comput. Methods Eng. **25**, 437–478 (2018)

Zhang, X., Zhu, B.: Topology Optimization of Compliant Mechanisms. Springer Singapore (2018)

Chapter 10
Machinability Study of Polymeric Parts Fabricated by Additive Manufacturing Under a Dry Milling Process

P. Arnés-Urgellés, J. Bayas, E. A. Ramírez, F. Maldonado, C. G. Helguero, and J. L. Amaya

Abstract Additive manufacturing (3D printing) is rapidly becoming a viable substitute into material subtraction processes due to the design flexibility it offers for complex parts fabrication. Being a relative novelty, meeting specific applications' requirements, such as dimensional tolerances and surface roughness, implicate an aggressive increase in fabrication costs. Machining of 3D printed parts is proposed by the authors as a method to attain these requirements. This study focuses on the influence of cutting parameters on the machinability of pieces produced by two different AM technologies: MultiJet Printing (MJP) and fused deposition modelling (FDM). All tests were performed on acrylonitrile butadiene styrene (commonly referred to as ABS), measuring improvement of surfaces' roughness as a machinability indicator and comparing it to injection moulded polyoxymethylene copolymer (POM) for reference purposes. With cutting speed, feed rate and cut depth as the process parameters, 13 terns were formed. Milling processes were executed on 30 x 30 x 10 mm block-shaped 3D prints and surface roughness values were obtained via a portable roughness tester. It was found that the most influential parameter was feed rate, consistently with previous studies conducted in metallic elements. Parts fabricated by FDM presented a higher machinability ratio when compared to MJP, with a value of 1.27. This is interpreted as a high machinability with respect to the reference material, proving that the surface of a 3D printed ABS part could be improved with post-fabrication machining.

Keywords Additive manufacturing · Post-process machining · Surface roughness · Machinability · Milling

P. Arnés-Urgellés (✉) · J. Bayas · E. A. Ramírez · F. Maldonado · C. G. Helguero · J. L. Amaya
ESPOL Polytechnic University, Guayaquil, Guayas EC090112, Ecuador
e-mail: parnes@espol.edu.ec

10.1   Introduction

Additive manufacturing (AM) of polymeric parts, commonly referred to as 3D printing, is considered a suitable prototyping tool given its low production time and geometrical restrictions when compared to traditional manufacturing technologies; nowadays, the development of this process has enabled applications to go beyond prototyping and into direct service (Levy et al. 2003). Unfortunately, the steep correlation between investment in AM equipment and mechanical finishing acts as a limitation factor when considering employing this manufacturing alternative for certain applications with restrictive dimensional and roughness requirements, for example, when printing parts for a mechanical coupling. To overcome this, the possibility of incorporating subsequent machining to the AM process of polymers was explored by the authors.

The combination of AM and traditional machining operations has been studied for metallic materials (Olivier et al. 2011; Kruth et al. 2005; Isaev et al. 2016; Konstantinos et al. 2015) which has gained special interest given that additive manufacturing technology has now further uses than prototyping (Olivier et al. 2011). This arrangement implies a cutback in waste material when compared to operations based solely on material removal. This results in a decrease in manufacturing time, energy consumption and feedstock, positively impacting environmental care and overall processes (Jeremy et al. 2015).

To establish the compatibility of both processes, it is necessary to consider the 3D printed polymeric parts' machinability. This term refers to the relative ease of a material to be machined under the appropriate tools and cutting conditions. The factors that have an impact on machining performance are the material's properties, the tool's geometry and the cutting parameters. There are different perspectives from which to analyse machinability, these being the amount of cutting force exerted, the wearing of the tool, or the surface's quality (Kalpakjian and Schmid 2014; Mills 2012; Seker and Hasirci 2006); but most published literature refers only to metals (Sikdar 2007; Thiele 1990; Nourredine et al. 2003), whose response to cutting conditions may not translate very well into polymers due to the properties differences. Prior studies conducted in metallic elements established that among the tested cutting parameters, feed rate was the most influential one (Gaitonde et al. 2008). For this purpose, the following study focuses on the influence of cutting parameters on 3D printed pieces, *i.e.* feed rate, spindle rotations and depth of cut, aiming to obtain the highest decrease on surface roughness.

To the authors knowledge, the only machinability index that refers to polymers was proposed by Davim & Mata for glass fibre reinforced plastic (Paulo Davim et al. 2008), which considers the specific cutting pressure and surface roughness, each with a weighing factor. However, due to the unavailability of referential work regarding machining of additive manufactured polymeric parts, the authors opted for a simplified approach that would allow the determination of a tendency or behaviour to be recognized in the present exploratory study. The proposed index considers a benchmark approach. The method consists in determining the machinability index

MI as the ratio between the surface roughness *Ra* of the base or reference material and the test material, as presented in Eq. (10.1). Values of *MI* greater than the unit refer to an increase of surface quality, and thus, an ease of the tested material to be machined. Accordingly, *MI* below the unit corresponds to materials that are more difficult to machine.

$$MI_{\text{test material}} = \frac{Ra_{\text{base material}}}{Ra_{\text{test material}}} \tag{10.1}$$

10.2   Materials and Methods

This section details the methodology followed to establish the machinability of 3D printed parts and consequently find the cutting parameters that provide an improvement to surface finish.

10.2.1   Equipment and Materials Set-Up

Among the different AM technologies, this study focuses on fused deposition modelling (FDM) and MultiJet Printing (MJP). Regarding the employed equipment, FDM processes were carried on in a 3DSystems Cube 3D printer and MJP process on a 3DSystems ProJet 3510 SD. Milling machining operations were carried on a ROLAND MDx-40A, 3-axis CNC milling machine, using a high-speed steel (HSS) end mill of 6 mm in diameter.

Even though a wide range of polymeric materials are used in additive manufacturing, acrylonitrile butadiene styrene (commonly referred to as ABS) was selected due to its commercial availability and compatibility with a wide range of 3D printers. Process parameters considered a layer thickness of 200 μm and 30–32 μm, for FDM and MJP, respectively. Due to the process characteristics, MJP pieces are considered solid (100% infill percentage), while FDM specimens were printed with a honeycomb internal pattern, resulting in a 10% infill percentage.

Since the chosen definition of machinability involves a base material as a reference, injection moulded polyoxymethylene copolymer (POM) was selected due to its machinability ease, similarity in hardness and applications to ABS, and commercial availability.

10.2.2 Optimal Conditions Determination

Given that thermoplastics are being subjected to machining, it is important to consider their low thermal conductivity, low elasticity modulus and the loss of rigidity with heat application; this translates into a need to use sharp cutting tools with positive attack angles to reduce the exerted forces, along with large relief angles, low feed rates and cutting depths and high rotational speeds (Kalpakjian and Schmid 2014).

10.2.2.1 Surface Roughness Measurement

Surface roughness values, both prior and post machining, were determined by a Phase-II SRG-4500 portable roughness tester. In accordance with the employed surface roughness instrument's measuring range, 30 x 30 x 10 mm block-shaped samples were designed; post-process cleaning was conducted, and dimensions were verified after the printing processes.

The workpiece was prepared by marking different reference points for testing; measurements were taken in three different points of each piece to obtain an average value. Roughness was measured in a cross and longitudinal route, relative to the cut feed direction; for each tern of cutting conditions, a replica was made for error calculation. Only specimens with errors below 10% were considered for further testing. Additionally, measurements of non-machined pieces were obtained for reference purposes.

10.2.2.2 Cutting Parameters Variation

Maximum values for feed rate, spindle speed and cutting depth were 2500 mm/min, 15,000 rpm and 0.175 mm, respectively. These conditions correspond to the milling equipment's limitations and the available literature on finishing processes (Benardos and Vosniakos 2003) given that the aim of this study was to reduce roughness. Decrements of 500 mm/min of feed rate were tested, as well as decrements of 2500 rpm for the spindle rotation and 0.025 mm for the depth of cut. Minimum considered values were 500 mm/min, 5000 rpm and 0.075 mm, for feed rate, spindle rotation and depth of cut, correspondingly.

Initially, feed rate was varied, setting rotational speed at the highest value and cut depth at its minimum, according to common cutting conditions in finishing operations. For each feed rate value, surface roughness was measured and plotted, aiming to identify a tendency and determining the value that would yield in the lowest roughness. Using said value, a second test considered a variation in spindle rotation, while maintaining a constant value of depth of cut and feed rate; similarly, resulting in the determination of an optimal rotational value (minimum roughness). Lastly, cut depth was varied and the prime value found following the same steps.

10.2.3   Machinability Index Development

To develop the machinability index, the base material's original roughness was measured, and the workpiece was machined using the determined optimal cutting conditions. With all the roughness values obtained, Eq. (1) was used and comparisons were made.

10.3   Results and Discussion

Prior to machining, it was found that the workpieces average surface roughness was 0.685 µm longitudinal and 3.325 µm cross-directional for MJP specimens. For the elements fabricated with FDM, the roughness tester presented an "out of range" warning, therefore the maximum measurable value of the instrument was assumed, this being 40 µm. For the control element of the base material Polytec 1000, values of 1.273 µm longitudinal and 1.524 µm cross-directional were obtained.

For the first phase of testing, the maximum rotation speed value (15,000 rpm) and the minimum depth of cut (0.075 mm) were set, as feed rate was varied from 500 to 2500 mm/min. As shown in Fig. 10.1a, the best surface roughness for longitudinal direction measurements was obtained for a feed rate value of 1000 mm/min in the FDM case, while for MJP the lowest surfaced roughness was obtained to the lowest feed rate value. In the cross-direction (Fig. 10.1b), both technologies were consistent with their results; the best surface finish was attained with the lowest feed rate value of 500 mm/min.

In the FDM case, there was a stagnation region between minimal and maximum tested values, from both longitudinal and cross-directional perspective; even though for the latter it was less perceivable. On the other hand, surface roughness on MJP is overall smaller than in FDM, especially for the cross-direction, which is attributed to the manufacturing process and technology accuracy; *i.e.* MJP has lower printing
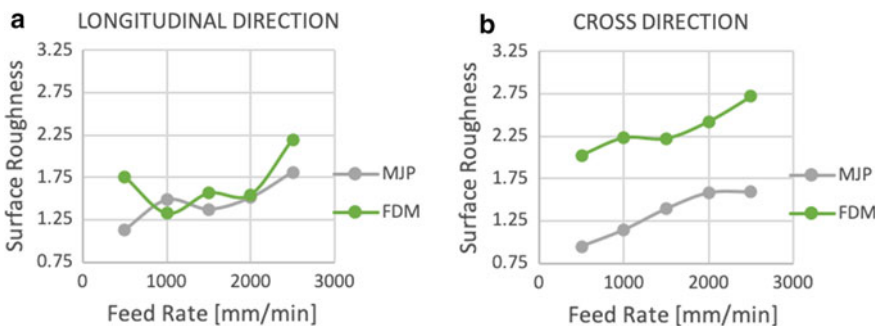
Fig. 10.1 Average roughness curve (Ra) versus feed rate for each 3D printing technology. **a** Longitudinal direction data. **b** Cross-direction data
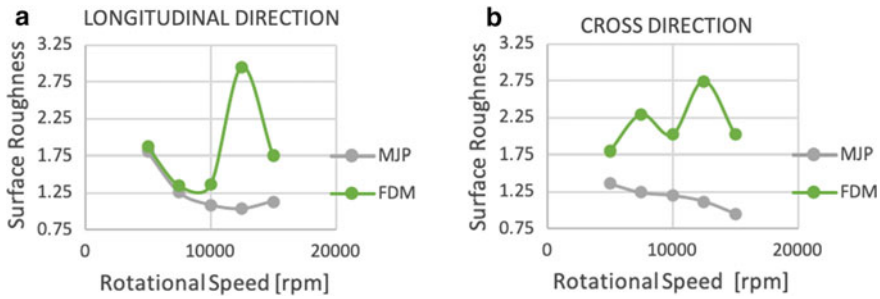
Fig. 10.2 Average roughness curve (Ra) versus rotational speed for each 3D printing technology. **a** Longitudinal direction data. **b** Cross-direction data

tolerances and delivers a solid workpiece, whereas FDM's plastic filaments are observable.

For the second phase of the test, a feed value 500 mm/min and a depth of cut 0.075 mm were set, while spindle speed was varied. In Fig. 10.2a, MJP showed steady variations, and even though the lowest surface roughness corresponds to 12,500 rpm, the relative variation with the 15,000 rpm test is of 8.85%; additional data need to be collected to determine if there is a stagnation region or if roughness will decrease even further. As Fig. 10.2b depicts, for MJP the highest rotation speed value of 15,000 rpm yielded an optimal surface roughness. However, FDM technology evidenced optimal surface roughness at the lowest tested rotational speed, 5000 rpm, even though the exposed behaviour was not consistent enough to predict the response to other values.

In the third phase of the test, the depth parameter was varied, and the feed rate and spindle values were constant. Here, deviations were made with respect to the initially established methodology; the original range for depth was of 0.075 to 0.175 mm, but upon noticing the forming tendency the authors decided to move said range to 0.050–0.150 mm in an attempt to see if surface roughness would decrease even further.

As presented in Fig. 10.3a, for the data obtained in a longitudinal direction relative to the feed route, for both technologies the lowest surface roughness corresponds to the lowest depth tested. For cross-directional data (Fig. 10.3b), however, MJP showed that for the smaller depth (0.05 mm) a certain surface roughness value (1.122 µm) was obtained; then, as depth was augmented, roughness decreased to a minimum and subsequently commenced a gradual increase which sustained for the rest of the tested depths. For the case of printing by FDM, it was not possible to observe a strictly increasing behaviour, albeit it was determined that the best surface finish occurred at the lowest depth, being consistent with longitudinal data.

For the testing of the Polytec 1000 base material, the combination of cutting parameters that generated the best surface roughness for each 3D printing technology tested was used. Table 10.1 shows the lowest roughness values obtained for MJP and FDM along with the base material's results obtained when machined with
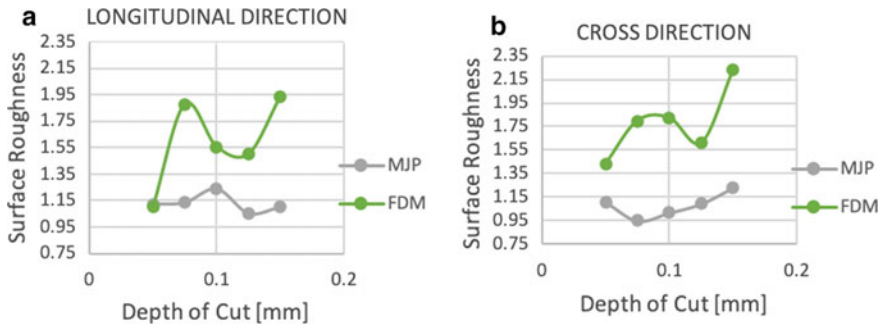
Fig. 10.3 Average roughness curve (Ra) versus Depth of cut for each 3D printing technology. **a** Longitudinal direction data. **b** Cross-direction data

Table 10.1 Average roughness (Ra) of materials under optimal cutting conditions

	Longitudinal direction (μm)	Cross-direction (μm)	Average (μm)
MJP	1.123	0.949	1.0362
POM under MJP cutting conditions	0.565	0.831	0.6980
FDM	1.099	1.432	1.2653
POM under FDM cutting conditions	1.792	1.416	1.6040

the respective optimal cutting conditions. An average is calculated among longitudinal and cross-direction in an attempt to obtain a more accurate representation of the workpiece's topology. It is possible to notice that MJP's average roughness is surpassed by FDM's, but the contrary is true for their correspondingly machined base material; POM under MJP cutting conditions' average roughness is lower than the case for FDM.

Using Eq. (1), a milling machinability index of 0.67 and 1.27 was obtained for MJP and FDM printing technology, respectively. According to what was established, this would translate into MJP workpieces having a higher roughness than the base material when machined under the same conditions, *i.e.* worse output with the same input, while FDM specimens presented a better response than the base material to the same cutting conditions.

It is important to notice that even after machining, MJP produced pieces maintained a lower surface roughness than FDM ones, however, the difference among these two was greatly reduced; initially FDM surface values could not be measured for they exceeded the instrument's range; therefore, the maximum was assumed which is 40 μm while MJP's was 2.005 μm; after milling, there was a relative variation of 18% among the two. FDM pieces had a greater improvement (38.7347) than MJP ones (0.9688), surpassing MJP's initial roughness when milled.
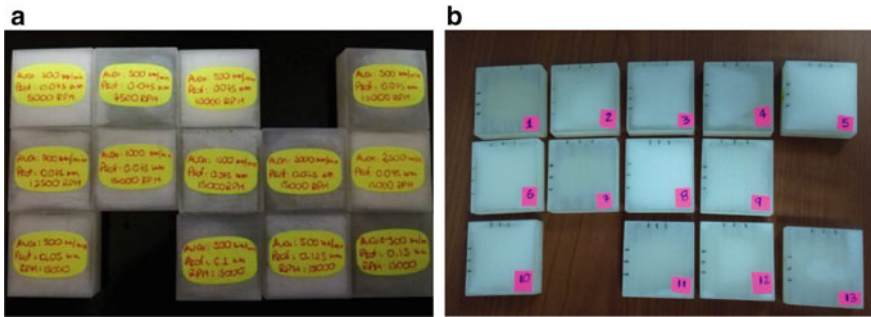
Fig. 10.4 MJP produced workpieces. **a** Before milling **b** After milling
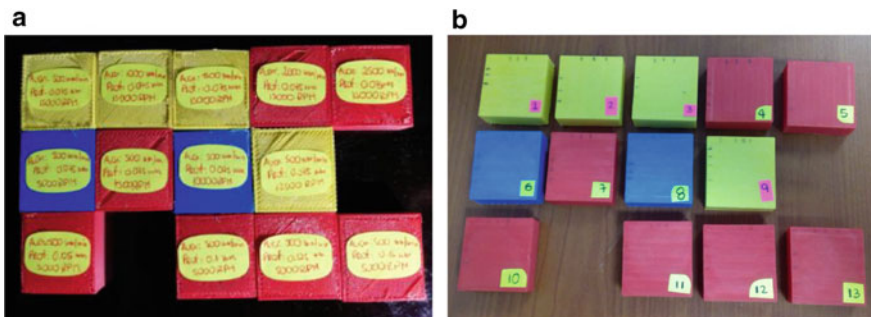
Fig. 10.5 FDM produced workpieces. **a** Before milling **b** After milling

Figure 10.4a and b shows the block-shaped workpieces prior and post-machining for MJP produced specimens, respectively. For every combination of parameters tested, a workpiece was marked accordingly. Visible changes were not perceived after performing the milling operations.

Figure 10.5a and b depicts the before and after machining workpieces produced by FDM printing technology. It is observable that the recently printed FDM workpieces had uneven surfaces, visible filaments clearly showing the printing direction, while after machining, the filament's orientation is less perceivable, and surfaces have an even finish.

10.4 Conclusions

In this exploratory study, it was possible to observe additive manufactured work-pieces' responses when subjected to milling, a traditional machining operation. The tests were conducted in ABS blocks which were manufactured via two different technologies: MultiJet Printing (MJP) and fused deposition modelling (FDM). Both

technologies showed compatibility with the milling process, since the workpiece's surface roughness was enhanced; however, FDM results yielded into bigger improvement, reducing over 38 μm in roughness, with the assumed initial roughness, given it exceeded the instrument's range. This was obtained by using a feed rate of 500 mm/min, 5000 rpm for spindle speed and a cutting depth of 0.05 mm; minimum feed rate, spindle speed and cutting depth tested. For MJP, the best surface roughness was obtain for a feed rate of 500 mm/min, a spindle speed of 15,000 rpm and a cutting depth of 0.075 mm; the variation achieved for this printing technology was of 0.9688 μm.

For the FDM, it is advised to measure roughness in more than one orientation given that the sensor-stylus radius is smaller than the plastic filament thickness, measuring in the same direction could result into the probe collecting skewed data, whereas a cross-sectional approach relative to the printing trajectory would ensure the probe's path not to be constrained by said pattern.

Among the considered cutting parameters, it was found that feed rate was the most influential one, consistently with previous studies conducted in metallic elements. This was concluded from the variability of the data; for spindle speed and depth of cut, the variation was relatively smaller than the response obtained for feed rate variations.

The milling machinability index obtained for MJP and FDM produced pieces was of 0.67 and 1.27, respectively. Recalling that the base material was assigned the unit as a reference value, this would indicate that MJP was less machinable than the POM, resulting in a higher surface roughness when exposed to the same cutting conditions. By contrast, FDM presented a better response than the base material, to the same parameters' arrangement.

The results would encourage an FDM workpiece to be machined if the implementation requires so, since the final FDM workpiece roughness even surpassed non-machined MJP pieces, this being 1.2653 μm and 2.005 μm, respectively. It would not be advisable to machine MJP workpieces for the improvement obtained is not considered relevant for the majority of applications. Functions such as mechanical couplings, assemblies, and elements subject to force transmission, according to material properties, would greatly benefit from the reduction of surface roughness using FDM technology.

As future work, the authors aim to obtain additional data in an attempt to develop equations that would describe a tendency so that behaviour of 3D printed polymers subjected to milling operations can be predicted. A more in-depth roughness analysis is also on the horizon for future works, incorporating surface roughness profiles and the workpieces integrity.

References

Benardos, P.G., Vosniakos, G.C.: Predicting surface roughness in machining: a review. Int. J. Mach. Tools Manuf **43**(8), 833–844 (2003)

Gaitonde, V.N., Karnik, S.R., Paulo Davim, J.: J. Mater. Processing Technol. **204** (1), 459 (2008)

Isaev, A., Vladimir, G., Petr, P., Mihail, K., Yuriy, I., Andrey, V.: Machining of thin-walled parts produced by additive manufacturing technologies. In: Procedia CIRP. vol. 41, pp. 1023–1026. (2016)

Jeremy, F., Bayley, C., Bhogal, S., Iribarne, M.: Comparing environmental impacts of additive manufacturing vs traditional machining via life-cycle assessment. Rapid Prototyping J. **21**(1):14–33 (2015)

Kalpakjian, S., Schmid, S.R., Vijay Sekar, K.S. In: Manufacturing Engineering and Technology, 7th Ed, p. 591, M. Cohen Pearson, Singapore (2014)

Konstantinos, S., D'Alvise, L., Schoinochoritis, B., Chantzis, D.: Additive manufacturing and post-processing simulation: laser cladding followed by high speed machining. In: International Journal of Advanced Manufacturing Technology (2015)

Kruth, J.P., B. Vandenbroucke, van, J. Vaerenbergh, P. Mercelis.: Benchmarking of different SLS/SLM processes as Rapid Manufacturing techniques (2005)

Levy, G., Kruth, J.P., Schindel, R.: Rapid manufacturing and rapid tooling with layer manufacturing (LM) technologies, state-of-the-art and future perspectives. ANNALS- CIRP. **52**, 589–610 (2003)

Mills, B.: Machinability of engineering materials. In: Springer Science & Business Media (2012)

Nourredine, B., Rodriguez, J., Asfour, S.: Development of an aggregate indicator to assess the machinability of steels. J. Mat. Processing Technol. **134** (2), 159–165 (2003)

Olivier, K., Mognol, P., Hascoët, J.-Y.: A new DFM approach to combine machining and additive manufacturing. In: Computers in Industry. vol. 62 (7), pp. 684–692 (2011)

Paulo Davim, J., Mata, F.: New machinability study of glass fibre reinforced plastics using polycrystalline diamond and cemented carbide (K15) tools. Mat. Des. **28**(3), 1050–1054 (2007)

Seker, U., Hasirci, H.: Evaluation of machinability of austempered ductile irons in terms of cutting forces and surface quality. J. Mater. Process. Technol. **173**(3), 260–268 (2006)

Sikdar, S.K.: Machinability of nickel based superalloys with carbide and ceramic tools in milling (2007)

Thiele, Eugene W.: Comparative Machinability of Brasses, Steels and Aluminum Alloys: CDA's Universal Machinability Index. Society of Automotive Engineers, Warrendale, PA (1990)

Chapter 11
Mechanical Characterization of 3D Printed Specimens

J. Galante, G. M. F. Ramalho, M. Q. dos Reis, R. J. C. Carbas, E. A. S. Marques, and L. F. M. da Silva

Abstract Additive manufacturing (AM), also known as 3D printing, has been showing significant growth in recent years. Due to the several advantages, these processes provide, such as high process speed, the possibility for non-conventional geometries and a large range of materials; AM is quickly becoming an industry standard for both prototyping and end-user products. There are several 3D printing technologies available in the market, the most prevalent being fused deposition modeling (FDM), also known by fused filament fabrication (FFF). FDM is widely used as it is highly versatile and has the lowest entry level cost of any AM technology. Due to the layer-by-layer nature of the production procedure, 3D printed materials tend to behave with highly anisotropic properties. The main aspect that governs the anisotropy in FDM is the printing orientation. In order to study these effects, as well as select the optimal materials for future work, bulk specimens were produced from three different materials: polylactic acid (PLA), polycarbonate (PC), and thermoplastic polyurethane (TPU). These specimens were then submitted to tensile testing. In this work, the printing orientations used to manufacture the tested materials were 0°, 45°, and 90° for 100% line infill, with the bulk specimens being produced flat on the printing bed. Steps were taken to prevent layer adhesion failure as well as optimize the production of flexible materials, in this case TPU. The results were then compared with the specifications given by the supplier for FDM and with the raw material properties found in the literature. As expected, for all the specimens, infill orientation played a major role on both tensile strength and elongation. With the results presented in this work, it was possible to select TPU and PC as the most interesting materials to combine, given their broadly different properties. As for future

J. Galante (✉) · G. M. F. Ramalho
Laboratório de Sistemas e Tecnologia Subaquática (LSTS), 4200-465 Porto, Portugal
e-mail: galante@lsts.pt

J. Galante · G. M. F. Ramalho · R. J. C. Carbas · L. F. M. da Silva
Departamento de Engenharia Mecânica, Faculdade de Engenharia, Universidade do Porto, 4200-465 Porto, Portugal

M. Q. dos Reis · R. J. C. Carbas · E. A. S. Marques · L. F. M. da Silva
Instituto de Ciência e Inovação em Engenharia Mecânica e Engenharia Industrial (INEGI), 4200-465 Porto, Portugal

work, a multi-material specimen will be produced, varying the percentage of each material as well as the placement and distribution on the testing bulk.

Keywords 3D printing · FDM · Mechanical properties of materials · Rapid prototyping · Anisotropy · PLA · TPU · PC

11.1 Introduction

As technologies evolve and reach higher levels of maturity, comes the time to revisit well established solutions. Either to gear them toward greater efficiency or to solve previous constraints accepted in the past, keeping up with current advancements is a challenge that both companies and researchers alike must strive to achieve (Dudek 2013). Compiling information and devising methods to test, validate, and ultimately entwine knowledge into functional technology is paramount in order to provide availability and efficient use of resources.

With the advent of additive manufacturing and the widespread availability of reliable machines, came a race toward its greater use in all areas. Even though mostly used in prototyping, 3D printing as it is often called, is becoming a robust and reliable form of production for small series of complex components and more importantly, a way to produce never before seen geometries with a myriad of different materials, shedding some of the limitations associated with conventional production technologies (Yao et al. 2019; Andreas 2011).

Additive manufacturing has gone from being used exclusively for prototyping or solving highly specialized problems, to being a plausible solution for most industries and applications (Andreas 2011; Lopes et al. 2018). One of the main technologies used in additive manufacturing is fused filament fabrication (FFF) or fused deposition modeling (FDM). This technology works by applying layers of melted thermoplastic one on top of the other in order to create the desired part, as it can be seen in Fig. 11.1.

One of the main benefits of this technology is the low entry cost of equipment and overall production prices. FDM printing has become a standard for office prototyping and development of complex parts (Ngo et al. 2018; Tamburrino et al. 2019). Although this technology allows for the creation of complex parts, with low design constraints, the major drawback is that the parts tend to be anisotropic and overall weaker than parts created by injection molding or traditional machining processes (Ngo et al. 2018). With additive manufacturing and FDM expanding into more sectors and widening the possible applications, especially when used in conjunction with other technologies, such as topology optimization or generative design, it is vital to further the understanding of these technologies and their limitations. To accomplish this, it is necessary to test a broad array of materials, with different properties, benefits, and limitations, in order to determine how they behave under different stress loads and how their mechanical characteristics vary, depending on the variables used during fabrication (Ćwikła et al. 2017).
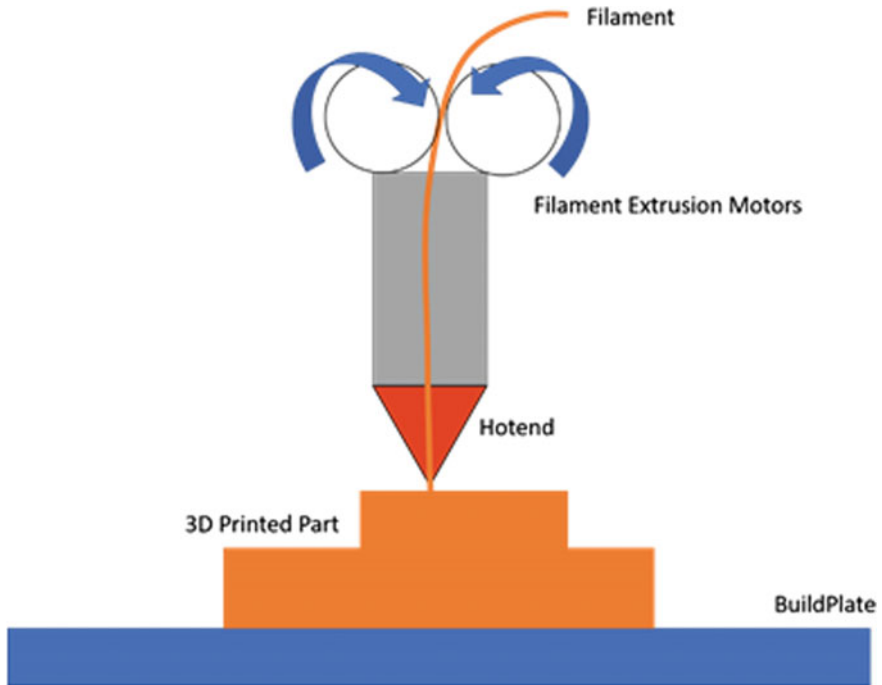
Fig. 11.1 Schematic representation of FDM printing

One of the first design parameters that need to be determined is how much infill should be used. One of the main objectives of the current work is to relate the infill configuration with the mechanical strength of additively manufactured parts. To understand what is considered infill material, first it is necessary to understand how a part is created on the computer. The program that generates the G-code, also known as a slicer, creates an outer shell that encompasses the overall shape of the part, then the same program generates the path the nozzle of the 3D print must travel, so it can fill all the area of the part, before moving on to the next layer. All the material that is placed inside this shell is called infill, and it can have many different configurations, occupy varied percentages of the available volume and be extruded with any orientation on the printing plane, as it can be seen in Fig. 11.2.

This parameter is important, as most of the volume for common geometries of 3D printed parts is composed of the infill. This has been further examined by Fernandez-Vicente et al. (2016) where it is possible to see that the most common printing patterns used only cause a 5% difference in maximum tensile strength when applied to lower infill densities, while the density of infill material played the largest role in tensile strength. In this work, it is possible to see that a 100% infill density is recommended for parts where the goal is to obtain the highest tensile strength; thus, the parts made for this study were done with 100% infill density. Other than the basic patterns, this study did not specify differences in infill orientation.
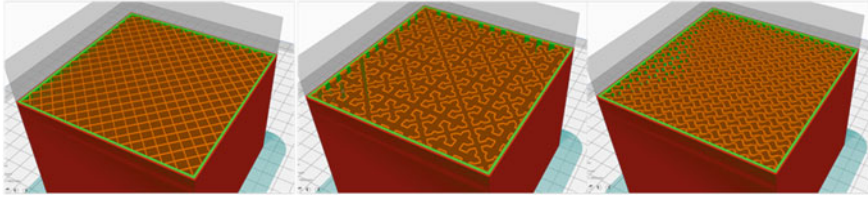
Fig. 11.2 Different possible Infill patterns and orientations, commonly used in 3D printing

This paper is divided into sections which correspond to the steps taken to determine the mechanical properties of the available materials, when 3D printed with FDM technologies. In the first section, the main aspects of 3D printing will be detailed, with a brief breakdown of the possible parameters that will be studied. Then, the actual materials chosen will be detailed, with their mechanical properties discussed, along with the experimental setup, basic parameters for the produced specimens and finally the equipment used in testing. In the last section, the test results will be shown and discussed followed by the presentation of the main conclusions and the steps that will be taken in future work.

11.2 Materials and Methods

11.2.1 Materials Tested

The materials chosen for this study were polylactic acid (PLA), thermoplastic polyurethane (TPU), and polycarbonate (PC). These three materials were selected based on their availability.

The rationale behind the choice of PLA, PC, and TPU for testing followed two main considerations: the first was the low cost and overall common use of these materials, since they are already applied in mainstream applications. The other consideration was if the material was possible to use in engineering applications that demanded high strength or flexibility that common FDM materials could not achieve. Thus, the chosen materials were PLA, PC, and TPU, where PLA fills the role of the control subject, since it is the easiest to print and the most common material available for entry level FDM printers. PC is one of the strongest thermoplastics available for FDM while also used for demanding applications such as bullet proof panels (Singh et al. 2017) and TPU, an extremely flexible and resistant material that could, arguably, be used as a substitute for rubber materials in certain applications (Seefried et al. 1975).

Among all the materials used, PLA has the lowest melting point, with a recommended printing temperature between 200 and 210 °C, while compared with polycarbonate printing temperature of around 270 °C, the highest of the tested materials. In regard to the overall tensile strength of each material, PC has the highest overall

Table 11.1 Mechanical properties and printing parameters for PLA, PC, and TPU (Ultimaker Support 2020)

	Ultimaker PLA	Ultimaker PC	Ultimaker TPU 95A
Young's modulus	2346.5 MPa	1904 MPa	26 MPa
Yielding stress	49.5 MPa	–	8.6 MPa
Tensile stress at break	65.3 MPa	75.5 Mpa	59 MPa
Elongation at yield	3.30%	–	55%
Elongation at break	5.20%	5.90%	580%
Printing temperature	200–210 °C	260–280 °C	220–235 °C
Build plate temperature	60 °C	110 °C	70 °C

bulk values with 54 MPa while PLA has less than 47 MPa and TPU ranges from 20 to 90 MPa.

Table 11.1 compares the main mechanical properties of each material used, and the values were taken from the datasheets given by the supplier, Ultimaker.

11.2.2 Printing Orientation

As stated previously, when producing a FDM 3D printed part there is a large number of parameters that can be altered and chosen by the user to better suit the needs of a specific component.

One of the main parameters is the orientation of the deposited materials in regard to the overall part geometry. Normally, there are three main directions that can be used: 0, 45, and 90°, measured in relation to the loading direction (Ahn et al. 2002). These orientations can be seen in Fig. 11.3.

The main difference between these orientations is the change of the mechanical properties of the part they induce, as every FDM 3D printed part can be considered as anisotropic (Ahn et al. 2002). This alteration of mechanical properties is caused mainly by the difference in cohesion between the directly extruded plastic and the ability of the material to melt previous layers and create a bond. When extruding material, a continuous bead of filament is deposited and thus has the highest strength under tension as it does not depend on the bonding between layers.

Finally, the heating and cooling of thermoplastic causes internal stress in the part and that can be reflected on the mechanical properties depending on the loading direction. This was further studied by Grasso et al. (Grasso et al. 2018) where it is possible to see that greater temperature differences of the material and the ambience,
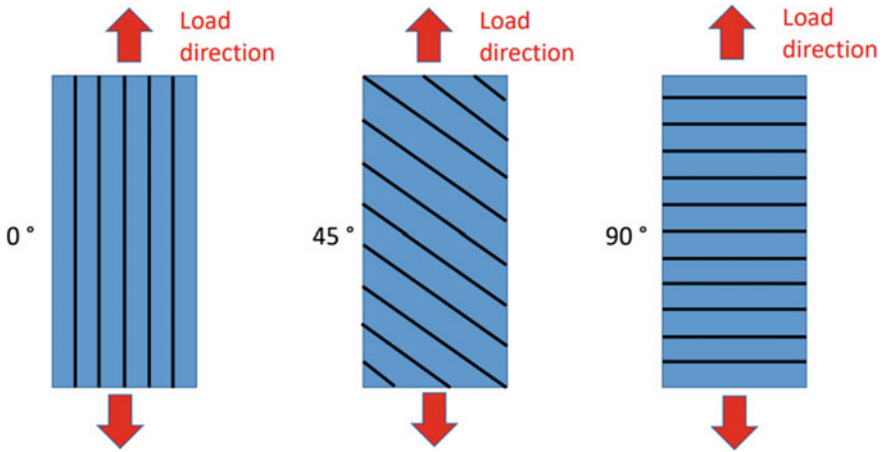
Fig. 11.3 Overall printing orientations, defined in regard to the loading direction

during and after the printing process, because internal stresses to occur and that it is necessary to precisely control these parameters to achieve functional parts. These characteristics can lead to defects in the parts and weak points, other than creating an overall anisotropic effect. One of the defects, weak layer adhesion, can be seen in Fig. 11.4 where adjacent layers did not fully bond with one another, leading to delamination of the part.
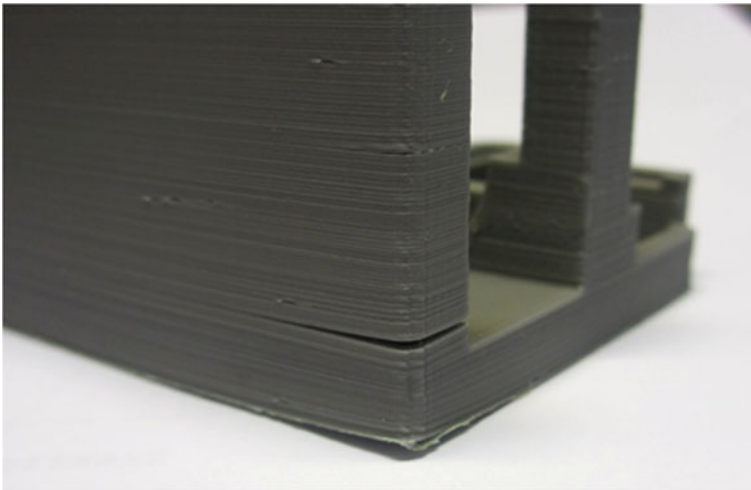
Fig. 11.4 Weak adhesion caused by temperature variation during the printing process
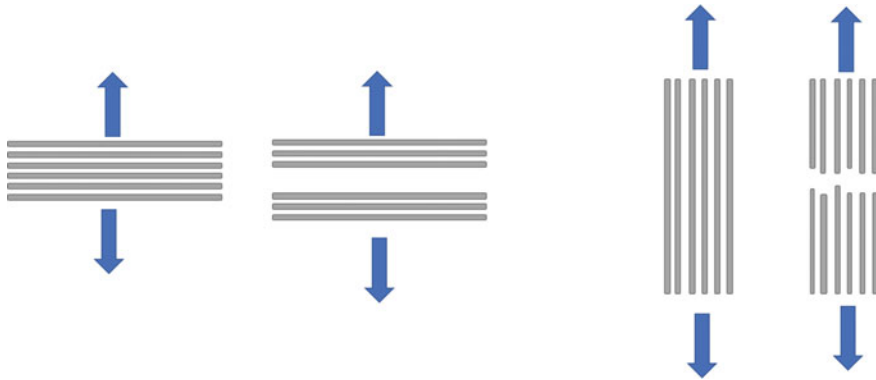
Fig. 11.5 Representation of the possible printing directions and the bonding issues caused by tensions in each directions

This failure to bond between layers has been studied further by Gao et al. (2020) where it is possible to see that, by further controlling the process, via implementation of more heat sources a more even temperature allows further melting of layers facilitating the molecular diffusion and entanglement that is crucial for a successful adhesion.

By altering the printing chamber temperature, it was possible to minimize the layer adhesion problem for the specimens tested in this paper.

Figure 11.5 shows a schematic representation of the layer lines, as well as the direction for the loading force, displays bonding layer failure, as it can occur not only on a horizontal surface but also vertically, as applying the load parallel to the layer lines should result on a failure by line rupture and a perpendicular load resulting in layer adhesion failure. Thus, the printing directions are important to denote and analyze, as it is not always possible to print in the optimal configuration, mostly due to the limitations of support material and available printing area placement.

These anisotropic properties are normally seen as a large disadvantage of the fabrication process but, by understanding the differences in mechanical properties, these parts can be printed in an orientation that allows for the strongest axis to be in the same direction as the load intended to be applied to the part.

11.2.3 Experimental Setup

The experiments were conducted with tensile specimens shaped according to BS 2782 standard, as seen in Fig. 11.6. This was chosen as it is the standard for testing polymers and thus allows for a direct comparison between previous results found in the literature of bulk materials and the test performed with 3D printed specimens (Yang et al. 2008; Sebe et al. 2000; Khalil and Ismail 2000).
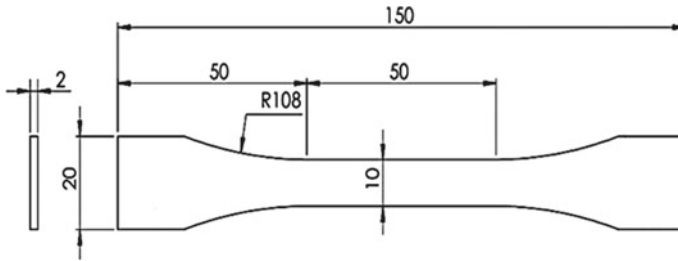
Fig. 11.6 Dimensions [mm] of the specimen used for the tensile strength test

Three specimens were produced for each orientation, per material, resulting in a total of 27 specimens tested. This allows for possible deviations on the results to be accounted for and permits a statistically relevance for the results. This also allows possible defects to be detected and the specimens redone, in order to eliminate outliers from the data and statistically determine if there is an infill direction more susceptible to causing defects. It is important to denote the difference between the appearance of defects and the susceptibility of a determined material or infill direction to the presence of these defects, as depending on the results it may be possible to determine that all parts can have defects but only few are susceptible, or affected by them.

As stated previously, the three configurations that were used correspond to 3D printed specimens with 0, 45, and 90° angles of infill and the minimum allowed shell thickness of 0.4 mm. As the shell is a continuous extrusion and is always extruded in the direction of the tensile test, minimal shell thickness was used as a way to minimize the effect of the continuous material. In Fig. 11.7, it is possible to observe how the infill orientation is simulated in the slicer and the test specimens that were created.

The chosen printing parameters were 100% infill as the only influence in the part properties should come from the direction of the infill and not the quantity of material used. The other configuration that was chosen was printing temperature, where the
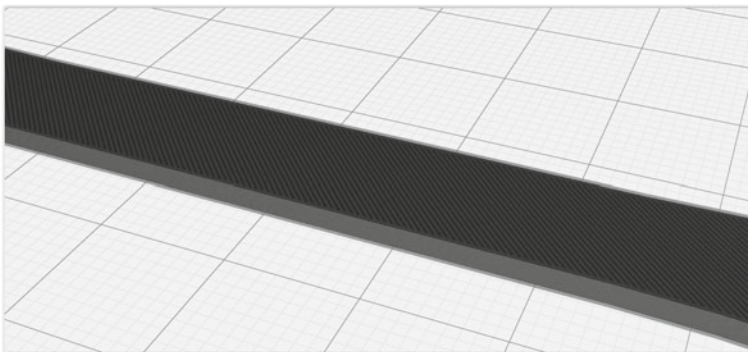
Fig. 11.7 Representation of slicing at 45° of printing direction

hottest temperature possible that did not alter the print quality for each material was chosen, as this would allow for the most optimal conditions for the layers of each model to fuse and reduce the possibility of layer separation. Finally, the rest of the settings were chosen based on the recommended parameters from the printer and material supplier, where these standard parameters were chosen in order to reduce customization and allow a broader use. The chosen test was a quasi-static tensile strength test where the specimen was stretched until rupture at a constant rate.

11.2.4   Equipment Used

To create the 3D printed parts, the chosen equipment was the Ultimaker 3 extended as it is considered to be as a consumer level and industry standard equipment, that is versatile and economical.

This 3D printer utilizes FDM technology and has an overall X/Y resolution of 0.320 mm while its Z-axis resolution is 0.020 mm. The minimum wall thickness that is possible to produce with the available configuration of the printer is 0.4 mm and with an overall build volume of $215 \times 215 \times 300$ [mm]. This 3D printer also possesses the capability for dual material printing, which can allow for further studies in bonding of different types of materials, layer adhesion between them and other different possible configurations. In Fig. 11.8, it is possible to see the Ultimaker 3D printer with a protective case that reduces the temperature gradient in the printing chamber which in turn allows for better quality control and cohesion between the produced parts (Ultimaker S3 2020).

The mechanical properties were determined using a Instron 3367 universal testing machine (Fig. 11.9) under a rate of 1 mm/min. The machine is equipped with a load cell of 30 kN. The displacement was measured with a video device. Three specimens were tested to failure for each condition, at room temperature (23 °C) and 55% relative humidity. In Fig. 11.10, it is possible to see the specimens being tested.

11.3   Experimental Results

The following plotted results show the average of the three tests of each printing direction where any premature failure was distracted and tested again.

11.3.1   PLA

Out of all the materials that were tested, PLA was the stiffest and failure presented little deformation. Due to poor bonding between layers, Fig. 11.11 shows that the

Fig. 11.8 Ultimaker 3D printer used on the fabrication of the specimens
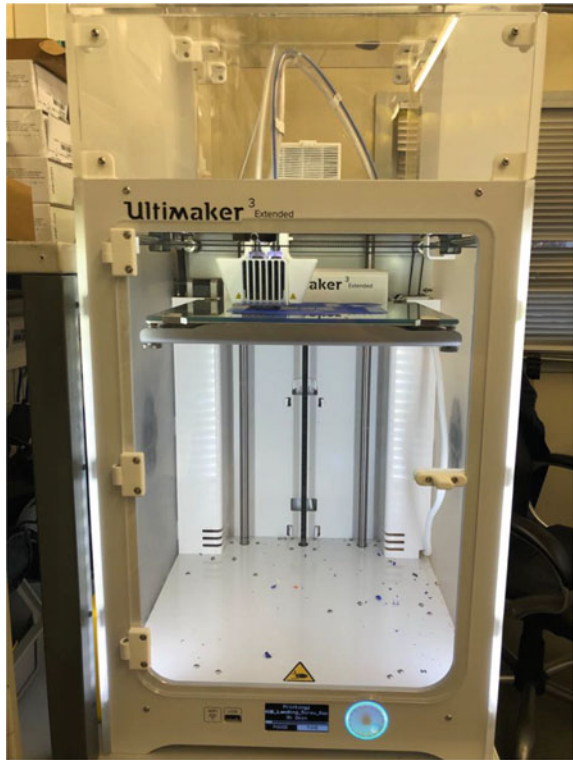
specimens that were printed at 90° presented the lowest tensile strength having a value at least 50% lower than the other printing directions under study.

Table 11.2 shows the experimentally obtained mechanical properties of the PLA polymer as a function of orientation. The lowest strength was achieved with a 90° orientation.

In Fig. 11.12, it is possible to see that the failure in the specimen is along the printing direction and it occurs directly between one segment and the one adjacent to it. It is also possible to denote that due to the existence of a necessary shell, there is a slight deformation on the edges where the printing direction changes from 90 to 0°.

11.3.2 PC

Polycarbonate was the material with the highest tensile strength out of all materials under study, with a maximum value of 72 MPa on the 0° axis. Compared to other materials, it had the highest layer adhesion with the 90° configuration, having almost as much tensile strength as the other configurations. This shows that PC is the least

Fig. 11.9 Instron 3367 universal testing and camera testing apparatus
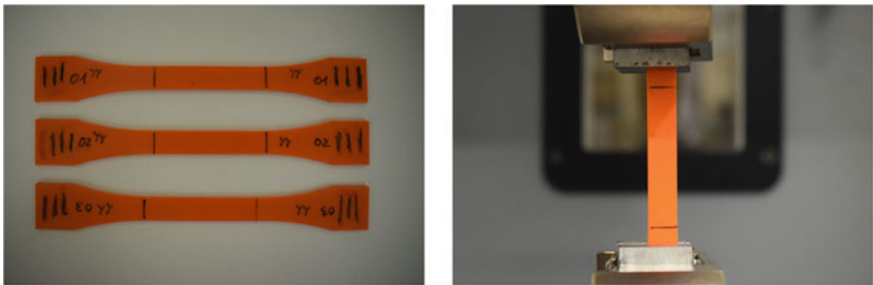
Fig. 11.10 Specimens tested per material and print direction, along with the test setup

anisotropic of all materials being tested, and this is mostly due to the high overall deposition temperatures that strongly bond the layers together.

Table 11.3 shows the experimentally obtained mechanical properties of the PC polymer as a function of orientation. It can be seen independently of printing orientation that the strength properties are similar.

In Fig. 11.14, it is possible to see that there was a large plastic deformation of the test specimens for PC in the 0° direction. This occurred in all three tests and can be also observed in Fig. 11.13, where this plastic deformation is seen before the
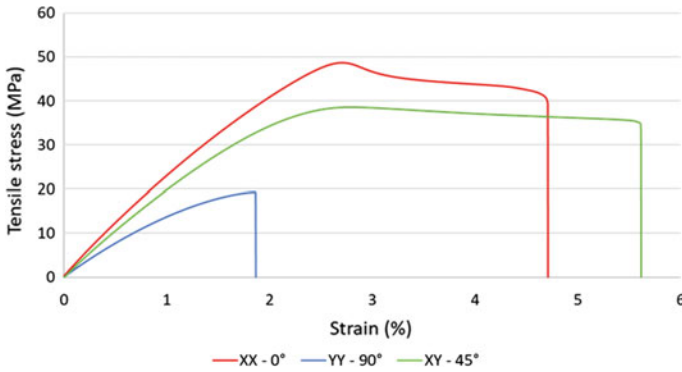
Fig. 11.11 Representative PLA stress–strain curves for the three different printing directions

Table 11.2 Tensile properties of PLA

	Tensile strength (MPa)	Elongation (%)	Young's modulus (MPa)
PLA 0°	49 ± 0.8	4.8 ± 0.6	1920 ± 38.7
PLA 45°	37 ± 0.7	5.7 ± 0.8	1727 ± 43.0
PLA 90°	18,4 ± 1.1	1.8 ± 0.7	1022 ± 32.2
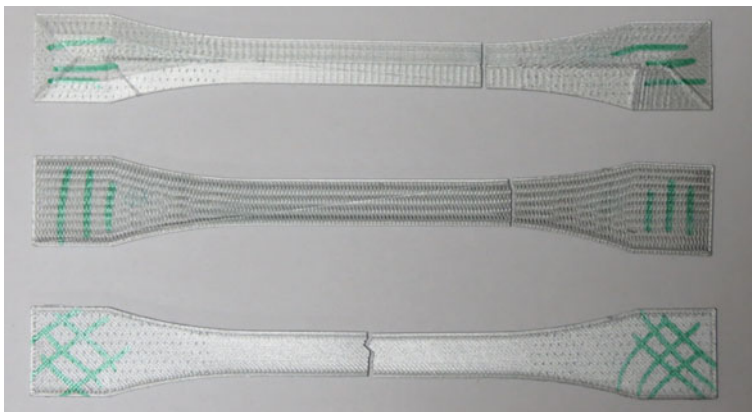
Fig. 11.12 Close up figure of failed specimens, evidencing reduced plastic deformation of the part

Table 11.3 Tensile properties of PC

	Tensile strength (MPa)	Elongation (%)	Young's modulus (MPa)
PC 0°	72 ± 1.9	9.0 ± 0.3	1665 ± 72.6
PC 45°	66 ± 0.3	10.5 ± 0.8	1650 ± 23.1
PC 90°	65.5 ± 1.1	8.2 ± 0.4	1634 ± 67.2
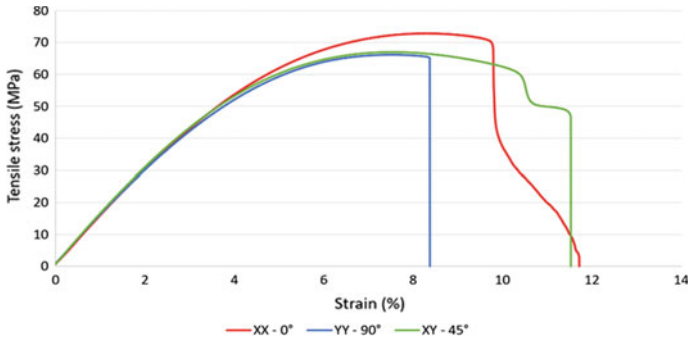
Fig. 11.13 Representative PC stress–strain curves for the three different printing directions
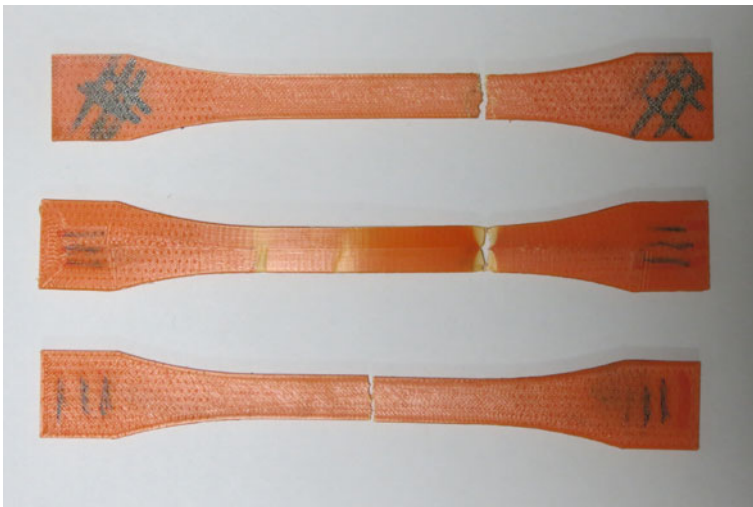
Fig. 11.14 Close up figure of three PC specimens with some plastic deformation

failure (red curve) and is caused normally by the rupture of part of the filaments while debonding of the horizontal layers does not allow for total rupture of the specimen.

11.3.3 TPU

Out of the tested materials, TPU presented the largest elongation with a deformation over 100% before failure when compared to the other materials. Although it presented this large deformation, it also had the lowest levels of adhesion between the layers, causing it to be highly anisotropic.

Table 11.4 Tensile properties of TPU

	Tensile strength (MPa)	Elongation (%)	Young's modulus (MPa)
TPU 0°	34 ± 0.5	710 ± 25	23 ± 1.1
TPU 45°	42.5 ± 1.1	490 ± 10	26 ± 1.3
TPU 90°	13 ± 0.2	180 ± 20	27 ± 0.9
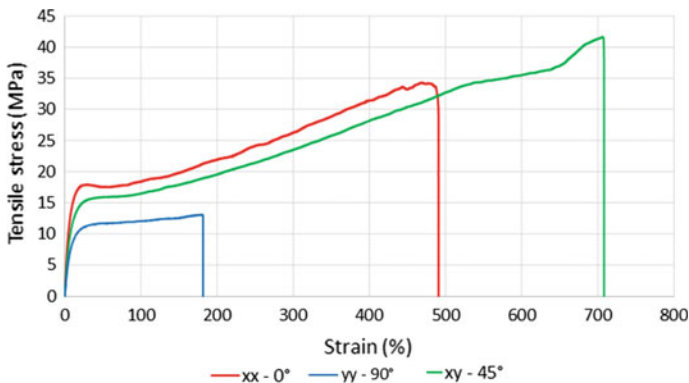
Fig. 11.15 Representative TPU stress–strain curves for the three different printing directions

Table 11.4 shows the experimentally obtained mechanical properties of the TPU polymer as a function of orientation.

In Fig. 11.15, it is possible to see the difference between each printing direction and the extreme elongation that the material suffered before rupture. It is important to denote that although this material has a large strain at failure compared to the other materials, it possesses a reduced amount of plastic deformation. It is possible to see that there is no major plastic deformation on the TPU specimens, as a clear brittle fracture line is shown in Fig. 11.16.

11.3.4 Comparison with Commercially Available Bulk Materials

Other than the overall material differences, it is important to compare these materials with their extruded bulk counterparts (non-3D printed) that serve as industry standards to understand how properties differ and how the material properties can be locally controlled in a 3D printing process. In Fig. 11.17, it is possible to see that PLA suffered the highest reduction in tensile strength compared to the bulk specimens, while PC had all print directions near the bulk specimen value. It is important to note that given the margin of error for PC, orientations other than the 90° specimen all could be comparable to the bulk values. It is also possible to observe

Fig. 11.16 Close up figure of the TPU specimens with very different deformation for each orientation, from top to bottom 0°, 45°, and 90°
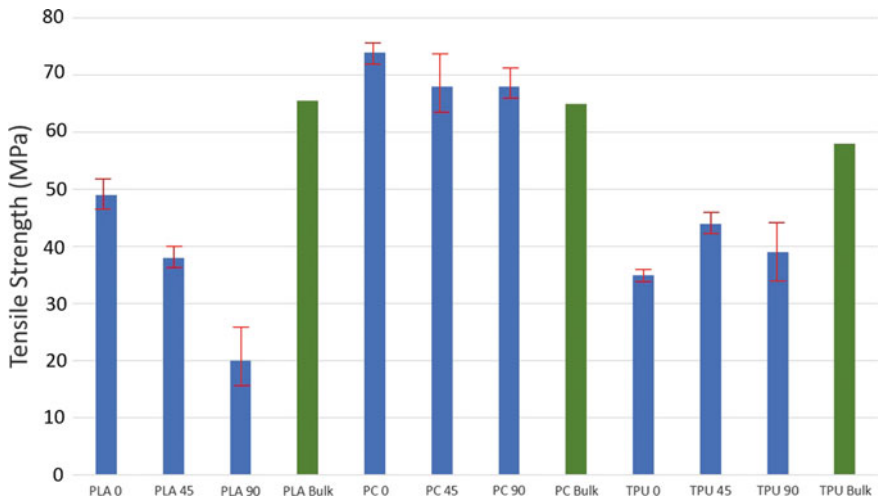
Fig. 11.17 Tensile strength of the test specimens and the bulk test subjects

that PLA oriented at 90° has the lowest tensile strength. This is because it has the lowest temperature for printing and requires the lowest enclosure temperature, thus not allowing layers to bond properly.

11.4   Conclusions

As expected, FDM 3D printing presents very high anisotropy for most materials. This behavior is more prevalent on the moving axis but also very detrimental for any orientation perpendicular to the loading axis. By testing bulk specimens on three

different materials, this behavior became apparent and the layer adhesion problem was mainly displayed on the 90° orientation. In contrast, by orienting the layer lines with the loading force axis, both PLA and PC exhibited the highest tensile strength. Only TPU presented different results, with its highest tensile strength being in the specimens made with 45° between layer lines. As for strain, TPU has been able to expand more than seven times its initial length for the 45° results. Compared to the PLA and PC that only reached 5 and 10% in strain at failure, respectively, TPU is a very flexible material and as such was expected to behave differently. Given these results, TPU is an interesting material for many applications where high toughness and flexibility are desired, that should unlock a novel range of applications for 3D printed parts, especially when combined with other materials.

The results also show that these 3D printed materials are weaker than their extruded, commercial counterparts. When the results are compared to the datasheets provided by suppliers, all materials displayed lower values for tensile strength and Young's modulus. This is to be expected, as a consequence of the nature of the FDM process. Another problem present in this work was the reliability of the produced parts, as some presented premature failure due to the production defects. Additional specimens had to be tested for each material, in order to definitively eliminate this problem from the results. By further optimizing the temperature and production lead time, it is possible to diminish the number of bulks with defects.

11.5 Future Work

As for future work, it is suggested that more materials should be tested. Other materials are available for 3D printing specimens suitable for testing, such as Nylon, ABS, and PTEG. Combining different materials to improve tensile strength or achieve differential strain values on a single part will prove fundamental to achieve better performance, lighter structures and more reliable parts on future projects.

From the results presented in this paper, the next step will be to produce a specimen made of PC entwined with TPU. By combining these two different materials, functionally graded specimens will be developed, further testing the applications of AM technologies.

References

Ahn, S.H., Montero, M., Odell, D., Roundy, S., Wright, P. K.: Anisotropic material properties of fused deposition modeling ABS. Rapid Prototyping J. (2002)

Andreas, G.: Understanding Additive Manufacturing—Rapid Prototyping. Rapid Tooling, Rapid Manufacturing (2011)

Ćwikła, G., Grabowik, C., Kalinowski, K., Paprocka, I., Ociepka, P.: The influence of printing parameters on selected mechanical properties of FDM/FFF 3D-printed parts. In IOP Conf. Ser. Mater. Sci. Eng **227**(1) (2017)

Dudek, P.F.D.M.: FDM 3D printing technology in manufacturing composite elements. Arch. Metall. Mater. **58**(4), 1415–1418 (2013)

Fernandez-Vicente, M., Calle, W., Ferrandiz, S., & Conejero, A.: Effect of infill parameters on tensile mechanical behavior in desktop 3D printing. 3D Printing Addit. Manuf. **3**(3), 183–192 (2016)

Gao, X., Qi, S., Kuang, X., Su, Y., Li, J., Wang, D.: Fused filament fabrication of polymer materials: A review of interlayer bond. Addit Manuf. 101658 (2020)

Grasso, M., Azzouz, L., Ruiz-Hincapie, P., Zarrelli, M., Ren, G.: Effect of temperature on the mechanical properties of 3D-printed PLA tensile specimens. Rapid Prototyping J. (2018)

Khalil, H.A., Ismail, H.: Effect of acetylation and coupling agent treatments upon biological degradation of plant fibre reinforced polyester composites. Polym. Testing **20**(1), 65–75 (2000)

Lopes, L.R., Silva, A.F., Carneiro, O.S.: Addit. Manuf **23**, 45 (2018)

Ngo, T.D., Kashani, A., Imbalzano, G., Nguyen, K.T., Hui, D.: Additive manufacturing (3D printing): A review of materials, methods, applications and challenges. Compos. B Eng. **143**, 172–196 (2018)

Sebe, G., Cetin, N.S., Hill, C.A., Hughes, M.: RTM hemp fibre-reinforced polyester composites. Appl. Compos. Mater. **7**(5–6), 341–349 (2000)

Seefried, Jr., C.G., Koleske, J.V., Critchfield, F.E.: Thermoplastic urethane elastomers. I. Effects of soft-segment variations. J. Appl. Polym. Sci. **19**(9), 2493–2502 (1975)

Singh, K.J., Ahuja, I.S., Kapoor, J.: Chemical assisted ultrasonic machining of polycarbonate glass and optimization of process parameters by Taguchi and grey relational analysis. Adva. Mater. Process. Technol. **3**(4), 563–585 (2017)

Tamburrino, F., Graziosi, S., Bordegoni, M.: Virtual Phys Prototype **14**, 316 (2019)

Ultimaker S3: https://ultimaker.com/3d-printers/ultimaker-s3, Website accessed 16 Oct 1010 (2020)

Ultimaker Support—Material: https://support.ultimaker.com/hc/en-us/categories/360002336619-Materials, Website accessed 16 Oct 1010 (2020)

Yang, S.L., Wu, Z.H., Yang, W., Yang, M.B.: Thermal and mechanical properties of chemical crosslinked polylactide (PLA). Polym. Testing **27**(8), 957–963 (2008)

Yao, T., Deng, Z., Zhang, K., Li, S.: A method to predict the ultimate tensile strength of 3D printing polylactic acid (PLA) materials with different printing orientations. Compos. B Eng. **163**, 393–402 (2019)

Part IV
Tribology

Chapter 12
Microstructure and High-Temperature Oxidation Behavior of ZrB$_2$–ZrO$_2$–MoSi$_2$–Al Coatings for the Protection of Carbon/Carbon Composites

V. Y. Novikov, M. G. Kovaleva, I. Y. Goncharov, M. N. Yapryntsev, Y. N. Tyurin, V. V. Sirota, O. N. Vagina, I. N. Pavlenko, and O. V. Kolisnichenko

Abstract The ZrB$_2$–ZrO$_2$–MoSi$_2$–Al composite coatings were prepared on the carbon/carbon composite using a new multi-chamber detonation accelerator by thermal spraying methods from micropowders. The initial powders ZrB$_2$-xMoSi$_2$ (x = 24, 35, 45 wt%) with 5wt% Y$_2$O$_3$ and 20wt% Al. Y$_2$O$_3$ were successfully used as a stabilizer of the high-temperature tetragonal and cubic modification of zirconia. Aluminum was added as an oxidizing agent during spraying and creating "plastic" lamellae and nano-dispersed inclusions and relieves internal stresses. In the present work, the microstructure, elemental and phase composition of coating were investigated by scanning electron microscopy (SEM) and X-ray diffraction (XRD) before and after annealing at 1500 °C in air for 1 h. Described coatings are characterized by the lower than 1% porosity and good adhesion to the substrate. The uniform and dense lamellar-like microstructure of the ZrB$_2$–ZrO$_2$–MoSi$_2$–Al coatings contributed to its good oxidation-resistant at high temperatures. As-sprayed coating consisted of the t–ZrO$_2$, h–ZrB$_2$, m–ZrO$_2$, t–MoSi$_2$ and fcc–Al. A significant content of aluminum in the initial powder mixtures during high-temperature oxidation leads to formation of a new phase—mullite (3Al$_2$O$_3$ · 2SiO$_2$). The ZrO$_2$ spherical particles in 3Al$_2$O$_3$ · 2SiO$_2$ matrix were formed at 1500 °C. Evolution of the microstructure of a mullite formed during high-temperature annealing in air, depending on the content of molybdenum silicide in the initial powders, was clearly described and discussed in the current work.

V. Y. Novikov (✉) · M. G. Kovaleva · I. Y. Goncharov · M. N. Yapryntsev · O. N. Vagina · I. N. Pavlenko
Belgorod State National Research University, Belgorod 308015, Russia
e-mail: novikov_v@bsu.edu.ru

Y. N. Tyurin · O. V. Kolisnichenko
E.O, Paton Electric Welding Institute NASU, Kyiv 03650, Ukraine

V. V. Sirota
Belgorod State Technological University named after V.G. Shoukhov, Belgorod 308015, Russia

12.1 Introduction

Carbon/carbon (C/C) composites have many advantages over traditional materials (low density, high specific strength and retention of mechanical properties at high temperatures) (Devi and Rao 1993). However, application of C/C during prolonged exposure to high temperature is limited by the internal reactivity of carbon with oxygen above 500 °C (Jacobson and Curry 2006; Lu et al. 2016; Niu et al. 2017). One of most widely used methods for improving carbon–carbon composites oxidation resistance is to apply such coatings as MoSi$_2$, ZrSiO$_4$, SiO$_2$–SiC, ZrB$_2$–SiC (Zhi-Qiao et al. 2007; Hui-Chao et al. 2005; Li et al. 2014; Zhang et al. 2011). In this study, a ZrB$_2$–MoSi$_2$–Al coating was chosen as the oxidation protective coating for C/C composites, and a new multi-chamber detonation accelerator (MCDS) was used to form this coating. Zirconium diboride (ZrB$_2$) is an attractive thermal protection material for carbon/carbon (C/C) composites due to its high melting temperatures, good thermal conductivities and outstanding thermochemical properties. Including silicide into ZrB$_2$ can significantly promote the oxidation protection ability of ZrB$_2$ coating because of a stable compound silicate glass layer formation (Li et al. 2019).

High-temperature oxidation leads to the formation of a new phase mullite (3Al$_2$O$_3$ · 2SiO$_2$). Mullite is most commonly found in two crystalline forms—acicular and prismatic. The acicular mullite reinforces the glass phase, resulting in increased refractoriness compared to a material containing prismatic mullite. The formation of mullite depends on temperature and the presence of additives and impurities. Mullite is formed in a prismatic form when heated to relatively low temperatures, since it is more stable. Acicular mullite formed during heating to high temperatures (>1300 °C). The difficulty of sintering mullite in a single annealing is explained by the one-sided diffusion of SiO$_2$ into the Al$_2$O$_3$ grain; a pore forms in place of the SiO$_2$ grain. A strong crystalline mullite framework is formed on the basis of Al$_2$O$_3$ grains, which, in the absence of a sufficient amount of the liquid phase, prevents sintering and pore closure (Lee 2004).

12.2 Experimental

The composition of powder 80 (71/60/50ZrB$_2$—24/35/45MoSi$_2$—5Y$_2$O$_3$)—20 Al, all in wt% (Fig. 12.1a) with particle size in range of 1–25 µm was used to deposit a dense layer on the carbon/carbon composites. Flat specimens (10 × 10 × 5 mm) of 3D C/C composites (density of 1.9 g/cm^3) were used as substrates. The composite powder was prepared by solid-state mixing route. Y$_2$O$_3$ was successfully used as a stabilizer of high-temperature tetragonal and cubic modification of zirconia (Liu
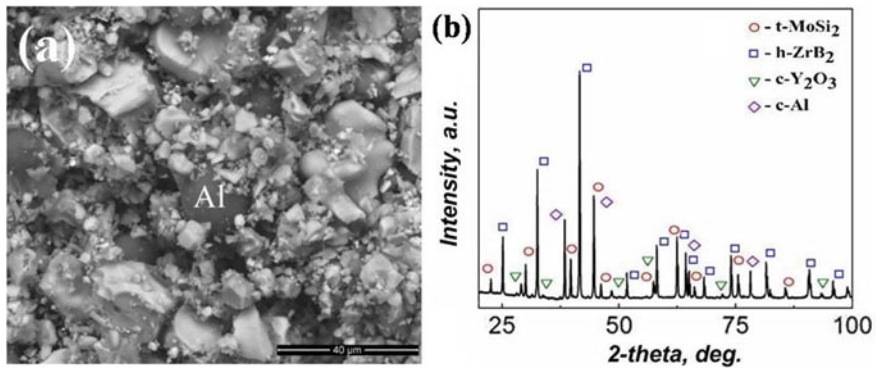
Fig. 12.1 SEM-BSE micrograph (**a**) and XRD diffraction pattern (**b**) of the composite powder ZrB$_2$–MoSi$_2$–Al

et al. 2018). Aluminum was added as a bond for the oxidizing agent during of the spraying and creating "plastic" lamellae and nano-dispersed inclusions, which will relieve internal stresses (Li and Ohmori 2002; Kovaleva et al. 2019).

In the present study, a new multi-chamber detonation accelerator (MCDS) (Kovaleva et al. 2019, 2013; Vasilik et al. 2012) was employed to deposit the ZrB$_2$–ZrO$_2$–MoSi$_2$–Al coating. The coating was deposited with a frequency of 20 Hz. The movement speed was 1500 mm/min; the distance from the exit section of the barrel to the treated plate was 80 mm. A barrel with a throat diameter of 16 mm and length of 500 mm was adopted. The flow rate of the fuel mixture components (m^3/h) was oxygen (4.0*/3.6**), propane + butane (0.75*/0.68**) and air (0.12*/0.12**) (*cylindrical form combustion chamber, **combustion chamber in the form of a disk). The powder feed rate was 850 g/h. The powder and cross-sectional surface of the samples were investigated using a scanning electron microscope (SEM) (Quanta 600 FEG). Porosity was determined by metallographic method using an Olympus GX51 microscope. The phase composition was determined by diffractometer Rigaku Ultima. High-temperature oxidation of experimental samples was carried out using an electric muffle furnace Nabertherm GmbH LHT 04/17. The samples were placed in an oven and heated at a rate of 5 °C/min from 23 to 1500 °C. The samples were slowly cooled from 1500 to 50 °C at 5 °C/min for 5 h in an oven and then cooled to room temperature outside the oven.

12.3   Results and Discussion

The results of the study of the microstructure and elemental composition of the composite coatings are shown in Fig. 12.2 and in Table 12.1. Figure 12.2 shows SEM images of the microstructure of a cross section of samples with composite coatings.

Zr24MoY/20Al

Zr35MoY/20Al
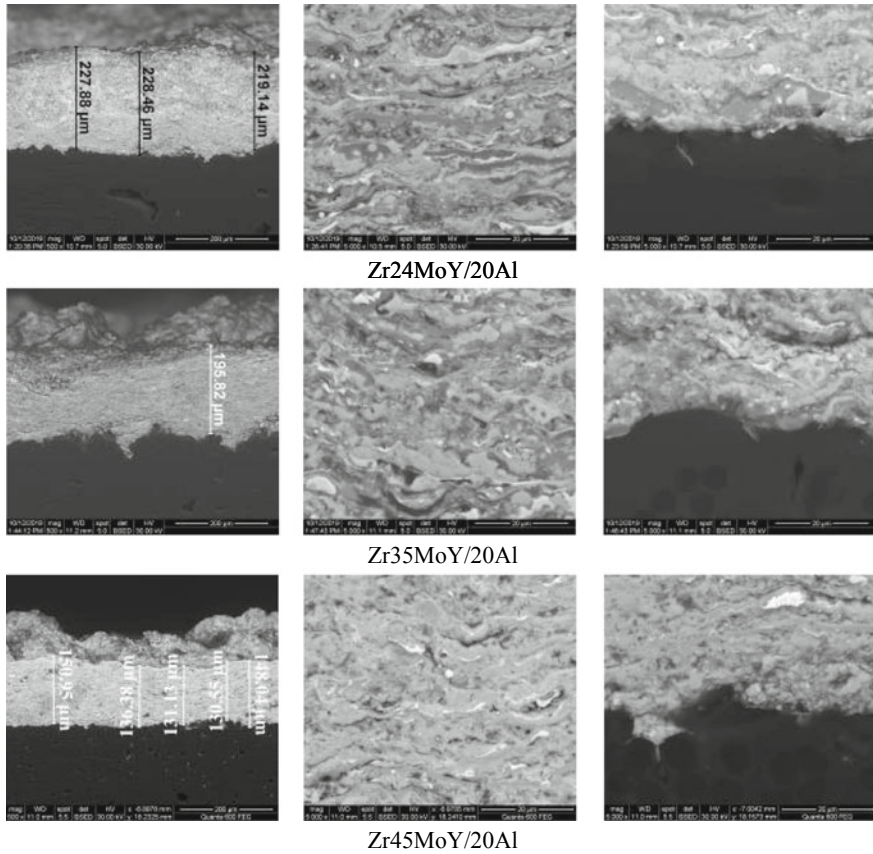
Zr45MoY/20Al

Fig. 12.2 Microstructure of the cross section of the specimens with a composite coatings

Table 12.1 Elemental composition of composite coatings

Coating	Elemental composition, wt%					
	O	Zr	Mo	Al	Si	Y
Zr24MoY/20Al	14.97	43.70	12.88	16.07	6.68	5.69
Zr35MoY/20Al	14.54	32.45	19.51	17.75	10.25	5.50
Zr45MoY/20Al	15.13	29.27	24.94	17.92	8.84	3.90

It was found that the porosity of the obtained composite coatings was 0.02–1.00% and correlates with the technological requirements for industrial coatings (porosity ~2 to 7%).

Investigation of the microstructure of the cross section of samples with composite coatings showed that uniform dense coatings with good adhesion to the substrate were obtained, the bulk of the coating material was deformed and densely packed,

Table 12.2 Phase composition of composite coatings

Coating	Phase	Space group
Zr24MoY/20Al	$t–ZrO_2$	137:P42/nmc
Zr35MoY/20Al	$h–ZrB_2$	191:P6/mmm
	$c–Al$	225:Fm-3 m
Zr45MoY/20Al	$m–ZrO_2$	14:P121/c1
	$t–MoSi_2$	139:I4/mmm

but the presence of unmelted zirconium particles was observed in the coatings. Zirconium has a low thermal conductivity, which complicates the uniform heating of dispersed particles and their deformation during the formation of the coating. Apparently, during the deposition of coatings, the middle of the coarse fractions (>15 μm) of the powder did not heat up and practically did not deform upon impact on the substrate. High rates of deformation of dispersed particles cause their fragmentation into smaller fragments and the formation of particles with sizes from 50 to 1000 nm. Thus, the fine fractions of the powder were heated, deformed to the state of thin lamellas, filled the space between the coarse particles and formed a dense coating.

It can be concluded that there are no defects based on the results of studying the morphology of the boundary between the coating and the substrate. It can be seen that in the contact zone of the coatings with the substrate, a mixed structure is observed, consisting of coating islands in the substrate of a very different shape and size. Some of the powder material has penetrated deeply and is firmly bonded to the substrate material.

X-ray diffraction results of composite coatings are shown in Table 12.2. The phase analysis of composite coatings showed that the coatings consist of tetragonal and monoclinic ZrO_2, hexagonal ZrB_2, fcc-Al and tetragonal $MoSi_2$ (Table 12.2).

The microstructure and surface morphology of ZrB_2–$MoSi_2$–Al composite coatings after high-temperature oxidation are shown in Fig. 12.3.

The sputtering process is carried out in air, and the powder material reacts with oxygen to form new phases, including ZrO_2, which is the product of the reaction of ZrB_2 particles with oxygen during the deposition process (Lu et al. 2016; Niu et al. 2017). The MoO_3 and B_2O_3 phases were not found.

The reactions can be described as follows (Lu et al. 2016; Niu et al. 2017):

$$2ZrB_2(s) + 5O_2(g) \rightarrow 2ZrO_2(s) + 2B_2O_3(g) \tag{12.1}$$

$$2MoSi_2(s) + 7O_2(g) \rightarrow 2MoO_3(g) \rightarrow 4SiO_2(l) \tag{12.2}$$
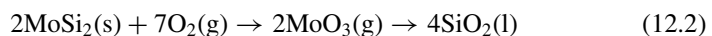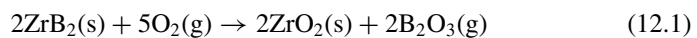
It was found that the addition of aluminum to the initial powder mixture during high-temperature oxidation of the coating formed from it leads to the formation of a new phase—mullite ($3Al_2O_3 \cdot 2SiO_2$) in the form of the finest intertwined needle-shaped crystals that penetrate (reinforce) the glass phase (Fig. 12.4).

The structure of Zr24MoY/20Al composite coatings after oxidation is dense, without cracks, and has a low porosity (less than 1.0%) (Fig. 12.3). This is mainly

Zr24MoY/20Al   Zr35MoY/20Al   Zr45MoY/20Al
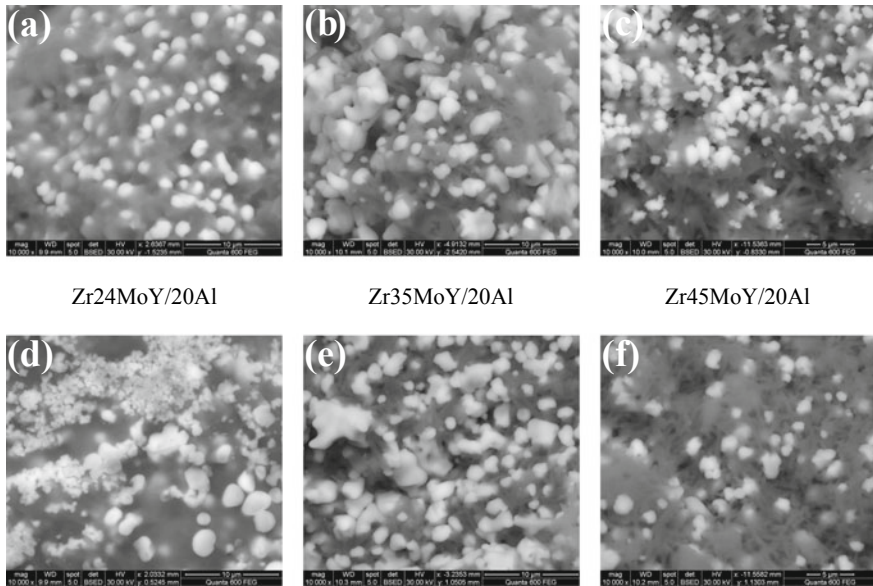
Fig. 12.3 Microstructure and morphology of composite coatings ZrB_2–$MoSi_2$–Al after high-temperature oxidation: surface of coatings (**a**, **b**, **c**), cross section (**d**, **e**, **f**)

caused by the melting of SiO_2 at 1500 °C, which filled the interlayer pores. It was found that the white phase (globular grains) consists of ZrO_2 (Figs. 12.4 and 12.5b), the light gray phase is mullite ($3Al_2O_3 \cdot 2SiO_2$), amorphous SiO_2 and Al_2O_3 with a hexagonal crystal lattice (Figs. 12.4 and 12.5c). ZrO_2 (white phase in Figs. 12.3 and 12.5) is randomly distributed in a glassy matrix. Glassy SiO_2 has a low oxygen diffusion coefficient at 1473 K and can reduce the rate of oxygen penetration through the coating (Opeka et al. 1999; Guo 1995).

The phase analysis of Zr45MoY/20Al composite coatings showed that the coatings consist of tetragonal, cubic (stabilized by yttrium) and monoclinic ZrO_2, orthorhombic mullite ($3Al_2O_3 \cdot 2SiO_2$) (Table 12.3). The XRD results show that with an increase in the $MoSi_2$ content in the initial powder, an increase in the content of mullite and formation of an acicular structure are observed in the investigated coatings after annealing. The Al_2O_3 content decreases to a value below the sensitivity threshold of this method. It can be explained by the fact that Al_2O_3 interacts with SiO_2 (obtained by oxidation of the initial $MoSi_2$ powder in the course of reaction with oxygen) to form mullite. Also, for Zr45MoY/20Al coatings, in contrast to the previous samples, there is a high content of tetragonal ZrO_2 is observed. It is known that silicon oxide destabilizes the high-temperature ZrO_2 phases (Okovity 2015). Thus, an increase in the content of the glass phase formed during high-temperature oxidation can facilitate the transition from the cubic to the tetragonal ZrO_2.

Fig. 12.4 XRD patterns of composite coatings ZrB$_2$–MoSi$_2$–Al after high-temperature oxidation
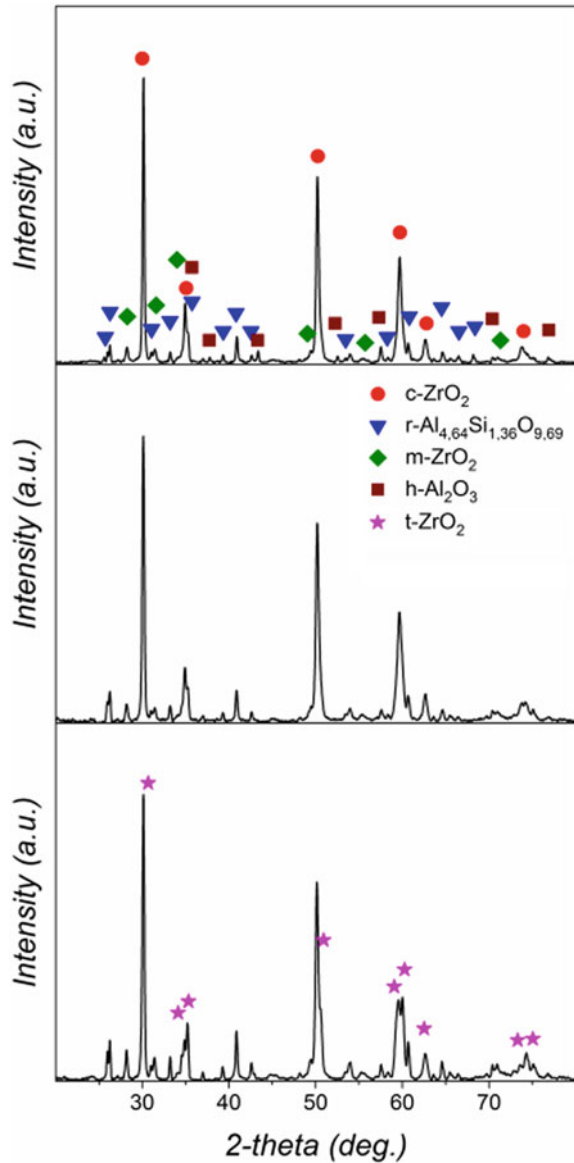
12.4 Conclusions

(1) Uniform dense coatings with good adhesion to the substrate were obtained, the bulk of the coating material was deformed and tightly packed, but the presence of unmelted zirconium particles in the coatings was observed. The porosity of the composite coatings was 0.02–1.00%.

(a)   (b)   (c)
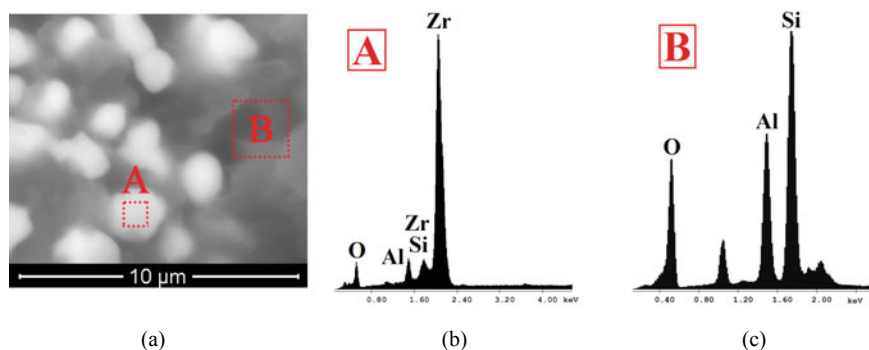
Fig. 12.5 SEM image of the surface of the composite coating Zr24MoY/20Al after annealing in air (1500 °C, 1 h) (**a**), elemental composition of the white phase (**b**), elemental composition of the gray phase (**c**)

Table 12.3 Phase composition of composite coatings after high-temperature oxidation

Coating	Phase composition, %				
	$c–ZrO_2$	$o–Al_{4.64}Si_{1.36}O_{9.69}$	$m–ZrO_2$	$h–Al_2O_3$	$t–ZrO_2$
Zr24MoY/20Al	35	47	5	13	–
Zr35MoY/20Al	35	57	6	2	–
Zr45MoY/20Al	5	62	3	–	30

(2) The visible boundary of the adhesion of the composite coatings to the C/C substrate has no defects. In the contact zone of the coatings and the substrate, a mixed structure is observed, consisting of coating islands in the substrate with different shape and size. Some of the powder material has penetrated deeply and is firmly bonded to the substrate material.

(3) Composite coatings consist of tetragonal and monoclinic ZrO_2, hexagonal ZrB_2, fcc–Al, tetragonal $MoSi_2$.

(4) It was found that an increase in the content of $MoSi_2$ in the initial powder mixture during high-temperature oxidation of the coating formed from it leads to an increase in the content of mullite ($3Al_2O_3 \cdot 2SiO_2$), which is formed in the form of the finest intertwined needle-shaped crystals.

(5) It was shown that an increase in the $MoSi_2$ content in the initial powder mixture during high-temperature oxidation of the coating formed from it leads to one-sided diffusion of SiO_2 into the Al_2O_3 grain with the formation of mullite. In place of the initial glass phase SiO_2, pores are formed.

References

Devi, G., Rao, K.: Carbon carbon composites: An overview. Def. Sci. J. **43**, 369–383 (1993)

Guo, M.: Multilayered coatings for protecting carbon-carbon composites from oxidation. Carbon **33**(4), 449 (1995)

Hui-Chao, Z., Fu-Hai, L., Feng, W.J.: Study on properties of $ZrSiO_4$ ceramic coatings by plasma spray. Guangdong Non-Ferrous Met. **15**(1), 30–32 (2005)

Jacobson, N.S., Curry, D.M.: Oxidation microstructure studies of reinforced carbon/carbon. Carbon **44**(7), 1142–1150 (2006)

Kovaleva, M., Tyurin, Y., Vasilik, N., Kolisnichenko, O., Prozorova, M., Arseenko, M., Danshina, E.: Deposition and characterization of Al2O3 coatings by multi-chamber gas-dynamic accelerator. Surf. Coat. Technol. **232**, 719–725 (2013)

Kovaleva, M., Goncharov, I., Novikov, V., Yapryntsev, M., Vagina, O., Pavlenko, I., Sirota, V., Tyurin, Y., Kolisnichenko, O.: Effect of heat treatment on the microstructure and phase composition of ZrB_2–$MoSi_2$ coating. Coatings **9**, 779 (2019)

Lee, K.N.: US Patent 6759151 (2004)

Li, C.J., Ohmori, A.: Relationships between the microstructure and properties of thermally sprayed deposits. J. Therm. Spray Technol. **11**, 365–374 (2002)

Li, Y., Zhou, W., Xiao, P., Luo, H., Wen, Z.L.: The anti-oxidation behavior and infrared emissivity property of $SiC/ZrSiO_4$–SiO_2 coating. J. Mater. Sci.: Mater Electron. **25**, 5433–5440 (2014)

Li, C., Li, G., Ouyang, H., Lu, J.: ZrB_2 particles reinforced glass coating for oxidation protection of carbon/carbon composites. J. Adv. Ceram. **8**(1), 102–111 (2019)

Liu, F., Li, H., Gu, S., Yao, X., Fu, Q.: Effect of Y_2O_3 on the oxidation properties of $ZrSi_2/SiC$ coating prepared by SAPS on the carbon-carbon composites. Ceram. Int. **44**, 15065–15071 (2018)

Lu, W., Qian-gang, F., Ning-kun, L., Sun, J.: Improvement of the adhesion strength of $MoSi_2$–ZrB_2 coating by optimizing particle spraying and subsequent heat treatment. J. Therm. Spray Technol. **25**, 1280–1288 (2016)

Niu, Y., Wang, Z., Zhao, J., Zheng, X., Zeng, Y., Ding, C.: Comparison of ZrB_2-$MoSi_2$ composite coatings fabricated by atmospheric and vacuum plasma spray processes. J. Therm. Spray Technol. **26**, 100–107 (2017)

Okovity, V.V.: Selection of oxides for stabilization of zirconium dioxide while obtaining thermal barrier coatings. Sci. Tech. **5**, 26–32 (2015). (In Russian)

Opeka, M.M., Talmy, I.G., Wuchina, E.J., Zaykoski, J.A., Causey, S.J.: Mechanical, thermal, and oxidation properties of refractory hafnium and zirconium compounds. J. Eur. Ceram. Soc. **19**, 2405–2414 (1999)

Vasilik, N., Tyurin, N., Kolisnichenko, O.: RU Patent 2506341 (2012)

Zhang, W.Z., Yi, Z., Lemuel, G., Xiang, X., Bai-Yun, H.: Preparation and oxidation property of ZrB_2–$MoSi_2/SiC$ coating on carbon/carbon composites. Trans. Nonferrous Met. Soc. China. **21**, 1538–1544 (2011)

Zhi-Qiao, Y., Xiang, X., Pen, X., Feng, C., Hong-Bo, Z., Bai-Yun, H.: Oxidation behavior of Mo–Si coated C/SiC composites. Aerosp. Mater. Technol. **10**(6), 39–43 (2007)

Chapter 13
Attempts to Increase the Adhesion of Boron Nitride Coatings to Sintered Carbides Blades

Maciej Jan Kupczyk

Abstract It can be stated that adhesion of coating to substrate depends on several factors, i.e., parameters of the coating process, kind of coating and substrate and in particular surface preparation of the substrate. The paper aims at showing that special preparation of substrate surface results in increased adhesion of super-hard, wear-resistant coatings deposited on cutting insert made of sintered carbides. During investigations, the surfaces of the cutting blades made of sintered carbides were prepared by the following different procedures: chemical etching, degreasing with subsequent ultrasonic cleaning, low- and high-temperature sputtering of substrate surface. Boron nitride coatings were deposited on the sintered carbides by the pulse-plasma method at different values of discharge voltage. The adhesion force (critical load) of the coatings to a substrate was estimated using the scratch test. Obtained results of investigations pointed to the influence of a surface preparation on critical load values. Essential influence of the discharge voltage on the adhesion was observed. The critical load results received during the scratch test were confirmed by observations of a scratches using scanning electron microscope and X-ray micro-analysis images. In order to observe how the system coating–substrate deforms under the influence of a loaded diamond stylus and the details of the surface morphology before and after depositing the boron nitride coating on the substrate, tests were carried out using a profilometer. The purpose of the research, which was to define the parameters of the production process of coatings with cubic boron nitride, at which a coating with the most favorable technological properties (good adhesion, dense structure) is obtained, was fully implemented.

Keywords Adhesion · Super-hard coating · Cutting inserts

M. J. Kupczyk (✉)
Institute of Mechanical Technology, Poznan University of Technology, ul. Piotrowo 3, 60-965 Poznan, Poland
e-mail: maciej.kupczyk@put.poznan.pl

13.1   Introductory Notes

13.1.1   Boron Nitride and Its Possible Applications

In addition to hard compounds, more and more attention is drawn to super-hard materials for wear-resistant coatings. The very high hardness of diamond and considerable shear strength make it an unrivaled material for wear-resistant coatings (Michalski 1994; Mitura et al. 1994; Sokolowska 1991). However, diamond, due to its significant chemical affinity to iron (and for obvious reasons to coal), is not suitable for cutting tools used for machining iron and its alloys. It easily reacts with iron, limiting the possibility of its effective use in the form of diamond coatings in steel processing. For this reason, the manufactured diamond-coated exchangeable cutting inserts are primarily used for machining non-ferrous materials such as brass, aluminum, and copper (Michalski 1994; Mitura et al. 1994; Sokolowska 1991; Burakowski and Wierzchon 1999; Kupczyk 2015).

In this respect, boron nitride is much more advantageous due to the much lower chemical affinity for iron than diamond, it can be used for the coating of blades machining iron alloys with carbon, i.e., steel, cast steel, and cast iron. Moreover, boron nitride coatings effectively protect the substrates against oxidation (Kupczyk 2015).

The use of cubic boron nitride with a hardness much higher than that of transition metal nitrides and carbides in the form of a coating deposited on the machining blade should significantly reduce the abrasive wear of the blade, increase its resistance to diffusion wear, and also increase the already mentioned resistance to oxidation. The possibility of limiting the diffusion wear of cutting inserts would be particularly desirable in the case of cemented carbides blades, for which this form of wear, apart from abrasive wear, largely determines their durability in the machining process (Kupczyk 1997).

There are numerous data in the literature on the effective application of diamond coatings (Mitura et al. 1994; Sokolowska 1991) in the case of their application for the machining of non-ferrous metals and their alloys and for the cutting of ceramics, while in the case of coatings made of cubic boron nitride, there are no such positive reports. Tests that were carried out up to the beginning of this research program did not bring a satisfactory result, mainly due to the insufficient adhesion of the coating to the cutting blades. For this reason, research on increasing the adhesion of the super-hard boron nitride coating to cutting blades, including cemented carbides, seems to be crucial.

13.1.2   Adhesion Measurement Method Selection

When selecting the method of measuring adhesion, it was guided that the test used should allow the measurement of high adhesion forces, be quantitative, simulating

the type of load occurring during the operation of the tested products, non-destructive or weakly destructive, giving easily interpretable results, with the highest possible repeatability of the obtained measurement results (reproducibility) and with a short measurement time.

The advantage of quantitative tests lies not only in the absolute assessment of the adhesive strength, but also in the possibility of comparing and selecting the most advantageous variant of the coating-substrate system and the method of coating application.

The above conditions are met by the scratch test, which is also characterized by a short measurement time. This method belongs to the group of mechanical quantitative methods. The principle of measuring the adhesion force using the scratch test is to move the loaded diamond tip of the indenter over the test surface (most often it is a Rockwell 120° indenter) and measure the normal load applied to the stylus, at which the coating loses adhesion to the substrate. The load at which it loses adhesion is called the critical load or the critical force and is used as a measure of the adhesion of the coating to the substrate. In this test, the loads are applied in steps or gradually increase.

A particularly important feature of the method, especially in industrial conditions, is its effectiveness, determined by the number of measurements of a given quantity in a given period. The concept of method effectiveness is related to its speed. The measure of the speed of the method is the time needed to perform one measurement. It should be noted, however, that not in every case increasing the measurement speed is beneficial as it may increase the spread of the measurements. If the scattering of results is large, should be reduced the speed, which may result in a decrease in performance. Following the above principles, the work (Kupczyk 1997) specifies such values of scratch test parameters for which the highest possible repeatability of results and method productivity are obtained. These parameters are defined as the standard parameters of the scratch adhesion test. These included draw speed dx/dt, load speed dL/dt, and their relative dL/dx ratio, as well as the stylus tip radius R and the maximum number of scratches for a single diamond tip i_{max}.

When establishing the standard terms, the following were taken into account:

– variability of L_c as a function of dL/dx for the assumed R value,
– measurement time,
– scatter of measurement results,
– variability of L_c as a function of dL/dt for the adopted value of dx/dt,
– variation of L_c as a function of dx/dt for the adopted value of dL/dt.

Following the results of research on the influence of scratch parameters on the value of the critical load presented in (Kupczyk 1997), the following variant was adopted in the research presented in this paper, considered the most favorable in terms of the above criteria.

Earlier tests have shown that the above-adopted values of scratch test parameters allow to obtain repeatable test results while maintaining the highest possible efficiency; i.e., they allow obtaining repeatable measurement results even in the event of some deviations from their recommended values during tests. As stated

(Kupczyk 1997), a change in one of the dx/dt, dL/dt or dL/dx values by even 20–30% while maintaining the other recommended values should not significantly affect the measured L_c value, which is a measure of practical adhesion.

13.1.3 Basic Assumptions and the Role of Substrate Preparation Before Coating Deposition

Almost always, the chemical composition of the substrate surface differs from that of the material core. Treatment of the substrate surface prior to coating, e.g., by machining, grinding, polishing, etc., changes not only its mechanical, but also chemical structure. The treatment prior to coating can have both positive and negative effects on the adhesion of the coating to the substrate. Hence, it is extremely important that the surface obtained as a result of it is fully "defined" and "repeatable." There are many physical and chemical methods for cleaning and preparing the surface of the substrate, but in any case, to fully "define" the surface, it is necessary to define the type of contaminants to be removed. In other words, in a practical sense, a clean surface is one that does not contain significant amounts of undesirable material.

It should be emphasized that the presence of surface impurities may prevent diffusion and reactions between atoms of the material deposited with the substrate surface. Even very thin layers of oxides or carbon—from 10×10^{-7} mm to 100×10^{-7} mm—can constitute, as stated (Kupczyk 1997), an effective barrier preventing good bonding. Since oxides and adsorbed hydrocarbons are common contaminants on metal surfaces, removal is a major problem in achieving good adhesion.

Various surface cleaning procedures are discussed in some thin coating publications, and the most valuable in this range are the items (Kupczyk 1997; Butler et al. 1970; Cailler et al. 1989; Cailler and Lee 1989; Chapman 1969; Lahmar et al. 1991; Lee et al. 1990; Perry 1981).

13.2 Conditions of Investigations

13.2.1 The Method Used and the Conditions for the Production of Boron Nitride

The pulse-plasma method (Michalski 1994; Sokolowska 1991) developed at the Faculty of Materials Science and Engineering of the Warsaw University of Technology was used to obtain BN coatings. The essence of this method is the use of impulse electrical discharges for the generation of plasma, as a result of which a highly ionized and non-isothermal plasma is generated. The advantages of the pulse-plasma process are the ease of its conduct and control as well as the simplicity of the device structure and its versatility.

The working chamber of the device is a quartz tube. A pulse discharge is generated between two graphite electrodes. The electrodes are cuboids with dimensions of 60 × 40 × 20 mm. They are placed parallel with their largest surfaces to each other and placed 200 mm from the closing plate of the chamber. The pulsed electrical discharge between the graphite electrodes is initiated by an ignitron which completes the circuit containing the capacitor bank with a capacity of 200 µF. Ignitron is controlled by an electronic system that allows you to adjust the frequency of triggering pulses and control their number. The capacitor bank is powered from a DC power supply with adjustable output voltage in the range from 0 to 10 kV (Michalski 1994; Sokolowska 1991; Kupczyk et al. 2002).

In the same plate closing the chamber, in which the electrode current passages are located, there is an inlet for gases constituting the working atmosphere of the process. The inlet is in the axis of the chamber. Gases are supplied from the cylinder through pressure reducers. The amount of gases supplied to the chamber is regulated by needle valves. The flowing gases are a carrier of boron, which is obtained as a result of the evaporation of boroamine from a vessel heated by a resistance furnace. The furnace is powered by an autotransformer. The temperature in the tank is controlled by a thermocouple inserted into it through a teflon bushing (Kupczyk et al. 2002) (Fig. 13.1).

The working chamber is heated by an external resistance furnace, which allows to obtain a temperature of 1300 K inside the chamber. The stove is made of a quartz tube, on which the kanthal tape is wound and is insulated with ceramic wool and covered with a sheet. The furnace is powered by an autotransformer.

The second plate, closing the chamber, is cooled by the water flowing through it in order to protect the seals against high temperature. This plate includes an outlet for a vacuum pump, a connector for a vacuum gauge probe and a gland for a thermocouple

Fig. 13.1   Picture of the plasma-pulse device used for the production of BN coatings

controlling the temperature in the chamber. The device uses a rotary vacuum pump with a capacity of 30 l/min. A resistance vacuum gauge is used to measure the pressure in the chamber. The vacuum gauge head is insulated from the chamber with a Teflon joint to prevent damage by electrical surges during the process (Kupczyk et al. 2002).

13.2.2 Test Stand for Adhesion Measurement

The adhesion tests based on the assessment of the acoustic emission signal level, measured with the amplitude of vibration acceleration in the tested frequency band, were performed with the use of an automatic, computer-aided scratch test device (Kupczyk 1997; Kupczyk and Wieczorowski). This device is equipped with two measurement lines for determining the level of vibration and acoustic signal. It enables:

– manual or automatic start of recording after exceeding the preset signal level (autotourge);
– automatic detection of the waveform with a given amplitude level;
– registration of waveforms in the range of 5–100 s with a step of 0.01 s;
– waveform visualization with the possibility of reading the current time and amplitude values;
– analysis of the time signal with smoothly regulated averaging time (0.02–1.00 s) taking into account (Fig. 13.2a):

    (a)   positive and negative envelope of the signal,
    (b)   envelope from the absolute value of the signal,
    (c)   signal intensity,
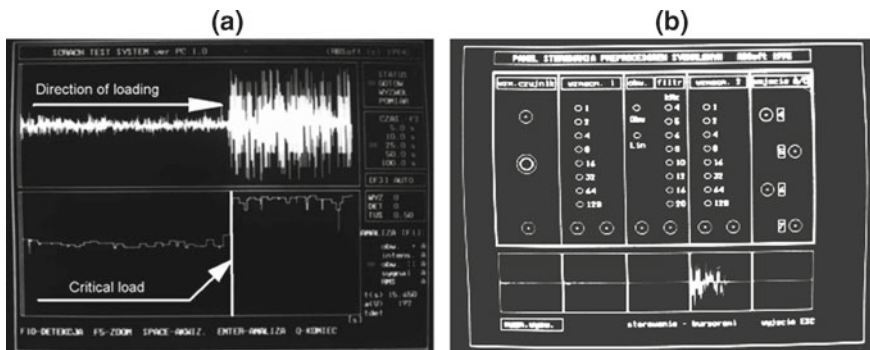   (d)   the current actual value of the signal.

Fig. 13.2 Image of: **a** computer screen with run of vibration signal (actual value and positive envelope), **b** signal preprocessor control panel

The measuring station has been equipped with, among others, a signal preprocessor intended for recording signals and for their preliminary analog processing, which enables:

– use of low-pass filtering to separate the frequencies that trigger registration and to perform anti-aliasing functions;
– use of band-pass filtration in eight ranges;
– signal smoothing;
– capacitive and voltage matching of signals from piezoelectric sensors;
– signal pre-amplification 2–128 times;
– signal secondary amplification 2–128 times.

The signal preprocessor is also equipped with a sensor preamplifier with stepless gain control 10–400 times (potentiometer).

Control software coupled with the signal preprocessor enables:

– remote control of individual blocks of the signal processor;
– simultaneous, 4-stream preview of the signal in individual stages of pre-processing;
– automatic saving of signal processing configuration.

Figure 13.2b shows the control panel for the signal preprocessor, which was used to set the signal gain and frequency band selection.

The scratch test stand allows the measurement of the critical load value using:

– different values of the speed of the stylus in relation to the tested sample (dx/dt),
– step load on the stylus ($dL/dt = 0$),
– gradual build-up of load ($dL/dt > 0$),
– different values of the ratio of the speed of load growth to the speed of the stylus (dL/dx).

13.2.3 Substrate Preparation Procedures

Many works concern the influence of substrate preparation on the adhesion of the coating to it, e.g., (Kupczyk 1997; Butler et al. 1970; Cailler et al. 1989; Cailler and Lee 1989; Chapman 1969; Lahmar et al. 1991; Lee et al. 1990; Perry 1981; Mertens et al. 2012; Ooi et al. 2006; Othman and Bushroa 2015). In presented investigations, the adhesion tests were carried out for boron nitride coatings applied to H20S sintered carbide inserts with variously prepared surfaces. Cutting inserts with a surface were used:

– degreased,
– etched,
– low-temperature sputtering,
– high-temperature sputtering.

Table 13.1 Parameters of the surface preparation process by low-temperature sputtering

Specification	I and U values after $t = 0, 20, 40, 60$ min			
Current–voltage conditions	t_0	t_{20}	t_{40}	t_{60}
I [mA]	90	90	90	90
U [kV]	1	2	2,3	2,6

**Table 13.2** Parameters of the surface preparation process by high-temperature sputtering

Specification	I and U values after $t = 0, 20, 40, 60$ min			
Current–voltage conditions	t_0	t_{20}	t_{40}	t_{60}
I [mA]	90	90	90	90
U [kV]	1	2	3,2	3,6

The surfaces of the samples were degreased prior to etching. The etched samples were rinsed under a stream of water. The parameters of low-temperature and high-temperature sputtering processes are presented in Tables 13.1 and 13.2.

13.2.4 Conditions of Complementary and Verification Tests

A stereoscopic microscope was used for the initial verification of test results, performed directly on the test bench. In the case of verifying a few, questionable results, the scratch observations were carried out on the JMS-50A Yeol scanning microscope and the XMA-50A X-ray microanalyzer of the same company and on the VEGA—TS 5135 scanning microscope. Scanning microscopy also turned out to be necessary for the study the morphology of the scratches and the structure of the tested coatings. Surface studies with the use of secondary electrons (SEI), supplemented with observations carried out with the use of reflected (BEI), and absorbed (AEI) electrons, providing not only the topographic image of the surface, but also some information about the chemical composition of the studied micro-area, proved to be particularly useful. Moreover, qualitative surface microanalyses were used in the research. Qualitative surface microanalysis was primarily used to assess the degree of removal of the coating material from the channel formed during scratching.

It should be mentioned that a comparison of the results of the adhesion force obtained on the basis of the assessment of the acoustic and vibration signal with the L_c values determined by scanning microscopy and X-ray microanalysis images is possible only in the case of damage of the coating in the form of peeling exposing the substrate (Kupczyk and Wieczorowski). Such was the case in the discussed research, hence it was possible to make such a comparison. The length of the segment between the point where the stylus was originally placed (load $L = 0$ N) and the place of exfoliation was initially determined using a micrometric screw coupled with a sample holder in a scanning microscope (JSM-50A microscope), and then automatically on
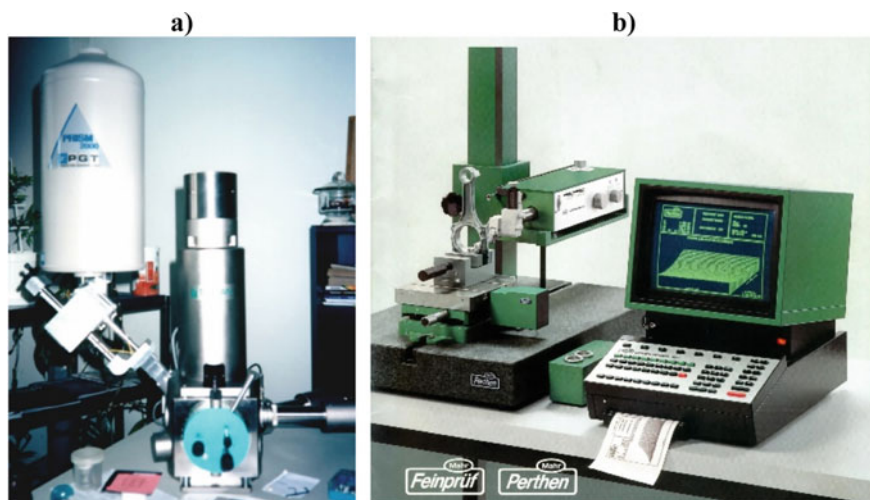
Fig. 13.3 Pictures of: **a** the VEGA—TS 5135 scanning microscope, **b** S8P 6.22 profilometer produced by Perthen Mahr

a newly purchased microscopy (VEGA—TS 5135 of the English company Tescan—Digital Microscopy Imaging, equipped with an X-ray microanalyzer) working at the Institute of Materials Science and Technology of the Poznan University of Technology (Fig. 13.3a). The place where the stylus was originally applied to the sample was identified on the basis of the first traces of deformation of the coating visible on the microscope screen.

13.2.5 Application of the Profilometer in Adhesion Tests

In order to observe the method of deformation of the coating-substrate system under the influence of a loaded diamond stylus and the details of the surface morphology before and after depositing the boron nitride coating on the substrate, tests were carried out using a profilometer.

Scratch and surface profilograms of boron nitride coatings and cutting inserts made of sintered carbides were made using the Perthen Mahr S8P 6.22 profilometer at the Department of Metrology and Measurement Systems of the Poznan University of Technology (Fig. 13.3b).

The critical load value, surface morphology, and the occurring damage of the coating and substrate were assessed after the scratch adhesion test was performed on the basis of:

– 2D images,
– 3D images.

13.3   Results of Tests on Adhesion

13.3.1   Basic Research Results

The adhesion tests were carried out for boron nitride coatings applied to H20S sintered carbide plates with variously prepared surfaces. Cutting inserts with a surface were used:

– degreased with acetone,
– etched with KOH + $K_3Fe (CN)_6$ solution for 20 s,
– etched with KOH + $K_3Fe (CN)_6$ solution for 40 s
– low-temperature sputtering,
– high-temperature sputtering.

The adhesion of the coatings to the substrates was measured by the scratch method described in point 2.2. The critical load values for coatings applied on tiles with variously prepared substrate are given in Tables 13.3, 13.4 and 13.5.

The following internal parameters of the scratch adhesion test were used during the tests:

– loading rate $dL/dt = 300$ N/min,
– scratching speed $dx/dt = 7.5$ mm/min,
– ratio $dL/dx = 40$ N/min,
– gradual load in the range of 0–200 N,
– tip radius of the diamond stylus $R = 0.20$ mm.

Determination of the critical load value using the scratch test was performed with the measurement repeated 6 times for each variant.

Table 13.3 Results of measurements of the critical load value obtained on the basis of the evaluation of the vibration signal during scratching the H20S sample coated with the boron nitride coating produced at a discharge voltage of 3.0 kV

No	Preparation of the substrate surface	Critical load L_c [N]	Mean deviation ΔL_c [N]	Confidence interval $\pm\Delta$
		Discharge voltage 3.0 kV		
1	Degreasing	14.7	3.31	±3.41
2	Chemical etching: 20 s	18.6	3.09	±3.18
3	Chemical etching: 40 s	11.8	2.68	±2.76
4	Low-temperature sputtering	22.3	3.22	±3.32
5	High-temperature sputtering	16.2	2.91	±3.00

Table 13.4 Results of measurements of the critical load value obtained on the basis of the evaluation of the vibration signal during scratching the S20S sample coated with the boron nitride coating produced at a discharge voltage of 4.5 kV

| No	Preparation of the substrate surface	Critical load L_c [N]	Mean deviation ΔL_c [N]	Confidence interval $\pm\varDelta$
		Discharge voltage 4.5 kV		
1	Degreasing	19.1	3.19	±3.29
2	Chemical etching: 20 s	27.4	3.41	±3.51
3	Chemical etching: 40 s	22.5	2.92	±3.01
4	Low-temperature sputtering	**38.6**	**3.53**	**±3.64**
5	High-temperature sputtering	18.4	3.47	±3.57

Table 13.5 Results of measurements of the critical load value obtained on the basis of the evaluation of the vibration signal during scratching the S20S sample coated with the boron nitride coating produced at a discharge voltage of 6.0 kV

No	Preparation of the substrate surface	Critical load L_c [N]	Mean deviation ΔL_c [N]	Confidence interval $\pm\varDelta$
		Discharge voltage 6.0 kV		
1	Degreasing	20.3	2.82	±2.90
2	Chemical etching: 20 s	26.2	3.11	±3.20
3	Chemical etching: 40 s	23.6	3.28	±3.79
4	Low-temperature sputtering	28.7	3.27	±3.37
5	High-temperature sputtering	19.0	2.77	±2.85

Adhesion tests for variously prepared substrates have shown that low-temperature sputtering of the substrate is the most advantageous from the point of adhesion increase. The etching of the substrate has a positive effect on increasing the adhesion of the coating, as long as the process does not take too long. It can be assumed that it is related to the mechanical anchoring of the coating in the unevenness formed on the surface of the substrate as a result of its etching. However, an etching that is too long leads to a weakening of the cemented carbide, especially its metallic binder. Graphical interpretation of the results of adhesion tests of boron nitride coatings deposited on H20S cemented carbide cutting inserts is shown in Fig. 13.4.
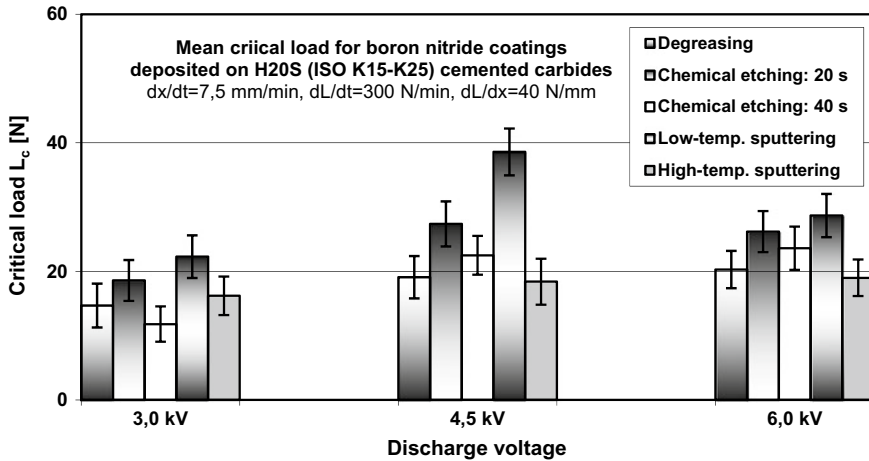
Fig. 13.4 Graphical interpretation of the test results for the adhesion of boron nitride coatings deposited on cutting inserts made of H20S sintered carbides (order from left: degreasing, chemical etching: 20 and 40 s, low-temperature sputtering, high-temperature sputtering)

13.3.2 Results of Comparative and Verification Tests

13.3.2.1 Comparative Research Using Scanning Microscopy and X-ray Microanalysis

As already mentioned in the test methodology, in order to confirm the obtained results of the measurements of the adhesion force (critical load) measured with the scratch test, based on the assessment of the acoustic and vibration signal (vibration acceleration amplitude in the tested frequency band), scratch observations were carried out using:

(a) scanning microscopy

  – secondary electron images (SEI),
  – absorbed electron images (AEI);

(b) X-ray microanalysis (XMA)

  – surface qualitative microanalysis of:

    tungsten, cobalt, nitrogen, boron, titanium;

(c) profilometer
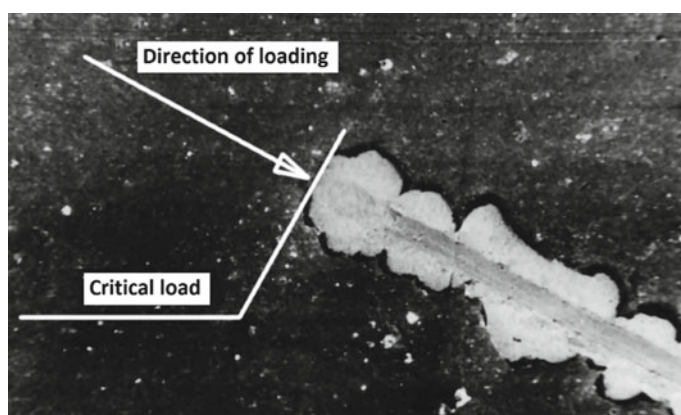
  – 2D images,
  – 3D images.

As already mentioned in the research methodology, the observations of images created by secondary and absorbed electrons were made on the JSM-50A scanning microscope, and surface qualitative microanalysis using the JXA-50A X-ray microanalyzer and on the computer-assisted scanning microscope VEGA—TS 5135.

An exemplary comparison of the results of the adhesion force (critical load) tests according to the vibration signal evaluation and the images of scanning microscopy and X-ray microanalysis is presented in Table 13.6.

Figure 13.5 shows the scratch formed during the coating adhesion test. The picture clearly shows the place where the coating detached from the substrate while Fig. 13.6 shows the image formed by the secondary electrons (SEI) of the scratch, the image formed by the absorbed electrons (AEI), image of the surface qualitative microanalysis of Co + N occurrence and image the surface qualitative microanalysis of the tungsten occurrence.

Table 13.6 Set of the results of the adhesion force (critical load) tests according to the vibration signal evaluation and images of scanning microscopy and X-ray microanalysis

Preparation of the substrate surface	The value of the critical load in [N] according to the measurement of the vibration signal	The value of the critical load in [N] according to the assessment of SE and AE images
Degreasing	19.1 ± 3.29	17.8 ± 2.8
Chemical etching: 20 s	27.4 ± 3.51	24 ± 2.7
Chemical etching: 40 s	22.5 ± 3.01	20.6 ± 3.0
Low-temperature sputtering	$\mathbf{38.6 \pm 3.64}$	$\mathbf{35.2 \pm 3.1}$
High-temperature sputtering	18.4 ± 3.57	15.8 ± 2.5

Fig. 13.5 Image of the scratch on boron nitride coating deposited on cemented carbides substrate (coating thickness: $6 \pm 0.6\,\mu\text{m}$, magnification: $\times 84$)
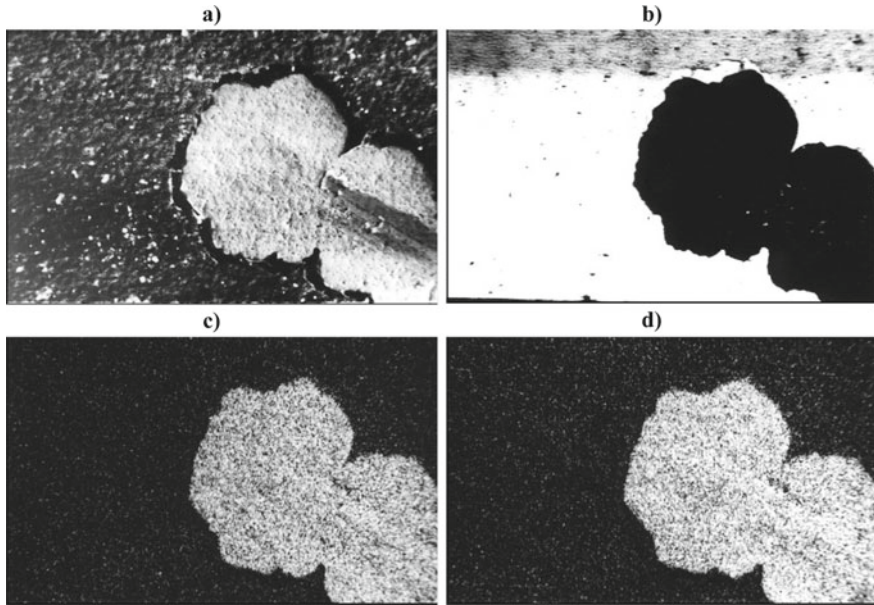
Fig. 13.6 Images of: **a** secondary electrons, **b** absorbed electrons, **c** surface qualitative microanalysis of Co + N occurrence, **d** surface qualitative microanalysis of the presence of tungsten, scratch of BN coating on a sintered carbide cutting insert (coating thickness: 6 ± 0.6 μm, magnification: ×210)

The observations made with the use of scanning microscopy and X-ray microanalysis confirmed the test results obtained on the basis of the vibration signal evaluation.

13.3.2.2 Surface Roughness Tests

The tests were carried out on uncoated H20S carbide cutting inserts and covered with boron nitride after low-temperature sputtering (the most advantageous variant of substrate preparation) at various discharge voltage parameters. The set of the surface roughness measurement results (Ra roughness parameter) is presented in Table 13.7. A representative value of the roughness parameter Ra was determined on the basis of the arithmetic mean of five measurements made for each of the four samples of a given type.

Figure 13.7 shows examples of 3D prints of the roughness of the surface of the uncoated cutting insert and the surface of cemented carbide coated with boron nitride.

Tests with the use of a profilometer showed a high smoothness of boron nitride coatings produced by the pulsed-plasma method, especially at a discharge voltage of 4.5 kV, greater than that of the cemented carbide surfaces.

Table 13.7 Results of surface roughness measurements for uncoated and coated with boron nitride coating cemented carbide cutting inserts
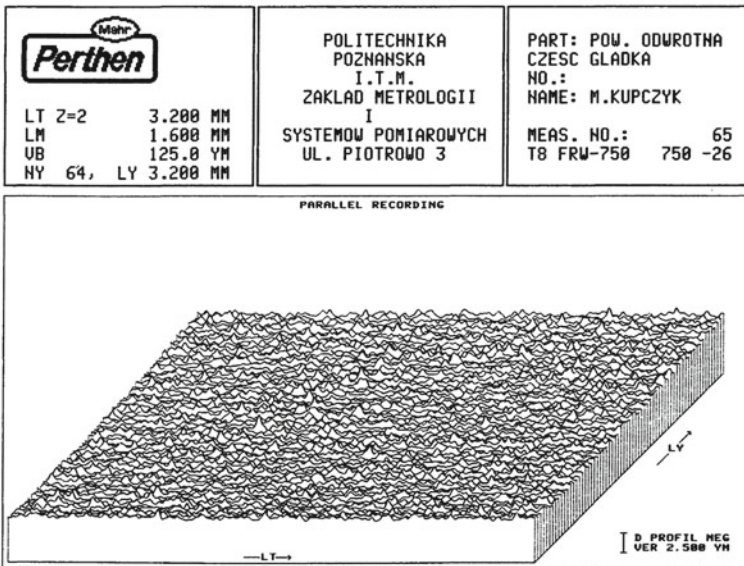
No. of cutting inserts	Cutting inserts type	Discharge voltage	Values of successive roughness measurements R_a [μm]					Mean values of Ra [μm]
			1	2	3	4	5	
1	COATED WITH BORON NITRIDE (H20S + BN)	3.0 kV	0.38	0.37	0.35	0.40	0.36	0.367
2			0.34	0.37	0.33	0.38	0.35	
3			0.33	0.39	0.38	0.42	0.32	
4		4.5 kV	0.16	0.18	0.17	0.19	0.15	0.147
5			0.11	0.12	0.19	0.13	0.14	
6			0.17	0.17	0.16	0.14	0.18	
7		6.0 kV	0.25	0.24	0.27	0.25	0.27	0.265
8			0.26	0.28	0.25	0.28	0.27	
9			0.29	0.21	0.28	0.29	0.28	
10	UNCOATED H20S		0.26	0.24	0.25	0.23	0.23	0.239
11			0.23	0.25	0.22	0.25	0.22	
12			0.25	0.25	0.22	0.24	0.24	

Based on the observation of images of boron nitride coatings produced by the pulse-plasma method, it was found that these coatings are characterized by a different structure depending on the discharge voltage value used (Figs. 13.8, 13.9 and 13.10). At the lowest discharge voltage (3.0 kV), the structure of the coating is not very compact (porous). The coatings, moreover, have a coarse-grained structure with relatively significant surface irregularities. Coatings produced at higher discharge voltages have a more favorable structure. The coating produced at a discharge voltage of 4.5 kV is the most compact and has the lowest surface roughness.

13.4 Conclusions

The aim of the research, which was to determine the parameters of the manufacturing process of coatings from cubic boron nitride, in which a coating with appropriate technological properties is obtained, has been achieved. It was found that the technological properties of the boron nitride coating (obtaining a fine-grained structure of the coating, low surface roughness, good adhesion of the coating to the substrate) were primarily influenced by the voltage–current conditions of the process and especially the discharge voltage in the process of coatings production by the pulsed-plasma method and the way of preparing the substrate. Low-temperature sputtering has been found to be the most advantageous surface preparation method to ensure good adhesion. It is important that the substrate preparation temperature and coating application processes do not exceed the tempering temperature of the substrate or
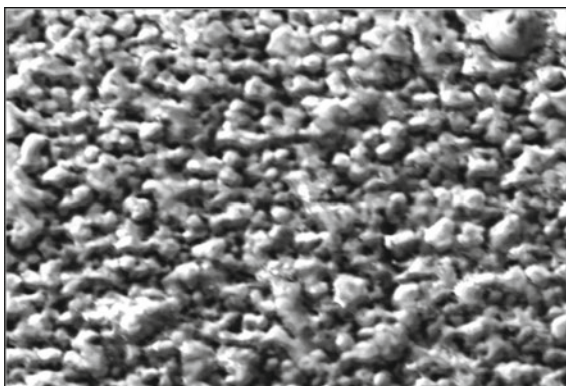
a)

b)
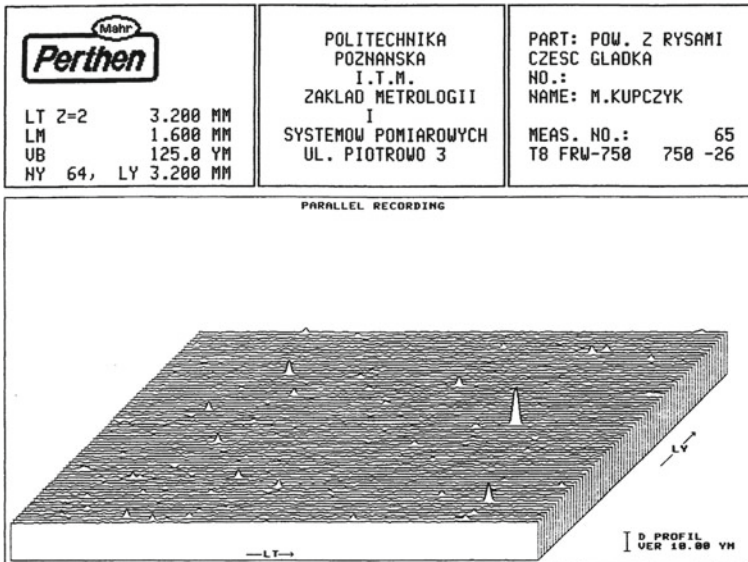
Fig. 13.7 3D prints of the surface roughness of a cemented carbides cutting inserts: **a** uncoated, **b** coated with boron nitride using 4.5 kV of discharge voltage

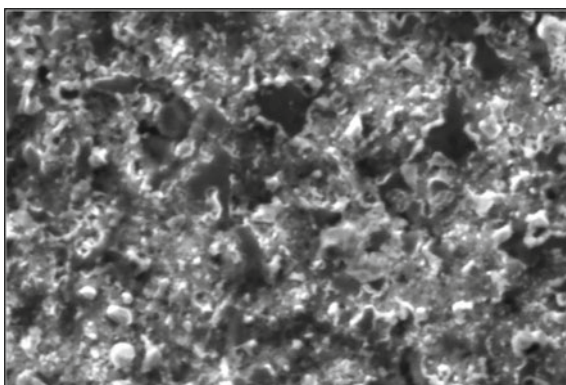**Fig. 13.8** SE image of the surface of boron nitride coatings obtained at a discharge voltage of 3.0 kV, (magnification of ×2000)

Fig. 13.9 SE image of the surface of boron nitride coatings obtained at a discharge voltage of 4.5 kV, (magnification of ×2000)
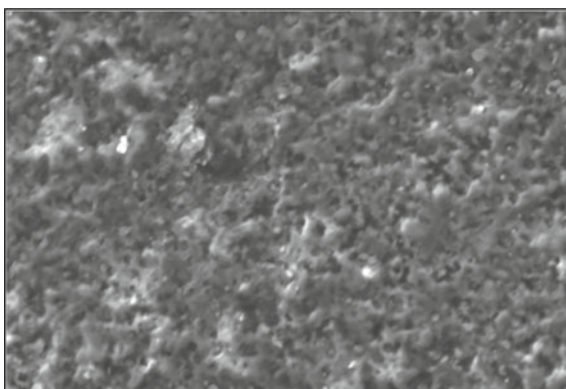
Fig. 13.10 SE image of the surface of boron nitride coatings obtained at a discharge voltage of 6.0 kV, (magnification of ×2000)

change the chemical composition of the surface layer of the substrate. Therefore, most likely, the high-temperature sputtering process and the highest value of the discharge voltage turned out to be unfavorable for the cemented carbide substrate.

And so, from the point of view of ensuring appropriate technological properties, the most favorable value of the discharge voltage is 4.5 kV. With this voltage value, it obtains:

– the most compact coating structure,
– the smoothest surface of the coating (Ra = 0.147 μm).

Obtaining the coatings with higher surface roughness (Ra = 0.367 μm) at $U = 3.0$ kV results from the not very compact structure of the coating in the form of weakly compact granules of many times larger sizes than the grains of the fine-crystalline structure obtained at the discharge voltage of 4.5 kV. Moreover, coatings with a porous structure, according to Griffith's theory, are much weaker in terms of strength and more prone to brittle fracture due to the easy propagation of the resulting cracks in materials with such a structure.

The aforementioned parameters of the substrate preparation and coating production process have a decisive impact on the value of the adhesion force of the boron nitride coating to the substrate. This is an extremely important parameter, because, as already emphasized in the introduction to the paper, based on previous own research, the wear-resistant coating, even with the right chemical composition, compact structure, high hardness and relatively low brittleness, becomes useless when its adhesion to the substrate is too low. In this case, as a result of high unit pressures accompanying the steel cutting process, the coating is almost immediately removed from the rake face at the point of chip impact and from the flank face at the point of contact with the workpiece. In the case of boron nitride coatings produced mainly by PVD methods, insufficient adhesion was the main reason for the lack of their effective application so far. Based on the results of research and analyzes, there is a serious indication that cutting inserts prepared according to the procedure indicated in the paper will be characterized by appropriate operating properties during machining. The experience obtained earlier shows that the adhesion obtained after low-temperature sputtering of the substrate should be sufficient.

Obviously, the obtained test results require verification during the operation of replaceable cutting inserts, i.e., during machining of construction materials.

References

Burakowski, T., Wierzchon, T.: Surface engineering of metals—principles, equipment, technologies. CRC PRESS LLC, Catalog No. 8225, Boca Raton—London—New York—Washington D.C. (1999). ISBN 0-8493-8225-4

Butler, D.W., Stoddart, C.T.H., Stuart, P.R.: The stylus or scratch method for thin films adhesion measurement. J. Phys. **D3**, 877 (1970)

Cailler, M., Lee, G.H.: Scratch adhesion test of magnetron-sputtered copper coatings on aluminum substrates: Effects of the substrate preparation. Thin Solid Films **168**, 193–205 (1989)

Cailler, M., Lahmar, A., Lee, G.H.: Adhesion studies of magnetron-sputtered copper films on chemically etched nickel substrates. Thin Solid Films **182**, 167–184 (1989)

Chapman, B.N.J.: The adhesive of thin films. Ph.D. Thesis, Department of Electrical Engineering, Imperial College, London (1969)

Kupczyk, M.: Technological and functional quality of cutting edges with wear resistant coatings. Series: Dissertations. No. 320. Poznan University of Technology Publishers, Poznan (1997). ISSN 0551-6528

Kupczyk, M.J.: Surface engineering—cutting tools. ISBN 978-83-7775-396-5, Poznan University of Technology Publishers, Poznan (2015)

Kupczyk, M., Wieczorowski, K.: Unit for measuring the adhesion of anti-wear layers to the substrate, especially those deposited on the surfaces of cutting tools, Patent Pat-981/PP/1993 and P 301807/1994 (1994)

Kupczyk, M., Michalski, A., Misiak, W., Lejwoda, A.: Research on the technological and functional properties of hard boron nitride coatings applied by the pulse-plasma method (PPD) on cutting blades, Report KBN No. 7T08A 011 17, contract No. 962/T08/99/17, Poznan (2002) (unpublished)

Lahmar, A., Lee, G.H., Cailler, M., Constantinescu, C.: Adhesion studies of magnetron sputtered copper films on steel substrate: effects of heat treatments. Thin Solid Films **198**, 115 (1991)

Lee, G.H., Cailler, M., Kwon, S.C.: Adhesion studies of magnetron-sputtered copper films on nickel substrates: Effects of substrate surface pretreatments. Thin Solid Films **185**, 21–33 (1990)

Mertens, T., Gammel, F.J., Kolb, M., Rohr, O., Kotte, L., Tschöcke, S., Kaskel, S., Krupp, U.: Investigation of surface pre-treatments for the structural bonding of titanium. Int. J. Adhes. Adhes. **34**, 46–54 (2012)

Michalski, A.: Crystallization of metastable types of boron nitride from gas phase. In: Proceeding of 4th Summer School "Modern Plasma Surface Technology", Koszalin, 90 (1994)

Mitura, S., Sokolowska, A., Szmidt, J.: Future applications of diamond. In: Proceeding 4th Summer School "Modern Plasma Surface Technology", Koszalin, 107 (1994)

Ooi, N., Hector, L.G., Jr., Adams, J.B., Stanzione, D., Jr.: First principles study of the aluminum-cubic boron nitride interface. J. Adhesion **82**, 779–803 (2006)

Othman, M.F., Bushroa, A.R., Abdullah, W.N.R.: Evaluation techniques and improvements of adhesion strength for TiN coating in tool applications: A review. J. Adhes. Sci. Technol. **29** (7), 569–591 (2015)

Perry, A.J.: Adhesion studies of ion-plated TiN on steel. Thin Solid Films **81**, 357–366 (1981)

Sokolowska, A.: Unconventṇhesis. PWN Publishers, Warsaw (1991). ISBN 83-01-10848-7

Chapter 14
Microstructure, Hardness, Wear and Corrosion Resistance of Heat-Treated 7075 Aluminum Alloy Casting Mahmoud Tash

Mahmoud Tash

Abstract The present study was undertaken to investigate the effect of homogenization and aging treatment on the performance of cast AA7075 aluminum alloy. Different heat treatments such as T4, T6, T7 and double aging (DA) were carried out to acquire an understanding of their effect on the alloy performance. Aging treatments were performed at RT, 180 °C (1-5 h), 180 °C (1-6 h) preaged at 120 °C (3-6 h) and 220 °C (1-8 h). Hardness (micro and macro), corrosion and wear measurements were evaluated for all conditions. Specimens were corrosion tested using cyclic anodic polarization technique. Friction force, friction coefficient and wear rate measuring were carried out using a computerized pin-on-disc machine. The microstructure was examined for all conditions using optical and scanning electron microscopy (SEM). Line scans for Zn, Mg, Fe, Si, Cu and Al were obtained from different conditions using energy-dispersive X-ray spectroscopy (EDX). The results reveal that Al-Cu-Zn-Mg, Al–Si-Mg-Zn, Al–Si-Mg and Al–Fe-Cu-Mg-Zn-rich intermetallic phases were formed such as (Al8.85Cu0.81ZnMg1.35, Al7.2Si3.43Zn0.25 Mg, Al0.94SiMg and Al15.3FeCu1.1Zn0.21 Mg 0.55). Additionally, the wear and corrosion resistance resulted of the AA7075 aluminum alloy were remarkably improved after homogenization and double aging at 125 °C - 6 h plus 180 °C -3 h or aging at 125 °C -3 h plus 180 °C for 5 h.

Keywords AA7075 al alloy · Aging · Microstructure hardness · Wear and corrosion

14.1 Introduction

High-strength 7xxx aluminum alloys are commonly used in aircraft structure applications due to its excellent response to age hardening and a high strength-to-density ratio. Precipitation hardening AA7075 alloy has been adapted extensively in the

M. Tash (✉)

Department of Mining, Petroleum and Metallurgical Engineering, Faculty of Engineering, Cairo University, Giza 12613, Egypt
e-mail: mahmoud_tash1@yahoo.com

marine, automotive and highly stressed structural applications. This alloy is widely used in aircraft fittings, gears, and shafts, fuse, missile, and regulating valve parts, where there is a fundamental design requirement for higher wear, corrosion resistance and mechanical performance (Polmear 1996; Smith 1993).

Different intermetallic phases are formed during solidification of AA7075 aluminum alloy, depending on the alloy composition, additions and solidification conditions. It was reported that during solidification of AA7075 aluminum alloy, a dendritic network of Al was formed at 620 °C, followed by the precipitation of the Al_3Fe intermetallic phase, and therefore, the Mg_2Si phase at about 565 °C, and finally the formation of eutectic precipitates of $Al + MgZn_2 + Al_2Cu + Al_2Mg_3Zn_3$ (T-phase) at 470 °C, where a state of non-homogenous structure is obtained (Bäckerud et al. 1990). Constituent Al3Fe and Al7Cu2Fe intermetallic particles and dispersed Al3Ti and Al3Zr particles are formed during solidification. Homogeneous dispersion of the precipitates on the dendrite matrix or along the grain boundaries improves the corrosion resistance of 7075 aluminum alloy (Ramgopal et al. 2002; Birbilis and Buchheit 2004; Huang and Franke 2006). Constituent and/or dispersed particles are reported to cause pitting corrosion due to their active and/or noble galvanic interaction with the dendrite matrix. (Zhang and Frankel 2003). Birbilis and Buchheit (Birbilis and Buchheit 2004) reported that MgZn2 or Mg2Si had the highest corrosion rate, while Al3Ti had the lowest corrosion rate. For 7075-T6 aluminum alloys, undissolved constituent particles existing in the alloy accelerate the local corrosion pitting due to the difference in electrochemical activity between the particles, and the matrix and between this heterogeneous particle's phases (Lunarska et al. 1987).

The effect of heat treatment on the microstructure, pitting corrosion and mechanical properties of AA 7075 alloys have been studied by several researchers (Minoda et al. 2003; Wei et al. 1998; Kaya and Atapek 2007; Emani 2009; Oliveira et al. 2004; Andretta et al. 2003). After homogenization process, dendrite segregation is eliminated, metastable precipitates vanish, soluble elements such as magnesium, silicon and zinc are diffused into solid solution, and therefore, the as-cast microstructure transforms into homogeneous structure. However, Fe-containing phase is not dissolved during homogenization treatment, which is harmful to the alloy performance and mechanical properties (Minoda et al. 2003). Wear, pitting corrosion and mechanical properties of AA7075 aluminum alloys are affected by alloying addition such as Cu, Cr, Fe, Mn, Zn and Zr, which either dissolve or form intermetallic compounds within the microstructure and achieve the required strength through precipitation (age) hardening treatment. After heat treatment of AA7075, the precipitate phases such as Mg2Si, Al2Cu and MgZn2 are formed within the dendrite matrix and along grain boundaries (Ramgopal et al. 2002; Zhang and Frankel 2003). The solution heat treatment temperature is the main factor controlling the alloying elements precipitation in the grain boundaries, i.e. large amounts of Mg, Si and Al along with a lesser amount of Zn and Cu. An improvement of strength and wear resistance of AA7075 aluminum alloys is achieved by controlling the size and dispersion of the precipitate particles by solution and aging treatment (Meyveci et al. 2010). Aging to the peak condition formed a complex precipitation of GP-zones and coherent metastable precipitates, while stable and incoherent precipitates start forming in the

over-aged condition. The GP zones and/or semi-coherent MgZn2 (ή) phases are formed, in the temperature range of 20–250 °C (Berg et al. 2001).

In general, the mechanical properties of T6-tempered are controlled by the precipitation sequence in AA7075 aluminum alloy, i.e. supersaturated solid solution (αSSSS) → GP-zones- → η'(MgZn2) → η (MgZn2). The G-P zones are coherent, metastable, solute clusters of Zn, Mg and Cu. However, The metastable η' (MgZn2) or Mg (ZnCuAl)2 platelet particles are semi-coherent within the grains of alloy matrix. Moreover, the non-coherent plates or rods η (MgZn2) and Cu-rich intermetallic θ (Al2Cu) phases are formed along the grain boundaries of AA 7055 aluminum alloy (Zhu et al. 2004). According to Park (Park 1988), the high hardness or strength of the AA7075 aluminum alloy is believed to arise from the high concentration of the fine η' particles within the matrix. The hardness or strength increases as the η' grows to optimum size and distribution. They reach a peak maximum value and then begin to decrease as this η' coarsens excessively and starts transforming to η (Zhu et al. 2004). The microstructure variations (i.e. precipitates size, distribution and volume fraction) affect the mechanical properties and pitting corrosion of AA7075 aluminum alloy. The precipitation of coarse particles has produced a significant reduction in the general/pitting corrosion resistance and low mechanical properties (Ghosh et al. 2015). The high T7 temper corrosion resistance was due to the change in the size and distribution of MgZn2 and Mg2Si precipitates/particles.

In heat-treatable AA7075, there is a tendency for zones relatively free from precipitation to be formed along grain boundaries. This heterogeneous structure gives rise to poor stress corrosion properties. It was reported that a better mechanical property has obtained for AA7075 alloy after double aging treatment due to fine η' particles precipitation within the dendrite matrix. Also, double aging enhances the corrosion resistance of AA7075 alloy since the grain boundary precipitate-free zone in the alloy is removed (Emani 2009). Using a combination of T6 and T73 tempers was recommended to resist stress corrosion cracking (Oliveira et al. 2004; Andretta et al. 2003). However, addition of trace Ag has a beneficial effect in refining the precipitate structure and removing the (PFZ) which improve the alloy corrosion resistance (Smallman 1970). Zielinski et al. (2004) have reported that the T6-tempered treatment (121 °C/24 h) proved the best mechanical properties but with highest susceptibility to stress corrosion cracking (SCC).

The microstructure of AA7075 aluminum alloy is characterized by high intermetallic particles at grain boundaries and inside the grains. Investigation of solidification data and the effect of homogenization, T6-temper, and double aging heat treatment on the microstructure evolution, hardness, wear, corrosion properties and performance of the AA7075 aluminum alloy are very necessary to achieve the optimum properties and the better alloy performance in service.

14.2   Materials and Methodology

Chemical composition (wt%) of AA7075 alloy is listed below in Table 14.1. Weighing of 300 gm from AA7075 alloy was melted in a SiC crucible. Al-5Ti-1B grain-refiner (2.5 gm master alloy) was added to the melt followed by stirring and degassing for 15 min using pure, dry argon. The temperature of the melt was maintained at a 850 ± 5 °C. Following degassing, the melt was poured at 750 ± 5 °C into a preheated graphite mold (i.e., at 550 ± 10 °C).

The solidification curves were plotted, and solidification data obtained were analyzed using thermal analysis technique. A high-sensitivity chromel–alumel (type K) thermocouple was attached to the mold system. The temperature–time data was recorded, and from the first and second derivatives of the solidification cooling rates, different solidification data were obtained. For the solidified AA7075 aluminum alloy, the main reactions observed after solidification were detected. The as-cast samples were homogenized for 8 h at 470 °C, followed by solution treated at 470 °C for 2 h and then cooling in cold water, finally different aging was carried out at 180°C (1-5 h) and 220°C (1-8 h). Double aging (DA) was performed at 120°C (3-6 h) followed by aging at 180C (1-6 h). Macro- and microhardness measurements were carried out for different conditions using a Vickers hardness tester with 10 kgf applied load, and 1kgf, respectively according to ASTM E92. Each hardness data point represents at least the average of five readings.

The wear and corrosion tests were performed for AA7075 in the as-cast, homogenized and different aging treatment conditions. The wear test was performed on standard specimen of 8 mm diameter and of 12 mm height according to ASTM G99 standard. A pin-on-disc machine was used for performing wear test. The pin is loaded vertically downward onto horizontal disc of 100 mm dia. The hardness of disc material that made of stainless steel is 62 HRC. Friction force and coefficient were measured. The wear rate is calculated by knowing the weight loss of AA7075 samples before and after performing the wear test. An electronic weighing scale is used for measuring the weight loss. The test velocity of 0.628 m/s was applied for a time of 600 s, and under a load of 20 N. These test parameters were fixed constant for all tested materials. The sliding distance (L ==π*D*RPM*Time) was calculated, and the value of 376.8 m was obtained. Worn surfaces of AA7075-tested specimens were imaged and characterized by using SEM. Corrosion measurements were performed for different conditions using a Potentiostat/Galvanostat in sodium chloride environment. Corrosion potential (E corr), current (I corr) and rate (CR) were deduced from the polarization curves using Autolab software. Microstructure examination was carried out on polished and etched samples using optical and SEM

Table 14.1   Chemical composition (wt%) of AA7075 alloy

| Alloy code/Alloying	Element (wt%)											
	Si	Cu	Mg	Fe	Mn	Zn	Ag	Zr	Ti	Cr	Pb	Al
Cast AA7075	0.40	1.54	2.20	0.262	0.02	5.85	0.00	0.02	0.10	0.37	0.03	89.19

to examine the precipitate distribution. The etched used was 1 ml HF (48%) plus 200 ml distilled water. Analysis of various particles detected in the microstructure of AA7075 was obtained by energy-dispersive X-ray spectrometer (ED).

14.3   Results and Discussion

14.3.1   Thermal Analysis

Thermal analysis is a powerful tool used for understanding the solidification process in a quantitative manner for achieving enhanced castings properties for AA7075 castings (Hosseini et al. 2013; Hernandez and Sokolowski 2006). Numerous useful solidification data can be obtained. This can be achieved by monitoring the temperature during solidification. The first and second derivatives are obtained from the recorded temperature − time curves, where the onset of major parts of the four solidification reactions is observed as shown in Fig. 14.1. Solidification data results for the AA7075 base alloy, i.e., nucleation temperature (TN), minimum reaction temperature (TM) and end of solidification temperature (TS)) were listed in Table 14.2. The reactions observed during the solidification in Fig. 14.1 are due to the formation of the α-Al dendritic network (peak#1), followed by the precipitation of the precipitation of the Al3Fe intermetallic particles (peak #2), and the precipitation of small dark particles Mg2Si (peak #3) and finally, the precipitation of Al2Cu, MgZn2 and Al2Mg3Zn3 (peak #4).
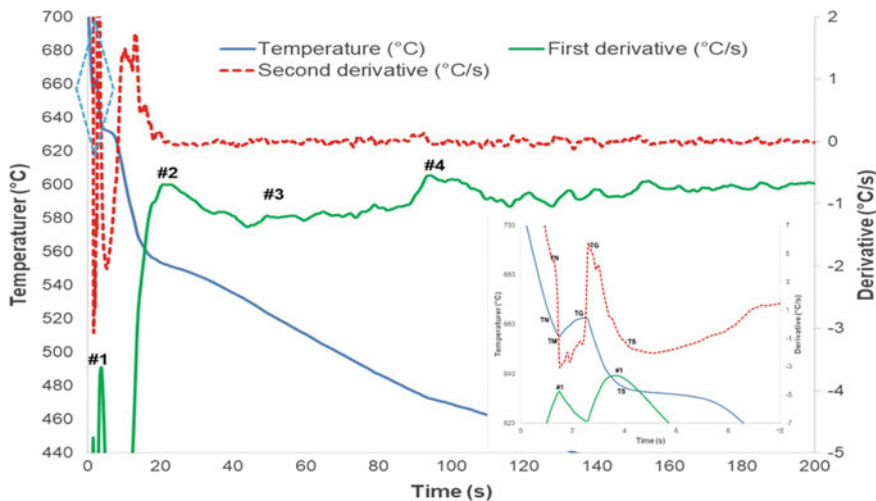
Fig. 14.1 Solidification cooling curves and their first and second derivatives obtained, and the main reactions observed during solidification for the AA7075 aluminum alloy

Table 14.2 Solidification data obtained for AA7075 alloy

Reactions/phases	TN	tN	TM	tM	TS	tS	ΔT N-S	Δt N-S	CR = ΔT/Δt
1. Al, dendrite	641.62	2.2	630.83	4	628.2	7.2	13.42	5	2.68 °C/s
2. Al3Fe intermetallic phases	628.2	7.2	604.26	12.3	556.9	20.5	71.3	13.3	5.36 °C/s
3. Mg2Si intermetallic phases	556.9	20.5	513.53	40.6	477.89	65.6	79.01	45.1	1.75 °C/s
4.Al2Cu + MgZn2 + Al2Mg3Zn3	477.89	65.6	468.84	76.1	463.65	85.4	14.24	19.8	0.72 °C/s
Total solidification cooling rate SCR, °C/s									2.139 °C/s

The solidification data obtained for AA 7075 in this work are in agreement with Bâckerud et al. (1990), where the nucleation temperature (TN), i.e. the first noticeable change on the derivative of the cooling curve; the minimum temperature (TM) prior to recalescence; and the end of solidification temperature (TS), see Table 14.2. The solidification cooling curve, first derivative curve and second derivative curve at the beginning of solidification (0–10 s), i.e., the formation of the α-Al dendritic network (peak #1) are enlarged in Fig. 14.1, indicating solidification data for α-Al dendritic. The main reactions observed during the solidification of AA7075 were due to the formation of a dendritic network of α-Al at 630.83°C, followed by the precipitation of the Al_3Fe intermetallic phase, and the Mg_2Si phase, at 604.26°C and 565°C, respectively and finally the formation of eutectic precipitates of $Al + MgZn_2 + Al_2Cu + Al_2Mg_3Zn_3$ (T-phase) at 468.84°C. The solidification data for eutectic precipitates formation (peak #4) agree with Bäckerud et al. (1990).

The precipitation temperature for Al3Fe phase was 628.2°C and for Mg2Si phase was 557 °C , Table 14.2. The precipitation temperature of Al3Fe phase is higher than that of Mg2Si (557 °C) or eutectic Al2Cu + MgZn2 + Al2Mg3Zn3 phases (477.89 °C). Consequently, Mg2Si, MgZn2, Al2Mg3Zn3 and Al2Cu could be dissolved into the alloy matrix after homogenization and solution heat treatment, while Al3Fe phase is hardly dissolved, which is detrimental to alloy mechanical performance.

14.3.2   Microstructure of AA7075 Alloy

Figure 14.2 displays the microstructures for AA7075 alloy after homogenization and aging treatment. Examples of optical micrographs taken from as homogenized Fig. 14.2a, naturally aged Fig. 14.2b, artificially aged at 180°C-5 h and 220°C-8 h Fig. 14.2c, d, aging at 180 (3 and 5 h) as well as 125 °C preaging (3, 5 and 6 h) Fig. 14.2e–i, respectively. A dendritic microstructure is apparent in all micrographs in Fig. 14.2. Also, it is apparent that with increasing aging temperature or double aging time, the precipitate particles becomes coarser and more numerous. Figure 14.2a shows a micrograph for the homogenized sample at 470 °C for eight hour and furnace cooling, very fine precipitates appear uniformly dispersed throughout the matrix. An equiaxed microstructure appear in Fig. 14.2b for naturally aged (T4) sample. small An equiaxed microstructure of small grain size for duplex aged specimens are observed than those of natural and artificial aging (T4, 180 °C (five hour) and 220 °C (eight hours)), see Fig. 14.2b–i. Very coarse equiaxed microstructure is apparent for sample preaged at 180 (6 h) and aged (6 h) at 125 °C. The microstructure of the peak-aged (T6) temper and double aged conditions contains ή transition phase before the formation of the stable η-MgZn2 phase. The ή transition phase particles are heterogeneously nucleated on dislocation lines. Overall, high concentration of η-MgZn2 coarse transition phase particles is formed in the 220 °C-8 h aged condition.

Figure 14.3 shows the microstructure of as cast AA7075 aluminum alloy at solidification cooling rates of 1.7 °C/s. A dendritic microstructure is apparent in optical micrographs, Fig. 14.3a. The rich Cu-intermetallic phases Al2.82Cu(Mg0.48,
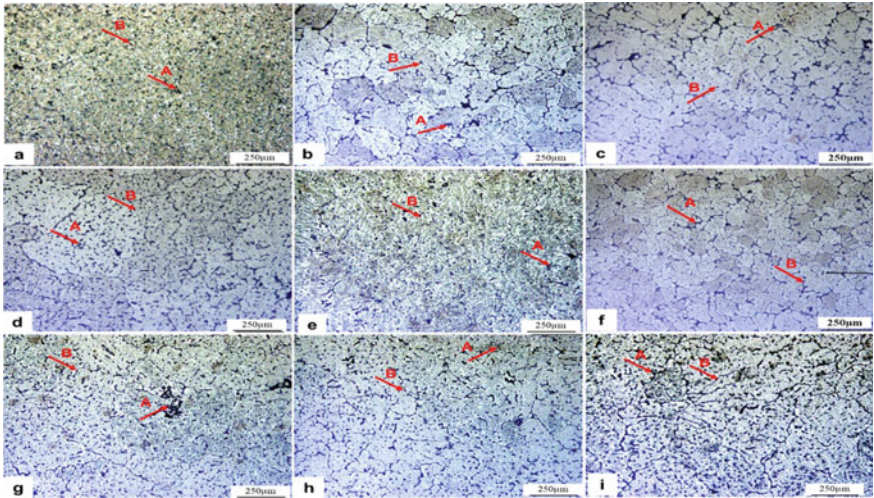
Fig. 14.2 Optical micrographs taken from AA7075 alloy **a** homogenized 470C-8 h, FC, **b** T4_RT-195 h, **c** T6_180 °C - 5 h, **d** T6_220 °C _8h, **e–f** DA-125 °C -(3, 6 h) + 180 °C -3 h, and **g–i** DA-125 °C (3, 5, and 6 h) + 180 °C (5 h)
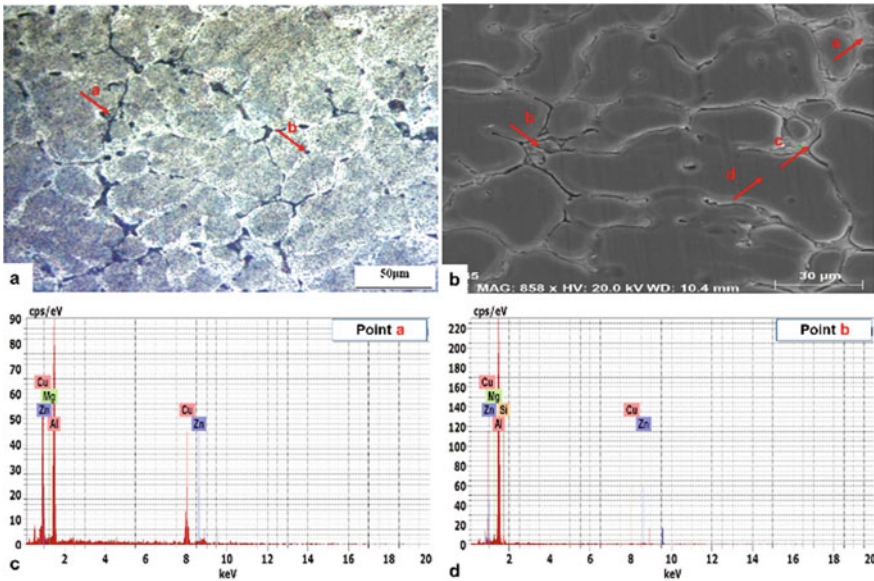
Fig. 14.3 Optical and SEM micrographs taken from the as-cast AA7075 alloy **a–d**, Point **a** Al2.82Cu(Mg0.48, Zn0.52) 0.224, Point **b** Al17 SiZn0.59Mg0.62Cu0.2, Point **c** Al5.2Cu (Mg0.52, Zn0.48) 0.374, and Point **d** Al 63 Mg 0.97 ZnAg0.34

Zn0.52)0.224 and Al5.2Cu (Mg0.52, Zn0.48)0.374 are observed in Point (a) and Point (c) in Fig. 14.3b, respectively with different proportion of Cu. Both Cu-intermetallic phases contains Zn and Mg which indicate that both Zn and Mg go partially in formation of Cu-intermetallic phases. The presence of Al17 SiZn0.59Mg0.62Cu0.2 compact script intermetallic phase are observed in the microstructure, see Point (b) in Fig. 14.3b. The matrix analysis is Al 63Mg0.97ZnAg0.34, which indicate that both Ag, Zn and Mg form solid solution with the Al matrix. It can be concluded that both Zn and Mg are partially going in solid solution and in the formation of Cu-intermetallic phases. The EDS spectra of Point (a) and Point (b), marked in Fig. 14.3b, are presented in Fig. 14.3c, d, respectively. The EDS spectra show the formation of the Al5.62Cu1.668Mg0.228Zn0.102 and Al15.3FeCu1.1Mg0.55Zn0.21Ag0.029 intermetallics. Moreover, the eutectic Cu intermetallic Al10.88Cu Zn1.23Mg1.66 are observed in the microstructure but not presented.

SEM micrographs taken from the homogenized AA7075 alloy are shown in Fig. 14.4. The undissolved rich Al-Cu-Mg-intermetallic phase particles observed in the homogenized microstructure with low and high Zn content, i.e. 5.74CuMg1.09Zn0.11 and Al8.3CuMg1.57Zn2.374, respectively are marked by Point (a) and Point (b) in Fig. 14.4a, respectively. Their EDS spectra are presented in Fig. 14.4b, c, respectively. After homogenization treatment, Mg2Si, AlCuMgSi
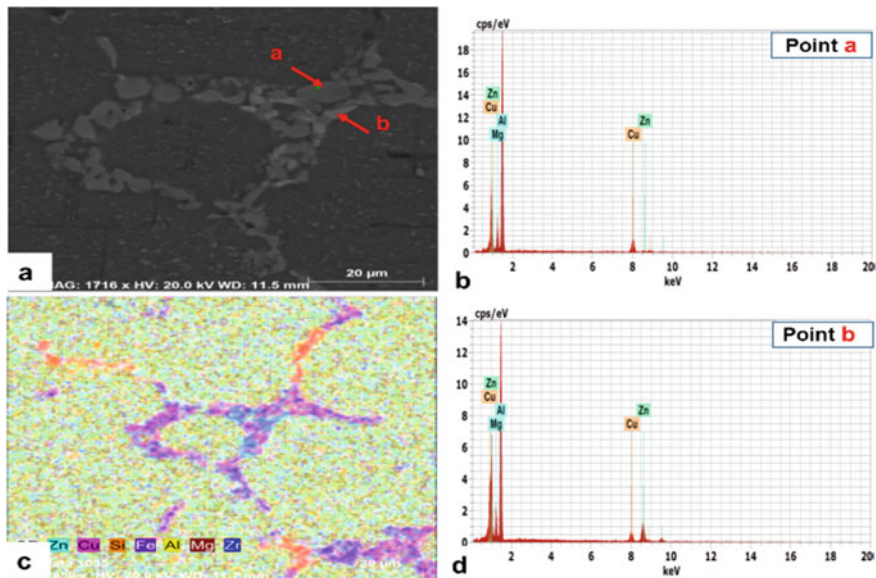
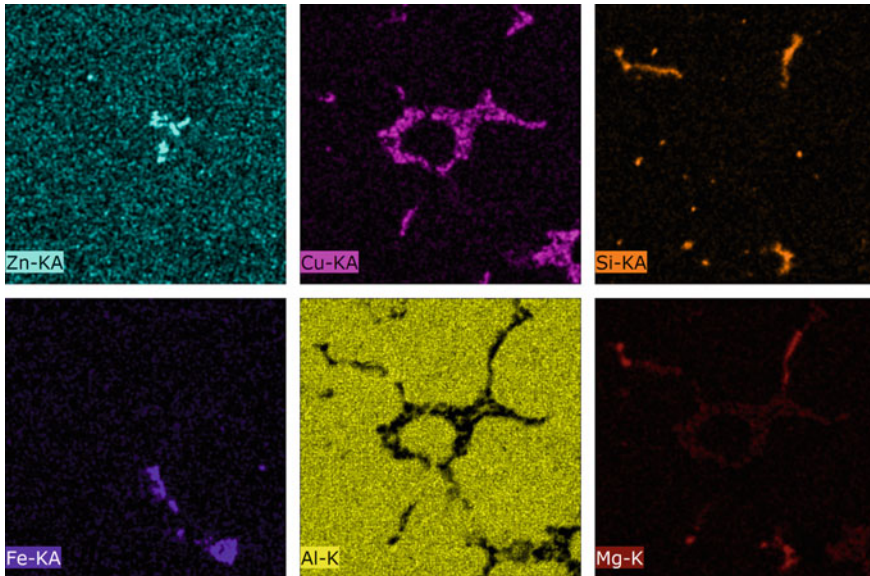
Fig. 14.4 SEM micrographs taken from the as homogenized AA7075 alloy. **a–d** homogenized, Point **a** Al72.28Mg13.73Cu12.61Zn1.38 or Al 5.74CuMg1.09Zn0.11, and Point **b** Al62.62Mg11.85Cu7.57Zn17.97. or Al8.3CuMg1.57Zn2.374

and MgZn2 phases had been dissolved into matrix, although the rich Al-Cu-Mg-intermetallic phase particles with low and high Zn content, i.e., 5.74CuMg1.09Zn0.11 and Al8.3CuMg1.57Zn2.374 intermetallic phases were dissolved rarely, the phases were spheroidized and their size become smaller. The Al-Cu-Zn-Mg-rich intermetallic phases reveal a discontinuous precipitate along the grain boundaries. The presence of Al8.85Cu0.81ZnMg1.35-rich intermetallic phases particles (b) within the grain boundary and within the α-Al dendrite are observed in the microstructure in Fig. 14.4. To better understand these observations, X-ray mapping of intermetallic phases found in SEM micrographs of the homogenized condition is presented in Fig. 14.5.

SEM micrographs taken from AA7075 alloy after homogenization treatment and naturally aged (T4) at room temperature for (195 h), Fig. 14.6. The undissolved rich Al-Cu-Mg-intermetallic phase particles with low and high Cu content, i.e. Al79.64Cu15.32Mg3.8Zn0.94Fe0.11Si0.19 (Point c) and Al65.37 Cu29.9Mg3.97Zn0.69Sb0.06 (Point a) respectively in Fig. 14.6a are observed in the T4 microstructure, and their EDS spectra are presented in Fig. 14.6b, c, respectively. The matrix analysis is Al94.21Mg3.28 Zn1.99 Cu0.4Fe.012, which indicate again that Zn, Cu and Mg form solid solution with the Al matrix. Again, it can be concluded that Zn and Mg are partially going into solid solution and in the formation of Cu-intermetallic phases. The undissolved rich Al-Cu-Mg-intermetallic phase particles with low Cu content marked as Point (a), and with composition


Fig. 14.5 X-ray mapping of intermetallic phases found in the as homogenized AA7075 alloy showing the undissolved AlCu-rich intermetallic phases
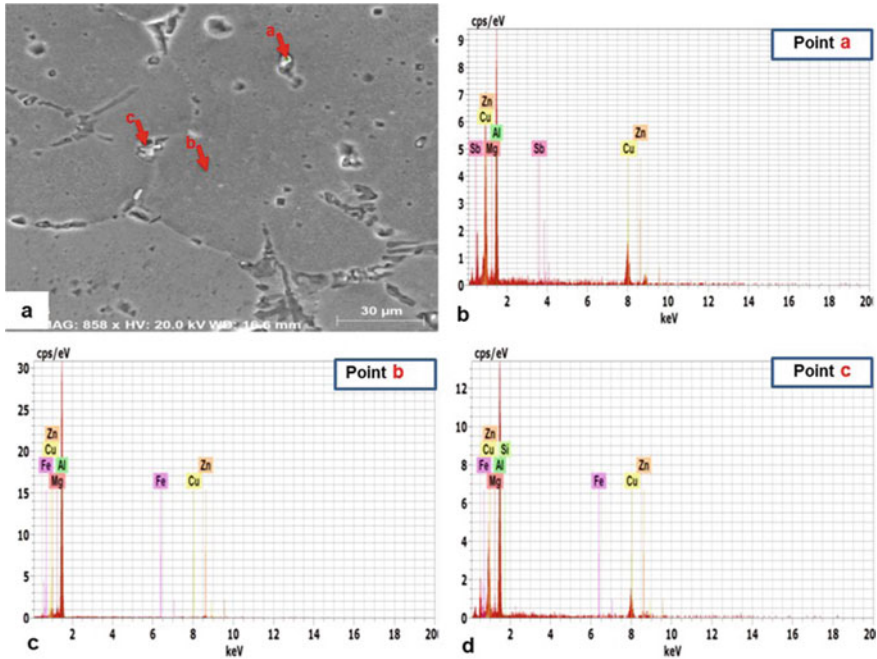
Fig. 14.6 SEM micrographs taken from the As T4 AA7075 alloy **a–d**, Point **a** Al65.37Zn0.69Cu29.9Mg3.97Sb0.06, Point **b** Al94.21Mg3.28Cu0.4Zn1.99Fe.012, and Point **c** Al79.64Cu15.32Mg3.8Zn0.94Fe0.11Si0.19

of Al84.26Cu6.44Fe3.89Zn1.35Mg3.23Si0.7Sb0.13, is observed in the microstructure, see Fig. 14.7. Also, the matrix analysis of Point (b) in the same micrograph is Al93.73Zn2.27Cu0.33Mg3.55Si0.11. To better understand these observations, X-ray mapping of intermetallic phases found in SEM micrographs of naturally aged T4 condition is presented in Figs. 14.7a and 14.8.

SEM micrographs taken from AA7075 alloy after homogenization treatment and artificially aged (T6) at 180C (5 h) are presented in Fig. 14.9. The undissolved rich Al–Ti-Zr-Mg-Cu-Fe-Zn-Cr and Al-Zn-Mg-Cu intermetallic phase particles, i.e., Al71.1Ti14.24Zr3.15Mg2.79Cu2.16Fe2.35Zn1.98Cr1.84Sn0.27Sb0.12 (Point a) and Al89.37Zn3.69Mg3.48Cu2.98Fe0.09Sb0.39 (Point c) respectively in Fig. 14.9 are observed in the microstructure. The matrix analysis is Al93.8Mg3.36Zn2.25Cu0.58 (Point b) which indicates again that Zn, Cu and Mg form solid solution with the Al matrix. Their EDS spectra are presented in Figs. 14.9b–d. Again, the undissolved rich Al-Cu-Mg-intermetallic phase particles with low and high Cu content, i.e., Al78.82Cu15.48Mg3.8Zn1.36Si0.42Fe0.05Sb0.03 (Point b) and Al58.69Cu29.46Mg5Si4.8Zn1.76Sb0.25Fe0.04 (Point a) respectively in Fig. 14.10 are observed in the T6 microstructure, and their EDS spectra are presented in Fig. 14.10c, d, respectively. To better understand these observations, X-ray mapping
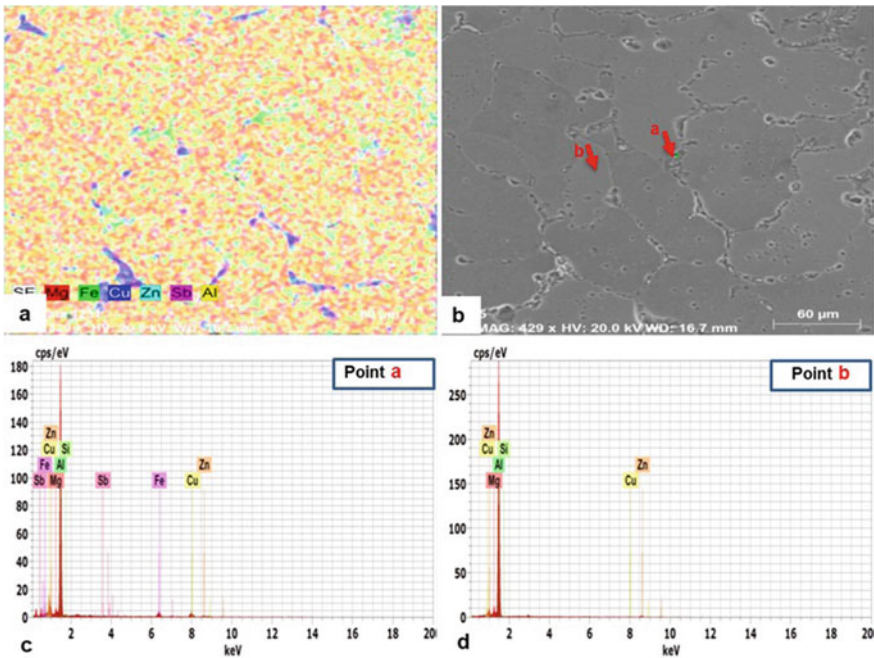
Fig. 14.7 SEM micrographs taken from the as T4 AA7075 alloy. **a–d**, Point **a** Al84.26Cu6.44Fe3.89Zn1.35Mg3.23Si0.7Sb0.13, and Point **b** Al93.73Zn2.27Cu0.33Mg3.55Si0.11

of intermetallic phases found in SEM micrographs of the T4 condition is presented in Figs. 14.10a and 14.11.

14.3.3 Macro and Micro Hardness of AA7075 Alloy

Hardness results of AA7075 aluminum alloy at different heat treatment conditions are illustrated in Fig. 14.12. It is observed from Fig. 14.12 that the hardness is remarkably improved with different double aging treatments conditions (such as preaging at 120 °C-3, 5, 6 h plus aging at 180 °C-3, 5 h). The as homogenized macro- and microhardness values are increased from 79 and 86.3HV to (186.5–195) and (190.5-203HV), respectively. The obtained peak values of double aged samples are almost 1.47 (195HV) and 1.35 (203HV) of the homogenized one. The significant increase in macro and microhardness are mainly due to the presence of undissolved intermetallic particles phases (such as Al8.85Cu0.81ZnMg1.35-rich intermetallic particles) formed during solidification in the matrix. After homogenization and solution heat treatments, Ag, Zn and Mg form solid solution with the Al dendrite and strengthen the matrix. Aging process controls the microstructure of the
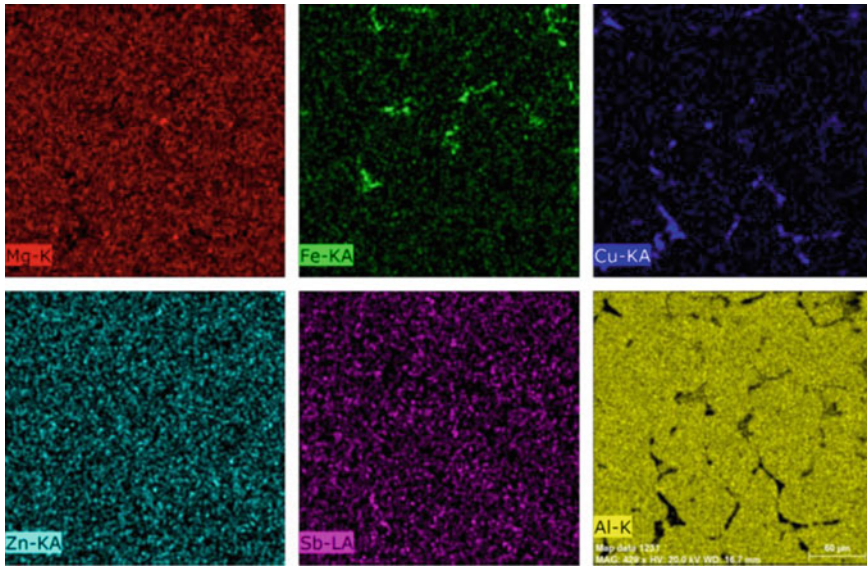
Fig. 14.8 X-ray mapping of intermetallic phases found in the as T4- AA7075 alloy showing the reduction in undissolved AlCu-rich intermetallic phases

grain boundary particles, which is the main parameter controlling the hardness and mechanical properties of AA7075 aluminum alloy. It is believed that the fine dispersion of small ή particles in the aluminum matrix increases the hardness and strength of 7075 aluminum alloy. The high strength of T6 temper arises from the high concentration of particles and the presence of many fine coherent ή (MgZn2) particles in the microstructure. The precipitation of η' (MgZn2), β(Mg2Si), and θ (Al2Cu) phases after aging treatment throughout the grain and grain boundaries strengthen the alloy matrix (Kaya and Atapek 2007; Emani 2009).

14.3.4   Wear Resistance of AA7075 Alloy

Measured data, friction coefficient and calculated wear rate are listed in Table 14.3. The wear rate can be calculated by dividing mass loss (kg) or volume (mm^3) by sliding distance (m). Equation (14.1) used for conversion of mass loss to volume loss, where the density of AA7075 is taken as 2.81 g/cm^3 (Smith 1993). The steady-state wear rate for AA7075 was calculated using Eq. (14.2) (Radhika and Raghu 2015).

$$\text{Volume loss}\left(\text{mm}^3\right) = \text{Mass loss(Kg)}/\text{Density}\left(\text{g/cm}^3\right), \tag{14.1}$$
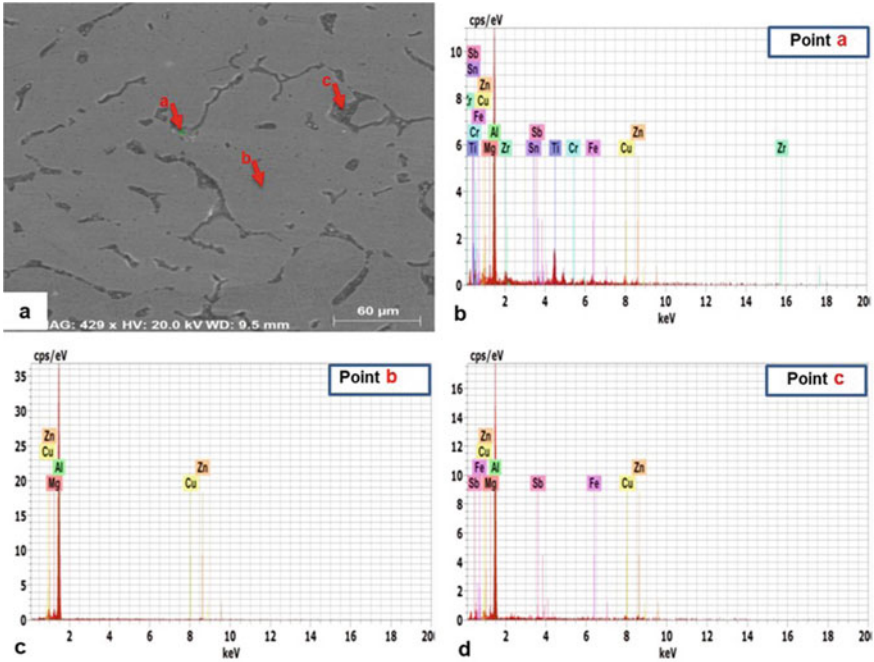
Fig. 14.9 SEM micrographs taken from the as T6 AA7075 alloy **a–d**, Point **a** Al71.1Ti14.24Zr3.15Mg2.79Cu2.16 Fe2.35Zn1.98Cr1.84Sn0. 27Sb0.12, Point **b** Al93.8Mg3.36Zn2.25Cu0.58, and Point **c** Al89.37Zn3.69Mg3.48Cu2.98Fe0.09Sb0.39

$$\text{Wear rate}\left(\text{mm}^3/\text{m}\right) = \text{Mass loss(g)}/\text{Density}\left(\text{g/mm}^3\right) * \text{Sliding Distance(m)},$$
(14.2)

Figure 14.13 shows the variations of wear rate of the different heat-treated samples, compared with the as-cast condition, the heat-treated samples show excellent wear properties. Compared to the wear rate value of the as-cast condition, the values of the homogenized, T4, 180 °C-5 h, and double aging 120 °C-6 h plus 180 °C-5 h samples are 0.3, 0.446, 0.446, and 0.515, respectively. The observed increase in wear resistance after heat treatment may be explained due to the undissolved hard, stable, wear-resistant Al3Fe, β(Mg2Si), Al2Cu, MgZn2 and Al2Mg3Zn3 intermetallic particles phases formed during solidification and the precipitation of η' and η(MgZn2) intermetallic particles phases after aging treatment. After homogenization and solution heat treatment, the η' and η (MgZn2), Al8.85Cu0.81ZnMg1.35-rich intermetallic particles phases are homogenously precipitated inside the matrix and within the grain boundaries. However, Mg and Zn form solid solution and strengthen the aluminum matrix, which improve the alloy wear characteristics.

The wear rate of the AA7075 alloy is remarkably decreased (up to 51.5%) with double aging heat treatment at 120°C-3 h plus 180°C-5 h due to the precipitation of fine magnesium silicide, CuAl2 and MgZn2 intermetallic particles within the
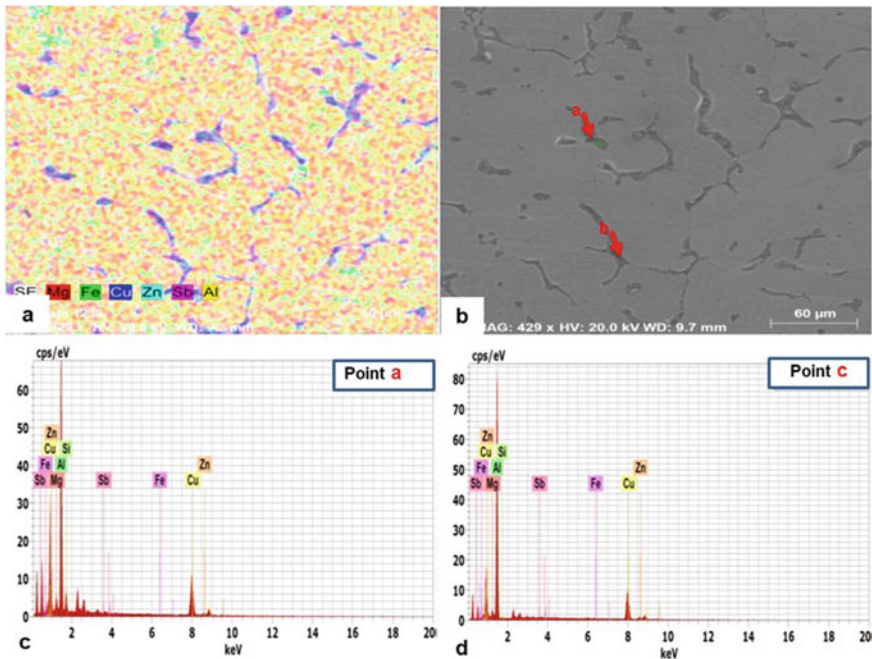
Fig.   14.10 SEM   micrographs   taken   from   the   as   T6   AA7075   alloy.
a–d   Point   **a**   Al58.69Cu29.46Mg5Si4.8Zn1.76Sb0.25Fe0.04,   and   Point
b Al78.82Cu15.48Mg3.8Zn1.36Si0.42Fe0.05Sb0.03

grain boundaries of the Al dendrite matrix. Homogenization, aging and double aging
treatment are remarkably improved the wear resistance of the AA7075 alloy. A
severe adhesive wear was observed on the as-cast sample as shown in SEM images
in Fig. 14.14. Consequently, the width of the wear track enlarged as the contact
area between the pin and the as-cast sample increased. The width of the wear track
decreased with aged samples, Fig. 14.14. The amount of the debris removed from
the as-cast sample toward the sides of the wear track was much more than that in the
double aged samples.

14.3.5   Corrosion Resistance

The observed increase in corrosion resistance may be explained due to the homog-
enized and fine size of the $MgZn_2$-intermetallic particles. The AlCuMgZnAg-rich
intermetallic particles were homogenously distributed along the Al matrix grain
boundaries resulting in removing the precipitate free zone and improving corrosion
resistance. The observed corrosion rate of homogenized AA7075 alloy is very low
(0.009 mm/y) in comparison to as-cast and heat-treated samples, Table 14.4. The
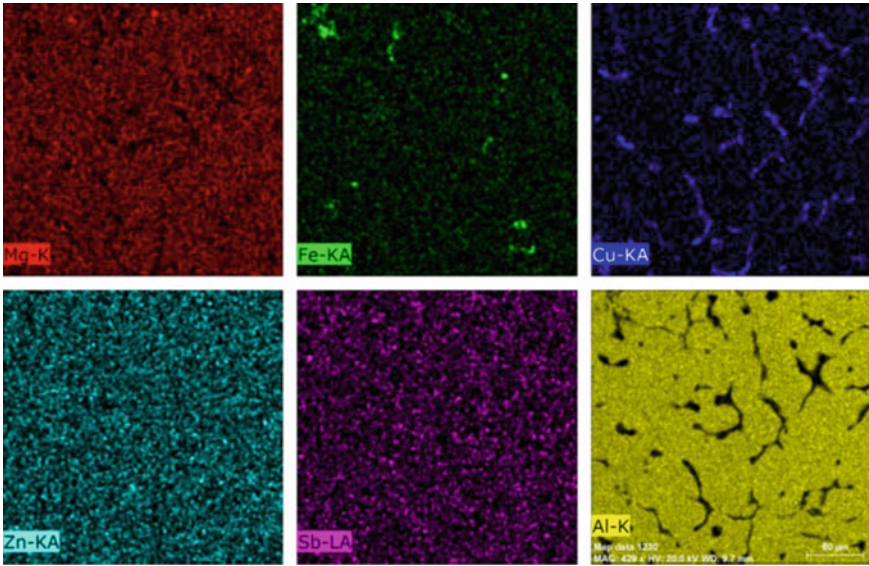
Fig. 14.11 X-ray mapping of intermetallic phases found in the as T6- AA7075 alloy showing the reduction in undissolved AlCu-rich intermetallic phases
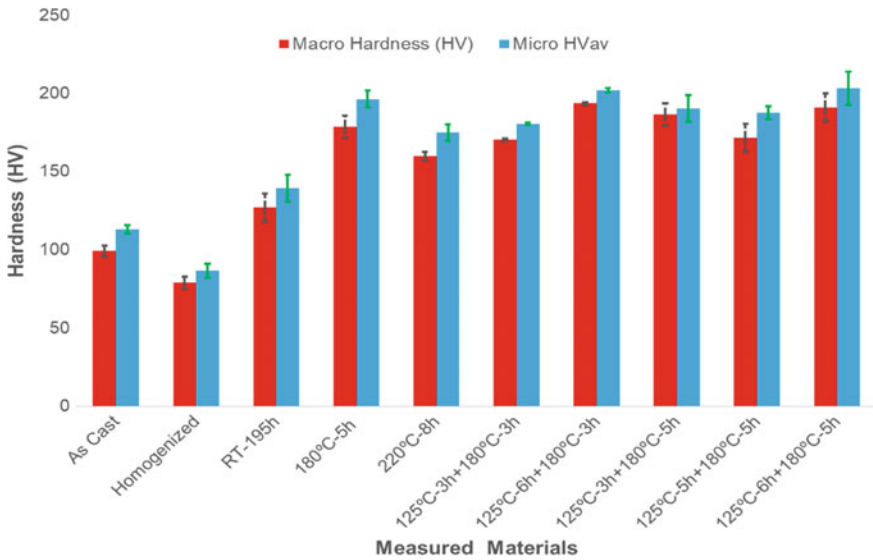
Fig. 14.12 Hardness of AA7075 alloy at different condition, i.e., as cast, homogenized 470C-8 h, FC, T4, Aged_180 °C - 5 h and 220 °C _8h, DA-125 °C (3, 5, and 6 h) + 180 °C (3, and 5 h), and DA-125 °C -6 h + 180 °C -1 h

Table 14.3 Measured data, friction coefficient, and calculated wear rate, i.e., weight loss (kg)/sliding distance (m) or wear rate, i.e., volume (mm^3)/sliding distance (m)

Sample	Mass loss, g	Sliding distance, m	Wear rate (kg/m)	Wear rate (mm3/m)	Frictional force, N	Coefficient of friction
As Cast	0.13	376.8	3.45011E-07	0.12,277,958	3.28	0.164
Homogenized	0.068	376.8	1.80467E-07	0.06,422,316	3.24	0.162
T4_RT-195 h	0.072	376.8	1.91083E-07	0.068,001	3.3	0.165
T6_180 °C-5 h	0.072	376.8	1.91083E-07	0.068,001	3.32	0.166
T6_220 °C-8 h	0.093	376.8	2.46815E-07	0.08,783,462	3.18	0.159
DA_125 °C-3 h + 180 °C-3 h	0.109	376.8	2.89278E-07	0.10,294,595	3.28	0.164
DA_125 °C-6 h + 180 °C-3 h	0.091	376.8	2.41507E-07	0.0,859,457	3.2	0.16
DA_ 120 °C-3 h + 180 °C-5 h	0.063	376.8	1.67197E-07	0.05,950,087	3.22	0.161
DA_120 °C-5 h + 180 °C-5 h	0.11	376.8	2.91932E-07	0.10,389,041	3.3	0.165
DA_120 °C-6 h + 180 °C-5 h	0.106	376.8	2.81316E-07	0.10,011,258	3.16	0.158
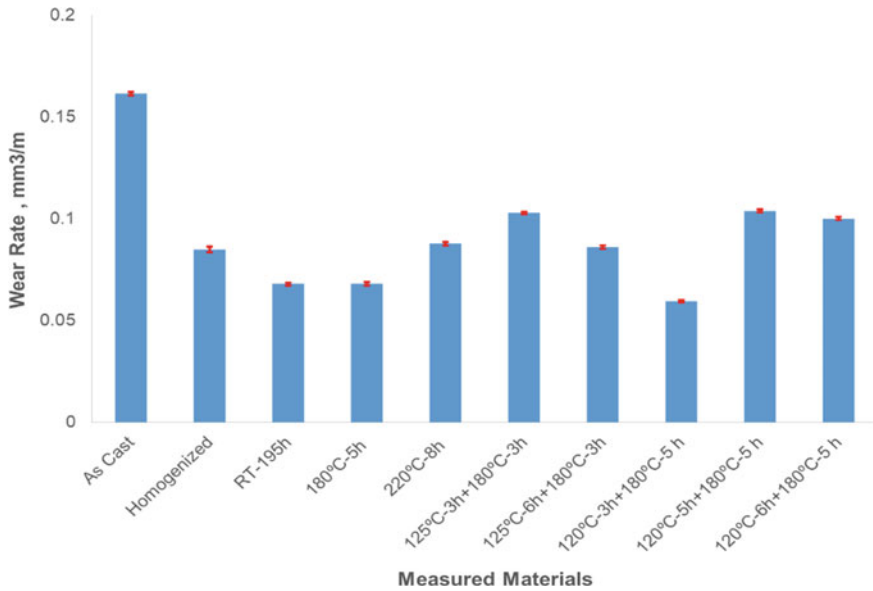
Fig. 14.13 Wear rate mm3/m of AA7075 alloy at different condition, i.e., as cast, homogenized 470 °C -8 h, FC, T4, Aged_180 °C - 5 h and 220 °C _8h, DA-125 °C (3, 5, and 6 h) + 180 (3, and 5 h), and DA-125 °C -6 h + 180 °C -1 h
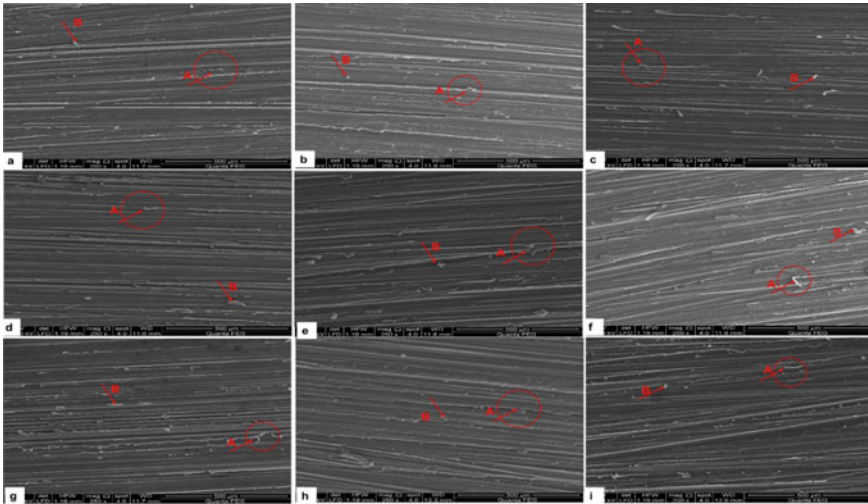
Fig. 14.14 SEM micrographs taken from worn surface of AA7075 alloy at different condition, i.e., **a** as cast, **b** homogenized 470 °C -8 h, FC, **c** T6_180 °C - 5 h, **d** T6_220 °C _8h, **e–f** DA-125 °C -(3, 6 h) + 180 °C -3 h, **g–i** DA-125 °C (3, 5, and 6 h) + 180 °C (5 h)

Table 14.4 Corrosion parameters derived from the polarization curves of the as-cast, homogenized, and heat-treated AA7075 alloy samples in 3.5% NaCl at RT

Sample	I corr (A/cm2)	E corr (V)	CR (mm/y)
As cast	−0.812	3.584×10^{-6}	0.0391
Homogenized	−0.858	8.494×10^{-7}	0.0093
T4_RT-195 h	2.29×10^{-6}	−0.818	0.0190
T6_180 °C-5 h	2.61×10^{-6}	−0.762	0.0220
T6_220 °C-8 h	8.03×10^{-6}	−0.775	0.0680
DA_125 °C-3 h + 180 °C-3 h	−0.812	3.584×10^{-6}	0.0391
DA_125 °C-6 h + 180 °C-3 h	−0.826	2.524×10^{-6}	0.0275
DA_ 120 °C-3 h + 180 °C-5 h	2.14×10^{-6}	−0.78	0.0180
DA_120 °C-5 h + 180 °C-5 h	8.04×10^{-7}	−0.79	0.0070
DA_120 °C-6 h + 180 °C-5 h	2.55×10^{-6}	−0.778	0.0220

corrosion resistance of the AA7075 alloy is remarkably improved with double aging treatment at 125 °C-5 h plus 180 °C-5 h. A high corrosion rate accompanied with more active corrosion potential due to aging at T7 200 °C for 1 h or 8 h. Wei et al. (1998) have observed extensive matrix dissolution around the Fe–Mn-containing and the Al2Cu particles due to Cu deposition onto the particles and Al and Mg dissolution from Al2CuMg particles. As a result, galvanic coupling between these particles and the matrix occurred, which accelerate pitting corrosion of 7075-T6 aluminum alloys (Wei et al. 1998). According to Gao et al. (1998), Fe-Cu-Mn-rich

intermetallic particles act as cathodic to the matrix and promote dissolution of the adjacent matrix. However, Al–Mg-Zn-rich intermetallic particles are anodic with respect to the matrix of AA7075 aluminum alloys and tend to dissolve themselves. Corrosion pits are developed at constituent particles in aluminum alloys due to the differences of electrochemical potentials between the particles and the alloy matrix and between particles themselves, and they act as stress concentration sites leading to stress corrosion cracking (Bartges 1994).

Localized pitting corrosion remains a problem in high-strength AA7075 aluminum alloys containing (Cu, Mg, Zn, Mn, Fe and Cr) due to the differences in electrochemical of the precipitates/particles over the alloy matrix (Zhu et al. 2018). These particles can be either anodic or cathodic with respect to the matrix aluminum. In addition to the strengthening precipitates/particles ($MgZn_2$, and Mg_2Si), elements such as Cu and Fe form intermetallic phases such as Al_7Cu_2Fe and (Al, Cu) 6 (Fe, Cu) are detrimental to the localized corrosion resistance of AA7075 aluminum alloys. The Mg $(ZnCuAl)_2$-rich intermetallic particles containing Zn, Mg and Cu are highly dispersed in the Al solid solution. Dissolution of Al solid solution and/or dealloying of Mg $(ZnCuAl)_2$-rich intermetallic particles in the matrix causes potential breakdown and results in the formation of a passive layer, which limit the depth of attack, making it a transient process in AA 7075 aluminum alloy (Zhu et al. 2018). At high applied potential, the stable pits formed on the matrix by breakdown of the formed passive film. Pitting corrosion usually occurs in the Al matrix near Cu- or Fe-containing intermetallic particles owing to galvanic interaction with the Al matrix (Zhu et al. 2018).

14.4   Conclusions

Based on the thermal analysis, microstructure examination and mechanical performance (hardness, wear and corrosion) results obtained, the following conclusions may be drawn:

1. Al–Mg-Cu-Zn-, Al–Si-Mg-, Al-Cu- and Al–Fe-Cu-Mg-rich intermetallic particles phases such as $Al_{10.88}Zn_{1.23}Mg_{1.66}Cu$, $Al_{7.2}Si_{3.43}MgCu_{0.11}Zn_{0.25}$, $Al_{5.62}Cu_{1.668}Mg_{0.228}Zn_{0.102}$ and $Al_{15.3}FeCu_{1.1}Mg_{0.55}Zn_{0.21}$ are detected in the microstructure of AA7075 Alloy within the α-Al dendrites.
2. Mg and Zn in AA7075 are partially formed solid solution with Al matrix-rich intermetallic particles phases and η' and η'$(MgZn_2)$ intermetallic particle phase precipitation during T4, T6, T7 and double aging (DA) temper treatments.
3. Hardness of AA7075 alloy is remarkably improved after T4, T6, T7 and double aging (DA) temper heat treatment due to the precipitation of η' and η'$(MgZn_2)$ intermetallic particles phases.

4. Wear resistance of AA7075 alloy is remarkably improved after homogenization, T4, T6, T7 and double aging (DA) temper heat treatment.
5. Corrosion resistance of AA7075 alloy casting is remarkably improved after homogenization and double aging treatment at 125 °C (5 h) plus 180 °C (5 h).

References

Andretta, F., Terryn, H., de Wit, J.H.W.: Effect of solution treatment on galvanic coupling between intermetallics and matrix in AA7075-T6. Corr. Sci. **45**, 1733–1746 (2003)

Bäckerud, S.L., Krol, E., Tamminen, J.: (1990) Solidification Characteristics of Aluminum Alloys, vol. 1. Wrought, Oslo, Norway

Bartges, C.W.: Changes in solid solution composition as a function of artificial ageing time for aluminium alloy 7075. J. Mate. Sci. Lett. **13**, 776–778 (1994)

Berg, L.K., Gjnnes, J., Hansen, V., Li, X.Z., K-Wedel, M., Waterloo, G.: GP zones in Al–Zn–Mg alloys and their role in artificial ageing. Acta Mater. **49**, 3443–3451 (2001)

Birbilis, N., Buchheit, R.G.: Corrosion damage accumulation on high strength aluminum alloys: Some advances in understanding the role of intermetallics. Corr. Mater. **29**, 4–10 (2004)

Emani, S.V.: Double aging and thermomechanical heat treatment of AA7075 aluminum alloy extrusions. J. Mater. Sci. **44**(23), 6384–6391 (2009)

Gao, M., Feng, C.R., Wei, R.P.: An analytical electron microscopy study of constituent particles in commercial 7075-T6 and 2024-T3 alloys. Metall. Mater. Trans. A **29**, 1145–1151 (1998)

Ghosh, R., Venugopal, A., Sankaravelayudham, P., Panda, R., Sharma, S.C., George, K.M., Raja, V.S.: Effect of thermomechanical treatment on the environmentally induced cracking behavior of AA7075 alloy. J. Mater. Eng. Perf. **24**(2), 545–555 (2015)

Hernandez, F.C.R., Sokolowski, J.H.: Thermal analysis and microscopical characterization of Al − Si Hypereutectic alloys. J. Alloy. Compd. **419**, 180–190 (2006)

Hosseini, A., Shabestari, S.C., Gholizadeh, R.: Study on the effect of cooling rate on the solidification parameters, microstructure, and mechanical properties of LM13 alloy using cooling curve thermal analysis technique. Mater. Des. **50**, 7–14 (2013)

Huang, T., Franke, G.S.: Influence of grain structure on anisotropic localised corrosion kinetics of AA7xxx-T6 alloys. Corr Eng Sci and Tech **41**, 192–199 (2006)

Kaya, A.I., Atapek, H.: Effect of aging temperature and of retrogression treatment time on the microstructure and mechanical properties of alloy AA 7075. Met. Sci. Heat Treat. **49**(9–10), 443–447 (2007)

Lunarska, E., Trela, E., Szklarska-Smialowska, Z.: Pitting corrosion of powder metallurgy AlZnMg alloys. Corrosion **43**(4), 219–228 (1987)

Meyveci, A., Karacan, I., Calıgulu, U., Durmus, H.: Pin-on-disc characterization of 2xxx and 6xxx aluminium alloys aged by precipitation age hardening. J. of Alloy. Comp. **491**, 278–283 (2010)

Minoda, T., Uchida, H., Shibue, K., YOSHIDA, H.: Influence of iron content on mechanical properties of Al − Mg − Si alloy sheets. J. Japan Inst. Light Met **53**(11), 523–527 (2003)

Oliveira Jr., A.F., De Barros, M.C., Cardoso, K.R., Travessa, D.N.: The effect of RRA on the strength and SCC resistance on AA7050 and AA7150 aluminum alloys. Mater. Sci. Eng., A **379**(1–2), 321–326 (2004)

Park, J.K.: Influence of retrogression and reaging treatments on the strength and stress corrosion resistance of aluminium alloy 7075-T6. Mater. Sci. Eng., A **103**, 223–231 (1988)

Polmear, I.J.: Recent developments in light alloys. Mater. Trans., JIM **37**(1), 12–31 (1996)

Radhika, N., Raghu, R.: Evaluation of dry sliding wear characteristics of LM 13 Al/B4C composites. Tribol. Indus. **37**(1), 20–28 (2015)

Ramgopal, T., Gouma, P.I., Frankel, G.S.: Role of grain-boundary precipitates and solute-depleted zone on the intergranular corrosion of aluminum alloy 7150. Corrosion **58**(8), 687–697 (2002)

Smallman, R.E.: (1970) Modern Physical Metallurgy. 3rd edn., p. 427

Smith, W.F.: (1993) Structure and properties of engineering alloys. 2nd edn, pp. 176–242. McGraw-Hill Series

Wei, R.P., Liao, C.M., Gao, M.: A transmission electron microscopy study of constituent- particle-induced corrosion in 7075-T6 and 2024-T3 aluminum alloys. Metall. Mater. Trans. A **29A**, 1153–1160 (1998)

Zhang, W., Frankel, G.S.: Transitions between pitting and intergranular corrosion in AA2024. Electro Acta **48**, 1193–1210 (2003)

Zhu, G.W., Li, D., Liu, P.Y., Liu, J.H., Guo, B.I.: Influences of Li on corrosion resistance of 7075 and 7055 aluminum alloys. Mater. Forum **28**, 805–810 (2004)

Zhu, Y., Sun, K., Frankel, G.S.: Intermetallic Phases in Aluminum Alloys and Their Roles in Localized Corrosion. J. Electrochem. Soc. **165**(11), C807–C820 (2018)

Zielinski, A., Chrzanowski, J., Warmuzek, M., Gazda, A., Jezierska, E.: Influence of retrogression and reaging on microstructure, mechanical properties and susceptibility to stress corrosion cracking of an Al-Zn-Mg alloy. Mater. Corr. **55**(2), 77–87 (2004)

Part V
Forming

Chapter 15
Numerical Simulation of a Cylindrical Cup Test for Validation of Anisotropic Materials Using Non-associated Flow Rule

R. L. Amaral, A. D. Santos, D. G. Wagre, S. S. Miranda, D. J. Cruz, and J. César de Sá

Abstract A numerical analysis based on associated flow rule (AFR) and non-AFR is presented and applied to anisotropic sheet metals. The models are defined in the quadratic form of the Hill'48 anisotropic function under a general three-dimensional stress condition. The anisotropic parameters for the yield function are identified using the directional planar yield stresses, bulge yield stress and shear yield stress. On the other hand, those for the plastic potential function are determined using the directional r-values. Three different models were implemented into the finite element code, through a developed user subroutine. Two models (r-values based and σ-based) related to AFR and a full expression related to the non-AFR are analyzed for the cup drawing test. Capabilities of the developed model for predicting the anisotropic behavior of sheet metal are investigated by considering cup heights and through-thickness strain distributions obtained from the simulations. Numerical results were compared with experimental data. Such comparisons and corresponding analysis demonstrate that the developed material model considering 3D conditions can improve accuracy when predicting the anisotropic behavior. Furthermore, the simple formulations are efficient and user-friendly for computational analyses and to solve common industrial sheet metal forming problems.

Keywords Dual-Phase steels · Sheet metal forming · Limiting drawing ratio · Swift test · Deep drawing cylindrical cup

R. L. Amaral (✉) · A. D. Santos · D. G. Wagre · S. S. Miranda · D. J. Cruz · J. C. de Sá
INEGI, Institute of Science and Innovation in Mechanical and Industrial Engineering, R. Dr. Roberto Frias, 400, 4200-465 Porto, Portugal
e-mail: ramaral@inegi.up.pt

A. D. Santos · J. C. de Sá
FEUP, Faculty of Engineering, University of Porto, R. Dr. Roberto Frias, 4200-465 Porto, Portugal

15.1 Introduction

Sheet metal forming is one of the most common metal processing manufacturing technologies, representing an important sector due to corresponding production volume and competitiveness. Among the several sheet metal forming operations, deep drawing is one example where higher accuracy is required relative to the final product's geometry and mechanical properties. Taking this into account, it has therefore become apparent that the traditional trial-and-error method of optimizing metal forming operations is no longer adequate and currently existing methodologies are able to be incorporated for efficiency and accuracy of results.

An effective way of reducing the time and costs involved in optimizing manufacturing processes is the use of numerical simulation. Indeed, numerous complex forming operations have been simulated numerically in order to predict and optimize critical parameters, so that during the tryout of a forming process, it is possible to foresee various phenomena that are usually found in the formed part, such as fracture, excessive thinning, wrinkles, buckling, springback and other surface defects.

The simulation of sheet metal forming processes receives continuously increasing attention from the material science society and the computational community. Due to its high efficiency and relatively low cost, numerical simulation has become an essential tool for optimizing the process parameters and solving the problems in the design stage of products and the manufacturing processes. Therefore, for the accurate numerical modeling of sheet metal forming processes, the use of suitable material models that correctly describe material behavior is currently a fundamental need.

One of the characteristics of rolled sheet metal materials is that they exhibit anisotropic behavior, which affects the formability of the final part (Wali et al. 2016) and is commonly described by the Lankford coefficients (r-value) and yield stresses for defined orientations relative to the rolling direction. Hence, an accurate and appropriate anisotropic constitutive model is essential to improve the accuracy and efficiency of the manufacturing process numerical simulations.

Various anisotropic models have been proposed to analyze and reproduce the sheet metal forming processes anisotropic behavior. The classical Hill'48 (Hill 1948) quadratic function, which applies the yield stresses to describe anisotropy, is the original yield function for anisotropic sheet metals.

Like Hill'48 yield criterion, other proposed models to reproduce the anisotropic sheet metal behavior have been developed based on the associated flow rule (AFR) (Barlat et al. 1997; Yoon et al. 2006; Ming and Pantalé 2018), which follows the classical normality rule, stating that the yield surface and plastic potential surface are identical. Although the Hill'48 function has a simple quadratic form and can describe the orthotropic anisotropy for some metals with accuracy, it shows some limitations in accurately predicting material behaviors under complex loading conditions.

Advanced AFR anisotropic constitutive models with very complex expressions are being used to improve the numerical predictions. However, while accuracy may

be improved, the parameter identification process becomes more complex and challenging. Also, some studies (Stoughton 2002; Cvitanic et al. 2008) show that some anisotropic materials cannot always satisfy the AFR constraints.

As an alternative, recent efforts (Wali et al. 2016; Cvitanic et al. 2008; Taherizadeh et al. 2009; Wang et al. 2014; Lian et al. 2018; Tang et al. 2019; Wu et al. 2020) have been made to develop numerical analysis methods based on non-associated flow rule (NAFR) formulations. The plastic flow rule is disassociated from the yield criteria by introducing a new expression for the plastic potential. This type of formulation is able to reproduce simultaneously and independently the plastic flow (r-values) and the plastic yielding (yield stress coefficients).

Although the concept of NAFR to improve elastoplastic behavior was discussed by Melan back in 1938 (Melan 1938), it seems that the engineering applications are relatively recent. The NAFR constitutive model could be implemented to improve the accuracy of solutions. Still, the work conjugate rule should be followed to keep the theoretical continuity (Safaei et al. 2018; Mendiguren et al. 2018).

In this work, a NAFR formulation using the Hill'48 yield criterion was developed and implemented in the commercial FE code Abaqus via a user-defined material subroutine (VUMAT). To evaluate its performance and accuracy on the results of FE simulations, a deep drawing cylindrical cup test was performed, using the dual-phase steel (DP780). The corresponding numerical model was created based on a 3D Abaqus/Explicit analysis.

Cup height evolution along with different directions relative to the rolling direction and through-thickness strain were extracted and compared with available experimental data.

15.2 Non-associated Flow Rule Formulation

In general, the development of plasticity criteria is based on the associated flow rule (AFR), in which the yield and plastic potential functions are identical and follow the assumption of normality, as shown in Fig. 15.1. Of the implemented criteria in the numerical simulation of sheet metal forming processes, most are governed by the associated flow rule, in which the results obtained show a good similarity with the experimental data. However, studies have shown that for some anisotropic materials, both steel and aluminum alloys, the plastic behavior prediction accuracy would need improvement.

This fact is due to the limitation of AFR law in describing the yield stresses and the plastic anisotropic coefficients simultaneously through only one function, as shown in Fig. 15.2.

As seen in Fig. 15.2, the yield stresses are well modeled by the set of parameters *AFR-Set1*, but the plastic anisotropic coefficients are not correctly predicted. In the case of the *AFR-Set2*, the anisotropy coefficients are properly described; however, the evolution of yield stresses does not show any agreement with the experimental points.
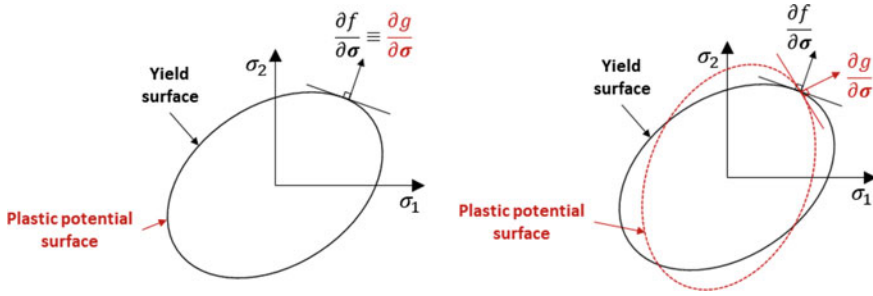
Fig. 15.1 Different types of plastic flow directionality: associated flow rule (left) and non-associated flow rule (right)
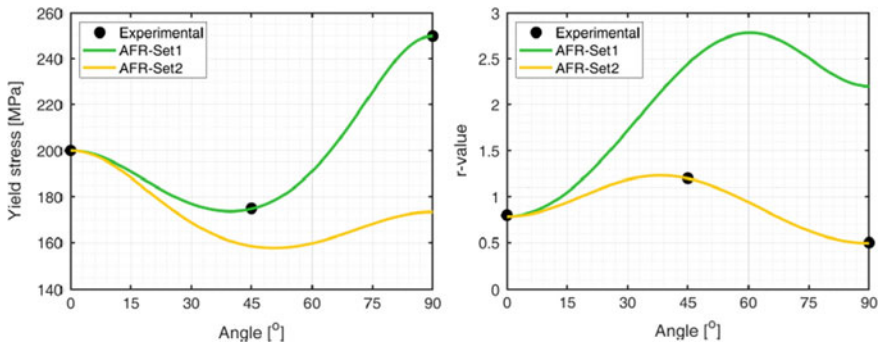
Fig. 15.2 Prediction of the yield stresses and r-values for different orientations relative to the rolling direction based on AFR using two sets of parameters: yield stresses (left) and plastic anisotropic coefficients (right)

To overcome the challenge of modeling the anisotropic behavior of metallic materials with accuracy, some more advanced and sophisticated models have been proposed to predict the material's behavior in these two aspects (yield stress and anisotropy coefficients) (Barlat et al. 2003; Barlat et al. 2005; Banabic 2005; Vegter and van den Boogaard 2006). Although the accuracy can be improved, the parameter identification process also becomes more complex, as more experimental data is needed, increasing the required work, verification time and computational cost.

To overcome the limitations of the associated flow rule, recently, increasing attention has been given to the non-associated flow rule (NAFR) and several approaches have been proposed (Stoughton 2002; Stoughton and Yoon 2006; Safaei et al. 2014), where the yield surface and the plastic potential surface are described by two unrelated and independent functions (Fig. 15.1). This approach allows the possibility of describing the material's behavior with higher accuracy, as shown in Fig. 15.3.

As seen from the predictions in Fig. 15.3, it is possible to describe both yield stresses and anisotropy coefficients. Since there are two functions for NAFR, the constitutive coefficients can also be separated, one set for the yield surface and
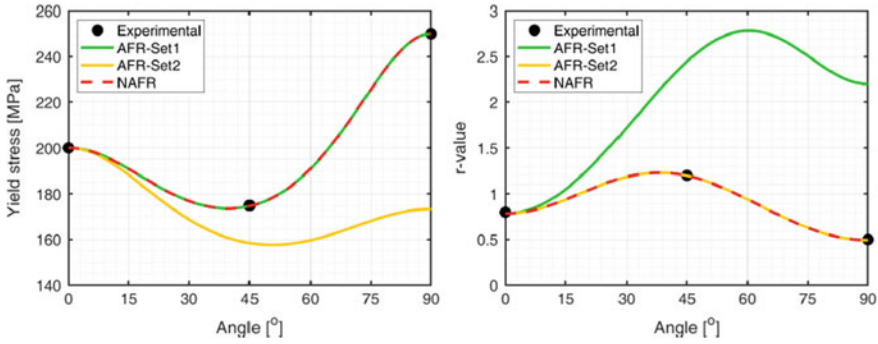
Fig. 15.3 Comparison of the yield stresses and r-values predictions for different orientations relative to the rolling direction based on AFR and NAFR: yield stresses (left) and plastic anisotropic coefficients (right)

another for the plastic potential surface. This independence reduces the difficulty and complexity in the identification process of such parameters compared with the AFR (Stoughton 2002). However, for both cases, there is an increasing complexity of mathematical formulations with an increase in the constitutive model flexibility.

The formulation algorithm presented in box 1 shows the integration scheme and variables identification process used in the formulation of NAFR. Usually, for the AFR model, the plastic multiplier is equal to the equivalent plastic strain increment $(\Delta\lambda = \Delta\bar{\varepsilon}^p)$, and the following scheme can be used in an AFR formulation, assuming that $\frac{\partial\psi}{\partial\boldsymbol{\sigma}} = \frac{\partial\phi}{\partial\boldsymbol{\sigma}}$ and $\frac{g(\boldsymbol{\sigma})}{f(\boldsymbol{\sigma})} = 1$. Although, for the case of NAFR, this does not happen anymore ($\Delta\lambda \neq \Delta\bar{\varepsilon}^p$ because $\frac{\partial\psi}{\partial\boldsymbol{\sigma}} \neq \frac{\partial\phi}{\partial\boldsymbol{\sigma}}$ and $\frac{g(\boldsymbol{\sigma})}{f(\boldsymbol{\sigma})}$ can take any positive value), so a more complex and precise approach is needed (Mendiguren et al. 2018; Stoughton 2002), as expressed from Eqs. 15.7–15.10. Finally, the consistency condition ensures that the stress state remains on the yield surface during plastic deformation.

Box 1: Algorithm of state update procedure for NAFR implementation

1. Elastic predictor

   (i) Given an elastic trial strain $\varepsilon^e_{n+1} = \varepsilon^e_n + \Delta\varepsilon^e$, evaluate elastic trial stress:

$$\boldsymbol{\sigma}^{\text{trail}}_{n+1} = \boldsymbol{\sigma}_n + \boldsymbol{D} : \Delta\boldsymbol{\varepsilon}^e \tag{15.1}$$

   (ii) Check plastic consistency:

$$\text{if} \quad \phi\big(\boldsymbol{\sigma}^{\text{trail}}_{n+1}, \bar{\varepsilon}^p_n\big) = f\big(\boldsymbol{\sigma}^{\text{trail}}_{n+1}\big) - \boldsymbol{\sigma}_Y\big(\bar{\varepsilon}^p_n\big) \leq 0 \tag{15.2}$$

$$\boldsymbol{\sigma}_{n+1} = \boldsymbol{\sigma}^{\text{trail}}_{n+1} \tag{15.3}$$

$$\bar{\varepsilon}^p_{n+1} = \bar{\varepsilon}^p_n \tag{15.4}$$

$$\boldsymbol{\varepsilon}^P_{n+1} = \boldsymbol{\varepsilon}^P_n \tag{15.5}$$

else go to 2.

2. Plastic corrector by solving the system for the unknowns

  (i) Newton-Raphson method is computed for each step (i) as follow:

$$d\Delta\lambda = \frac{\phi\left(\boldsymbol{\sigma}^{\text{trail}}_{n+1}, \bar{\varepsilon}^p_n\right)^i}{\left(\frac{\partial\phi}{\partial\boldsymbol{\sigma}} : \boldsymbol{D} : \frac{\partial\psi}{\partial\boldsymbol{\sigma}} + H \frac{g(\boldsymbol{\sigma})}{f(\boldsymbol{\sigma})}\right)^i_{n+1}} \tag{15.6}$$

$$\boldsymbol{\sigma}^{i+1}_{n+1} = \boldsymbol{\sigma}^i_{n+1} - d\Delta\lambda\left(\boldsymbol{D} : \frac{\partial\psi}{\partial\boldsymbol{\sigma}^i_{n+1}}\right) \tag{15.7}$$

$$\Delta\lambda^{i+1}_{n+1} = \Delta\lambda^i_{n+1} + d\Delta\lambda \tag{15.8}$$

$$\Delta\bar{\varepsilon}^p_{n+1} = \Delta\lambda^{i+1}_{n+1}\left(\frac{g(\boldsymbol{\sigma})}{f(\boldsymbol{\sigma})}\right)^i_{n+1} \tag{15.9}$$

$$\bar{\varepsilon}^{p(i+1)}_{n+1} = \bar{\varepsilon}^{p(i)}_{n+1} + \Delta\bar{\varepsilon}^p_{n+1} \tag{15.10}$$

$$\text{if } \phi\left(\boldsymbol{\sigma}^{i+1}_{n+1}, \bar{\varepsilon}^{p(i+1)}_{n+1}\right) \cong 0 \tag{15.11}$$

Update variables
else go to (i)

3. Return

15.2.1 Hill'48 Yield Function

In 1948, Hill introduced a generalization of the von Mises quadratic isotropic criterion for anisotropic materials (Hill 1948), being one of the most popular and comprehensive yield functions used in sheet metal forming processes simulation. When the axes of the coordinate system match with the axes of orthotropy, the equivalent stress of Hill'48 yield function is given by the following expression:

$$f(\boldsymbol{\sigma}) = \bar{\sigma}_f = \left[\begin{array}{c} F^*\left(\sigma_{yy} - \sigma_{zz}\right)^2 + G^*(\sigma_{zz} - \sigma_{xx})^2 + H^*\left(\sigma_{xx} - \sigma_{yy}\right)^2 \\ +2\left(L^*\tau_{yz}^2 + M^*\tau_{yz}^2 + N^*\tau_{xy}^2\right) \end{array} \right] \quad (15.12)$$

where F, G, H, L, M e N are the anisotropic material parameters, σ_{xx}, σ_{yy} and σ_{zz} are the yield stresses in the rolling direction (x), transversal direction (y) and thickness direction (z), respectively, being τ_{xy}, τ_{yz} and τ_{zx} the shear stress components.

Hill'48 criterion parameters identification method is based on yield stresses using Eq. 15.13 and assuming that $G + H{=}1$.

$$\begin{cases} F^* = \frac{\sigma_0^2}{2}\left(\frac{1}{\sigma_{90}^2} + \frac{1}{\sigma_b^2} - \frac{1}{\sigma_0^2}\right) \\ G^* = \frac{\sigma_0^2}{2}\left(-\frac{1}{\sigma_{90}^2} + \frac{1}{\sigma_b^2} + \frac{1}{\sigma_0^2}\right) \\ H^* = \frac{\sigma_0^2}{2}\left(\frac{1}{\sigma_{90}^2} - \frac{1}{\sigma_b^2} + \frac{1}{\sigma_0^2}\right) \\ N^* = \frac{1}{2}\frac{\sigma_0^2}{\tau_{xy}^2} \end{cases} \quad (15.13)$$

where σ_0 and σ_{90} are the angles 0° and 90° relative to the rolling direction, respectively; σ_b the biaxial yield stress (for thin metal sheets, it is very demanding to measure the tensile yield stress in the through-thickness direction) and τ_{xy} the yield stress obtained from a shear test.

The expressions to identify the parameters L^* and M^* are omitted in Eq. 15.13, as for small thickness materials, such as the case of sheet metal materials, it is challenging to evaluate the out-of-plane shear yield stress (τ_{yz} and τ_{zx}) using the standard experimental tests. Therefore, it is assumed that $L = M{=}1.5$.

Several authors (Park and Chung 2012; Wu et al. 2019) started to use another approach to calculate the parameter N by using the yield stress σ_{45}, as expressed in Eq. 15.14. This method is used due to the difficulty in carrying out and obtaining data from shear tests.

$$N^* = \frac{\sigma_0^2}{2}\left(\frac{4}{\sigma_{45}^2} - \frac{1}{\sigma_b^2}\right) \quad (15.14)$$

By applying a NAFR formulation, the plastic potential surface is no longer defined by the yield surface function $f(\boldsymbol{\sigma})$. Although the Hill'48 function can used to define both yield and plastic potential surfaces by using different sets of parameters, a new function $g(\boldsymbol{\sigma})$ is needed. This is a requirement to accurately reproduce the anisotropic material behavior, as previously presented in Sect. 15.2.

The expression that defines the plastic potential and the corresponding equivalent stress is given by:

$$g(\boldsymbol{\sigma}) = \bar{\sigma}_g = \left[\begin{array}{c} F\left(\sigma_{yy} - \sigma_{zz}\right)^2 + G(\sigma_{zz} - \sigma_{xx})^2 + H\left(\sigma_{xx} - \sigma_{yy}\right)^2 \\ +2\left(L\tau_{yz}^2 + M\tau_{yz}^2 + N\tau_{xy}^2\right) \end{array} \right] \quad (15.15)$$

The parameters F, G, H and N present in Eq. 15.15 are commonly identified based on the plastic anisotropy coefficients for 0º, 45º and 90º relative to the rolling direction, i.e. r_0, r_{45} and r_{90}, respectively. The identification of the parameters is defined by:

$$\begin{cases} F = \frac{r_0}{r_{90}(1+r_0)} \\ G = \frac{1}{1+r_0} \\ H = \frac{r_0}{1+r_0} \\ N = \frac{1}{2}\left[\frac{(r_0+r_{90})(1+2r_{45})}{r_{90}(1+r_0)}\right] \end{cases} \tag{15.16}$$

The ability to accurately reproduce the sheet metal material behavior is directly dependent on the methodology used to identify the constitutive Hill'48 parameters. For example, the AFR can describe the yield stresses evolution (Fig. 15.3 left) and the plastic anisotropic coefficients evolution (Fig. 15.3 right) for different angles relative to the rolling direction, using one function but based only on stress parameters c or on r-values (Fig. 15.3 AFR-Set2).

In the case of the NAFR (Fig. 15.3), it is possible to describe both yield stresses and anisotropy coefficients since there are two functions and the constitutive coefficients can also be separated, one set for the yield stresses and another for the r-values evolution.

## 15.3 Material Mechanical Behavior

The sheet material used in the present study is a DP780 steel, a material of current interest in the automobile industry for its good balance on strength and formability due to their microstructure, in which a hard martensitic is dispersed in a ductile ferritic matrix. The mechanical characterization of DP780 steel has also been addressed by Amaral et al. (Amaral et al. 2017). Several experimental tests were performed to obtain fundamental material properties: uniaxial tensile test, hydraulic bulge test, shear test and also the evaluation of the plastic strain ratios. Table 15.1 presents all the collected information of DP780 needed to identify the Hill'48 yield criterion parameters considering associated flow rule and non-associated flow rule formulations. The Swift law describes the hardening behavior of DP780, and the corresponding stress–strain flow curve is shown in Fig. 15.4.

Different methodologies were considered regarding the various possibilities of reproducing material anisotropic behavior based on r-values or yield stresses, using associated and non-associated flow rules. Figure 15.5 presents the terminology used in this study to identify the different methods.

The *SiP* corresponds to the parameters identified considering yield stresses and using the N parameter based on yield stress at 45º relative to the rolling direction (σ_{45}). On the other hand, the *S3D* corresponds to the constitutive parameters also

Table 15.1 Mechanical properties of the dual-phase steel

Elastic modulus [GPa]	210	
Poisson's ratio	0.3	
Thickness [mm]	0.8	
Yield stress [MPa]	0°	526.2
	45°	537.7
	90°	517.8
Biaxial stress [MPa]	566.4	
Shear stress [MPa]	315.7	
r-values	0°	0.7
	45°	1.05
	90°	0.88
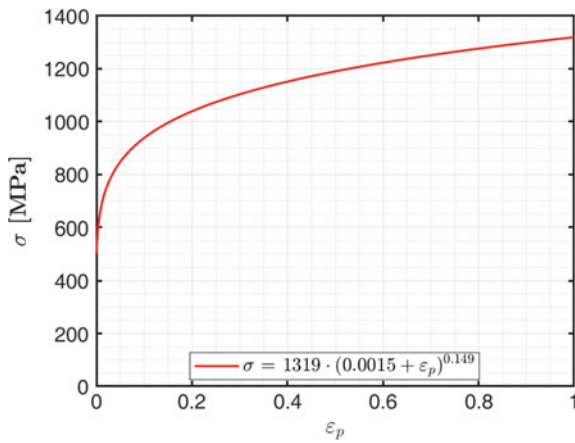
Fig. 15.4 True stress–strain flow curve of DP780 considering Swift hardening law

$$\sigma = 1319 \cdot (0.0015 + \varepsilon_p)^{0.149}$$

	Method		Terminology
1.	AFR	r-based	AFR-R
2.	AFR	σ-based	AFR-SiP (based on Np using σ_{45})
3.	AFR		AFR-S3D (based on N3D using τ_{xy})
4.	NAFR	r-based+ σ-inPlane	NAFR-SiP
5.	NAFR	r-based+ σ-3D	NAFR-S3D

Fig. 15.5 Terminology defined in the analysis of the different AFR and NAFR methods

Table 15.2 Identified Hill'48 yield criterion parameters for an associated flow rule considering the different methodologies (r-values based and stress based)

r-values based (**AFR-R**)					σ based (**AFR-SiP + AFR-S3D**)					
F	G	H	L = M	N	F*	G*	H*	L* = M*	Np*	N*$_{3D}$
0.468	0.588	0.412	1.5	1.64	0.45	0.42	0.58	1.5	1.48	1.39

identified based on yield stresses but using the shear stress (τ_{xy}) to calculate the N parameter.

Table 15.2 presents the identified Hill'48 yield criterion parameters for the associated flow rule formulation. Figure 15.6 shows the comparison between the obtained yield surfaces in the principal stress plane and the predicted evolution of the anisotropic plastic strain ratios (r-values) and the yield stresses for different angles relative to the rolling direction.

The comparison with the experimental data indicates that the evolution of anisotropy coefficients is properly described by the AFR using r-values. Still, the

Fig. 15.6 Hill'48 yield criterion prediction using an associated flow rule for DP780: **a** yield surfaces; **b** and **c** r-value and yield stress evolution with the angle relative to the rolling direction, respectively
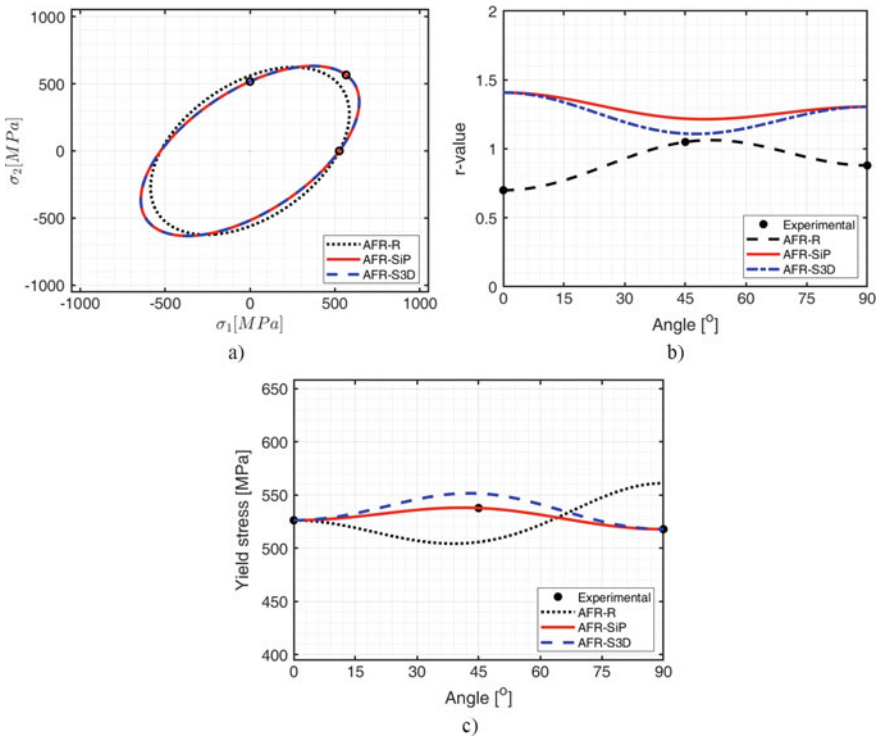
Table 15.3 Identified Hill'48 yield criterion parameters for a non-associated flow rule considering the different methodologies (r-values based and stress based)

Potential surface r-values based					Yield surface σ based					
F	G	H	$L = M$	N	F^*	G^*	H^*	$L^* = M^*$	Np^*	N^*_{3D}
0.468	0.588	0.412	1.5	1.64	0.45	0.42	0.58	1.5	1.48	1.39

evolution of yield stresses does not show any agreement with the experimental points. On the other hand, the stress-based parameters cannot predict the r-values, having an opposite tendency. A difference that can be observed between in-plane and 3D approaches is the yield stress at 45° prediction, since S3D does not use such property, it may not pass through the experimental point.

For a non-associated flow rule approach, the identified Hill'48 yield criterion parameters are presented in Table 15.3. The corresponding predicted yield and potential surfaces shown in Fig. 15.7, as well as the obtained r-values and yield stress evolution curves.
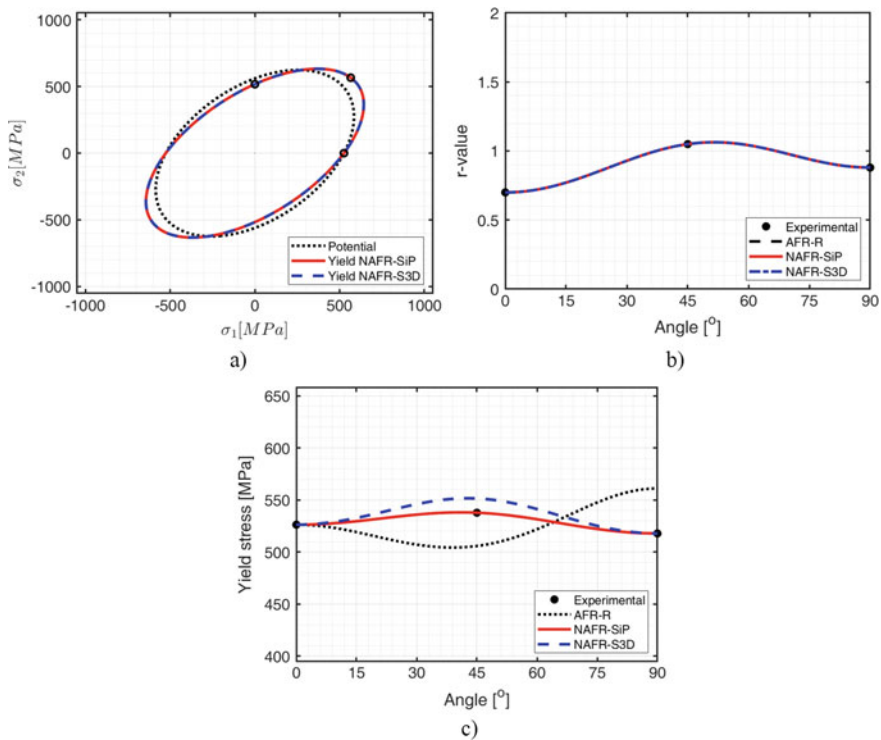
Fig. 15.7 Hill'48 yield criterion prediction using a non-associated flow rule for DP780: **a** yield and potential surfaces; **b** and **c** r-value and yield stress evolution with the angle relative to the rolling direction, respectively

One of the advantages of using the non-associated flow rule formulation is the capability to describe simultaneous the r-values and yield stress evolution, as seen in Fig. 15.7b–c). In the case of yield stress predictions, the same difference is observed for *SiP* and *S3D*, as already mentioned.

15.4   Cylindrical Cup Drawing Test

The cylindrical cup test is performed at a universal sheet metal testing machine, as shown in Fig. 15.8a. The experimental tool setup and schematic used for the cylindrical cup test is presented in Fig. 15.8b. Additionally, a lubricant was applied to both sides of the circular blank, having an initial diameter of 114 mm, to reduce the friction forces between the blank and tools contacting surfaces during the experimental tests.

A 3D finite element numerical model was implemented in Abaqus/Explicit code, using rigid tools with analytical surfaces. The blank is discretized with 8-node linear brick deformable elements with reduced integration (C3D8R, available in the Abaqus library), having three elements along the thickness. The mesh for the blank is presented in Fig. 15.9, considering half of the experimental blank due to the symmetry and according to the applied methodology.
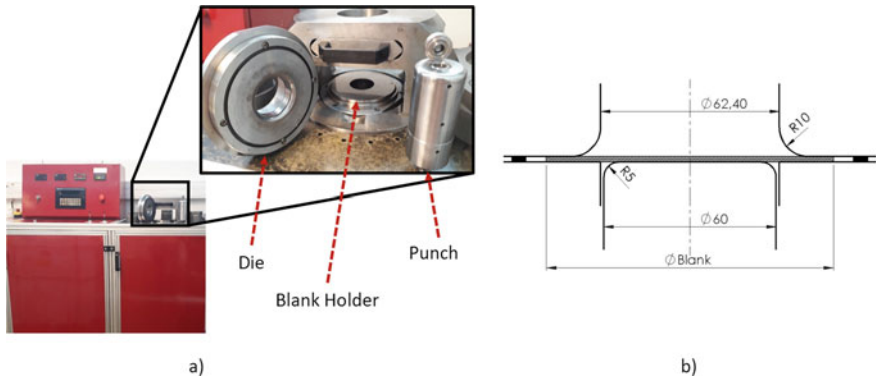
Fig. 15.8   a Universal testing machine with deep drawing cylindrical cup test setup (Amaral et al. 2019); **b** schematic view for cylindrical cup drawing test and corresponding tool dimensions [mm]
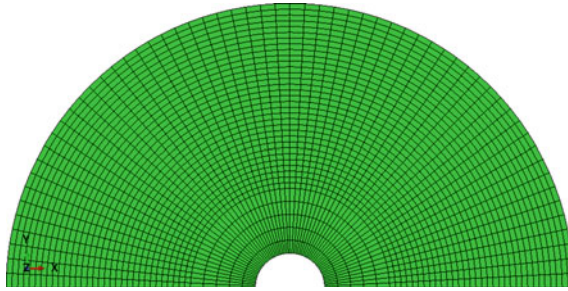
Fig. 15.9 Mesh used for cylindrical cup drawing test: total number of elements = 6660; three elements along thickness; blank thickness: 0.8 mm; blank size: 114 mm; element type: C3D8R (8-node linear brick)

15.4.1   Cup Height Evolution, Equivalent Stress and Strain Contours

The cylindrical cup deep drawing test represents a very effective test for evaluating anisotropic material models by analyzing the predicting behavior of earing cup height evolution and its amplitude. In this section, cup height evolution is being assessed by comparing the different anisotropic constitutive models.

Figure 15.10 presents a comparison of the earing cup height evolution obtained from the three implemented AFR approaches.

Regarding all the associated flow rule formulations, only the AFR-R approach (solid blue line) predicts the same earing profile and also the exact location when compared to the experimental data, but the amplitude between the maximum and minimum cup height is higher than the observed in the experiment. On the other
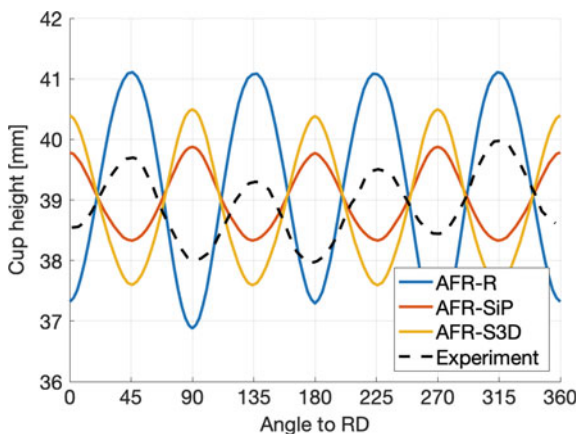
Fig. 15.10 Cup height evolution along with different angles to the rolling direction for AFR approaches and comparison with experiment
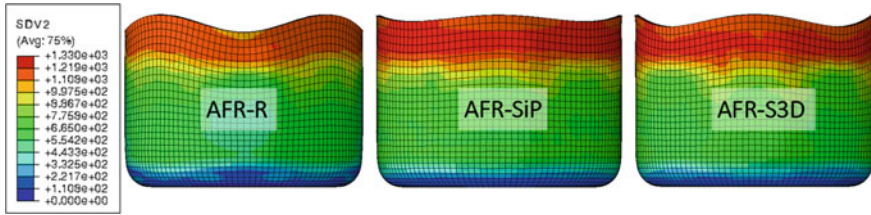
Fig. 15.11 Equivalent stress (SDV2) contours using an associated flow rule approach

hand, the associated formulations based on stress properties (AFR-SiP and AFR-S3D approaches) predict the opposite evolution of the earing profile and its highs and lows. It is also seen that the amplitude of these AFR approaches (AFR–SiP, AFR-S3D) is closer to the experimental result when compared to the AFR-R-based approach.

As for stress and strain distribution, Fig. 15.11 shows that different earing evolution is a primary reason for the visible differences seen on the main two kinds of observed contours. Additionally, for the same type of predicted earing evolution (AFR-SiP and AFR-S3D), the different amplitudes by these approaches also cause some difference in contours, especially seen on equivalent plastic strain results (Fig. 15.12).

Figure 15.13 compares the cup height evolution for the two NAFR approaches, and Figs. 15.14 and 15.15 for equivalent stress and equivalent plastic strain distributions, respectively.

Comparing the cup height evolution for the two NAFR approaches presented in Fig. 15.13, using as a reference the associated flow rule based on r-values, it can be observed that both approaches (NAFR-SiP and NAFR-S3D) have a better prediction for the cup height and earing profile, both in trend and accuracy. The AFR-R approach has non-conform amplitude or earing evolution, while the resulting NAFR approaches obtain a correct earing evolution and an approximate earing amplitude when compared to the experimental results.

As seen from Fig. 15.13, NAFR gives better results than the other AFR methods, even though the earing prediction of NAFR does not seem to be exactly as the experimental results.
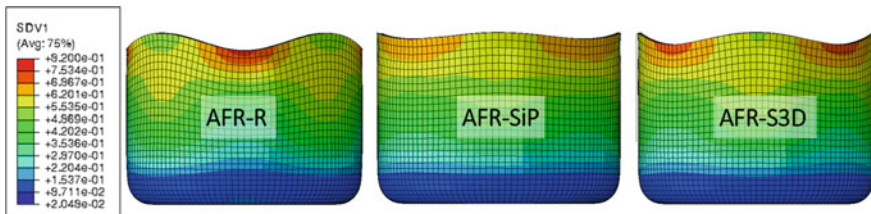
Fig. 15.12 Equivalent plastic strain (SDV1) contours using an associated flow rule approach
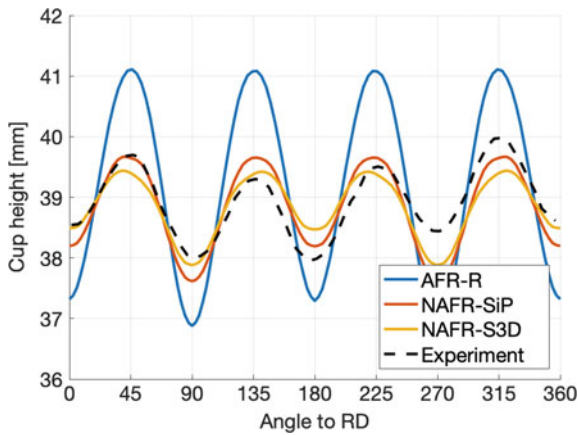
Fig. 15.13 Cup height evolution along with different angles to the rolling direction for NAFR approaches (NAFR-SiP and NAFR-S3D) and comparison with experiment and AFR-R
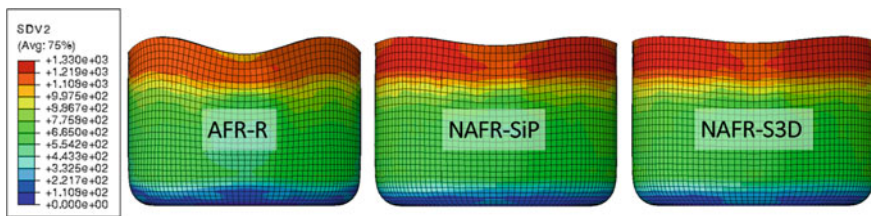
Fig. 15.14 Equivalent stress (SDV2) contours using a non-associated flow rule approach
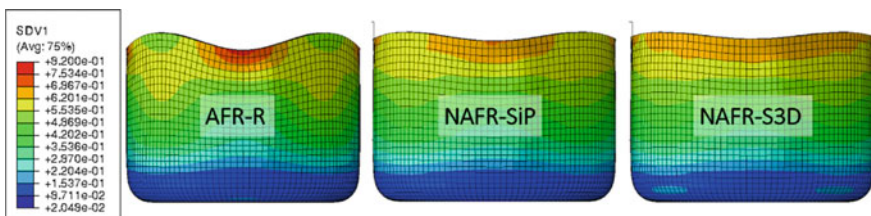
Fig. 15.15 Equivalent plastic strain (SDV1) contours using a non-associated flow rule approach

Comparing now NAFR formulations, it is not possible to evaluate which of the two NAFR approaches are closer to the best accuracy for predicting anisotropy for this cylindrical cup test, as both give representative good results. Also, these results and this analysis show that a step forward would be the improvement of higher accuracy concerning experimental results, which is a fundamental need when benchmarks for numerical validation are defined and performed.
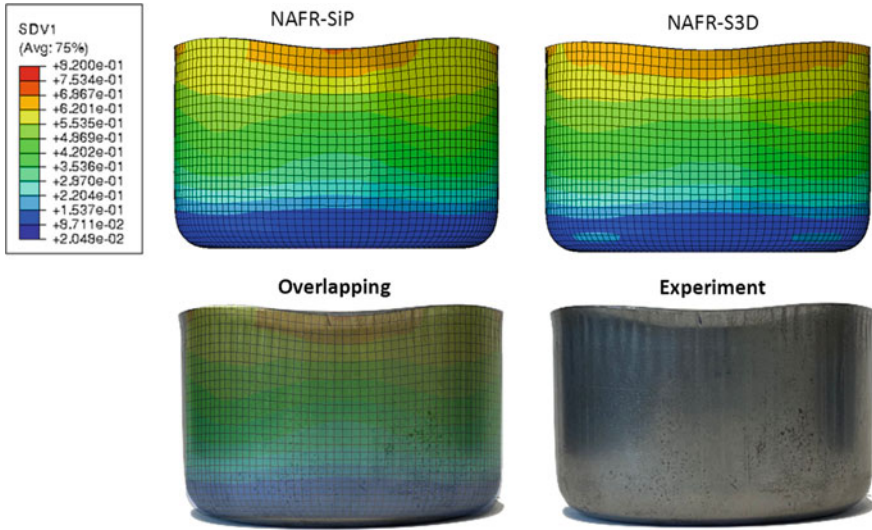
Fig. 15.16 View of earing cup profile from the experimental cup (right) and overlapping with simulation

Additional comparisons were performed considering the lateral view of the experimental and numerical geometries using one of the two NAFR approaches (NAFR-SiP). As shown in Fig. 15.16, both comparisons perform very well, as well as the overlapping between numerical and experimental geometries.

15.4.2 Wall Thickness Strain Distribution

A successful deep drawing process needs to consider the interaction between the blank, the die and the blank-holder. Accordingly, changes in the sheet metal thickness shall be modeled as accurately as possible in the simulation since they will influence the contact and friction stresses at the interfaces. Therefore, the analysis of predicted strain distribution through-thickness has been compared for each AFR and NAFR approaches, along with rolling (Fig. 15.17) and transverse (Fig. 15.18) directions for defined vertical sections.

The comparison between all AFR approaches shows that the three approaches are grouped into two types of behavior, and the differences are mainly on the vertical wall region (initial x-coordinate greater than 40 mm).

Considering the associated flow rule formulation with the stress-based approaches (AFR-SiP and AFR-S3D), both have very coincident thickness distribution. At the same time, AFR-R exhibits higher thickness strain along the vertical wall. Such two groups and the difference in strain distribution are related to the different earing evolution predictions, which directly influences the thickness due to constancy of
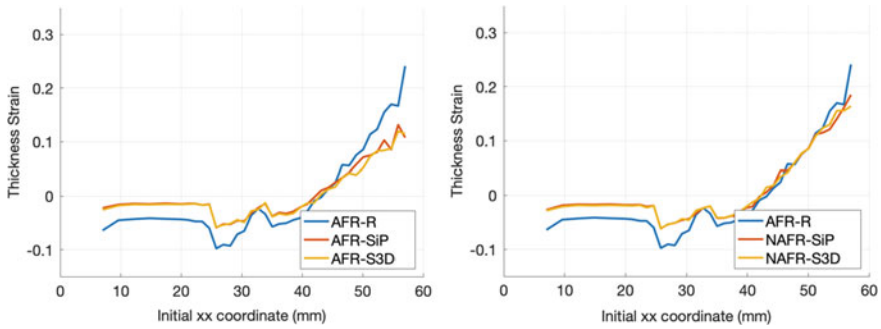
Fig. 15.17 Comparison of predicted thickness strain along rolling direction for AFR and NAFR approaches
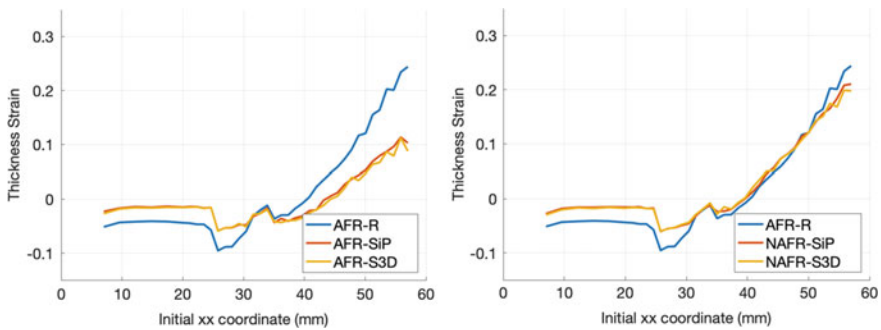
Fig. 15.18 Comparison of predicted thickness strain along transverse direction for AFR and NAFR approaches

volume in plastic deformation. The lower thickness strain for AFR-SiP/AFR-S3D behavior is related to higher cup height and lower thickness.

Comparing the NAFR approaches, it can be seen a similar behavior, close to the AFR-R approach, since the highs and lows of the earing profile are equal but have lower amplitude.

The predicted strain distribution for the vertical section of the cup along the transverse direction is shown in Fig. 15.18. The comparisons show that the tendencies observed for rolling direction are the same as for transverse direction. Although existing different thickness values between rolling and transverse directions for the same approach, the resulting strains show minimal differences. On the other hand, when comparing the various approaches, their differential at transverse direction is almost the same as for rolling direction, resulting in very similar tendencies (as with transverse direction).

15.5 Conclusions

This work, in the area of sheet metal forming, is focused on analyzing non-associated flow rule (NAFR) formulation using the anisotropic constitutive model Hill'48. The NAFR approach was developed and implemented in the FE code Abaqus via material user subroutine (VUMAT).

The quadratic function of this constitutive model was used to define both yield and plastic potential surfaces by using two sets of material parameters, enabling the accurate reproduction of the flow stress directionality, the anisotropic r-values and the shape of the yield surface simultaneously.

To evaluate and compare the obtained results from the proposed formulation, FE numerical simulations of a deep drawing cylindrical cup test were performed considering the dual-phase steel DP780.

The cup height evolution profiles and the wall thickness strain distribution of the cup show that the proposed NAFR model improves the accuracy of the obtained results and provides an effective and efficient approach to anisotropic sheet metal simulation prediction.

This comparative analysis also shows that NAFR models can reproduce the experimental anisotropic behavior of cylindrical cups, which is validated by the observed close agreement with experimental data.

References

Amaral, R.L., Santos, A.D., Sousa, J.A., Lopes, A.B.: The influence of microstructure on the mechanical behaviour of dual phase steels. Adv. Struct. Mat. **65**, 25–35 (2017)

Amaral, R.L., Santos, A.D., Miranda, S.S.: Limiting drawing ratio and formability behaviour of dual phase steels experimental analysis and finite element modelling. Adv. Struct. Mat. **98**, 469–486 (2019)

Banabic, D.: An improved analytical description of orthotropy in metallic sheets. Int. J. Plast **21**(3), 493–512 (2005)

Barlat, F., Becker, R.C., Hayashida, Y., Maeda, Y., Yanagawa, M., Chung, K., Brem, J.C., Lege, D.J., Matsui, K., Murtha, S.J., Hattori, S.: Yielding description for solution strengthened aluminum alloys. Int. J. Plast **13**(4), 385–401 (1997)

Barlat, F., Brem, J.C., Yoon, J.W., Chung, K., Dick, R.E., Lege, D.J., Pourboghrat, F., Choi, S.H., Chu, E.: Plane stress yield function for aluminum alloy sheets—part 1: theory. Int. J. Plast **19**(9), 1297–1319 (2003)

Barlat, F., Aretz, H., Yoon, J.W., Karabin, M.E., Brem, J.C., Dick, R.E.: Linear transfomation-based anisotropic yield functions. Int. J. Plast **21**(5), 1009–1039 (2005)

Cvitanic, V., Vlak, F., Lozina, Z.: A finite element formulation based on non-associated plasticity for sheet metal forming. Int. J. Plast **24**, 646–687 (2008)

Hill, R.: A theory of the yielding and plastic flow of anisotropic metals. Proceedings of the Royal Society London A **193**, 281–297 (1948)

Lian, J., Shen, F., Jia, X., Ahn, D.C., Chae, D.C., Münstermann, S., Bleck, W.: An evolving non-associated Hill48 plasticity model accounting for anisotropic hardening and r-value evolution and its application to forming limit prediction. Int. J. Solids Struct.9 **151**, 20–44 (2018)

Melan, E.: Zur Plastizität des räumlichen Kontinuums. Ingenieur-Archiv **9**, 116–126 (1938)

Mendiguren, J., Galdos, L., Argandoña, E.: On the plastic flow rule formulation in anisotropic yielding aluminium alloys. Int. J. Adv. Manuf. Tech. **99**, 255–274 (2018)

Ming, L., Pantalé, O.: An efficient and robust VUMAT implementation of elastoplastic constitutive laws in Abaqus/Explicit finite element code. Mech. Ind. **19**(3), 308 (2018)

Park, T., Chung, K.: Non-associated flow rule with symmetric stiffness modulus for isotropic-kinematic hardening and its application for earing in circular cup drawing. Int. J. Solids Struct. **49**, 3582–3593 (2012)

Safaei, M., DeWaele, W., Zang, S.L.: A rate-independent non-associated constitutive model for finite element simulation of sheet metal forming. In: Proceedings of 18th International Symposium of Plasticity and its Current Applications, pp. 61–63 (2018)

Safaei, M., Yoon, J.W., De Waele, W.: Study on the definition of equivalent plastic strain under non-associated flow rule for finite element formulation. Int. J. Plast **58**, 219–238 (2014)

Stoughton, T.B.: A non-associated flow rule for sheet metal forming. Int. J. Plast **18**(5–6), 687–714 (2002a)

Stoughton, T.B.: A non-associated flow rule for sheet metal forming. Int. J. Plast **18**, 687–714 (2002b)

Stoughton, T.B., Yoon, J.W.: Review of Drucker's postulate and the issue of plastic stability in metal forming. Int. J. Plast **22**, 391–433 (2006)

Taherizadeh, A., Green, D.E., Ghaei, A., Yoon, J.W.: A non-associated constitutive model with mixed iso-kinematic hardening for finite element simulation of sheet metal forming. Int. J. Plasticity **26**, 288–309 (2009)

Tang, B., Wu, F., Wang, Z., Zhang, S.: Study on non-associated plasticity with various forward Euler stress integration algorithms and its prediction of earing in cylindrical cup drawing. Int. J. Mech. Sci. **157–158**, 384–402 (2019)

Vegter, H., van den Boogaard, A.H.: A plane stress yield function for anisotropic sheet material by interpolation of biaxial stress states. Int. J. Plast **22**(3), 557–580 (2006)

Wali, M., Autay, R., Mars, J., Dammak, F.: A simple integration algorithm for a non-associated anisotropic plasticity model for sheet metal forming. Int. J. Numer. Meth. Eng. **107**, 183–204 (2016)

Wang, G., Qian, X., Li, X., Hou, H., Liu, Y., Lou, Y.: A study on compressive anisotropy and nonassociated flow plasticity of the AZ31 magnesium alloy in hot rolling. Math. Probl. Eng. **2014**, 1–9 (2014)

Wu, B., Ito, K., Mori, N., Oya, T., Taylor, T., Yanagimoto, J.: Constitutive equations based on non-associated flow rule for the analysis of forming of anisotropic sheet metals. Int. J. Pr. Eng. Man-GT, pp. 1–16 (2019)

Wu, B., Wang, H., Taylor, T., Yanagimoto, J.: A non-associated constitutive model considering anisotropic hardening for orthotropic anisotropic materials in sheet metal forming. Int. J. Mech. Sci. **169** (2020)

Yoon, J., Barlat, F., Dick, R., Karabin, M.: Prediction of six or eight ears in a drawn cup based on a new anisotropic yield function. Int. J. Plast **22**, 174–193 (2006)

Chapter 16
An Integrated Methodology for HER Determination in Hole Expansion Test

D. J. Cruz, A. D. Santos, R. L. Amaral, J. G. Mendes, S. S. Miranda, and J. V. Fernandes

Abstract Advanced high-strength steels (AHSS) are increasingly being used in the automotive industry due to their high yield and ultimate tensile strengths, allowing the production of lighter components for the car body structure without compromising safety standards. However, they present setbacks when compared with conventional steels, such as the edge cracking, which is caused by forming components with shear-cut edges. The hole expansion test (ISO 16630:2017) is a standard method used in industrial applications to evaluate the edge stretchability of sheet materials. However, this test requires being accurate on the visualization of the first cracking to occur, which is usually challenging and can be a subjective choice, often leading to inconsistent results and low reproducibility. Another problem is related to the possible influence of springback on the hole dimension. Due to this phenomenon, the hole diameter can be different when the punch is removed, thus giving inconsistency on measurements. In this work, a new methodology was used to improve the diameter measurement in the hole expansion test. Therefore, an instrumented device was developed to acquire the real-time evolution of the hole dimension throughout the test. This improvement helps in the detection of the appearance of the first edge crack and, consequently, allows a more accurate determination of the hole expansion ratio (HER). The proposed method was evaluated for different materials, and the corresponding HER values obtained with the developed method were compared with the traditional method. Additionally, numerical simulation was performed to complement the analysis of developed strategies.

Keywords Hole expansion test (HET) · Edge cracking · Advanced high strength steels (AHSS) · Circle hough transform (CHT) · Hole expansion ratio (HER)

D. J. Cruz (✉) · A. D. Santos · R. L. Amaral · S. S. Miranda
Institute of Science and Innovation in Mechanical and Industrial Engineering, INEGI, R. Dr. Roberto Frias, 400, 4200-465 Porto, Portugal
e-mail: dcruz@inegi.up.pt

A. D. Santos · J. G. Mendes
FEUP, Faculty of Engineering, University of Porto, R. Dr. Roberto Frias, 4200–465 Porto, Portugal

J. V. Fernandes
University of Coimbra, Centre for Mechanical Engineering, Materials and Processes, R. Luis Reis Dos Santos 290, 3030–194 Coimbra, Portugal

16.1   Introduction

During the last years, the automotive industry has been keeping the pace and efforts to address environmental concerns related to energy economy and emissions. Reducing the weight of vehicles is a primary method to answer these concerns and involves two basic strategies: vehicle design and materials selection. Instead of nonferrous light materials such as aluminium and magnesium, advanced high-strength steels (AHSS) have been used to meet the two goals above mentioned (Oh et al. 2015; Yoshida et al. 2013). These new materials typically have high yield and ultimate tensile strengths, which are critical to ensure passenger safety. However, they also present setbacks and challenges related to their processing. Several vehicle parts made of sheet metal have flanged holes that will be, subsequently, assembled with other components. During this manufacturing process, these holes are expanded and subjected to bending and stretching, which can lead to sheared edges and cracking through the sheet thickness. The formability of sheet steels during hole expansion is called "stretch-flangeability" and can be defined as a capability to resist an edge crack during edge stretching deformation (Santos et al. 2019).

The hole expansion test (HET) is one of the widely used methods to evaluate the resistance and stretchability of sheared edges. In this test, a sheet with a specified hole size is expanded by a conical punch until a visible through-thickness crack appears. The hole expansion ratio HER (%), which is defined according to the *ISO 16630:2009* standard (ISO 2017), is calculated according to:

$$HER(\%) = \frac{D_f - D_i}{D_i} \times 100 \qquad (16.1)$$

where $D_f [mm]$ and $D_i [mm]$ represent the inner diameter of the expanded hole and the initial diameter, respectively.

Usually, the crack occurrence is judged manually based on eye inspection and experience. However, in some cases, the operator cannot recognize the right moment to stop the test, leading to the crack propagation and, consequently, an increase in the final hole diameter (Hance 2017). This human subjectivity can conduct to errors and large deviations in the HER values.

There are several approaches to determine experimentally the crack initiation during the HET test. Dunckelmeyer et al. (2009) used the punch force–displacement curve to relate the appearance of through-thickness crack with a possible drop in the curve. This method proved to be insufficient since many micro-cracks are generated simultaneously and normally need a supplementary approach (Image Analysis, for example) (Choi et al. 2019). Leonhardt et al. (2019) used an automated pneumatic system to detect the crack.

One of the prospective methods to monitor the through-thickness crack is based on the digital image correlation (DIC) technique, which analyzes all cracks and their propagations with real-time images, continuously. Chen et al. (2011) used the DIC for measuring strain around the expanded hole on the upper surface of the specimen.

Li et al. (2016) used an ARAMIS system to observe the deformation of the specimen and study the influence of experiment methods—burr direction, method of processing hole, blank thickness and punch shape—on hole expansion ratio.

Kim et al. (2016) utilized a visual system for monitoring the edge expansion and investigated the effects of the pre-machined processes. Chiriac et al. (2008) utilized a Digital Recording and Measurement System (DRMS) to decrease the variability in hole expansion results. Dunckelmeyer et al. (2009) investigated the impact of the clamping force and penetration speed on the punch force–displacement using a video camera to monitor the edge expansion. Krempaszky et al. (2014) implemented a digital camera system with two charge-coupled device (CCD) cameras to provide precise 3D images of the through-thickness crack, which enables evaluation of the effects in pre-machined processes (Wang et al. 2014). Oh et al. (2015) developed an automated measurement program using image processing technology. Seungho Choi et al. (2019) developed a smart crack inspection algorithm, based on image processing technique, that facilitates the through-thickness crack inspection during the hole expansion test, making it possible to calculate the HER value, automatically.

Zubia et al. (Mendiguren et al. 2018) studied the influence of springback on the hole expansion ratio. In fact, when the punch is moved out, the hole diameter at the crack moment is reduced, and the measured value after the test can be affected by an error. These authors concluded that springback influence could not be neglected for some materials. For example, the third *Fortiform* 1050 steel is affected by a 40% error on the HER value due to the springback. Dunckelmeyer et al. (2009) also analyze the impact of the elastic springback on Complex Phase (CP600) steel and concluded that its influence on the HER value is small (<1%).

This paper mainly focuses on the development of a new methodology to acquire and automatically measure the real-time evolution of the hole diameter in hole expansion test. Three different dual-phase steels—DP500, DP600 and DP780—were tested, and the corresponding HER results were compared with the traditional manual method defined on ISO 16630:2009 (ISO 2017). Finally, the influence of the springback on HER values was evaluated for these materials.

16.2 Methodology

16.2.1 Test Setup

The universal test machine developed by Duarte et al. (1994) was used in this work. This hydraulic power equipment, Fig. 16.1, has high applicability on the study of plastic sheet metal forming behaviour, due to its flexible mechanical system. In fact, altering the tools (punch and die), it is possible to carry out several tests, such as hole expansion, Erichsen, Nakajima, Swift, Kwi and Fukuito (Sousa 2019). For HET the equipment provides, as outputs, the punch force and displacement.
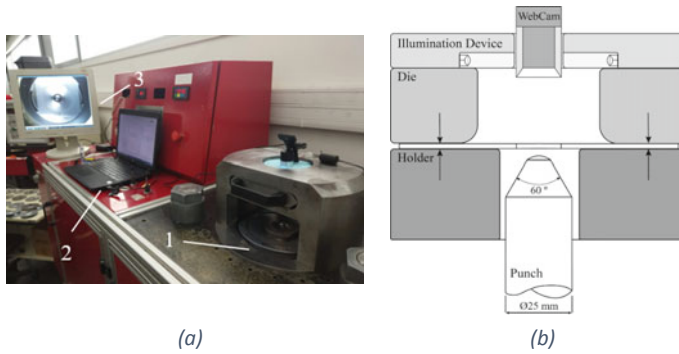
To acquire the real-time evolution of the hole dimension, the vision system represented in Fig. 16.1b was implemented. It contemplates a digital web camera with the maximum image resolution of 2560 × 2048 pixels and a maximum frame rate of 30 fps. It was also installed at the center of the top of the system an illumination device composed by a high-brightness LED strip to distribute light uniformly on the sheared surface of the hole.

To use the vision system more efficiently, a new conical punch was machined and coated with a black PVD layer. As represented in Fig. 16.2, this type of coating creates in the acquired image a high-contrast region between the sheared edge and the punch surface, crucial for the automatic hole diameter detection. Furthermore, the PVD layer allows the reflection of the sheet thickness on the punch surface. This reflection allows a clear view of the hole edge and helps the operator to analyze the initiation and propagation of the through-thickness cracks.

Fig. 16.2 Typical image obtained by the vision system developed
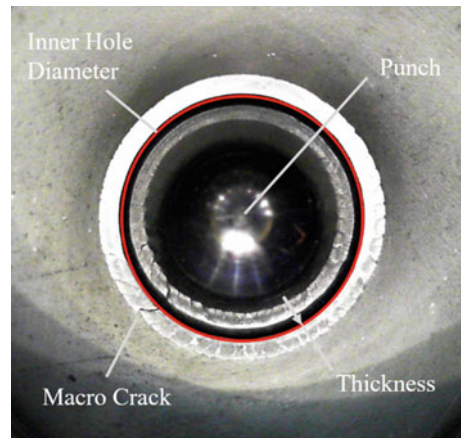
The vision system implemented is directly synchronized with the universal test machine; therefore, during each test, a video file is recorded, simultaneously with the displacement and punch force data.

16.2.2 Hole Diameter Measurement Algorithm

In order to detect and measure the hole diameter evolution, a post-processing MATLAB (2017b) algorithm was developed. The first step in the implemented method is the choice and extraction of the initial and final frame of analysis, using the recorded video. The initial image corresponds to the first punch-blank contact moment and the final the moment when the through-thickness crack occurs. This choice is decisive, since the respective hole diameters for the initial and final frame will define the HER value for each test. The algorithm also extracts, automatically, several images, between the initial and final frame that will provide the evolution of the hole diameter dimension during the test.

To detect and measure the diameter value in each image, a Hough transform (HT)-based algorithm (Smereka and Duleba 2008) was used. HT is a popular method of detecting circular or elliptical shapes of low-contrast images, and its main advantage is the robustness in the presence of noise, occlusion and variable lighting. The algorithm implements a voting process that maps image edge points into manifolds in an appropriately defined parameter space. Peaks in the space correspond to the parameters of detected curves. The circle Hough transform (CHT) is designed to find a circle in each image characterized by a center point (x_0, y_0) and a radius, r, in pixels (Mathworks 2020). The parameters used to apply the CHT algorithm are summarized in Table 16.1.

Using the CHT method, the hole diameter, D, for each picture is obtained according to Eq. (16.2):

$$D[mm] = 2r \times \alpha \tag{16.2}$$

where r represents the radius in pixels and $\alpha[mm/px]$ the system resolution. To know the α value, a calibration process was made on the implemented vision system using the gauge represented in Fig. 16.3. This gauge has marked circles with well-known diameters, D, in a range between 6 and 30 mm. Thus, applying the CHT

Table 16.1 Circle Hough transform (CHT) parameters

Circle hough transform (CHT) parameters	
Method	'Phase Code'
Edge threshold	0.4
Sensitivity	0.99
Object polarity	Dark

Fig. 16.3 Vision system
resolution obtained by
calibration for different
measurement plane
displacements, $\Delta d_{m.plane}$
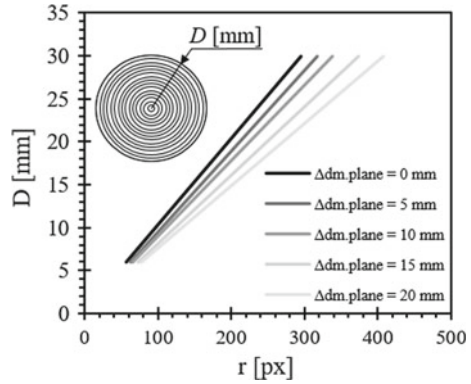
method for each circle, it is possible to know the corresponding r value in pixels and
consequently the system resolution.

In hole expansion test, as represented in Fig. 16.4, the punch moves vertically and
the plane where the internal diameter is measured approaches the camera succes-
sively. Consequently, the resolution, α, is modified throughout the test. To take this
into consideration, the calibration process was also carried out for different measure-
ment planes. The measurement plane is defined as the plane where the inner diameter
is measured and its vertical displacement is given by $\Delta d_{m.plane}$.

In the presented calibration process, the different measurement plane displace-
ments were defined by approaching the gauge into the camera, using the punch

Fig. 16.4 Schematic
representation of the relation
between the measurement
plane displacement,
$\Delta d_{m.plane}$, and the punch
displacement, Δd_{punch}, in
HET
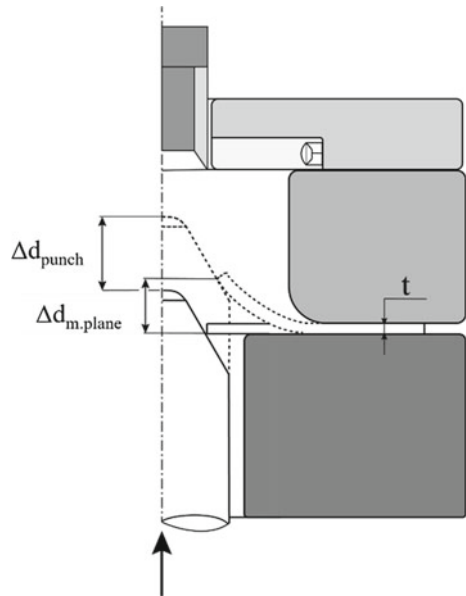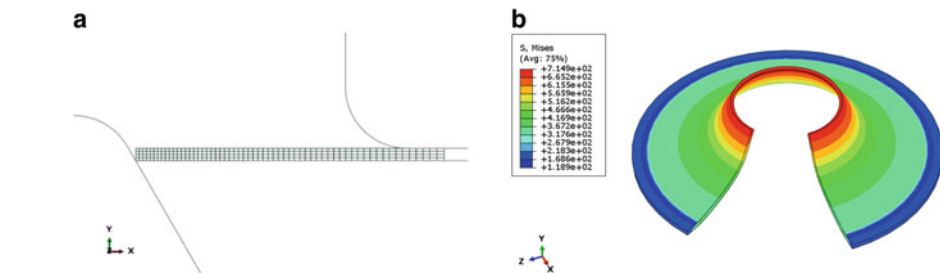
Fig. 16.5 Finite element simulation of HET for DP500 (t = 1.6 mm): **a** blank mesh distribution and **b** von Mises Equivalent stress for $\Delta d_{punch} = 10mm$

movement. However, in HET the measurement plane displacement, $\Delta d_{m.plane}$, and the punch displacement, Δd_{punch}, will not be coincident, due to the nature of the test. Therefore, to evaluate and predict the relation between the $\Delta d_{m.plane}$ and Δd_{punch}, a calibration model was developed by using finite element modeling and a virtual testing procedure.

The finite element analysis was carried out using commercially available ABAQUS (2007) software. The tools (conical punch, blank holder and die) and the blank with a central hole are naturally axisymmetric. Therefore, the hole expansion process was considered as an axisymmetric problem. The tools were regarded as discrete rigid bodies in the model. In contrast, four-node quadrilateral elements were chosen for meshing the blank. Along the thickness, four elements were taken and finer meshes were introduced near the hole region to capture the exact deformation behavior, as represented in Fig. 16.5. In this analysis, the planar anisotropy was not considered.

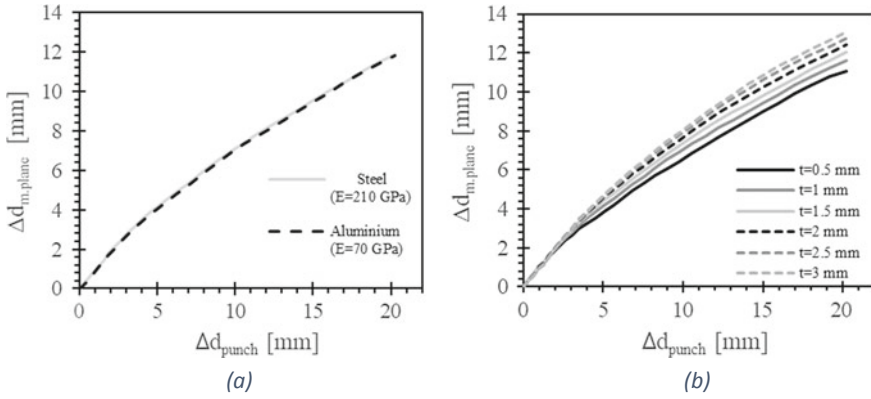Two different materials (steel and aluminium) with the same thickness were used. It was also evaluated the influence of the blank thickness between 0.5 and 3 mm. The results, Fig. 16.6, shown that the relation between Δd_{punch} and $\Delta d_{m.plane}$ is purely geometrical, and the results are independent of the specimen material. Inversely, the results are strongly dependent on the blank thickness. As shown in Fig. 16.7b, with the increase of the material thickness, the difference between the punch and blank displacements has a decreasing behavior. Using the presented numerical simulation results, it was possible to describe the measurement plane displacement as a function of the material thickness and the punch displacement $-\Delta d_{m.plane} = f(\Delta d_{punch}, t)$.

Using this approach, the developed algorithm detects automatically, for each image, the circle to measure and calculate the corresponding hole diameter, $D(mm)$, based on the input data of the radius, r, the correspondent punch displacement, Δd_{punch}, and the blank thickness, t. Figure 16.7 shows a typical example of the output result obtained by the algorithm for a 2-mm-thick material. It is also represented the reference curve obtained by numerical simulation.

In general, the evolution of diameter dimension obtained by the developed methodology follows a similar behaviour between numerical and experimental results.

Fig. 16.6 Relation between $\Delta d_{m.plane}$ and Δd_{punch}, obtained by numerical simulation: **a** for different materials (Steel and Aluminium) with the same thickness (t = 1.6 mm) and **b** for different blank thickness ($0.5 \leq$ t (mm) ≤ 3)
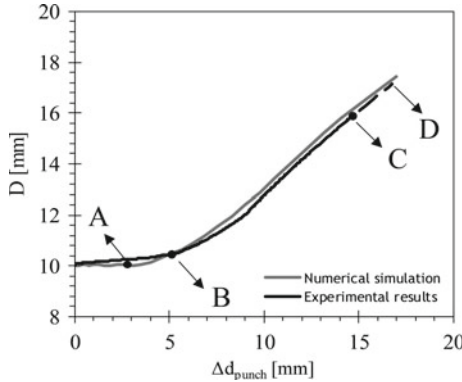
Fig. 16.7 "Hole Diameter" versus "Punch Displacement" evolution curve for 2 mm thickness material obtained by the developed algorithm. Continuous line represents the curve until fracture

Nonetheless, for a punch displacement, Δd_{punch}, between 0 and 5 mm the experimental hole diameter behavior is significantly dissimilar when comparing with the numerical simulation curve. In fact, at the beginning of the test, the blank is flat and the inner and outer diameters are coincident. With the punch movement, the blank thickness tilt and became visible on the captured image. Therefore, at the beginning of the test—Point A—the algorithm only has the ability to detect the outer diameter (Fig. 16.7a) but starts to detect the inner diameter at Point B (Fig. 16.7b).

The Point C (Fig. 16.7c) and Point D (Fig. 16.7d) correspond to the moment of through-thickness crack, and the moment when the test was stopped, respectively. The time between these two moments corresponds to the response time of the test operator, between the crack visualization and the test stop (Fig. 16.8).
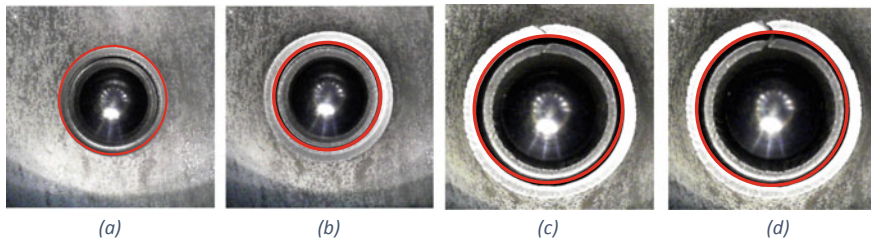
Fig. 16.8 Hole diameter detection by the CHT method for different punch displacement values

16.3   Experimental Tests

The automatic test method was applied to testing a series of samples for advanced high-strength steels (AHSS), namely three grades of dual-phase (DP) steel sheets (DP500, DP600 and DP780), with an initial thickness of 0.8 mm (Amaral et al. 2017a,b,c). These materials have high applicability on the automotive industry, and its stretchability of sheared edges was studied by several authors (Santos et al. 2019; ISO 2017; Wang et al. 2014; Hashimoto et al. 2010; Xu et al. 2012; Yoon et al. 2016). The central holes in specimens with 90×90 mm were performed by punching, with at a cutting clearance of 15% of sheet thickness. To assure the repeatability and to study the dispersion of the results, five samples for each material were tested. Table 16.2 shows the mechanical tensile properties for each material in the rolling direction (RD). The initial hole diameter, also presented in this table, was measured using a digital 3-point internal micrometer. For each material, the hole expansion test was performed with a constant punch speed of 0.5 mm/min, and the video was recorded at 5 fps.

16.3.1   Results and Discussion

The hole diameter variation, D, determined with the developed automatic method, is shown in Fig. 16.9. For each material, it is presented a representative curve of the hole diameter as a function of the punch displacement, up to the point of initiation of

Table 16.2 Tensile properties (RD) and additional information for selected dual-phase steels (DP)

Material	Thickness	Yield strength	Ultimate tensile strength	Uniform elongation	Initial hole diameter
	[mm]	[MPa]	[MPa]	[%]	[mm]
DP500	0.8	379.7	558.7	16.4	9.997 ± 0.002
DP600	0.8	429.6	645.3	16.1	9.994 ± 0.003
DP780	0.8	521.2	818.2	13.1	9.994 ± 0.002

Fig. 16.9 "Hole Diameter" versus "Punch Displacement" evolution curve for the three materials until macro crack through thickness observed
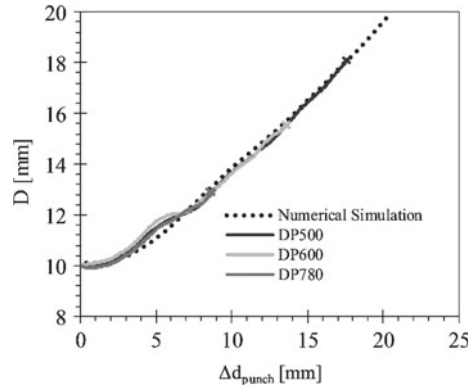
a crack through the thickness. In this experimental work, the excessively expanded crack morphology (macro fracture) defined by Li et al. (2018) was adopted as the criterion to stop the hole expansion.

As previously observed in numerical simulation, the experimental results confirm that the hole expansion evolution is mainly a geometrical issue, so that for a given punch displacement, the corresponding hole diameter value is independent of the material. In this case, as the selected materials have the same sheet thickness (t = 0.8 mm), the evolutions of the hole diameter are coincident and its comparison with the numerical results follows exactly the same trend. It is also visible, for a punch displacement between 2 and 7 mm, the limitations already mentioned for current developed methodology. The rise of diameter value for this punch displacement is artificial, and it is not indicative of any damage evolution in the material.

The corresponding HER values for each material are shown in Fig. 16.11. As already mentioned, the automatic method calculates the HER value using as final image the frame when the first macrocrack appears. In contrast, the manual method, according to ISO 16630, evaluates the diameter after the test is stopped and the punch has been removed. It is visible for both scenarios that the DP500 steel has the highest HER value followed by DP600 and the DP780 steel. Comparing the methods, the automatic procedure provides more conservative HER values (5–6% less, when compared with the manual process) and a significative reduction in the variability of the results.

It is important to note that the two methods do not assess the same diameter or the same test conditions. The final diameter obtained by the automatic method, unlike the manual, does not take into account the springback effect on the material when the punch is removed. To evaluate the springback influence on the results, an additional analysis was performed. Using the automatic method, a comparison is performed between the diameter of the hole at the time of the test stop (Fig. 16.10a) and the hole diameter obtained at the time after the punch was removed (Fig. 16.10b). These two figures express the hole diameter before and after springback, respectively. In the presented results, Fig. 16.12 and Table 16.3, the automatic method can perform measurements with an accuracy of ± 0.1 mm.

(a)   *(b)*
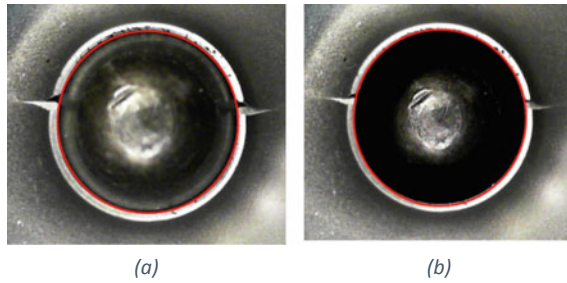
Fig. 16.10 Hole diameter obtained by the automatic method for **a** before springback (punch in contact) and **b** after springback (punch removal)
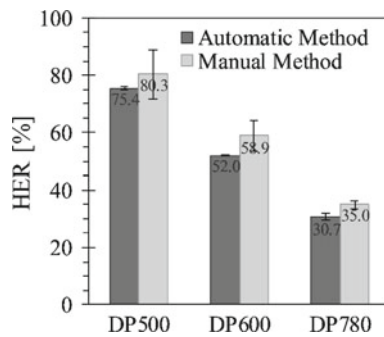
Fig. 16.11 Hole Expansion ratio (HER) for the selected materials obtained with the manual and automatic method
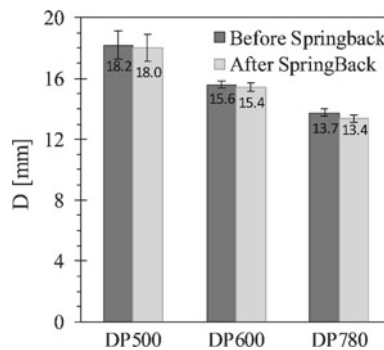
Fig. 16.12 Springback influence on the final hole diameter measurements

Table 16.3, it is visible that the springback has a minimal influence on the hole diameter (<3%) for these materials. The comparison between the hole diameter after springback obtained by two methods (automatic and manual) indicates that the automatic method can perform measurements with an accuracy of ± 0.1 mm.

Table 16.3 Springback effect analysis for the selected materials

Material	Hole diameter [mm]			Springback effect [%]
	Automatic method		Manual method	
	Before Springback	After Springback	After Springback	
DP500	18.2 ± 0.9	18.0 ± 0.9	18.045 ± 1.039	0.8
DP600	15.6 ± 0.2	15.4 ± 0.2	15.391 ± 0.164	1.1
DP780	13.7 ± 0.2	13.4 ± 0.2	13.450 ± 0.116	2.8

16.4 Conclusions

In this work, a new methodology is presented corresponding to the development of an automatic procedure with the objective of a more efficient and accurate methodology for diameter measurement in the hole expansion test and determination of a material HER. Accordingly, a new experimental vision system was designed to record the test region during the test. Using a webcam, the evolution of the hole is recorded simultaneously with the punch displacement and force data acquisition signals. As a post-processing tool, a developed *MATLAB* algorithm is applied to the video to detect and measure the different hole diameters, which additionally creates the possibility of detecting the appearance of the first edge cracks and, consequently, allows a more accurate determination of the hole expansion ratio (HER). This methodology can be used for sheet materials between 0.5 and 3 mm and provides maximum accuracy in the order of ± 0.1 mm.

Numerical simulations were performed to complement the analysis of the hole expansion test. It was concluded that the evolution of the hole expansion is a geometric issue and it is independent of the tested material. On the other hand, it is extremely dependent on the thickness of the material.

Three AHSS steels—DP500, DP600 and DP780—were tested. As expected, the hole diameter evolution was similar because the three materials had the same thickness (t = 0.8 mm). However, the HER value obtained after the test was different. DP500 reached the higher HER value, followed by DP600 and DP780. The automatic methods provide higher accuracy for values of HER and less dispersion when compared with the manual method, for every selected material. The influence of the springback effect for these materials is almost insignificant (<3%).

References

ABAQUS (User's Manual (version 6.7)), H., Karlsson & Sorensen Inc., USA, 2007.: In.

Amaral, R., Santos, A., Sousa, J.A., Lopes, A.: The influence of microstructure on the mechanical behaviour of dual phase steels. In: Materials Design and Applications. Advanced structured materials, vol. 65. Springer, (2017)

Amaral, R., Santosa, A., Lopes, A.B.: Mechanical properties determination of dual-phase steels using uniaxial tensile and hydraulic bulge test. Ciência and Tecnologia Dos Materiais **29**, e239–e243 (2017). https://doi.org/10.1016/j.ctmat.2016.06.007

Amaral, R., Santos, A., Cesar de Sa, J., Miranda, S.: Formability prediction for AHSS materials using damage models. Journal of Physics: Conference Series **843**, 012018 (2017). https://doi.org/10.1088/1742-6596/843/1/012018

Chen, X., Yang, L., Chirac, C., Du, C., Zhou, D.: Measurement of strain distribution for hole expansion with digital image correlation (DIC) System. (2011). https://doi.org/10.4271/2011-01-0993

Chiriac, C., Chen, G.: Local Formability characterization of AHSS—digital camera based hole expansion test development. IDDRG 2008 Conference, pp. 16–18 (2008)

Choi, S., Kim, K., Lee, J., Park, S.H., Lee, H.-J., Yoon, J.: Image processing algorithm for real-time crack inspection in hole expansion test. International Journal of Precision Engineering and Manufacturing **20**(7), 1139–1148 (2019). https://doi.org/10.1007/s12541-019-00101-4

Duarte, J.F., Santos, A.D., Rocha, A.B.: Development of testing equipment for sheet metal forming analysis. Recent developments in sheet metal forming technology—18th Biennial Congress (1994).

Dünckelmeyer, M., Krempaszky, C., Werner, E., Doppler, C.: Instrumented hole expansion test.: Instrumented hole expansion test. Materials Science (2009)

Hance, B.: Practical application of the hole expansion test. SAE International Journal of Engines **10**, 247–257 (2017). https://doi.org/10.4271/2017-01-0306

Hashimoto, K., Kuwabara, T., Iizuka, E., Yoon, J.W.: Hole expansion simulation of high strength steel sheet. Int.J. Mater. Form. **3**(1), 259–262 (2010). https://doi.org/10.1007/s12289-010-0756-6

ISO 16630:2017—Metallic Materials—Sheet and Strip—Hole Expanding Test. In. (2009)

Kim, H., Shang, J., Beam, K., Samant, A., Hoschouer, C., Dykeman, J.: Development of new hole expansion testing method. Journal Physical: Conference Series **734**, 032025 (2016). https://doi.org/10.1088/1742-6596/734/3/032025

Krempaszky, C., Larour, P., Freudenthaler, J., Werner, E.: Towards more efficient hole expansion testing. IDDRG 2014 Conference, pp. 204–209 (2014)

Leonhardt, A., Kräusel, V., Paar, U.: Automated hole expansion test with pneumatic crack detection. IOP Conference Series: Materials Science and Engineering **480**, 012026 (2019). https://doi.org/10.1088/1757-899x/480/1/012026

Li, J., Wang, H., Yan, D.-w.: Influence of experiment methods on limit hole expansion ratio. DEStech Transactions on Engineering and Technology Research (2016). https://doi.org/10.12783/dtetr/amita2016/3697

Li, W., Xia, M., Peng, P., Jia, Q., Wan, Z., Zhu, Y., Guo, W.: Microstructural evolution and deformation behavior of fiber laser welded QP980 steel joint. Materials Science and Engineering: A **717** (2018). https://doi.org/10.1016/j.msea.2018.01.050

Mathworks: Image Processing Toolbox™ User's Guide (R2020a). (2020)

MATLAB R (2017b), The MathWorks, Inc., Natick, Massachusetts, United States.

Mendiguren, J., Zubia, B., Agirre, J., Galdos, L., SaenzdeArgandona, E.: Study on the influence of the springback on the hole expansion ratio characterization. Materials Science: Materials Review **1**(3) (2018). https://doi.org/10.18063/msmr.v1i1.408

Oh, S.H., Yang, S.H., Kim, Y.S.: A study of image processing based hole expansion test. In: Chan, K. (ed.) Testing and Measurement: Techniques and Applications. Phuket Island, Thailand (2015)

Santos, R., Pereira, A., Butuc, M.C., Vincze, G., Festas, A., Moreira, L.: Development of a device compatible with universal testing machine to perform hole expansion and erichsen cupping tests. Machines **8**, 1 (2019). https://doi.org/10.3390/machines8010002

Smereka, M., Duleba, I.: Circular object detection using a modified hough transform. Applied Mathematics and Computer Science **18**, 85–91 (2008). https://doi.org/10.2478/v10006-008-0008-9

Sousa, J.P.: Desenvolvimento de um Sistema de Controlo e Aquisição de Dados para Máquina Universal de Ensaios de Chapas Metálicas. Master Thesis 2019, Faculdade de Engenharia da Universidade do Porto, Portugal.: In.

Wang, K., Luo, M., Wierzbicki, T.: Experiments and modeling of edge fracture for an AHSS sheet. International Journal Fracture **187**(2), 245–268 (2014). https://doi.org/10.1007/s10704-014-9937-5

Xu, L., Barlat, F., Lee, M.-G., Choi, K., Sun, X.: Hole expansion of dual phase steels. WIT Transactions on the Built Environment **124**, 75–83 (2012). https://doi.org/10.2495/HPSM120071

Yoon, J.I., Jung, J., Joo, S.-H., Song, T.J., Chin, K.-G., Seo, M.H., Kim, S.-J., Lee, S., Kim, H.S.: Correlation between fracture toughness and stretch-flangeability of advanced high strength steels. Mater. Lett. **180**, 322–326 (2016). https://doi.org/10.1016/j.matlet.2016.05.145

Yoshida, H., Sato, K., Matsuno, T., Yoshida, T., Takahashi, Y., Nitta, J.: Evaluation and improving methods of stretch flangeability. Nippon Steel Technical Report, 18–24 (2013)

Part VI
Joining

Chapter 17
Prediction of Tensile Shear Strength of Resistance Spot Welded AA 5052 Using Regression Analysis Model

T. E. Abioye [ORCID]**, F. Z. Bin Redzuan, H. Zuhailawati, A. S. Anasyida, I. Suhaina, B. D. Bankong, and T. C. Akintayo**

Abstract Resistant spot welding (RSW) of aluminium alloys including AA 5052 is increasingly being applied in aerospace, automotive and marine industries because of the rapidity of the process and unique properties of AA 5052 including high strength-to-weight ratio, excellent corrosion resistance and lower cost. Common issue of concern with the RSW of aluminium alloys is the inconsistency in the weld quality. In this work, the tensile shear strength (TSS) and nugget size of the resistant spot welded 1.2 mm AA 5052 were investigated. The nugget size was optimised to meet AWS-D17.2 (aerospace) standard. The welding process parameters involved are weld current (ranging between 16.3 and 20.0 kA), weld time (0.2025–0.2475 ms) and weld pressure (0.936–1.144 bar). A combination of statistical analytical techniques including full factorial design of experiment, ANOVA, hierarchy rule and regression analysis was used to optimise and develop a mathematical model predicting the TSS of the weldment. The nugget sizes and the microstructure of the welded joints were examined using optical microscopy. The significance of the single effects and interaction effects of the parameters on the TSS was determined and reported. A maximum TSS of about 63.61 MPa was found, in this work, at 20.0 kA weld current, 0.2475 ms weld time and 1.144 bar weld pressure. This is an improvement over the highest obtainable (~41 MPa) in a typical local sheet metal company (Coraza System Malaysia Sdn. Bhd) in Malaysia. A numerical regression model with R^2 of 91.13% was developed for the TSS indicating high compatibility of the model to the experimental results.

T. E. Abioye (✉) · T. C. Akintayo
Industrial and Production Engineering Department, School of Engineering and Engineering Technology, Federal University of Technology Akure, Akure PMB 704, Ondo State, Nigeria
e-mail: teabioye@futa.edu.ng

T. E. Abioye · F. Z. B. Redzuan · H. Zuhailawati · A. S. Anasyida · I. Suhaina
Structural Materials Niche Area, School of Materials and Mineral Resources Engineering, Universiti Sains Malaysia, Engineering Campus, 14300 Nibong Tebal, Penang, Malaysia

B. D. Bankong
Mechanical and Aerospace Engineering Department, Air Force Institute of Technology, Kaduna PMB 2104, Kaduna State, Nigeria

17.1   Introduction

The current trend in the manufacturing industries (e.g. automotive and aerospace) for developing lightweight structures for increased speed and improved fuel economy has massively increased the demand and utilisation of aluminium alloys in these industries. AA 5052 is a typical aluminium alloy that is characterised with high strength (due to large inclusion of Mg into the solid solution of aluminium), high ductility and excellent corrosion resistance (Kim et al. 2008; Abioye et al. 2019a). Due to this combination of the aforementioned favourable properties, AA 5052 is now being utilised as replacement for steels in the construction of some structural components in ship building and car body construction (Shanavas et al. 2018). Among other uses, sheet metal of AA 5052 is specifically utilised in the fabrication of car doors and TV-screen frame at the back of passenger's seat in the aeroplanes (Abioye et al. 2019b). Often, joining of the sheet metals is required during the fabrication process.

Resistance spot welding has been established as a major sheet metal joining techniques that has been widely applied in aerospace and automotive industries (Wang et al. 2017). The reasons for its wide acceptance include low cost of its operation and high flexibility for automation in high-volume and/or rapid production (Zohoori-Shoar et al. 2017). However, there are some issues of concern associated with the resistance spot welding of aluminium alloys. These include inconsistency in the joint strength (Abioye et al. 2019c), requirements of high electrical current and high electrode pressure and high tendency for expulsion formation during welding process (Fukumoto et al. 2003; Lum et al. 2004). Another issue limiting the quality of resistance spot weld joint of aluminium alloys is the formation of non-conducting oxide film on the surface of the aluminium alloy (Luo et al. 2015; Muhamad Nabil et al. 2020). According to Luo et al. (2015), the oxide film formation which is often irregular over the aluminium alloy surface makes the contact resistance characteristics irregular at the faying interface during welding. Preheating AA 5052 prior to RSW has been performed by Luo et al. (2015) in order to reduce or remove the effect of irregular film formation. With the pre-heating, the contact resistance at the workpiece-to-workpiece faying interface was consistent and the weld quality in terms of the peak load and nugget size formation improved significantly.

Many other efforts have been geared towards improving the resistance spot weld quality of aluminium alloys. Prominent among these is the optimisation of the processing parameters including weld time, weld current, weld pressure and electrode tip diameter (Han et al. 2011; Manladan et al. 2017). Resistance spot welding of dissimilar thickness of AA 5052 (lap joint between 2 mm thick plate and 1.2–3.2 mm thick plate) has been performed by Din et al. (2016) in order to investigate the effect of varying metal thickness (on the weld quality of AA 5052). It was found that

increasing the lap joint thickness resulted in increased failure load, nugget size, weld time and coarsening of the joint microstructure. The weld quality of 2-mm-thick AA 6061-T6 resistance spot welds under varying welding conditions has been studied by Florea et al. (2012). The weld strength and surface appearance were found to improve with the welding current. However, reduction in the structural integrity of the joint was observed when the weld current was excessively high (in the range of 40–45 kA). Rashid et al. (2011) have also established that nugget size grows with increasing the weld current, and the weld strength has a direct relationship with the size of the nugget. So far the individual effect of each of the parameters on the resistance spot weld quality of aluminium alloys including AA 5052 had been extensively researched and reported in the literature. Till date, the study of interaction effect of the processing parameters on the weld quality is lacking and development of appropriate mathematical model predicting the weld strength of AA 5052 at varying RSW conditions is still scanty.

This work investigates the weld quality of resistance spot welding of AA 5052 at varying combinations of processing parameters. The single and interaction effects of the welding parameters including the weld current, weld time and weld pressure on the weld quality were studied. A regression mathematical model predicting the resistance spot weld strength at varying parametric combinations was developed and validated.

17.2 Materials and Method

17.2.1 Materials

AA 5052 sheet of 1.2 mm thickness was used as the workpiece in this research. The chemical composition of the AA 5052 sheet, as obtained from X-ray fluorescence (XRF) analysis, is given in Table 17.1. The material was machined to dimension 80 mm × 20 mm × 1.2 mm sheet in compliance with the AWS D17.2 (aerospace) specification. The surfaces of the machined sheets were cleaned with sodium hydroxide solution (NaOH) so as to avoid any form of contamination, oxide and dirt that may influence the weld quality.

Table 17.1 Chemical composition (wt.%) of as-received AA 5052 sheet

Elements	Al %	Si %	Fe %	Cu%	Mn %	Mg %	Cr%	Zn%
Composition (wt.%)	96.8	0.25	0.2	0.1	0.1	2.3	0.15	0.1

17.2.2 Resistance Spot Welding Process

A NASH medium-frequency Spot Welder (model: S-10-200MF) with rated capacity of 200 kVA was utilised for the entire welding process. The RSW process was performed using lap joint configuration, as shown in Fig. 17.1, under varying conditions. Full factorial experimental design with three factors and two levels (2^3 matrix) was utilised to obtain the varying RSW conditions. The factors are welding current, time and pressure. After trial experiment, the two levels for each factor are the maximum and minimum values that gave high-quality welds. As shown in Tables 17.2 and 17.3, there were 11 experimental runs obtained from 2^3 factorial plus 3 centre points. The three centre points were incorporated so as to demonstrate linearity between variables and responses during data analysis. As shown in Table 17.3, the standard order was randomised to avoid systematic error. Throughout the experiment, the electrode tip diameter, squeeze time and hold time were kept at 6 mm, 60 cycles and 50 cycles, respectively.
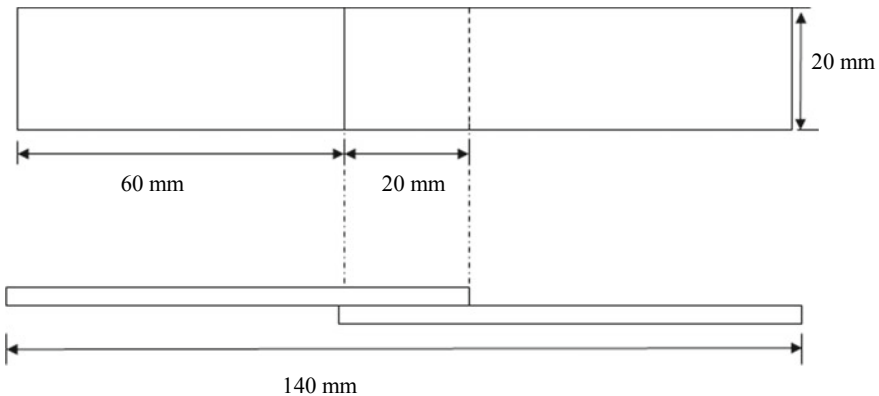
Fig. 17.1 Schematic configuration and dimensions of resistance spot welding specimens

Table 17.2 Range of the processing parameters utilised for the RSW

Parameters	Symbol	Unit	Range		
			Low	High	Average
Weld current	I	kA	16.3800	20.0200	18.2000
Weld time	T	ms	0.2025	0.2725	0.2375
Weld force/pressure	P	bar	0.9360	1.1440	1.0400

Table 17.3 Design matrix for 2^3 factorial design plus three centre points

Standard order	Run order	Centre point	Blocks	Weld current (kA)	Weld time (ms)	Pressure (Bar)
4	1	1	1	20.00	0.2475	0.936
8	2	1	1	20.00	0.2475	1.144
1	3	1	1	16.38	0.2025	0.936
3	4	1	1	16.38	0.2475	0.936
9	5	0	1	18.20	0.2250	1.040
11	6	0	1	18.20	0.2250	1.040
2	7	1	1	20.00	0.2025	0.936
7	8	1	1	16.38	0.2475	1.144
10	9	0	1	18.20	0.2250	1.040
6	10	1	1	20.00	0.2025	1.144
5	11	1	1	16.38	0.2025	1.144

17.2.3 Tensile Shear Strength Test

Tensile shear strength of the entire resistance spot-welded samples was obtained using an Instron tensile machine. In order to obtain the strength of the resistance spot-welded samples, each sample was pulled to tension at a speed of 10 mm/min until failure occurred. Thereafter, the maximum load (L; kN) was obtained and then converted to tensile shear strength (TSS; MPa) using Eq. (17.1).

$$\text{TSS} = \frac{4L}{\pi D^2} \tag{17.1}$$

where D is the average size (diameter) of the nugget in mm.

17.2.4 Weld Nugget Measurement

The microstructure and nugget size of each resistant spot-welded joint were examined using Stereo Zoom optical microscope incorporated with the ViS 2.90 software. Three different measurements were taken at three different sites of the weld nugget, and the average from these measurements was calculated and taken as the diameter of the weld nugget.

17.2.5 Development of the Model

A mathematical model was developed using ANOVA and regression analysis. Analysis of variance (95% confidence) was performed on the results obtained from the tensile shear tests using Minitab 18 software. The significance of each of the factors and interactions of the factors were determined from their P values. Any factor or interaction of factors with P value lower than 0.05 was considered significant; otherwise, it is said to be insignificant. In order to develop a valid model that fits well with the experimental data, hierarchy rule was utilised. In this rule, the most insignificant factor was first removed (considering the interaction of factors first) and then the ANOVA is repeated until a fitting model was obtained This means that the rule was first applied to three-way interactions and then two-way interactions before the single factors were considered. Thereafter, regression analysis was performed so as to generate mathematical equations that connect the significant factors with the responses. Contour plot was also developed in order to show the relationship between two continuous parameters and a fitted response in two dimensions. In order to validate the developed model, confirmation tests were performed and compared with real experimental data.

17.3 Results and Discussion

17.3.1 Experimental Data for Weld Nugget and Tensile Shear Strength

Table 17.4 presents the experimental results obtained for the weld nugget size and TSS at varying combinations of the parameters. Both the nugget size and TSS are the main criteria usually used to judge the resistant spot weld quality. The nugget size of the entire 11 runs ranged between 4.24 and 5.94 mm, as shown in Fig. 17.2. According to AWS 17.2 (aerospace) specification, the minimum weld nugget requirement size for sheet thickness of 1.2 mm is 4.32 mm. This implies that the nugget size from all experiments met the aerospace industry minimum standard except for the 3rd and 11th experimental runs which exhibited nugget sizes of about 4.3 and 4.24 mm, respectively. The TSS of the entire 11 experimental runs also ranged between 27.45 $\pm$ 1.4 and 63.61 $\pm$ 1.7 MPa. Analysis of the results presented in Table 17.4 revealed that both the nugget size and TSS followed similar trend with the utilised processing parameters. The interpretation of this is that the TSS increased as the weld nugget size increased.

According to Zhang et al. (2011), larger nugget size is an indication that sufficient heat energy input was available to completely melt the workpiece at the weld spot. Hence, a stronger fusion was formed after solidification of the weldpool. Consequently, a higher TSS is obtained for the resistant spot welds with larger weld nugget size. The maximum TSS (63.61 MPa) and highest nugget size (5.94 mm) were

Table 17.4 Experimental data for the tensile shear strength and nugget size

Run order	Weld current (kA)	Weld time (ms)	Pressure (Bar)	Weld nugget size (mm)	Tensile shear strength (MPa)
1	20.00	0.2475	0.936	5.29 ± 0.43	48.15 ± 1.6
2	20.00	0.2475	1.144	5.94 ± 0.14	63.61 ± 1.7
3	16.38	0.2025	0.936	4.30 ± 0.23	29.45 ± 2.2
4	16.38	0.2475	0.936	4.53 ± 0.12	33.86 ± 1.3
5	18.20	0.2025	1.04	4.67 ± 0.92	36.84 ± 1.9
6	18.20	0.2475	1.04	5.50 ± 0.21	49.1 ± 1.7
7	20.00	0.2025	0.936	5.02 ± 0.10	48.09 ± 1.5
8	16.38	0.2475	1.144	4.90 ± 0.27	34.53 ± 3.2
9	18.20	0.225	1.04	4.97 ± 0.11	47.66 ± 1.1
10	20.00	0.2025	1.144	5.79 ± 0.12	57.93 ± 2.6
11	16.38	0.2025	1.144	4.24 ± 0.25	27.45 ± 1.4

obtained when the parameters were set at 20 kA weld current, 0.2475 ms weld time and 1.144 bar weld pressure. Also, the minimum TSS (27.45 MPa) and highest nugget size (4.24 mm) were obtained when the parameters were set at 26.38 kA weld current, 0.2025 ms weld time and 1.144 bar weld pressure.

17.3.2   Regression Model

Full factorial design (FFD) was utilised to estimate the effect of the factors and their coefficients to the response (tensile shear strength) for the experiment. ANOVA including three-way interaction was performed on the results of the TSS. It was discovered that the P-value of the three-way interaction ($I * T * P$) is more than 0.005 indicating that its effect is insignificant. Based on the hierarchy rule, the insignificant factors and interaction of factors (starting from the three-way interaction) would be removed sequentially so as to refine the model. Consequently, the three-way interaction ($I * T * P$) was removed from the model, and the result of next ANOVA conducted without the three-way interaction ($I * T * P$) is presented in Table 17.5.

As shown in Table 17.5, the P-value of only weld current (0.003) is below 0.005 (for 95% confidence). This indicates that only the weld current factor is significant. Also, all the two-way interactions have *P*-value greater than 0.005. This means that they are all insignificant. In order to refine the model further, $I * T$ (P-value of 0.719) and $T * P$ (P-value of 0.609) were removed while $I * P$ interaction (*P*-value of 0.148) was retained because its *P*-value is the lowest among all the two-way interactions of factors. The result of the next ANOVA after the removal of $I * T$ and $T * P$ is presented in Table 17.6.
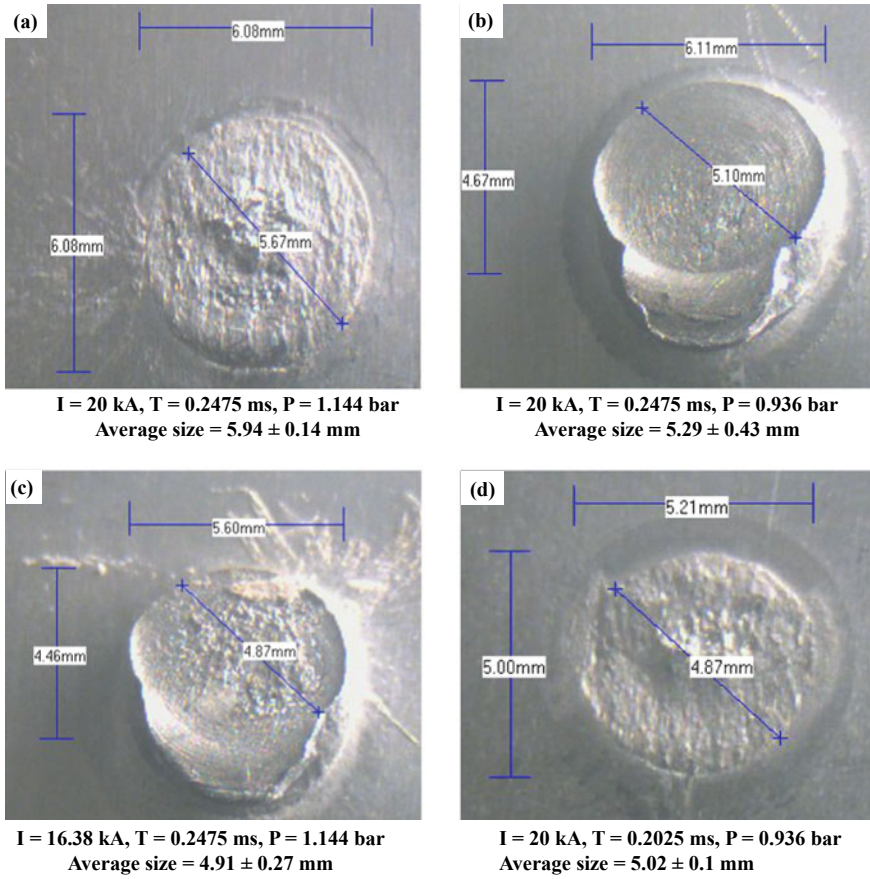
Fig. 17.2 Nugget sizes at varying RSW parameters

Table 17.5 Refined model after the removal of three-way interaction using hierarchy rule

Term	Effect	Coef	SE-Coef	T-value	P-value
Constant		43.2525	1.587	27.26	0.000
Weld current (I)	23.1252	11.5626	1.861	6.21	0.003
Weld time (T)	4.2992	2.1496	1.861	1.16	0.312
Pressure (P)	6.0075	3.0037	1.861	1.61	0.182
$I * T$	−1.4368	−0.7184	1.861	−0.39	0.719
$I * P$	6.6585	3.3293	1.861	1.79	0.148
$T * P$	2.06	1.03	1.861	0.55	0.609

Table 17.6 Refined model after the removal of $I * T$ and $T * P$ two-way interactions

Term	Effect	Coef	SE-Coef	T-value	P-value
Constant		43.2525	1.367	31.63	0.000
Weld current (I)	23.1252	11.5626	1.603	7.21	0.003
Weld time (T)	4.2992	2.1496	1.603	1.34	0.229
Pressure (P)	6.0075	3.0037	1.603	1.87	0.110
$I * P$	6.659	3.3290	1.603	2.08	0.083

Though the P-values of all the factors in the refined model presented in Table 17.6 are relatively smaller compared to that obtainable in Table 17.5, the weld current still remains as the only significant factor. However, the model presented in Table 17.6 is considered fitting because the difference between R^2 (91.13%) and R^2_{adj} (85.21%) for this refined model has reduced significantly to 5.92% after applying hierarchy rule three times. Also, the R^2 value obtained for the refined model shows that 91.13% of the data variation was explained by the model indicating that the model is highly reliable.

Further analysis was performed for this reduced ANOVA for the developing the regression model. The estimated coefficient of the regression model was obtained. The estimated coefficient came along with the standard error coefficient (SE coefficient). The mathematical model was generated from the estimated coefficient of the terms, as presented in Table 17.7. The positive value of the estimated coefficient of term (i.e. factor) shows that there is a synergistic effect whereby increase in the value of the factor will further contribute to the increase in the response (TSS) while the negative sign indicates an antagonistic effect whereby increase in the value of the factor will reduce the value of the response. The developed regression model predicting the tensile shear strength (TSS) of the AA 5052 resistant spot weld is presented in Eq. 17.2.

$$\text{TSS} = 193.018 - 11.9395\,I + 95.5389\,T - 291.238\,P + 17.8590\,I * P \quad (17.2)$$

In order to verify the adequacy of the model, analysis of the residual plots shown in Fig. 17.3 was done. As shown in Fig. 17.3a, most of the points in the normal probability plot clustered along the straight line. There is only one outlier at the bottom of the graph. The interpretation is that experimental errors were distributed

Table 17.7 Estimated coefficient of model from ANOVA

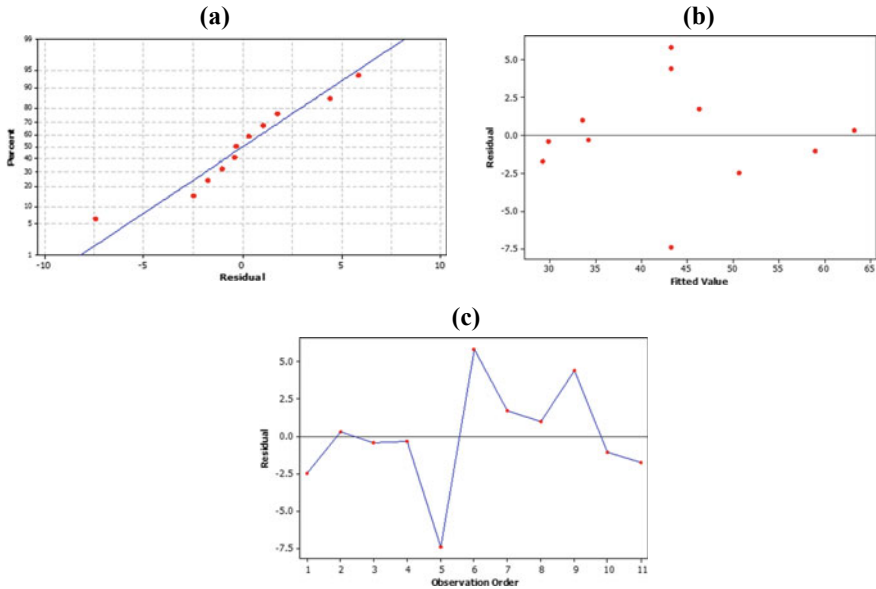| Term	Coefficient	SE coefficient	P-value
Constant	193.018	1.367	0
Weld current (I)	−11.9395	1.603	0.03
Weld time (T)	95.8389	1.603	0.229
Weld pressure (P)	−291.238	1.603	0.11
$I * P$	17.589	1.603	0.083

Fig. 17.3 Plot of residuals **a** normal probability, **b** versus fit, and **c** versus observation order

normally. Therefore, the regression assumption is satisfied (Zhao et al. 2016). The adequacy of the model was further clarified by analysing the standardised residual versus fits graph presented in Fig. 17.3b. Figure 4.5 shows the versus fits graph. The points (residuals) were prominently and randomly distributed between high (5) and low (−5) fitted values. The spreading of the residual points indicates that the residuals have non-constant variance (Vedrtnam et al. 2018). The developed mathematical regression model is therefore assumed to fit equally from low to high value of fits. Figure 17.3c shows the residual versus order plot. The trend of the versus order plot is fluctuating between +5 and −5 values. The pattern of the trend was random around the centre line of the plot. This shows that there are no errors that are correlated to one another since there were no specific trends for each of the experiments (Abioye et al. 2019b).

17.3.3 Variations of the Parameters with the Tensile Shear Strength of the Resistant Spot Welds

Table 17.8 presents the predicted values of the TSS using the developed mathematical regression model (see Eq. 17.2). The predicted values were compared with the experimental values for all the 11 parametric combinations utilised in this work. The deviation for the entire experimental runs is not more than 12%. This implies that the model can predict up to an accuracy of 88%. This is close to the accuracy of the

Table 17.8 Comparison of the experimental and predicted values of the TSS of AA 5052-resistant spot welds

Run order	Weld current (kA)	Weld time (ms)	Pressure (Bar)	Tensile shear strength (MPa)	Tensile shear strength (MPa)	Deviation (%)
				Experimental	Predicted	
1	20.00	0.2475	0.936	48.15	48.96	1.6
2	20.00	0.2475	1.144	63.61	64.75	1.8
3	16.38	0.2025	0.936	29.45	27.37	7.6
4	16.38	0.2475	0.936	33.86	31.66	6.9
5	18.20	0.2025	1.040	36.84	40.61	9.3
6	18.20	0.2475	1.040	49.1	44.91	9.3
7	20.00	0.2025	0.936	48.09	44.66	7.7
8	16.38	0.2475	1.144	34.53	34.01	1.5
9	18.20	0.2250	1.040	47.66	42.76	11.5
10	20.00	0.2025	1.144	57.93	60.45	4.2
11	16.38	0.2025	1.144	27.45	29.71	7.6

mathematical regression models developed by Abioye et al. (2019b) (91% accuracy) for predicting tensile strength of fibre laser weldment of AA 5052-H32 and Farayibi et al. (2016) (91% accuracy) for predicting the geometries of laser composite-clad made from Ti6Al-4 V wire and WC/W$_2$C powder.

As mentioned earlier, the weld current, pressure and time have direct relationship with the response (i.e. the TSS). Among all these single parameters, the ANOVA result shows that only the weld current is significant. Among the interactions, only the weld current-weld pressure interaction contributes significantly to the response. This interaction ($I * P$) effect was further analysed by generating a contour plot. As shown in Fig. 17.4, the contour plot shows the $I * P$ interaction effect on the TSS at a fixed welding time of 0.2025 ms. It is obvious that the TSS increased <30 MPa to >55 MPa as the weld current increased from 16.38 to 20 kA for welding pressure ranging between 0.936 and 1.125 bar at a fixed welding time of 0.2025 ms.

As shown in Fig. 17.4, the TSS increased as both the weld current and pressure increased. However, the effect of the change in pressure was not significant at low welding current. When weld current was set at about 19 kA, it is observed that the TSS changed from 40 to 45 MPa region at 0.950 bar to 45–50 MPa region at 0.980 bar and to 50–55 MPa region at about 1.10 bar. This is an indication that the $I * P$ interaction effect is significant and the interaction effect is more significant at high welding current. From the contour plot, the highest TSS can be obtained at weld current of 20 kA and weld pressure of about 1.125 bar. The highest value of TSS obtained at this parametric setting can be attributed to the fact that high weld current results in high heat energy transport to the interface of the workpieces during welding. This will cause sufficient melting of the workpieces at the welding spot thereby generating large weldpool, and large nugget is formed after solidification.
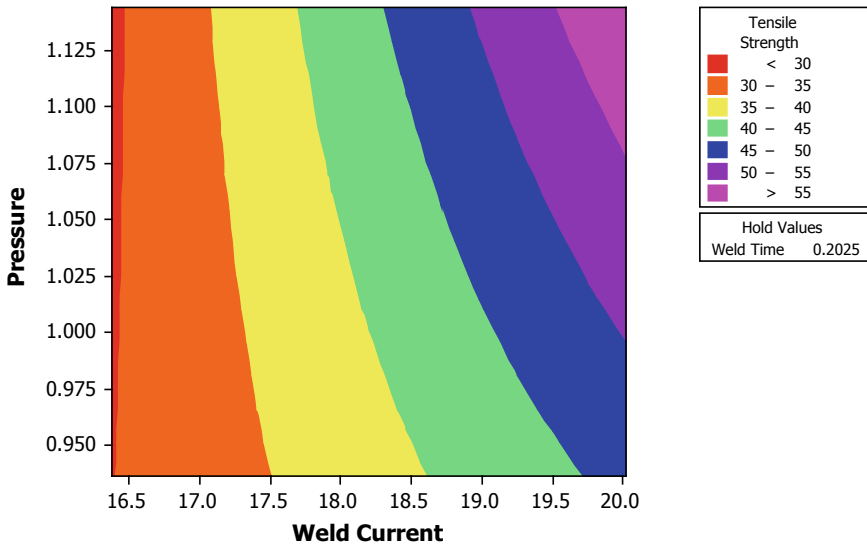
Fig. 17.4 Contour plot showing the weld current–pressure interaction effect

The large weld nugget formation has been established to contribute to the TSS of resistant spot weld joints (Aslanlar et al. 2008).

17.3.4　Confirmation Test

Confirmation test was performed to validate the generated model. In this confirmation test, 5 points were taken from the contour plot (Fig. 17.4) with different set of parameters and their predicted values were taken from the contour plot, as shown in Fig. 17.5. One of the five samples (i.e. point 2 corresponding to $I = 18.18$ kA, $T = 0.2025$ ms, $P = 1.04$ bar) is a the typical set of parameters that is being used for RSW of 1.2 mm thick AA 5052 in a local metal sheet company in Malaysia (Coraza Systems Malaysia Sdn. Bhd.). The experimental data were also obtained for these five parametric settings following the similar procedures explained in Sect. 17.2 of this manuscript. Both the predicted and experimental results obtained at the five parametric settings are presented and compared in Table 17.9.

　　The deviation between the predicted and experimental results obtained from the confirmation tests is no more than 3% for all the five selected points (parametric settings) on the contour plot (see Fig. 17.5). This is a further confirmation that the model is fairly accurate. The results obtained for the confirmation test sample 2 (~41 MPa) shows that the local metal sheet company in Malaysia (Coraza Systems Malaysia Sdn. Bhd.) has not been operating with the optimal parameters. The findings
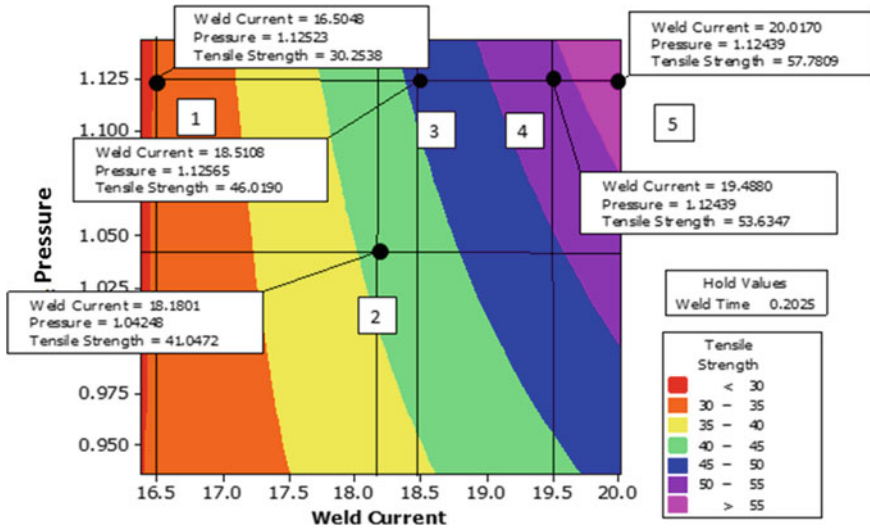
Fig. 17.5 Contour plot showing predicted values of TSS at some selected parametric settings

Table 17.9 Confirmation test results

Sample	Parametric setting			Nugget size (mm)	Tensile shear strength (Mpa)		
	Weld current (kA)	Weld time (ms)	Weld pressure (bar)		Experimental	Predicted	Error (%)
1	16.5	0.225	1.125	4.73	29.65	29.82	0.6
2	18.2	0.225	1.040	4.89	41.21	41.05	0.4
3	18.5	0.225	1.125	5.51	47.12	46.02	2.3
4	19.5	0.225	1.125	4.43	52.16	53.63	2.8
5	20.0	0.225	1.125	4.26	57.93	57.78	0.3

from this work show that Coraza Systems Malaysia Sdn. Bhd and any other sheet metal company can improve the quality of their 1.2 mm AA 5052-resistant spot welds by using the developed mathematical model.

17.4 Conclusion

Resistance spot welding of 1.2 mm thick AA 5052 has been investigated within a range of parameters (weld current, weld time and weld pressure), and a mathematical regression model predicting the tensile shear strength of the welds up to an accuracy of 88% has been successfully developed and validated. The TSS was found to vary

directly with nugget size. All the 11 fabricated weld nugget size conformed with the aerospace specification (AWS-D17.2) except for 2 samples produced at 16.38 kA, 0.2025 ms, 0.936 bar and 16.38 kA, 0.2025 ms, 1.144 bar which are below 4.32 mm. The sample produced at 20 kA weld current, 0.2475 ms weld time and 1.144 bar weld pressure exhibited the highest TSS (63.61 MPa) and nugget size (5.94 mm). The weld current has the most significant effect on the tensile shear strength of the weld. The generated contour plot for weld current–pressure interaction revealed that weld pressure is only significant when the current is up to about 19.5 kA (high) for the range of parameters utilised in this work.

References

Abioye, T.E., Mustar, N., Zuhailawati, H., Suhaina, I.: Parametric analysis of high power disk laser welding of 5052–H32 aluminium alloy. Mater. Today Proc. **17**, 599–608 (2019a)

Abioye, T.E., Mustar, N., Zuhailawati, H., Suhaina, I.: Prediction of the tensile strength of aluminium alloy 5052–H32 fibre laser weldments using regression analysis. Int. J. Adv. Manuf. Technol. **102**, 1951–1962 (2019b)

Abioye, T.E., Anas, N.M., Irfan, M.K., Anasyida, A.S., Zuhailawti, H.: Parametric optimization for resistance spot-welded thin-sheet aluminium alloy 5052–H32. Arab. J. Sci. Eng. **44**, 7617–7626 (2019c)

Aslanlar, S., Ogur, A., Ozsarac, U., Iihan, E.: Welding time effect on mechanical properties of automotive sheets in electrical resistance spot welding. Mater. Des. **29**(7), 1427–1431 (2008)

Din, N.A.M., Zuhailawati, H., Anasyida, A.S.: Resistance spot welding of AA5052 sheet metal of dissimilar thickness. IOP Conf. Ser. Mater. Sci. Eng. **114**(1), 012126 (2016). https://doi.org/10.1088/1757-899X/114/1/012126

Farayibi, P.K., Abioye, T.E., Clare, A.T.: A parametric study on laser cladding of Ti-6Al-4V wire and WC/W_2C powder. Int. J. Adv. Manuf. Technol. **87**(9–12), 3349–3358 (2016)

Florea, R.S., Solanki, K.N., Bammann, D.J., Baird, J.C., Jordon, J.B., Castanier, M.P.: Resistance spot welding of 6061–T6 aluminium: failure loads and deformation. Mater. Des. **34**, 624–630 (2012). https://doi.org/10.1016/j.matdes.2011.05.017

Fukumoto, S., Lum, I., Biro, E., Boomer, D.R., Zhou, Y.: Effects of electrode degradation on electrode life in resistance spot welding of aluminium alloy 5182. Weld. J. New York **82**(11), 307 (2003). https://doi.org/10.1016/j.jmapro.2017.02.003

Han, L., Thornton, M., Boomer, D., Shergold, M.: A correlation study of mechanical strength of resistance spot welding of AA5754 aluminium alloy. J. Mater. Process. Technol. **211**, 513–521 (2011)

Kim, J.K., Lim, H.S., Cho, J.H., Kim, C.H.: Bead-on-plate weldability of Al 5052 alloy using a disk laser. J. Achievements Mater. Manuf. Eng. **28**(2), 187–190 (2008)

Lum, I., Biro, E., Zhou, Y., Fukumoto, S., Boomer, D.R.: Electrode pitting in resistance spot welding of aluminium alloy 5182. Metall. Mater. Trans. A **35**(1), 217–226 (2004). https://doi.org/10.1007/s11661-004-0122-8

Luo, Z., Ao, S., Chao, Y.J., Cui, X., Li, Y., Lin, Y.: Application of pre-heating to improve the consistency and quality in AA5052 resistance spot welding. J. Mater. Eng. Perform. **24**, 3881–3891 (2015). https://doi.org/10.1007/s11665-015-1704-x

Manladan, S.M., Yusof, F., Ramesh, S., Fadzil, M., Ao, S.: A review on resistance spot welding of aluminium alloys. Int. J. Adv. Manuf. Technol. **90**, 605–634 (2017)

Muhamad Nabil, F.H., Syazfiqa, F.M., Zuhailawati, H., Abioye, T.E., Anasyida, A.S.: Parametric optimization of friction stir welding of dissimilar Al 5083 and Al 6061 alloys by using taguchi method. AIP Conf. Proc. **2267**, 020071 (2020). https://doi.org/10.1063/5.0015725

Rashid, M., Medley, J.B., Zhou, Y.: Nugget formation and growth during resistance spot welding of aluminium alloy 5182. Can. Metall. Q. **50**(1), 61–71 (2011). https://doi.org/10.1179/000844 311X552322

Shanavas, S., Dhas, J.E.R., Murugan, N.: Weldability of marine grade AA 5052 aluminium alloy by underwater friction stir welding. Int. J. Adv. Manuf. Technol. **95**, 4535–4546 (2018)

Vedrtnam, A., Singh, G., Kumar, A.: Optimizing submerged arc welding using response surface methodology, regression analysis, and genetic algorithm. Defence Technol. **14**, 204–212 (2018)

Wang, Y., Tao, W., Yang, S.: A method for improving joint strength of resistance spot welds of AA 5182-O aluminum alloy. J. Manuf. Proc. **45**, 661–669 (2017)

Zhang, W.H., Qiu, X.M., Sun, D.Q., Han, L.J.: Effects of resistance spot welding parameters on microstructures and mechanical properties of dissimilar material joints of galvanised high strength steel and aluminium alloy. Sci. Technol. Weld. Joining **16**(2), 153–161 (2011)

Zhao, D., Wang, Y., Liang, D., Zhang, P.: Modelling and process analysis of resistance spot welded DP600 joints based on regression analysis. Mater. Des. **110**, 676–684 (2016)

Zohoori-Shoar, V., Eslami, A., Karimzadeh, F., Abbasi-Baharanchi, M.: Resistance spot welding of ultrafine grained/nanostructured al 6061 alloy produced by cryorolling process and evaluation of weldment properties. J. Manuf. Proc. **26**, 84–93 (2017)